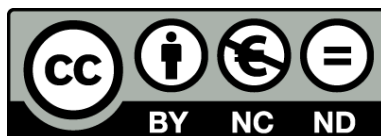




UNIVERSITAT DE
BARCELONA

Metal selenide-based cathodes for high-performance lithium-sulfur batteries

Dawei Yang



Aquesta tesi doctoral està subjecta a la llicència **Reconeixement- NoComercial – SenseObraDerivada 4.0. Espanya de Creative Commons.**

Esta tesis doctoral está sujeta a la licencia **Reconocimiento - NoComercial – SinObraDerivada 4.0. España de Creative Commons.**

This doctoral thesis is licensed under the **Creative Commons Attribution-NonCommercial-NoDerivs 4.0. Spain License.**

Tesi doctoral

Metal selenide-based cathodes for high-
performance lithium-sulfur batteries

Autor:

Dawei Yang

Director:

Prof. Andreu Cabot



UNIVERSITAT_{DE}
BARCELONA

Metal selenide-based cathodes for high-performance lithium-sulfur batteries

Memòria presentada per optar al grau de doctor per la
Universitat de Barcelona

Programa de doctorat en Nanociència

Autora:

Dawei Yang

Director:

Prof. Andreu Cabot

Tutor:

Prof. Frank Güell Vilà

Dawei Yang

Lloc on s'ha dut a terme la tesi

Institut de Recerca en Energia de Catalunya (IREC)



UNIVERSITAT DE
BARCELONA

Contents

Acknowledgements	6
List of publications	8
Authors' contributions	9
Preface	12
Summary of results	13
Resumen de Resultados	16
Acronyms	19
Chapter 1	21
1.1 Background	21
1.2 Principles of Lithium-Sulfur Batteries	22
1.3 Challenges of Lithium-Sulfur Batteries	24
1.3.1 The insulating nature of sulfur and Li_2S	24
1.3.2 High solubility of intermediate polysulfides in the electrolyte	25
1.3.3 The volume expansion going from sulfur to Li_2S upon lithiation	26
1.4 Potential solutions to the challenges of the sulfur cathode	26
1.4.1 Designing hosts based on physisorption	27
1.4.2 Designing hosts based on chemisorption	28
1.4.3 Designing hosts based on electrocatalysis	29
1.5 Strategies for improved adsorption-catalysis-conversion of LiPS	29
1.5.1 Heterostructure engineering	29
1.5.2 Doping engineering	30
1.5.3 Defect engineering	31
1.6 Sulfur hosts nanomaterial synthetic approaches	32
1.6.1 Kirkendall Effect	32
1.6.2 Colloidal synthesis in organic solvents	32
1.6.3 Aqueous synthesis method	33
1.7 Objectives	33
1.8 References	35
Chapter 2 ZnSe/N-doped Carbon Nanoreactor with multiple adsorption sites for Stable Lithium-Sulfur Batteries	40

2.1 Abstract	40
2.2 Introduction	41
2.3 Experimental section	42
2.4 Results and discussions	45
2.4 Conclusions	68
2.6 References	69
Chapter 3 NbSe₂ Meets C₂N: A 2D-2D Heterostructure Catalysts as Multifunctional Polysulfide Mediator in Ultra-Long-Life Lithium-Sulfur Batteries.....	73
3.1 Abstract	73
3.2 Introduction	74
3.3 Experimental section	75
3.4 Results and discussions	79
3.5 Conclusions	104
3.6 References	105
Chapter 4 Enhanced Polysulfide Conversion with Highly Conductive and Electrocatalytic Iodine-Doped Bismuth Selenide Nanosheets in Lithium-Sulfur Batteries	109
4.1 Abstract	109
4.2 Introduction	109
4.3 Experimental section	111
4.4 Results and discussions	114
4.5 Conclusions	132
4.6 References	132
Result and Discussions	137
Conclusions	139
Future work	141
CURRICULUM VITAE	142
Annex.....	146

Acknowledgements

Four years have passed so quickly. My graduation is just around the corner. I still remember my ignorant appearance when I just went abroad four years ago. I have learned a lot in the past four years, and I have grown a lot. I will never forget it.

First of all, I would like to thank my supervisor Prof. Andreu Cabot. Thank you for your guidance and help in the past few years. Your attitude and ability to scientific research are admirable and deeply touched me. Thank you for respecting each of our scientific research ideas and for giving guidance calmly, teaching me how to do scientific research better, and helping me publish papers. Thank you for your usual encouragement, patience, and help to make me a better version of myself.

Secondly, I would like to express my sincere gratitude to all the members of Functional Nanomaterials Group at IREC: Yu Liu, Yu Zhang, Junfeng Liu, Xiaoting Yu, Junshan Li, Yong Zuo, Chaoqi Zhang, Ruifeng Du, Mengyao Li, Congcong Xing, Xiang Wang, Zhifu Liang, Ke Xiao, Bingfei Nan, Canhuang Li, Ren He, Guifang Zeng, Xuan Lu, Xueqiang Qi, Evgenii Liashenko, Taisiia Berestok, Alberto Ramón Ferrer, Sergi V. S, Guillem Montaña, Pablo Guardia, thank you for all your caring, sharing, helping and discussing in the past four years, I feel very lucky to be one of the group. I will never forget many memorable funny moments in these years.

Also, I am grateful to Prof. Jordi Arbiol, Ting Zhang, Xu Han, Marc Botifoll and Maria Chiara Spadaro for checking the wonderful HRTEM of my samples. Those nice HRTEM images really play an important role in my project and publications. Thank you very much for all your help.

I would also like to thank Prof. Jordi Llorca for helping with the XPS measurement. Thank you for your great patience to arrange the meetings every time for discussing and sending us results with detailed XPS data analysis.

I would also like to thank to Prof. Joan Ramon Morante, who supplied many instruments, thanks Dr. Jordi Jacas Biendicho performed many measurements and corrections of the paper work and many valuable comments. Thank you as always for your help.

I also need to thank the “China Scholarship Council” for providing me the financial support that I am able to focus on my PhD research work abroad.

Finally, I would like to thank my family, my parents, my sister, and my good friends in China. Thank you for your continued support and encouragement. Thank you for listening to my grievances many times and alleviating my anxiety. Thank my parents for supporting my every important decision, my growth all the way is inseparable from your silent support. And, I also want to thank myself for being persistent and optimistic about life. You deserve everything you want. Wait for you to go through all the bitter will meet all the sweet.

List of publications

My PhD research work has been disseminated in three manuscripts, which have already been published or accepted in peer-reviewed journals. A full copy of each of the publications can be found in the Annex part. The following is the list of publications included in this thesis:

1. **Dawei Yang**, Chaoqi Zhang, Jordi Jacas Biendicho, Xu Han, Zhifu Liang, Ruifeng Du, Mengyao Li, Junshan Li, Jordi Arbiol, Jordi Llorca, Yingtang Zhou, Joan Ramon Morante, and Andreu Cabot, *ZnSe/N-Doped Carbon Nanoreactor with Multiple Adsorption Sites for Stable Lithium–Sulfur Batteries*. *ACS Nano* 2020, 14, 11, 15492–15504.
2. **Dawei Yang**, Zhifu Liang, Chaoqi Zhang, Jordi Jacas Biendicho, Marc Botifoll, Maria Chiara Spadaro, Qiulin Chen, Mengyao Li, Alberto Ramon, Ahmad Ostovari Moghaddam, Jordi Llorca, Jiaao Wang, Joan Ramon Morante, Jordi Arbiol, Shu-Lei Chou, Andreu Cabot, *NbSe₂ Meets C₂N: A 2D-2D Heterostructure Catalysts as Multifunctional Polysulfide Mediator in Ultra-Long-Life Lithium–Sulfur Batteries*. *Adv. Energy Mater.* 2021, 11, 2101250.
3. Mengyao Li⁺, **Dawei Yang^{+*}**, (Co-first author and corresponding author) Jordi Jacas Biendicho, Xu Han, Chaoqi Zhang, Kun Liu, Jiefeng Diao, Junshan Li, Marc Heggen, Rafal E. Dunin-Borkowski, Jiaao Wang, Graeme Henkelman, Joan Ramon Morante, Jordi Arbiol, Shu-Lei Chou, Andreu Cabot, *Enhanced Polysulfide Conversion with Highly Conductive and Electrocatalytic Iodine-Doped Bismuth Selenide Nanosheets in Lithium-Sulfur Batteries*. *Adv. Funct. Mater.* 2022, 2200529

Authors' contributions

The work within this thesis was carried out at Advanced Material Research Department in the Catalonia Institute for Energy Research. Dawei Yang, as PhD student, contributed to the experimental work, data analysis and manuscript writing for all the publications presented in this thesis. The contributions of co-authors for each article are shown below this paragraph. The impact factor in 2021 of the journals where the manuscripts were published is provided. All of the publications belong to the 1st quartile according to the Science Citation Index. None of these papers has been previously presented in any other PhD thesis. In all the publications, Andreu Cabot conceived and guided the projects, participated in the experiment design and manuscript writing.

Chapter 2:

Dawei Yang, Chaoqi Zhang, Jordi Jacas Biendicho, Xu Han, Zhifu Liang, Ruifeng Du, Mengyao Li, Junshan Li, Jordi Arbiol, Jordi Llorca, Yingtang Zhou, Joan Ramon Morante, and Andreu Cabot, *ZnSe/N-Doped Carbon Nanoreactor with Multiple Adsorption Sites for Stable Lithium–Sulfur Batteries*. *ACS Nano* 2020, 14, 11, 15492–15504.

Impact factor 2021: **15.881**

In this work, Dawei Yang designed the experiments, produced the nanomaterials and wrote the first draft of the manuscript. Chaoqi Zhang and Jordi Jacas Biendicho participated in part of the battery performance test. Ruifeng Du, Mengyao Li, Junshan Li and Joan Ramon Morante participated in data analysis. Yingtang Zhou performed the DFT calculations. Xu Han, Zhifu Liang and J. Arbiol participated in High Resolution TEM characterization, Jordi Llorca participated in X-ray photoelectron spectroscopy measurement. A. Cabot conceived and guided the project and supervised the work. The manuscript was corrected and improved by all authors.

Chapter 3:

Dawei Yang, Zhifu Liang, Chaoqi Zhang, Jordi Jacas Biendicho, Marc Botifoll, Maria Chiara Spadaro, Qiulin Chen, Mengyao Li, Alberto Ramon, Ahmad Ostovari Moghaddam, Jordi Llorca, Jiaao Wang, Joan Ramon Morante, Jordi Arbiol, Shu-Lei Chou, Andreu Cabot, *NbSe₂*

Meets C₂N: A 2D-2D Heterostructure Catalysts as Multifunctional Polysulfide Mediator in Ultra-Long-Life Lithium–Sulfur Batteries. *Adv. Energy Mater.* 2021, 11, 2101250.

Impact factor 2021: **29.368**

In this work, Dawei Yang, Chaoqi Zhang, Shu-Lei Chou and Andreu Cabot designed the experiment. Dawei Yang carried out the XRD, SEM, TGA, EDS, material preparation and electrochemical experiments. Zhifu Liang conducted the UV-Vis Spectrum and synthesized the part of materials. Zhifu Liang, Marc Botifoll, Maria Chiara Spadaro and Jordi Arbiol helped with the TEM, HRTEM, STEM-EELS maps experiments. Jordi Jacas Biendicho, Joan Ramon Morante participated part of the experiment of battery performances and involved in the scientific discussions. Mengyao Li performed the BET experiment with data collection and analysis. Jiaao Wang designed and conducted the DFT calculations. Qiulin Chen participated part of the DFT calculations. Jordi Llorca and Alberto Ramon carried out the XPS spectrum experiments. Ahmad Ostovari Moghaddam helped with the design of the TOC. Dawei Yang wrote the first draft of the manuscript. Dawei Yang, Chaoqi Zhang, Shu-Lei Chou and Andreu Cabot co-revised the manuscript in detail and all authors edited the manuscript.

Chapter 4:

Mengyao Li[†], **Dawei Yang^{+*}**, (Co-first author and corresponding author) Jordi Jacas Biendicho, Xu Han, Chaoqi Zhang, Kun Liu, Jiefeng Diao, Junshan Li, Marc Heggen, Rafal E. Dunin-Borkowski, Jiaao Wang, Graeme Henkelman, Joan Ramon Morante, Jordi Arbiol, Shu-Lei Chou, Andreu Cabot, Enhanced Polysulfide Conversion with Highly Conductive and Electrocatalytic Iodine-Doped Bismuth Selenide Nanosheets in Lithium-Sulfur Batteries. *Adv. Funct. Mater.*

Impact factor 2021: **18.808**

In this work, Dawei Yang, Mengyao Li, Shu-Lei Chou and Andreu Cabot conceived the concept and designed the experiment. Dawei Yang and Mengyao Li conducted the material preparation and electrochemical experiments. Xu Han, Marc Heggen, Rafal E. Dunin-Borkowski, and Jordi Arbiol helped with the morphology characterizations. Jordi Jacas Biendicho, Chaoqi Zhang and Joan Ramon Morante participated part of the experiment of battery performances. Junshan Li

and Kun Liu performed the BET experiments with data collection and analysis. Jiefeng Diao, Jiaao Wang and Graeme Henkelman designed and conducted the DFT calculations. Jordi Llorca carried out the XPS spectrum experiments. Dawei Yang and Mengyao Li wrote the paper. Dawei Yang, Mengyao Li, Shu-Lei Chou and Andreu Cabot co-revised the manuscript in detail and all authors edited the manuscript.

Prof. Andreu Cabot

Certify the information provided above is true.

Barcelona, 25th of March 2022

Preface

The chapters included in this PhD thesis cover the work developed by the PhD candidate Dawei Yang at the Catalonia Institute for Energy Research (IREC) in Sant Adrià de Besòs, Barcelona, in the period 2018-2022, supported by China Scholarship Council (No. 201806090276). The thesis is particularly focused on the construction of high-performance lithium-sulfur batteries (LSBs) based on metal selenide cathodes.

This thesis consists of four chapters. The first chapter mainly introduces the basic concepts of LSBs, as well as the current development status and the remaining challenges. Chapters 2 to 4 detail the investigation I performed in this field. With the overall goal of constructing metal selenide-based high-performance cathode materials for LSBs, the work presented in this thesis aims to address the following challenges: 1) Production of hollow-structured nanomaterials. 2) Production of materials with a high specific surface area and tuned electronic properties by combining two-dimensional materials to form a heterostructure. 3) Increase the conductivity of nanomaterials by doping with non-metallic elements. More specifically, in Chapter 2, a hollow nanoreactor structure, ZnSe/N-doped hollow carbon (ZnSe/NHC), is synthesized by a one-step selenization process. Within a LSB cathode, this composite not only efficiently traps lithium polysulfides (LiPS), but also can tune the volume expansion to prevent damage to the positive electrode due to the hollow design. In Chapter 3, I propose the synthesis of C₂N framework-supported NbSe₂ (C₂N@NbSe₂) nanosheets by a simple two-step method. The obtained material has a high specific surface area and is highly suitable as a cathode host material to tune the shuttle effect of LiPS and the Li-S conversion process. In Chapter 4, I demonstrate Bi₂Se₃ nanosheets doped with I to enhance the performance of LSBs.

Summary of results

Benefiting from an excitingly high energy density up to 2600 Wh kg^{-1} , lithium-sulfur batteries (LSBs) have attracted extensive research interest for the development of advanced energy storage technology that outperforms state-of-the-art lithium-ion batteries (LIBs). Moreover, the natural abundance and nontoxic nature of sulfur lead to economic benefits and environmental benignity, which particularly favor large-scale applications. Despite the convincing merits, the practical implementation of LSBs still suffers from several intractable technical challenges, such as the electrical resistivity of sulfur, the dissolution of lithium polysulfides (LiPS) with a severe shuttle effect, and the large volume variation during battery cycling, which seriously hinder this technology from yielding practically viable energy density and cyclability.

In response to these obstacles, the development of multifunctional sulfur hosts has emerged as a promising strategy to confine the sulfur species within the cathodic chamber, thus realizing effective inhibition of polysulfide shuttling and enhancement of the battery performance. With this new insight, much effort is devoted to searching for alternative materials with several specific properties that can make themselves the ideal cathodes for LSBs. Among all the candidates, metal selenides (MSe) stood out and have gained increasing attention in recent years. They are promising due to their strong adsorption to LiPS and electrocatalytic behaviours that can significantly accelerate the kinetic of the $\text{S} \leftrightarrow \text{LiPS} \leftrightarrow \text{Li}_2\text{S}_2/\text{Li}_2\text{S}$ conversion. Besides, they are relatively more cost-efficient than noble metals and much more conductive than the corresponding metal oxides/sulfides. The focus of this thesis is to develop MSe-based nanomaterials as sulfur host materials to improve the rate capability and cycling life of LSBs. The main research objectives are: a) Exploring earth abundant, low-cost and less toxic materials with high LSBs performance; b) Developing simple, scalable and cost-effective methodologies to produce LSBs materials and devices; c) Optimize the material conductivity via doping engineering. d) Design the heterojunction structures to meet the specific requirements of LSBs.

The thesis is divided into 4 chapters. Chapter 1 introduces the research status and development prospects of LSBs materials, and particularly cathode host materials. Chapter 2 proposes a MSe both as adsorber and catalyst and a nanoreactor architecture, ZnSe/N-doped hollow carbon

(ZnSe/NHC), to confine the LiPSs and accommodate volume changes. It demonstrates both experimentally and using density functional theory (DFT), that this material combination and the hollow geometry of the reactors provide three key benefits to the LSBs cathode: i) A highly effective trapping of LiPS due to the combination of sulfiphilic sites of ZnSe, lithiophilic sites of NHC and the confinement effect of the cage-based structure; ii) A redox kinetic improvement in part associated with the multiple adsorption sites that facilitate the Li⁺ diffusion; and iii) an easier accommodation of the volume expansion preventing the cathode damage due to the hollow design. As a result, LSBs cathodes based on S@ZnSe/NHC are characterized by high initial capacities, superior rate capability, and an excellent stability. Overall, this work not only demonstrates the large potential of MSe as cathode materials in LSBs, but also probes the nanoreactor design to be a highly suitable architecture to enhance cycle stability. The results in Chapter 2 were published in *ACS Nano* in 2020.

Chapter 3 presents an in-situ grown C₂N@NbSe₂ heterostructure with remarkable specific surface area as Li-S catalyst and LiPS absorber. DFT calculations and experimental results comprehensively demonstrate that C₂N@NbSe₂ is characterized by a suitable electronic structure and charge rearrangement that strongly accelerates the LiPS electrocatalytic conversion. Besides, heterostructured C₂N@NbSe₂ strongly interacts with LiPS species, confining them at the cathode. As a result, LSBs cathodes based on C₂N@NbSe₂/S exhibit a high initial capacity of 1545 mAh g⁻¹ at 0.1 C. Even more exciting, C₂N@NbSe₂/S cathodes are characterized by impressive cycling stability with only 0.012% capacity decay per cycle after 2000 cycles at 3 C. Even at a sulfur loading of 5.6 mg cm⁻², a high areal capacity of 5.65 mAh cm⁻² is delivered. These results demonstrate that C₂N@NbSe₂ heterostructures can act as multifunctional polysulfide mediators to chemically adsorb LiPS, accelerate Li-ion diffusion, chemically catalyze LiPS conversion, and lower the energy barrier for Li₂S precipitation/decomposition, realizing the “adsorption-diffusion-conversion” of polysulfides. The results were published in *Adv. Energy Mater.* in 2021.

Chapter 4 reports an innovative sulfur host, based on an iodine-doped bismuth selenide (I-Bi₂Se₃), able to solve the LSB limitations by immobilizing the LiPS and catalytically activating the redox conversion at the cathode. We detail here the synthesis of I-Bi₂Se₃ nanosheets and

thoroughly characterize their morphology, crystal structure and composition. We use DFT and experimental tools to demonstrate that I-Bi₂Se₃ nanosheets are characterized by a proper composition and micro- and nano-structure to facilitate Li⁺ diffusion and fast electron transportation, and to provide numerous surface sites with strong LiPS adsorbability and extraordinary catalytic activity. Overall, I-Bi₂Se₃/S electrodes exhibit outstanding initial capacities up to 1500 mAh g⁻¹ at 0.1 C and cycling stability over 1000 cycles, with an average capacity decay rate of only 0.012% per cycle at 1 C. Besides, at a sulfur loading of 5.2 mg cm⁻², a high areal capacity of 5.70 mAh cm⁻² at 0.1 C is obtained with an electrolyte/sulfur ratio of 12 μL mg⁻¹. This work demonstrated the doping is an effective way to optimize the metal selenide catalysts in LSBs. The results have been published in *Adv. Funct. Mater.* in 2022.

Finally, the main conclusions of this thesis and some perspectives for future work are presented.

Resumen de Resultados

Beneficiándose de la enorme densidad de energía de hasta 2600 Wh kg^{-1} , las baterías de litio-azufre (LSB) han atraído un amplio interés para el desarrollo de tecnología avanzada de almacenamiento de energía que supera a las baterías de iones de litio de última generación. Además, la abundancia natural y la naturaleza no tóxica del azufre conducen a beneficios económicos y benignidad ambiental, que favorecen particularmente las aplicaciones a gran escala. A pesar de los méritos convincentes, la implementación práctica de las LSB todavía sufre varios desafíos técnicos, como la resistividad eléctrica del azufre, la disolución de polisulfuros de litio (LiPS) con un efecto de lanzadera severo y la gran variación de volumen durante el ciclo de la batería, que dificultan seriamente que esta tecnología produzca densidad de energía y ciclabilidad prácticamente viables.

En respuesta a estas limitaciones, el desarrollo de hosts multifuncionales de azufre ha surgido como una estrategia prometedora para confinar las especies de azufre dentro de la cámara catódica, logrando así una inhibición eficaz del transporte de polisulfuro y una mejora del rendimiento de la batería. Con esta nueva perspectiva, se dedica mucho esfuerzo a la búsqueda de materiales alternativos con varias propiedades específicas que puedan convertirse en cátodos ideales para LSB. Entre todos los candidatos, los seleniuros de metales (MSe) se destacaron y han ganado una atención creciente en los últimos años. Son prometedores debido a su fuerte adsorción a LiPS y comportamientos electrocatalíticos que pueden acelerar significativamente la cinética de la conversión $\text{S} \leftrightarrow \text{LiPS} \leftrightarrow \text{Li}_2\text{S}_2/\text{Li}_2\text{S}$. Además, son relativamente más rentables que los metales nobles y mucho más conductores que los óxidos/sulfuros metálicos correspondientes. El objetivo de esta tesis es desarrollar nanomateriales basados en MSe como materiales host de azufre para mejorar la capacidad de velocidad y la vida útil de las LSB. Los principales objetivos de la investigación son: a) Explorar materiales abundantes en la tierra, de bajo costo y menos tóxicos con un alto rendimiento en LSB; b) Desarrollar metodologías simples, escalables y rentables para producir materiales para el cátodo de LSBs y celdas; c) Optimizar la conductividad mediante ingeniería de dopaje. d) Diseñar las estructuras de

heterounión para cumplir potencialmente con los requisitos específicos para la mejora de las LSB.

La tesis está dividida en 4 capítulos. El Capítulo 1 presenta el estado de la investigación y las perspectivas de desarrollo de los materiales para LSB y en particular para su cátodo. El capítulo 2 propone un MSe como adsorbente y catalizador y una arquitectura de nanorreactor, carbono hueco dopado con ZnSe/N (ZnSe/NHC), para atrapar los LiPs y acomodar cambios de volumen. En este capítulo, se demuestra tanto experimentalmente como utilizando la teoría de densidad funcional (DFT), que esta combinación de materiales y la geometría hueca de los reactores brindan tres beneficios clave al cátodo de las LSB: i) Una captura altamente efectiva de LiPS debido a la combinación de sitios sulfófilos de ZnSe, sitios litiofílicos de NHC y el efecto de confinamiento de la estructura basada en huecos; ii) Una mejora de la cinética redox en parte asociada con los múltiples sitios de adsorción que facilitan la difusión de Li^+ ; y iii) una acomodación más fácil de la expansión del volumen evitando el daño del cátodo debido al diseño hueco. Como resultado, los cátodos LSB basados en S@ZnSe/NHC se caracterizan por una alta capacidad inicial, capacidad de ciclado más rápido y una excelente estabilidad. En general, este trabajo no solo demuestra el gran potencial de los MSe como materiales de cátodo en LSB, sino que también prueba que el diseño del nanorreactor es una arquitectura muy adecuada para mejorar la estabilidad del ciclado. Los resultados del Capítulo 2 se publicaron en *ACS Nano* en 2020.

El capítulo 3 presenta una heteroestructura $\text{C}_2\text{N@NbSe}_2$ crecida *in situ* con una superficie específica notable como catalizador de Li-S y adsorbente de LiPS. Los cálculos DFT y los resultados experimentales demuestran de forma exhaustiva que el $\text{C}_2\text{N@NbSe}_2$ se caracteriza por una estructura electrónica adecuada y un reordenamiento de carga que acelera considerablemente la conversión electrocatalítica de LiPS. Además, el $\text{C}_2\text{N@NbSe}_2$ heteroestructurado interactúa fuertemente con las especies de LiPS, confinándolas en el cátodo. Como resultado, los cátodos LSB basados en $\text{C}_2\text{N@NbSe}_2/\text{S}$ exhiben una alta capacidad inicial de 1545 mAh g^{-1} a $0,1 \text{ C}$. Aún más emocionante, los cátodos $\text{C}_2\text{N@NbSe}_2/\text{S}$ se caracterizan por una impresionante estabilidad cíclica con una disminución de capacidad de solo $0,012 \%$ por ciclo después de 2000 ciclos a 3 C . Incluso con una carga de azufre de $5,6 \text{ mg cm}^{-2}$, se entrega

una alta capacidad de área de 5,65 mAh cm⁻². Estos resultados demuestran que las heteroestructuras C₂N@NbSe₂ pueden actuar como mediadores de polisulfuro multifuncionales para adsorber químicamente LiPS, acelerar la difusión de iones de litio, catalizar químicamente la conversión de LiPS y reducir la barrera energética para la precipitación/descomposición de Li₂S, logrando la "adsorción-difusión-conversión". de polisulfuros. Los resultados fueron publicados en *Adv. Energy Mater.* en 2021.

El Capítulo 4 informa sobre un innovador host de azufre, basado en un seleniuro de bismuto dopado con yodo (I-Bi₂Se₃), capaz de resolver las actuales limitaciones de las LSB inmovilizando el LiPS y activando catalíticamente la conversión redox en el cátodo. Aquí detallamos la síntesis de nanoláminas de I-Bi₂Se₃ y caracterizamos minuciosamente su morfología, estructura cristalina y composición. Usamos DFT y herramientas experimentales para demostrar que las nanoláminas I-Bi₂Se₃ se caracterizan por una composición adecuada y una micro y nanoestructura para facilitar la difusión de Li⁺ y el transporte rápido de electrones, y para proporcionar numerosos sitios de superficie con una fuerte capacidad de adsorción de LiPS y extraordinaria actividad catalítica. En general, los electrodos I-Bi₂Se₃/S exhiben capacidades iniciales sobresalientes de hasta 1500 mAh g⁻¹ a 0,1 C y estabilidad de ciclo durante 1000 ciclos, con una tasa de disminución de capacidad promedio de solo 0,012 % por ciclo a 1 C. Además, con una carga de azufre de 5,2 mg cm⁻² se obtiene una alta capacidad areal de 5,70 mAh cm⁻² a 0,1 C con una relación electrolito/azufre de 12 μL mg⁻¹. Este trabajo demostró que el dopaje es una forma efectiva de optimizar los catalizadores de seleniuro metálico en LSB. Los resultados han sido publicados en *Adv. Función Mater.* en 2022.

Finalmente, se presentan las principales conclusiones de esta tesis y algunas perspectivas de trabajo futuro.

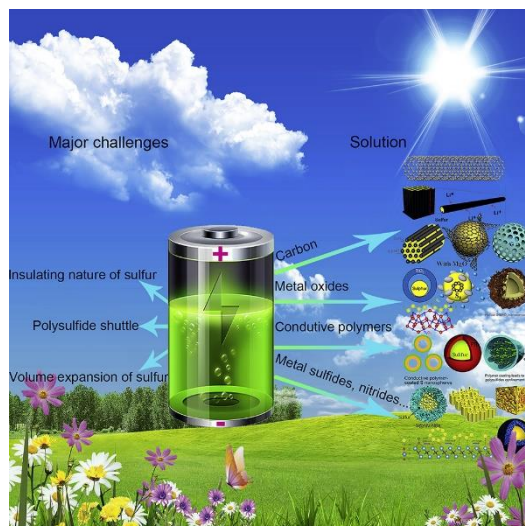
Acronyms

LiPS	Lithium polysulfides
LSBs	Lithium-sulfur batteries
LIBs	Lithium-ion batteries
MSe	Metal selenide
TMSe	Transition metal selenide
ΔE	Polarization potential
D_{Li^+}	Lithium ion diffusivity
C	Current rate
v	Scan rate
XRD	X-ray diffraction
SEM	Scanning electron microscopy
TEM	Transmission electron microscopy
STEM	Scanning transmission electron microscopy
HRTEM	High-resolution transmission electron microscopy
HAADF	High-angle annular dark-field imaging
EELS	Electron energy loss spectroscopy
DOS	Density of states
TGA	Thermogravimetric analysis
XPS	X-ray photoelectron spectroscopy
VASP	Vienna <i>ab initio</i> simulation package
GGA	Generalized gradient approximation
PBE	Perdew-Burke-Ernzerhof
EIS	Electrochemical impedance spectroscopy

BET	Brunauer–Emmett–Teller
DFT	Density functional theory
CV	Cyclic voltammetry
UV-vis	Ultraviolet-visible
EDX	Energy-dispersive X-ray
2D	Two-dimensional
Rct	Charge-transfer resistance
Eb	Binding energy
PVP	Polyvinyl pyrrolidone
NHC	N-doped hollow carbon
PVDF	Polyvinylidene difluoride
DOL	1,3-dioxolane
DME	1,2-dimethoxy ethane
LiTFSI	Lithium bis(trifluoromethanesulfonyl) imide
MMT	3-(4,5-dimethyl-2-thiazolyl)-2,5-diphenyl-2-H-tetrazolium bromide
DMF	N, N-dimethylformamide

Chapter 1

General Introduction



1.1 Background

With a rising world population, increasing energy demand and imminent climate change, there is significant emphasis today on creating a sustainable energy future for humanity while preserving our delicate environment at the same time.¹ To achieve this goal, we need to reduce our reliance on fossil fuels and turn to clean, renewable energy sources such as solar and wind power. However, the intermittent nature of these renewable sources necessitates advanced energy storage systems that can store the energy when it is present in excess and release it back to the grid on demand, in order to maintain a constant power supply to homes and industries.^{2,3} This is where batteries can play a crucial role because they represent an efficient means of storing and releasing energy electrochemically. Unfortunately, LIBs, which are commonly used in small portable electronics today, are unable to meet the high-energy demands of stationary grid energy storage.⁴⁻⁶ The limited energy density of these batteries also limits the widespread deployment of a variety of emerging mobile transport applications such as electric vehicles, which have much lower carbon dioxide emissions compared to gasoline-powered cars today.^{7,8} This has prompted an extensive worldwide search for new battery technologies that go beyond conventional LIBs.

LSBs represent a promising energy storage system that has drawn considerable attention due to their higher energy density compared to LIBs.⁹⁻¹² The key difference between these two forms of batteries lies in their mechanism of energy storage. LIBs operate based on intercalation of lithium ions into layered electrode materials, such as graphite anodes and lithium metal oxide cathodes.^{8,13} Because lithium ions can only be intercalated topotactically into certain specific sites, the theoretical energy density of LIBs is typically limited to $\sim 420 \text{ W h kg}^{-1}$ or 1400 W h L^{-1} (Figure 1).^{14,15} On the other hand, instead of intercalation, LSBs operate based on metal plating and stripping on the lithium anode side and a conversion reaction on the sulfur cathode side.^{8,14} The non-topotactic nature of these reactions endows lithium anodes and sulfur cathodes with high theoretical specific capacities of 3860 and 1673 mA h g^{-1} respectively. Together with an average cell voltage of 2.15 V, this gives LSBs a high theoretical energy density of $\sim 2500 \text{ W h kg}^{-1}$ or 2800 W h L^{-1} .¹⁶⁻¹⁸ Moreover, sulfur is cheap and readily abundant in the Earth's crust, which makes LSBs a particularly attractive and a potential low-cost energy storage technology.

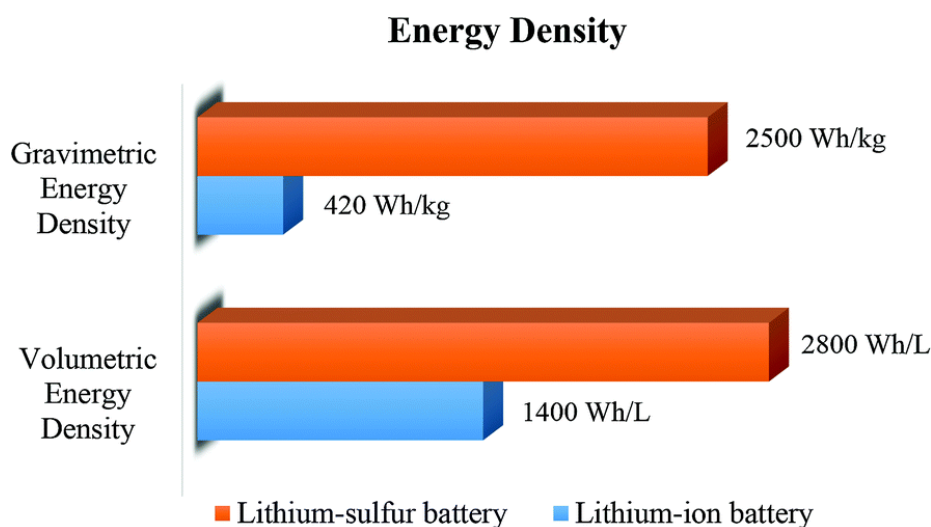


Figure 1. Energy density plots of lithium-sulfur vs. LIBs (based on graphite anodes and $\text{LiNi}_{1/3}\text{Mn}_{1/3}\text{Co}_{1/3}\text{O}_2$ cathodes).^{14,15}

1.2 Principles of Lithium-Sulfur Batteries

A Li-S cell is an electrochemical storage device through which electrical energy can be stored in sulfur electrodes. A schematic of the components in a single Li-S cell and its operation (charge and discharge) is shown in Figure 2.^{10,19} A conventional Li-S cell consists of a lithium metal anode, an organic electrolyte, and a sulfur composite cathode. Because sulfur is in the charged state, the cell operation starts with discharge. During the discharge reaction, the lithium

metal is oxidized at the negative electrode to produce lithium ions and electrons. The lithium ions produced move to the positive electrode through the electrolyte internally while the electrons travel to the positive electrode through the external electrical circuit, and thereby an electrical current is generated. Sulfur is reduced to produce lithium sulfide by accepting the lithium ions and electrons at the positive electrode. The reactions occurring during discharge are given below, and the backward reactions will occur during charge.²⁰⁻²⁴

Negative electrode: anodic reaction (oxidation, loss of electrons):



Positive electrode: cathodic reaction (reduction, gaining electrons):



Overall cell reaction (discharge):

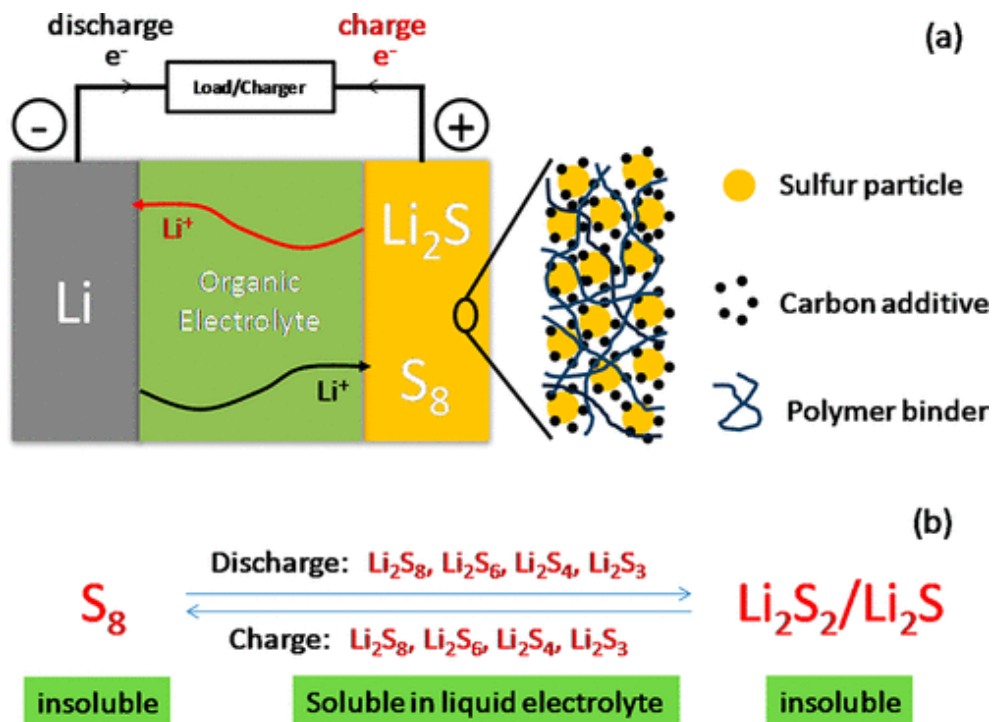
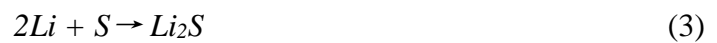


Figure 2. (a) Illustration of the charge (red)/discharge (black) process involved in a rechargeable Li-S cell consisting of lithium metal anode, organic electrolyte, and sulfur composite cathode and (b) charge/discharge process involving the formation of soluble LiPS (Li_2S_8 , Li_2S_6 , Li_2S_4 , and Li_2S_3) and insoluble Li_2S_2/Li_2S .¹⁹

The theoretical capacities of lithium and sulfur are 3.861 and 1.672 A h g⁻¹, respectively, which leads to a theoretical cell capacity of 1.167 A h g⁻¹ for the Li-S cell. The discharge reaction has an average cell voltage of 2.15 V. Hence, the theoretical gravimetric energy density for a Li-S cell is 2.51 W h g⁻¹.^{25,26}

Sulfur atoms show a strong tendency to catenation, forming long homoatomic chains or homocyclic rings of various sizes.²⁷ Octasulfur (cyclo-S₈), crystallizing at 25 °C as orthorhombic α-S₈, is the most stable allotrope at room temperature. During an ideal discharge process, cyclo-S₈ is reduced and the ring opens, resulting in the formation of high-order LiPS Li₂S_x (6 < x ≤ 8). As the discharge continues, lower order LiPS Li₂S_x (2 < x ≤ 6) are formed with the incorporation of additional lithium. There are two discharge plateaus at 2.3 and 2.1 V with ether-based liquid electrolytes, which represent the conversions of S₈ to Li₂S₄ and Li₂S₄ to Li₂S, respectively. At the end of discharge, Li₂S is formed, as shown in Figure 3.²⁸⁻³¹ During the following charge, Li₂S is converted to S₈ via the formation of the intermediate LiPS, resulting in a reversible cycle.³²⁻³⁴ However, the two charge voltage plateaus are normally overlapped with each other.

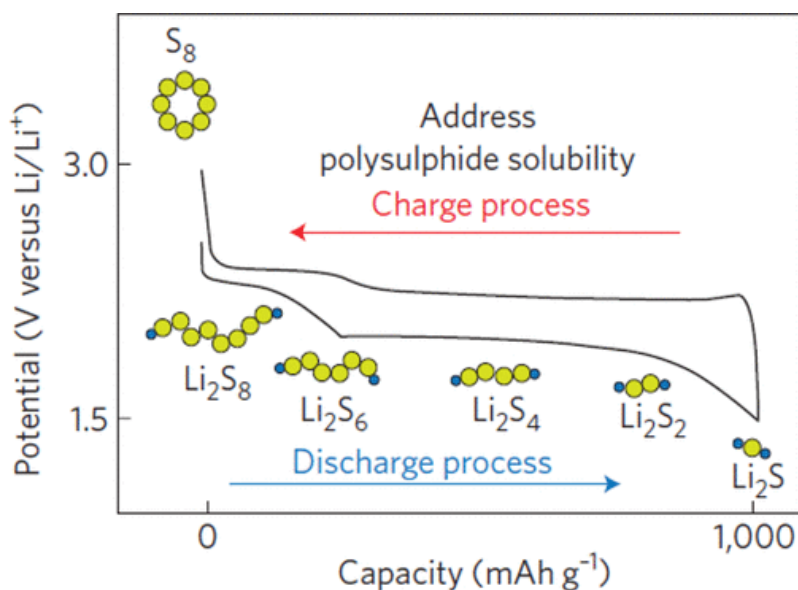


Figure 3. Voltage profiles of a Li-S cell.²⁸

1.3 Challenges of Lithium-Sulfur Batteries

1.3.1 The insulating nature of sulfur and Li₂S

Both sulfur and Li₂S are insulating for electrons and lithium ions, and this directly limits the electrochemical reactions and results in low utilization of the active material. In the upper

discharge plateau, despite the fast solid-liquid reaction kinetics, it is very challenging to achieve the theoretical capacity of 418 mAh g⁻¹. It has been reported that even after repeated cycles, unreacted sulfur still exists.³⁵ A uniform dispersion of sulfur and good electrical contact with conductive additives are required for the reduction of sulfur to long-chain polysulfides. In the lower discharge plateau, because the conversion reaction $\text{Li}_2\text{S}_2 + 2\text{Li}^+ + 2\text{e}^- \rightarrow 2\text{Li}_2\text{S}$ involves a solid-solid process, the polysulfides formed in the upper discharge plateau are difficult to completely reduce to Li₂S because of the sluggish reaction kinetics.³⁶ Theoretically, the capacity ratio of the lower discharge plateau to upper discharge plateau is expected to be 3,³⁷ but a value of ≈ 2.5 is more realistic. In practical conditions, the incorporation of sulfur in a conductive matrix is usually required,³⁷⁻⁴⁰ resulting in a decreased specific capacity. In addition, the common Li-S voltage profiles tend to show a higher polarization in the lower discharge plateau voltage due to limited kinetics for both electrons and lithium ions,^{41,42} which further results in a decrease in practical energy density.

1.3.2 High solubility of intermediate polysulfides in the electrolyte

LiPS generated during the conversion reaction are soluble in the most common organic electrolytes used for LSBs, which leads to some known problems, including low Coulombic efficiency, fast capacity decay, and high self-discharge rate.⁴³⁻⁴⁸ The details of their influence can be summarized as follows: 1) driven by the concentration gradient force (from the cathode to the anode), the soluble polysulfides migrate to the lithium anode where they are reduced to insoluble Li₂S, resulting in an irreversible loss of active material and passivation of the anode; 2) during charging, the migrating long-chain polysulfides are partially reduced to short-chain polysulfides by the lithium anode, which then shuttle back to the cathode driven by the electric field from the anode to the cathode, causing the well-known “shuttle effect” with low charging efficiency (Figure 4); 3) the repetitive dissolution and redeposition of active material species lead to a rearrangement of sulfur within the cathode, and this tends to passivate the cathode and increase the impedance due to the inhomogeneous distribution of insulating sulfur. Although the dissolution of polysulfides causes many problems, it is, on the other hand, essential for achieving high sulfur utilization. Since sulfur is not conductive, to ensure electron transport, which is a key factor during the electrochemical process, the reduction of sulfur can only take place on the surface of the conductive matrix. Due to the continuous dissolution of polysulfides, the remaining sulfur is exposed to the conductive matrix so that its reduction can progress. Therefore, the dissolution of polysulfides needs to be rationally balanced and controlled to achieve both high sulfur utilization and high cycling stability.

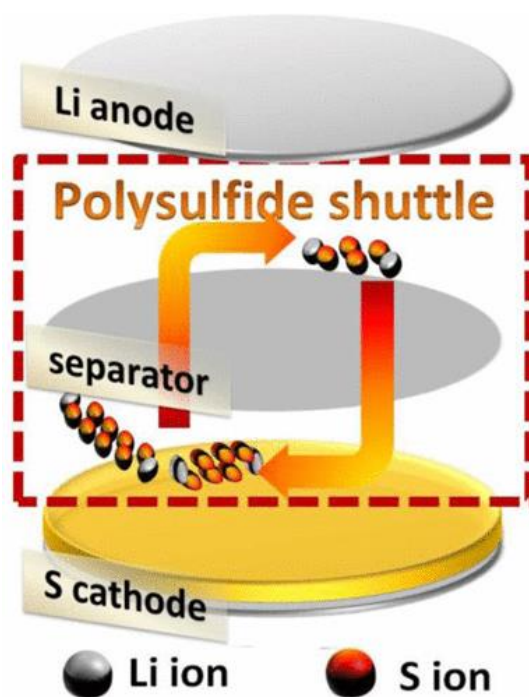


Figure 4. Illustration of the shuttle mechanism occurring in a Li-S cell.²⁸

1.3.3 The volume expansion going from sulfur to Li₂S upon lithiation

The density of octasulfur (2.07 g cm^{-3}) is higher than that of Li₂S (1.66 g cm^{-3}), resulting in a large volume expansion ($\approx 80\%$) upon lithiation.⁴⁹⁻⁵¹ The repeated volume variation of the electrode leads to pulverization of the cathode and the detachment of sulfur from the cathode conductive matrix. It is difficult for the isolated sulfur to be used in the following electrochemical reactions due to loss of electrical contact, resulting in a permanent capacity fade. In this regard, an appropriate void space needs to be provided to accommodate the volume change of the active material and preserve the structural integrity of the cathode, which leads to a decreased volumetric energy density of the cell. Indeed, due to the intrinsic low density of sulfur, the volumetric energy density of Li-S batteries is not expected to be much higher than that of state-of-the-art LIBs ($\approx 600 \text{ Wh L}^{-1}$).^{50,52,53} Therefore, the porosity of the electrode needs to be controlled for a balance between the volumetric energy density and performance.

1.4 Potential solutions to the challenges of the sulfur cathode

As discussed prior, insofar as these three challenges of sulfur cathode for LSBs have been identified, the promising solutions are constantly acclaimed, be it hosts, interlayers, binders, organosulfides or some combination of the four. To follow, new concepts and strategies have been testified by corresponding experimental and characterization methods. The number of highly cited articles relevant to host is the most among all the solutions, which is a result of

the interest of most researchers. As for the host design and synthesis, there is a rather obvious iteration in proposed concepts from earlier physisorption, succeeding chemisorption to current electrocatalysis, achieving strong anchor and fast conversion for S, LiPS and Li₂S within the electrode. These words frequently appear in the discussion regarding the experimental results. Conductive interlayer as a variant of host in the cathode is proposed and inserted between separator and cathode, which undertakes a crucial role in retarding the LiPS diffusion and accelerating its conversion rate. Polymer materials are also intensely explored in LiPS confinements, such as auxiliary coating and binder components. The latter is increasingly emphasized to function high mechanical adhesion and effective LiPS trapping simultaneously. Additionally, organosulfides are promising sulfur-based cathode materials alternative to current combination of sulfur and host (Figure 5). Only by understanding these origins behind the achievements, both knowledge and expertise are worthy of back tracing steps, helping guide us in the quest for ideal designs in electrode materials.

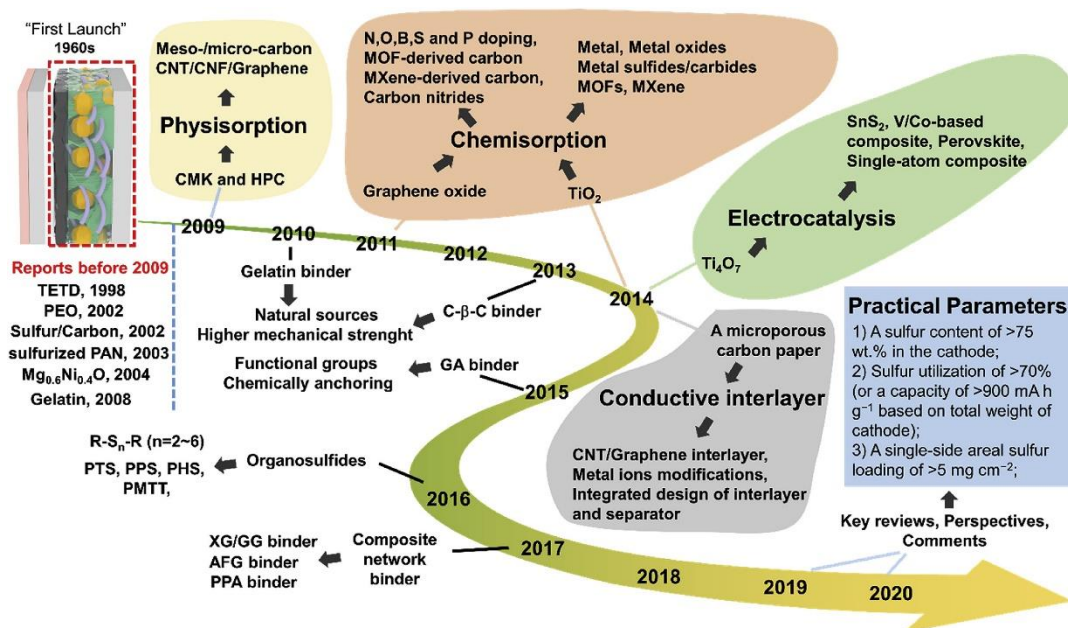


Figure 5. The timeline and derivations of these strategies in hosts, interlayers, binders or organosulfides.⁵⁴

1.4.1 Designing hosts based on physisorption

Strenuous efforts have been dedicated to solving the limitations of LSBs. For instance, most carbonaceous materials were used as the sulfur host at the cathode to improve the conductivity of sulfur cathodes, including porous carbon,⁵⁵ carbon nanotube,⁵⁶ graphene,⁵⁷ and nanofibers.⁵⁸ For example, a highly ordered mesoporous carbon (CMK-3) framework was fabricated to

encapsulate sulfur within the mesopore channels by a melting diffusion method and generated an intimate electrical contact with the insulating sulfur (Figure 6). The SBA-15 silica was employed as template for preparing the ordered mesoporous carbon (CMK-3). This CMK-3 carbon exhibited uniform and narrow mesopore diameter of 3.33 nm, good conductivity of 0.20 S cm⁻¹, and large pore volume of 2.1 cm³ g⁻¹. The sulfur content in CMK-3-sulfur composite was optimized to 60-70 wt%, which was lower than the theoretical value (79 wt%). The ordered mesoporous carbon could accommodate the volumetric expansion of sulfur during the charge/discharge process and provide lithium-ion diffusion channel.^{11,59} This has become the most popular method to synthesize various porous carbons for sulfur encapsulation.

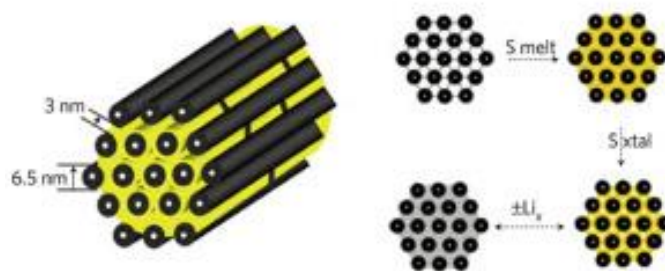


Figure 6. Schematic illustration of the unique ultra-microporous carbon/sulfur by one-step pyrolysis treatment and melt-diffusion process.¹¹

1.4.2 Designing hosts based on chemisorption

Although sulfur can be effectively encapsulated within the carbon host, successfully enabling an improved electrochemical behavior of sulfur cathode, the physical adsorption to suppress polysulfide shuttling is relatively limited, owing to a weak chemical interaction between nonpolar carbons and the polar LiPS. Thus LiPS form relatively strong polar bonds with modified carbon host, they can be effectively restrained within the cathode. To this end, carbon host materials are often advocated by heteroatom-doped modifications.⁶⁰⁻⁶³ The introduction of nitrogen within the carbon structure can promote interaction with Li and S atoms from LiPS as demonstrated for N-enriched mesoporous carbons.

On the other hand, compared with carbon-based materials, metal-based materials have been widely explored as a host for sulfur cathode, while their richness in oxygen, nitrogen and sulfur atoms naturally offers a strong affinity for LiPS and thus hinders the dissolution of LiPS into the electrolyte.⁶⁴ Further combined with morphology project (shape, porosity, size et al.), the resultant host provides an ideal architecture for physical encapsulation of sulfur and chemical binding of LiPS simultaneously. Historically, the nanosized Mg_{0.6}Ni_{0.4}O was proposed as one of the earliest iterations of inorganic host materials for LiPS adsorption.⁶⁵ Interestingly, it was

not until 2014 that inorganic materials were revisited. The infiltration of inorganic host materials into the development of sulfur cathode provides great prospects.

1.4.3 Designing hosts based on electrocatalysis

In addition to the chemisorption enhancement in the design of host materials, the interest of researchers has switched to the electrocatalytic roles of the metal-based materials on the redox reactions of LiPS.⁶⁶⁻⁷⁰ As early as 2014, these host materials are found as catalyst to enhance redox reaction kinetics between S and Li₂S. This conception is remarkably boosted by the CoS₂ that propels redox reaction of LiPS.^{71,72} Akin to the known merits of conductive enhancement and strong adsorption, accelerated redox reactions of LiPS greatly reduce their possibility of dissolving and diffusing into organic electrolyte. The experimental result shows a slow capacity decay rate of 0.034%/cycle at 2 C after 2000 cycles and a high initial capacity of 1368 mAh g⁻¹ at 0.5 C.

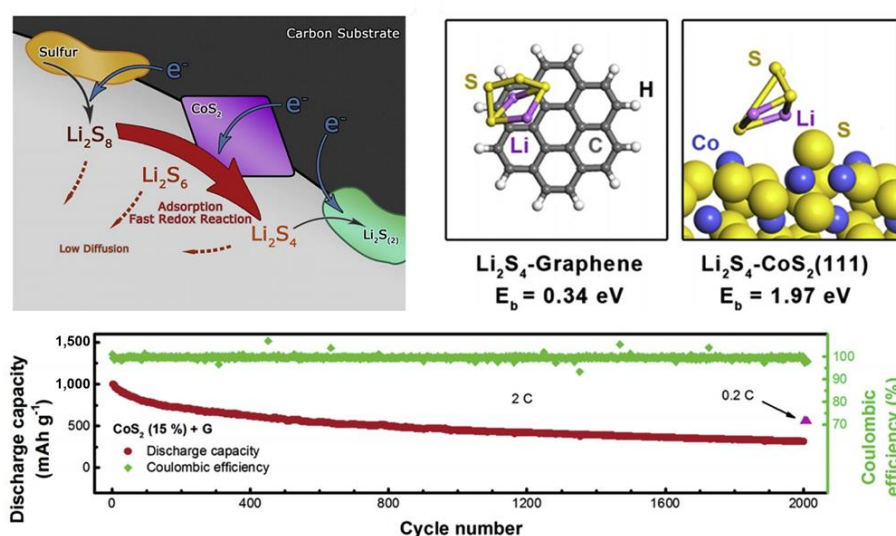


Figure 7. Schematic illustration of the discharge process, binding geometries and energies, and cycling performance in a CoS₂-incorporated carbon/sulfur cathode.⁷²

1.5 Strategies for improved adsorption-catalysis-conversion of LiPS

1.5.1 Heterostructure engineering

The design of heterostructure was proposed to construct a highly active interface for realizing a smooth trapping-diffusion-conversion of LiPS toward ultra-long life LSBs. A typical example for a heterostructure was built with the twinborn TiO₂-TiN that was synthesized by a simple reaction between TiCl₄ and urea and combines the merits of highly adsorptive TiO₂ and conductive TiN.^{73,74} The smooth interface between the twinborn TiO₂ (for trapping) and TiN

(for catalytic conversion) helps achieve an effective trapping, fast diffusion, and catalytic conversion of LiPS to insoluble $\text{Li}_2\text{S}_2/\text{Li}_2\text{S}$. Also, an in-plane graphene-TiC heterostructure by the in situ growth of TiC on a graphene plane was constructed that not only acts as the 2D growth template but also a carbon source for TiC formation.⁷⁵ The naturally formed in-plane interface greatly decreases the diffusion barriers of ion/electron to guarantee a more effective trapping and conversion of LiPS, expecting a super-high performance LSBs with an optimized preparation. In summary, constructing a smooth out/in-plane interface to simultaneously realize a fast trapping and catalytic conversion of LiPS is a promising way to produce an ultra-long life LSBs.

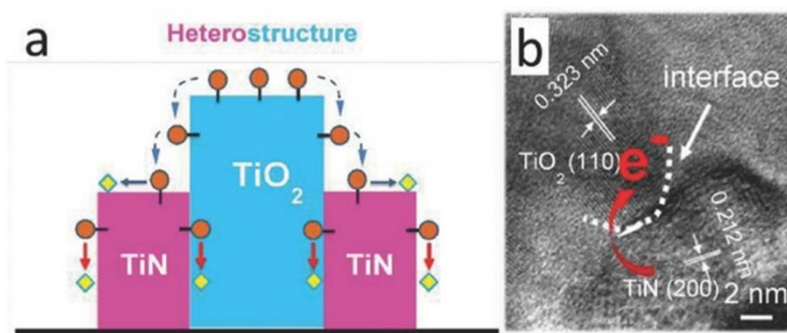


Figure 8. a) Schematic of the conversion process of LiPS on the TiO_2 -TiN heterostructure. b) High-resolution TEM images of the TiO_2 -TiN heterostructure.⁷⁴

1.5.2 Doping engineering

Heteroatom doping has been widely applied to the development of electrocatalysts for energy conversion reactions.⁷⁶⁻⁸⁰ As an example, metal phosphides such as Ni_2P have been demonstrated to be active catalysts for LiPS conversion and to improve with a certain degree of cation dopants and disorder in the original crystallographic framework.⁷⁸ The Co dopants in Ni_2P (denoted $\text{Ni}_2\text{Co}_4\text{P}_3$) can raise the d-band structure of metal sites and facilitate the interaction between catalyst and LiPS, thereby decreasing the activation barrier of LiPS conversion. Moreover, the terminal S atoms were adsorbed to the triply bridged metal sites via robust metal-S bonds. The S-S bond of LiPS was weakened due to the electron population redistribution, creating fast e^- and Li^+ pathways as well as a large surface area for charge transfer. It is found that an oxygen (O) atom has a suitable electron-regulating ability, which is not too strong to hamper Li^+ diffusion and not too weak to trap the LiPS via forming Li-O bonds.¹¹ Motivated by these studies, other high-performance catalyst for LSBs can be achieved by constructing hybrid architectures, e.g. O-doped Sb_2S_3 (Figure 9).⁷⁹

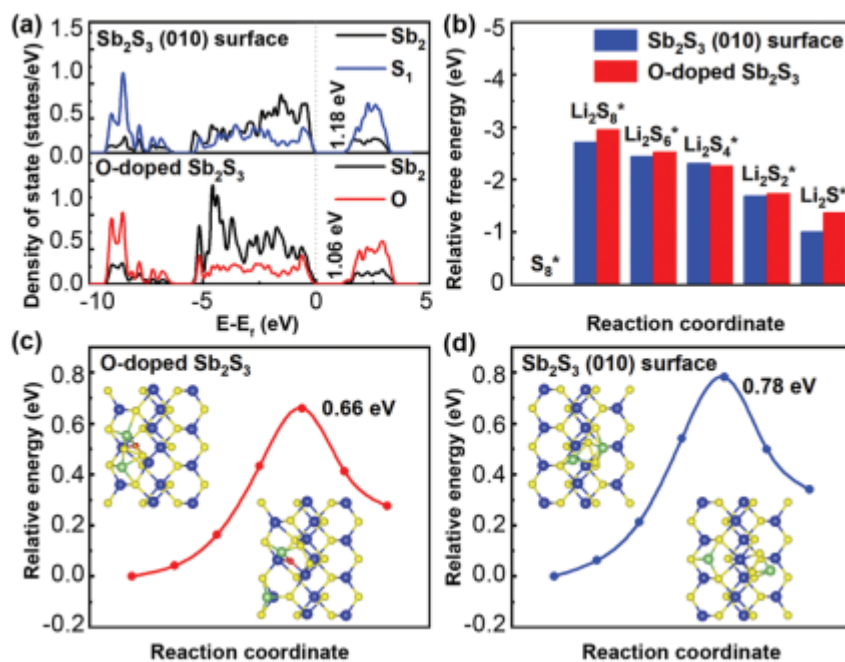


Figure 9. (a) Electron densities of the state of undoped/O-doped Sb_2S_3 (010). All energies are referenced to the Fermi level (E_f). (b) The binding energies between Li_2S_n ($n = 8, 6, 4, 2, 1$) and undoped/O-doped Sb_2S_3 (010). Top views of Li migration routes and their relevant energy profiles of Li_2S_2 decomposition on (c) O-doped Sb_2S_3 and (d) a perfect Sb_2S_3 (010) surface. The blue, yellow, red, and green balls were Sb, S, O, and Li atoms, respectively.⁷⁹

1.5.3 Defect engineering

Introducing defects into functional materials has been demonstrated as a highly effective approach to boost the catalytic abilities and polysulfide affinity in LSBs. Defect engineering can effectively enhance ionic diffusion and electronic conductivity because the introduction of defects can narrow band gaps and provide additional energy levels.⁸¹⁻⁸⁵ Additionally, the defects in nonpolar materials can improve the surface polarization, leading to enhanced absorption ability to LiPS in the LSBs. More importantly, the surface defects can facilitate the formation of free-radicals, which accelerates the conversion of LiPS.⁸⁶ Taking perovskite-type $\text{La}_{0.6}\text{Sr}_{0.4}\text{CoO}_{3-\delta}$ as an example, abundant oxygen defects act as the active centers participating in LiPS adsorption (Figure 10a).⁸² A sulfur-deficient Co_9S_8 catalytic material is further presented as a proof of concept (Figure 10b). Nanoparticles with a metallic Co_9S_8 core and a sulfur-deficient shell were decorated on the CNT surface. During the discharge-charge process, the polysulfide conversion could be catalyzed by the sulfur-deficient shell which was supported by a robust crystalline Co_9S_8 core.⁸⁷

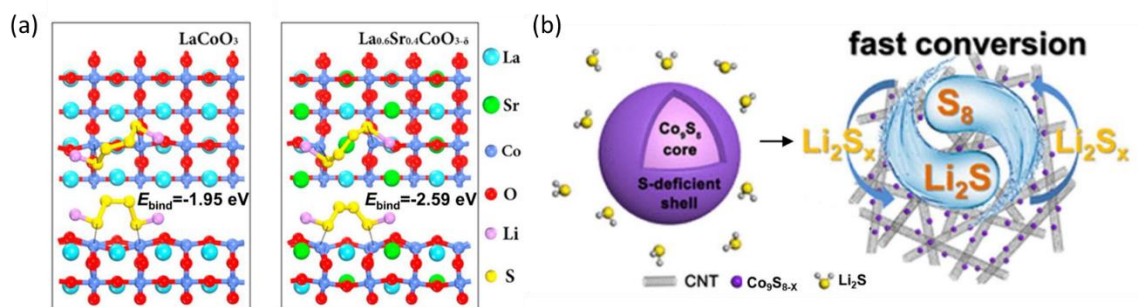


Figure 10. a) The most stable adsorption structures, after full relaxation, of Li₂S₄ on LaCoO₃ (110) and La_{0.6}Sr_{0.4}CoO_{3-δ} (110) surfaces, respectively.⁸² b) Schematic illustration of the synthesis of Co₉S_{8-x}/CNT and the conversion of Li₂S_x on the Co₉S_{8-x}/CNT surface.⁸⁷

1.6 Sulfur hosts nanomaterial synthetic approaches

1.6.1 Kirkendall Effect

The most widespread approach to obtain hollow metal sulfides and phosphides is the utilization of the Kirkendall effect during the synthesis.⁸⁸⁻⁹² Different diffusion rates of heterogeneous atoms at the interfaces drive this effect spontaneously. Among various examples of the Kirkendall effect, faster outward diffusion of metal atoms positioned at the core, in conjunction with slower inward movement of S and P atoms, can lead to the production of hollow metal sulfides and phosphides. Multiple small voids at the core, which appear in the early stage, coalesce into a large void of hollow structures during the process (Figure 11).

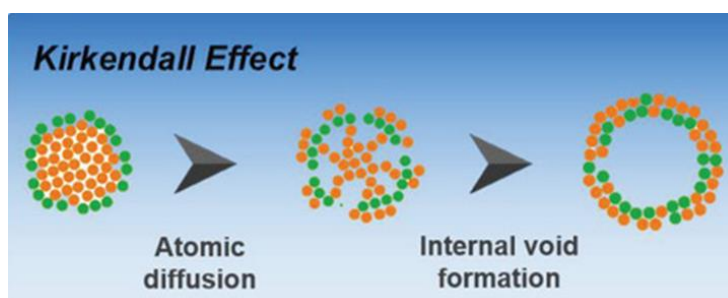


Figure 11. Representative schematic diagram of synthetic methodologies to morphology controlled nanostructures.⁹²

1.6.2 Colloidal synthesis in organic solvents

In colloidal synthesis, NPs can be produced through reaction or decomposition of molecular or atomic monomers which take place in solvent heated to required temperature. Reactions are usually performed under inert atmosphere in high boiling point solvents, e.g. oleylamine

(OAm), octadecene (ODE), oleic acid (OA), and trioctylphosphine (TOP).⁹³⁻⁹⁷ A standard synthetic facility to produce colloidal nanocrystals at lab scale is to use Schlenk line which allows to efficiently remove low boiling point organic impurities and perform experiment under inert atmosphere (Figure 11).

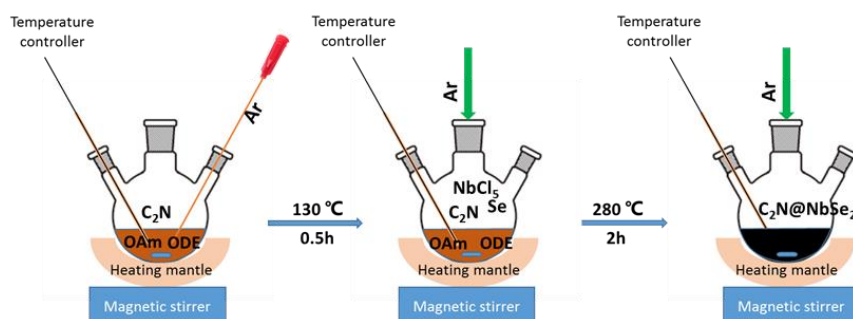


Figure 12. Scheme of a nanomaterial produced by colloidal synthesis in my work. (chapter 4).

1.6.3 Aqueous synthesis method

The use of surfactants and organic solvents generally facilitates the control of size, morphology, crystal structure, and defects. However, the organic surfactants that can control morphology through surface modification are commonly electrically insulating, which can drastically reduce the σ of the materials. Ligand replacement methods switch smaller species for long chain surfactant molecules, but sometimes involve using high toxicity chemicals, and introduce impurities, which again can adversely influence the transport behavior of the materials. For this situation, aqueous synthesis is a better choice.⁹⁸⁻¹⁰⁰ Aqueous synthesis is a synthesis method that simple, rapid, large scale, environmental friendly, low cost, surfactant-free and can also control the size of the nanomaterials. There are no organic surfactants on the nanomaterials synthesized by aqueous synthesis, so in general, the LSBs properties of the materials will be better.

1.7 Objectives

This thesis aims to demonstrate the production of high-performance LSBs by using MSe-based cathodes obtained by cost-effective and scalable solution synthesis routes. To produce high-performance LSBs, several main challenges need to be overcome. To solve the challenges, in this thesis the following specific objectives have been defined:

- a) To develop synthesis strategies to produce high quality metal selenide sulfur host materials based on relatively abundant elements such as ZnSe, NbSe₂, Bi₂Se₃, and Cu_{2-x}Se.

- b) To develop simple, large scale, environmental friendly, low cost, surfactant-free methods to synthesise sulfur hosts with hollow structures.
- c) To develop sulfur hosts with high surface area.
- d) Designing heterostructures with interfaced highly adsorptive and catalytic components as an effective way to realize a smooth trapping-diffusion-conversion of LiPS.
- e) To develop effective electron and hole doping strategies to control the charge carrier concentration of bottom-up assembled nanomaterials.

1.8 References

- [1] A. M. Omer, *Renew. Sustain. Energy Rev.* **2008**, *12*, 2265-2300.
- [2] S. B. Sani, P. Celvakumaran, V. K. Ramachandramurthy, S. Walker, B. Alrazi, Y. J. Ying, N. Y. Dahlan, M. H. A. Rahman, *Journal of Energy Storage* **2020**, *32*, 101902.
- [3] D. Champier, *Energy Convers. Manag.* **2017**, *140*, 167-181.
- [4] B. Dunn, H. Kamath, J.-M. Tarascon, *Science* **2011**, *334*, 928.
- [5] B. Diouf, R. Pode, *Renewable Energy* **2015**, *76*, 375.
- [6] H. Hesse, M. Schimpe, D. Kucevic, A. Jossen, *Energies* **2017**, *10*, 2107.
- [7] J. B. Goodenough, K. S. Park, *J Am Chem Soc* **2013**, *135*, 1167.
- [8] M. S. Whittingham, *Chemical Reviews* **2014**, *114*, 11414.
- [9] L. F. Nazar, M. Cuisinier, Q. Pang, *MRS Bulletin* **2014**, *39*, 436.
- [10] A. Manthiram, Y. Fu, S. H. Chung, C. Zu, Y. S. Su, *Chem Rev* **2014**, *114*, 11751.
- [11] X. Ji, K. T. Lee, L. F. Nazar, *Nat Mater* **2009**, *8*, 500.
- [12] A. Manthiram, Y. Fu, Y. S. Su, *Acc. Chem. Res.* **2013**, *46*, 1125-1134.
- [13] J. Xie, Y. C. Lu, *Nat Commun* **2020**, *11*, 2499.
- [14] Z. W. Seh, Y. Sun, Q. Zhang, Y. Cui, *Chem Soc Rev* **2016**, *45*, 5605.
- [15] P. Adelhelm, P. Hartmann, C. L. Bender, M. Busche, C. Eufinger, J. Janek, *Beilstein Journal of Nanotechnology* **2015**, *6*, 1016.
- [16] H. Zhang, J. Nai, L. Yu, X. W. Lou, *Joule* **2017**, *1*, 77.
- [17] T. Tang, Y. Hou, *Electrochemical Energy Reviews*, **2018**, *1*, 403–432.
- [18] X. Zhang, H. Xie, C. S. Kim, K. Zaghib, A. Mauger, C. M. Julien, *Materials Science and Engineering: R: Reports* **2017**, *121*, 1.
- [19] H. J. Peng, G. Zhang, X. Chen, Z. W. Zhang, W. T. Xu, J. Q. Huang, Q. Zhang, *Angew. Chem. Int. Ed.* **2016**, *55*, 12990
- [20] R. Fang, S. Zhao, Z. Sun, D. W. Wang, H. M. Cheng, F. Li, *Adv Mater* **2017**, *29*.
- [21] Q. Wang, J. Zheng, E. Walter, H. Pan, D. Lv, P. Zuo, H. Chen, Z. D. Deng, B. Y. Liaw, X. Yu, X. Yang, J.-G. Zhang, J. Liu, J. Xiao, *Journal of The Electrochemical Society* **2015**, *162*, A474.
- [22] S. S. Zhang, *Journal of Power Sources* **2013**, *231*, 153.
- [23] A. Kawase, S. Shirai, Y. Yamoto, R. Arakawa, T. Takata, *Phys Chem Chem Phys* **2014**, *16*, 9344.
- [24] X. Liu, J. Q. Huang, Q. Zhang, L. Mai, *Adv Mater* **2017**, *29*.
- [25] Terje A. Skotheim, Shoreham, N.Y., Google Patents: 1995.

- [26] D. Peramunage, S. Licht, *Science*, **1993**, *261*, 1029-1032.
- [27] R. Steudel, E.-M. Strauss, **1984**, *28*, 135.
- [28] P. G. Bruce, S. A. Freunberger, L. J. Hardwick, J. M. Tarascon, *Nat Mater* **2011**, *11*, 19.
- [29] H. Ye, J. Sun, S. Zhang, H. Lin, T. Zhang, Q. Yao, J. Y. Lee, *ACS Nano* **2019**, *13*, 14208.
- [30] Y. S. Su, Y. Fu, B. Guo, S. Dai, A. Manthiram, *Chemistry* **2013**, *19*, 8621.
- [31] S. F. Ng, M. Y. L. Lau, W. J. Ong, *Adv Mater* **2021**, *33*, e2008654.
- [32] J. Akridge, *Solid State Ionics* **2004**, *175*, 243.
- [33] Y. V. Mikhaylik, J. R. Akridge, *Journal of The Electrochemical Society* **2004**, *151*, A1969.
- [34] Yuriy V. Mikhaylik, Tucson, AZ, Google Patents: 2010.
- [35] S. Moon, Y. H. Jung, W. K. Jung, D. S. Jung, J. W. Choi, D. K. Kim, *Adv Mater* **2013**, *25*, 6547.
- [36] R. Fang, S. Zhao, S. Pei, X. Qian, P. X. Hou, H. M. Cheng, C. Liu, F. Li, *ACS Nano* **2016**, *10*, 8676.
- [37] J. Liang, Z.-H. Sun, F. Li, H.-M. Cheng, *Energy Storage Materials* **2016**, *2*, 76.
- [38] D.-W. Wang, Q. Zeng, G. Zhou, L. Yin, F. Li, H.-M. Cheng, I. R. Gentle, G. Q. M. Lu, *Journal of Materials Chemistry A* **2013**, *1*, 9382.
- [39] L. Borchardt, M. Oschatz, S. Kaskel, *Chemistry* **2016**, *22*, 7324.
- [40] J. W. Kim, J. D. Ocon, D. W. Park, J. Lee, *ChemSusChem*, **2014**, *7*, 1265-1273.
- [41] H. Wang, Y. Yang, Y. Liang, J. T. Robinson, Y. Li, A. Jackson, Y. Cui, H. Dai, *Nano Lett* **2011**, *11*, 2644.
- [42] X. Zhu, W. Zhao, Y. Song, Q. Li, F. Ding, J. Sun, L. Zhang, Z. Liu, *Advanced Energy Materials* **2018**, *8*, 1800201.
- [43] H. Li, S. Ma, H. Cai, H. Zhou, Z. Huang, Z. Hou, J. Wu, W. Yang, H. Yi, C. Fu, Y. Kuang, *Energy Storage Materials* **2019**, *18*, 338.
- [44] Z. Liang, D. Yang, P. Tang, C. Zhang, J. Jacas Biendicho, Y. Zhang, J. Llorca, X. Wang, J. Li, M. Heggen, J. David, R. E. Dunin - Borkowski, Y. Zhou, J. R. Morante, A. Cabot, J. Arbiol, *Advanced Energy Materials* **2020**, *11*, 2003507.
- [45] L. Zhang, X. Chen, F. Wan, Z. Niu, Y. Wang, Q. Zhang, J. Chen, *ACS Nano* **2018**, *12*, 9578.
- [46] Y. Liu, Y. Elias, J. Meng, D. Aurbach, R. Zou, D. Xia, Q. Pang, *Joule* **2021**, *5*, 2323.
- [47] M. Barghamadi, A. S. Best, A. I. Bhatt, A. F. Hollenkamp, M. Musameh, R. J. Rees, T.

- Rüther, *Energy Environ. Sci.* **2014**, 7, 3902.
- [48] Y. Diao, K. Xie, S. Xiong, X. Hong, *Journal of The Electrochemical Society* **2012**, 159, A421.
- [49] Z. Wei Seh, W. Li, J. J. Cha, G. Zheng, Y. Yang, M. T. McDowell, P.-C. Hsu, Y. Cui, *Nature Communications* **2013**, 4.
- [50] H. Ye, M. Li, T. Liu, Y. Li, J. Lu, *ACS Energy Letters* **2020**, 5, 2234.
- [51] J. Zhao, M. Yang, N. Yang, J. Wang, D. Wang, *Chemical Research in Chinese Universities* **2020**, 36, 313.
- [52] M. A. Pope, I. A. Aksay, *Advanced Energy Materials* **2015**, 5, 1500124.
- [53] C. Li, H. Zhang, L. Otaegui, G. Singh, M. Armand, L. M. Rodriguez-Martinez, *Journal of Power Sources* **2016**, 326, 1.
- [54] T. Liu, H. Hu, X. Ding, H. Yuan, C. Jin, J. Nai, Y. Liu, Y. Wang, Y. Wan, X. Tao, *Energy Storage Mater.* **2020**, 30, 346-366.
- [55] M. Wang, X. Xia, Y. Zhong, J. Wu, R. Xu, Z. Yao, D. Wang, W. Tang, X. Wang, J. Tu, *Chemistry – A European Journal* **2018**, 25, 3710.
- [56] L. Yuan, H. Yuan, X. Qiu, L. Chen, W. Zhu, *Journal of Power Sources* **2009**, 189, 1141.
- [57] Y. Zhang, Z. Gao, N. Song, J. He, X. Li, *Materials Today Energy* **2018**, 9, 319.
- [58] M. Liu, N. Deng, J. Ju, L. Fan, L. Wang, Z. Li, H. Zhao, G. Yang, W. Kang, J. Yan, B. Cheng, *Advanced Functional Materials* **2019**, 29, 1905467.
- [59] C. Dong, W. Gao, B. Jin, Q. Jiang, *iScience* **2018**, 6, 151.
- [60] F. Pei, T. An, J. Zang, X. Zhao, X. Fang, M. Zheng, Q. Dong, N. Zheng, *Advanced Energy Materials* **2016**, 6, 1502539.
- [61] T. Z. Hou, X. Chen, H. J. Peng, J. Q. Huang, B. Q. Li, Q. Zhang, B. Li, *Small* **2016**, 12, 3283.
- [62] D. Yang, C. Zhang, J. J. Biendicho, X. Han, Z. Liang, R. Du, M. Li, J. Li, J. Arbiol, J. Llorca, Y. Zhou, J. R. Morante, A. Cabot, *ACS Nano* **2020**.
- [63] M. Yu, J. Ma, H. Song, A. Wang, F. Tian, Y. Wang, H. Qiu, R. Wang, *Energy & Environmental Science* **2016**, 9, 1495.
- [64] R. Wang, C. Luo, T. Wang, G. Zhou, Y. Deng, Y. He, Q. Zhang, F. Kang, W. Lv, Q. H. Yang, *Advanced Materials* **2020**, 32, 2000315.
- [65] M.-S. Song, S.-C. Han, H.-S. Kim, J.-H. Kim, K.-T. Kim, Y.-M. Kang, H.-J. Ahn, S. X. Dou, J.-Y. Lee, *Journal of The Electrochemical Society* **2004**, 151, A791.
- [66] C. Zhang, R. Du, J. J. Biendicho, M. Yi, K. Xiao, D. Yang, T. Zhang, X. Wang, J. Arbiol, J. Llorca, Y. Zhou, J. R. Morante, A. Cabot, *Advanced Energy Materials* **2021**, 11, 2100432.

- [67] J. Li, Z. Niu, C. Guo, M. Li, W. Bao, *Journal of Energy Chemistry* **2021**, *54*, 434.
- [68] L. Zhang, D. Liu, Z. Muhammad, F. Wan, W. Xie, Y. Wang, L. Song, Z. Niu, J. Chen, *Adv Mater* **2019**, *31*, e1903955.
- [69] X. Li, B. Gao, X. Huang, Z. Guo, Q. Li, X. Zhang, P. K. Chu, K. Huo, *ACS Appl Mater Interfaces* **2019**, *11*, 2961.
- [70] M. Wang, L. Fan, X. Sun, B. Guan, B. Jiang, X. Wu, D. Tian, K. Sun, Y. Qiu, X. Yin, Y. Zhang, N. Zhang, *ACS Energy Letters* **2020**, *5*, 3041.
- [71] Q. Pang, D. Kundu, M. Cuisinier, L. F. Nazar, *Nature Communications* **2014**, *5*.
- [72] Z. Yuan, H. J. Peng, T. Z. Hou, J. Q. Huang, C. M. Chen, D. W. Wang, X. B. Cheng, F. Wei, Q. Zhang, *Nano Lett* **2016**, *16*, 519.
- [73] D. Liu, C. Zhang, G. Zhou, W. Lv, G. Ling, L. Zhi, Q. H. Yang, *Adv Sci (Weinh)* **2018**, *5*, 1700270.
- [74] T. Zhou, W. Lv, J. Li, G. Zhou, Y. Zhao, S. Fan, B. Liu, B. Li, F. Kang, Q.-H. Yang, *Energy Environ. Sci.* **2017**, *10*, 1694-1703.
- [75] T. Zhou, Y. Zhao, G. Zhou, W. Lv, P. Sun, F. Kang, B. Li, Q. H. Yang, *Nano Energy* **2017**, *39*, 291.
- [76] A. Hu, M. Zhou, T. Lei, Y. Hu, X. Du, C. Gong, C. Shu, J. Long, J. Zhu, W. Chen, X. Wang, J. Xiong, *Advanced Energy Materials* **2020**, *10*, 2002180.
- [77] W. Liu, C. Luo, S. Zhang, B. Zhang, J. Ma, X. Wang, W. Liu, Z. Li, Q.-H. Yang, W. Lv, *ACS Nano* **2021**, *15*, 7491.
- [78] Z. Shen, M. Cao, Z. Zhang, J. Pu, C. Zhong, J. Li, H. Ma, F. Li, J. Zhu, F. Pan, H. Zhang, *Advanced Functional Materials* **2019**, *30*, 1906661.
- [79] Y. Zhang, S. Yang, S. Zhou, L. Zhang, B. Gu, Y. Dong, S. Kong, D. Cai, G. Fang, H. Nie, Z. Yang, *Chemical Communications* **2021**, *57*, 3255.
- [80] Z. Gu, C. Cheng, T. Yan, G. Liu, J. Jiang, J. Mao, K. Dai, J. Li, J. Wu, L. Zhang, *Nano Energy* **2021**, *86*, 106111.
- [81] H. Zhang, L. Yang, P. Zhang, C. Lu, D. Sha, B. Yan, W. He, M. Zhou, W. Zhang, L. Pan, Z. Sun, *Advanced Materials* **2021**, *33*, 2008447.
- [82] Z. Hao, R. Zeng, L. Yuan, Q. Bing, J. Liu, J. Xiang, Y. Huang, *Nano Energy* **2017**, *40*, 360.
- [83] Z. Su, J. Liu, M. Li, Y. Zhu, S. Qian, M. Weng, J. Zheng, Y. Zhong, F. Pan, S. Zhang, *Electrochemical Energy Reviews* **2020**, *3*, 286.
- [84] L. Oakes, R. Carter, C. L. Pint, *Nanoscale* **2016**, *8*, 19368.
- [85] H. Ci, J. Cai, H. Ma, Z. Shi, G. Cui, M. Wang, J. Jin, N. Wei, C. Lu, W. Zhao, J. Sun,

Z. Liu, *ACS Nano* **2020**, *14*, 11929.

[86] M. Zhang, W. Chen, L. Xue, Y. Jiao, T. Lei, J. Chu, J. Huang, C. Gong, C. Yan, Y. Yan, Y. Hu, X. Wang, J. Xiong, *Advanced Energy Materials* **2019**, *10*, 1903008.

[87] H. Lin, S. Zhang, T. Zhang, S. Cao, H. Ye, Q. Yao, G. W. Zheng, J. Y. Lee, *ACS Nano* **2019**, *13*, 7073.

[88] J. Wang, A. C. Johnston-Peck, J. B. Tracy, *Chemistry of Materials* **2009**, *21*, 4462.

[89] A.-A. El Mel, R. Nakamura, C. Bittencourt, *Beilstein Journal of Nanotechnology* **2015**, *6*, 1348.

[90] T. Chen, L. Ma, B. Cheng, R. Chen, Y. Hu, G. Zhu, Y. Wang, J. Liang, Z. Tie, J. Liu, Z. Jin, *Nano Energy* **2017**, *38*, 239.

[91] Z. Ye, Y. Jiang, J. Qian, W. Li, T. Feng, L. Li, F. Wu, R. Chen, *Nano Energy* **2019**, *64*, 103965.

[92] J. Joo, T. Kim, J. Lee, S. I. Choi, K. Lee, *Adv Mater* **2019**, *31*, e1806682.

[93] J. Zhang, C. Du, J. Zhao, H. Ren, Q. Liang, Y. Zheng, S. Madhavi, X. Wang, J. Zhu, Q. Yan, *ACS Appl Mater Interfaces* **2018**, *10*, 37773.

[94] J. S. Son, J. H. Yu, S. G. Kwon, J. Lee, J. Joo, T. Hyeon, *Advanced Materials* **2011**, *23*, 3214.

[95] C. d. M. Donegá, *Chem. Soc. Rev.* **2011**, *40*, 1512.

[96] Y. Yin, C. K. Erdonmez, A. Cabot, S. Hughes, A. P. Alivisatos, *Advanced Functional Materials* **2006**, *16*, 1389.

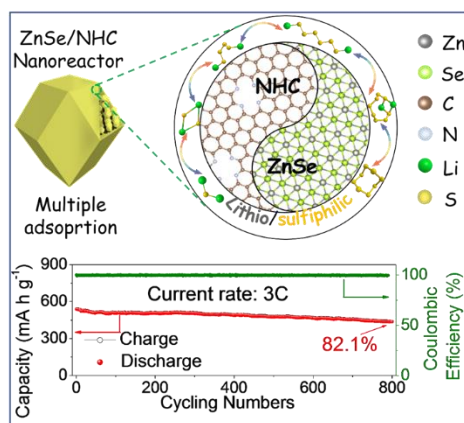
[97] Y. Wang, A. Chen, S. Lai, X. Peng, S. Zhao, G. Hu, Y. Qiu, J. Ren, X. Liu, J. Luo, *Journal of Catalysis* **2020**, *381*, 78.

[98] M. Li, Y. Liu, Y. Zhang, X. Han, T. Zhang, Y. Zuo, C. Xie, K. Xiao, J. Arbiol, J. Llorca, M. Ibáñez, J. Liu, A. Cabot, *ACS Nano* **2021**, *15*, 4967–4978.

[99] X. L. Shi, X. Tao, J. Zou, Z. G. Chen, *Advanced Science* **2020**, *7*, 1902923.

[100] S. S. Flaschen, *J. Am. Chem. Soc.* **1955**, *77*, 6194.

Chapter 2 ZnSe/N-doped Carbon Nanoreactor with multiple adsorption sites for Stable Lithium-Sulfur Batteries



2.1 Abstract

To commercially realize the enormous potential of LSBs several challenges remain to be overcome. At the cathode, the lithium polysulfide (LiPS) shuttle effect must be inhibited and the redox reaction kinetics need to be substantially promoted. In this direction, this work proposes a cathode material based on a TMSe as both adsorber and catalyst and a hollow nanoreactor architecture: ZnSe/N-doped hollow carbon (ZnSe/NHC). It is here demonstrated both experimentally and by means of density functional theory that this composite provides three key benefits to the LSBs cathode: (i) A highly effective trapping of LiPS due to the combination of sulfiphilic sites of ZnSe, lithiophilic sites of NHC, and the confinement effect of the cage-based structure; (ii) a redox kinetic improvement in part associated with the multiple adsorption sites that facilitate the Li⁺ diffusion; and (iii) an easier accommodation of the volume expansion preventing the cathode damage due to the hollow design. As a result, LSBs cathodes based on S@ZnSe/NHC are characterized by high initial capacities, superior rate capability, and an excellent stability. Overall, this work not only demonstrates the large potential of TMSe as cathode materials in LSBs but also probes the nanoreactor design to be a highly suitable architecture to enhance cycle stability.

2.2 Introduction

LSBs have emerged as one of the most promising energy storage technologies owing to their potential low cost and high theoretical energy density (2600 Wh kg^{-1}) compared to LIBs (420 Wh kg^{-1}).^[1-3] While large progress has been achieved in recent years, a number of challenges remain to be overcome to commercially realize their potential. First, the poor conductivity of sulfur and lithium sulfide results in a sluggish electron transport, which requires adding a high electrical conductivity support to the cathode. Besides, the severe volumetric expansion during lithiation causes the pulverization of the sulfur cathode and the detachment of part of the active material from the conducting framework, what calls for a strategy to contain the expansion and/or the active material.^[4-6] Additionally, the dissolution of intermediate LiPS into the electrolyte has associated a low coulombic efficiency (CE) and a rapid decline of capacity with cycling. Overcoming this limitation requires developing an efficient approach to immobilize the LiPS and enhance their redox kinetics.^[7,8]

One effective strategy to improve the electrochemical performance of LSBs is to use carbon-based materials such as porous carbon,^[9] graphene,^[10,11] carbon spheres,^[12] carbon nanotubes,^[13,14] and nanofibers,^[15] as high electrical conductivity sulfur host at the cathode. However, while carbon materials facilitate electron transport and transfer at the cathode, they are not able to suppress polysulfide shuttling owing to the weak chemical interaction between nonpolar carbons and polar LiPS.^[16,17] Therefore, carbon-sulfur composites generally suffer from rapid capacity decays during cycling.

To promote interaction with LiPS, some polar inorganic materials have been recently considered as cathode materials, including transition metal oxides,^[18,19] hydroxides,^[20] carbides,^[21] nitrides,^[22] and sulfides.^[23-25] These polar materials offer abundant LiPS adsorption sites and can even accelerate the catalytic conversion of LiPS to sulfur and solid Li-S phases, $\text{Li}_2\text{S}_2/\text{Li}_2\text{S}$, thus strongly reducing the loss of sulfur.^[26,27] However, most metal oxides and sulfides have inherently poor electrical conductivities, which result in a low sulfur utilization efficiency and a sluggish redox reaction kinetics upon cycling.

TMSe, such as NiCo_2Se_4 and Sb_2Se_3 , are emerging as promising candidates to host sulfur at LSBs cathodes.^[28,29] Compared with oxides and sulfides, selenides are characterized by higher electrical conductivities, similar polarities and in some cases enhanced catalytic activities. However, owing to their relatively high volumetric density, TMSe need to be combined with high surface area carbon materials to achieve efficient utilization. In this direction, Zhang et al. recently demonstrated a graphene/ CoSe_2 composited with superb electrocatalytic properties

toward polysulfide redox reactions at triple-phase interfaces.^[30] To step further beyond the state of the art, the carbon support need to be optimized and the most suitable TMSe selected. In terms of geometry, hollow structures and particularly hollow cages are a particularly interesting form of carbon. Hollow carbon materials can physically confine polysulfides, preventing the shuttle effect and promoting their conversion reaction. In terms of composition, the use of N-doped carbon can not only improve electrical conductivity, but also promote LiPS adsorption through Li-N chemical binding.^[31] On the other hand, Zn compounds and particularly ZnO and ZnS have recently gained high interest as cathode material in LSBs owing to their good adsorption capability, notable catalytic activity toward polysulfide conversion and low cost.^[32,33]

In this work, we hypothesize the yet unexplored selenide, ZnSe, to be an optimum candidate as sulfur host in LSBs when combined with hollow N-doped hollow carbon. We detail here the first synthesis of ZnSe nanoparticles decorating N-doped hollow polyhedrons (ZnSe/NHC). These particles are then tested as nanoreactors^[34,35] toward stable LSBs cathodes. The obtained results are rationalized with the help of density functional theory (DFT) calculations.

2.3 Experimental section

Synthesis of zeolitic imidazolate framework (ZIF-8): 5.95 g (0.02 mol) of $\text{Zn}(\text{NO}_3)_2 \cdot 6\text{H}_2\text{O}$ (98%, Alfa Aesar) was dissolved in 150 mL methanol. The obtained solution was poured into 150 mL of a methanol solution containing 6.16 g (0.075 mol) of 2-methylimidazole (99%, Acros Organics) and the mixed solution was stirred for 24 h at room temperature. The obtained white precipitate was collected, washed with methanol several times and dried overnight.

Synthesis of ZnSe/NHC: 100 mg of the as-obtained ZIF-8 powder and 250 mg of selenium powder (99%, Sigma Aldrich) were placed in two separated porcelain boats. The porcelain boats were placed within a tubular furnace having an Ar flow (100 mL min^{-1}), with the selenium boat upstream and the ZIF-8 powder downstream. The furnace was heated to $650 \text{ }^\circ\text{C}$ at a heating rate of $5 \text{ }^\circ\text{C min}^{-1}$ and maintained at this temperature for 2 h. After cooling to room temperature, the ZnSe/NHC powder was collected.

Synthesis of NHC: NHC was obtained by annealing ZIF-8 powder in the same conditions but without selenium. The obtained black powder was immersed in a 2 M HCl solution and stirred for 24 h to remove Zn. The precipitate was collected by filtration, washed with ethanol and dried at $60 \text{ }^\circ\text{C}$ overnight.

Synthesis of S@ZnSe/NHC, S@NHC and S@Super P: Sulfur was incorporated by means of a simple melting diffusion process. To obtain S@ZnSe/NHC, as-prepared ZnSe/NHC and

sublimed sulfur (99.98%, Sigma Aldrich) were well mixed at a 1:3 weigh ratio and heated at 155 °C for 12 h in a glass bottle under an Ar atmosphere. To remove the redundant sulfur outside of ZnSe/NHC, the powder was immersed in a 10 mL CS₂ and ethanol solution (1:4, volume ratio) for 10 min twice. For comparison, S@NHC and S@Super P (Super P from Alfa Aesar, 99%) were obtained by the same process.

Materials Characterization: Chemical compositions were analyzed by XRD patterns recorded at room temperature using a Bruker AXS D8 Advance X-ray diffractometer with Cu K radiation ($\lambda = 1.5106 \text{ \AA}$) operating at 40 kV and 40 mA. Field emission FESEM analyses were carried on a ZEISS Auriga microscope with an energy dispersive X-ray spectroscopy (EDS) detector operating at 20 kV. TEM characterization was carried out on a Zeiss Libra 120 (Carl Zeiss, Jena, Germany) operating at 120 kV. HRTEM and STEM studies were carried out using a field emission gun FEI Tecnai F20 microscope at 200 kV with a tested lattice resolution of 0.1 nm. HAADF STEM was combined with EELS in the Tecnai microscope by using a Gatan Quantum filter. XPS measurements were conducted at 150 W using a Phoibos 150 MCD-9 detector. TGA were performed to record the ration of S within prepared composites. UV–vis absorption spectra were tested on a PerkinElmer LAMBDA 950 UV–vis spectrophotometer. Nitrogen adsorption-desorption isotherms were measured to evaluate the specific surface area and the pore size distribution using a Brunauer–Emmett–Teller method (Tristar II 3020 Micromeritics system).

Electrochemical measurements: Working electrodes were prepared by mixing the active materials (S@ZnSe/NHC, S@NHC and S@Super P), Super P and PVDF binders with a weight ratio of 8:1:1 in N-methyl-2-pyrrolidone (NMP, 99.5%, Acros Organics). Then the slurry was coated on an aluminum foil and dried at 60 °C under vacuum overnight. Subsequently, the coated aluminum foil was punched into small disks having a sulfur loading of about 1mg cm⁻² and were assembled into coin cells in an Ar-filled glovebox. Li foil was used as the counter electrode and Celgard 2400 membranes as separators. The electrolyte was prepared by dissolving 1.0 M lithium bis(trifluoromethanesulfonyl) imide (LiTFSI) (99%, Acros Organics) in a mixture of 1,3-dioxolane (DOL, 99.5%, Alfa Aesar) and dimethoxymethane (DME, 99%, Honeywell) (1:1 v/v) with the addition of 0.2 M LiNO₃ (99.98%, Alfa Aesar). The amount of electrolyte was about 20 μL for each coin cell. Before cycling, all coin cells were aged for several hours to ensure a sufficient penetration of the electrolyte into the electrode. Galvanostatic charge/discharge (GCD) measurements were performed with a voltage window of 1.7–2.8 V vs. Li⁺/Li at different current densities using a Neware BTS4008 battery cycler. Cyclic voltammetry (CV) tests were performed on a battery tester BCS-810 from Bio Logic at

different scan rate in the range of 0.1–0.4 mV s⁻¹. Electrochemical impedance spectroscopy (EIS) tests were carried out using a sinusoidal voltage with amplitude of 10 mV in the frequency range 100 kHz to 0.01 Hz.

Synthesis of Li₂S₄ Solution and Adsorption Test: Sulfur and Li₂S (99.9%, Alfa Aesar) with a molar ratio of 3:1 were added to appropriate amounts of DME and DOL (volume ratio of 1:1) under vigorous magnetic stirring overnight, until a dark brown solution was formed. For the polysulfide absorption ability test, 20 mg active materials (ZnSe/NHC, NHC and Super P) were immersed into 3.0 mL 10 × 10⁻³ M Li₂S₄ solution, which was shaken and aged overnight.

Symmetric Cell Assembly and Measurements: The ZnSe/NHC (NHC and Super P) composite was mixed with Super P and PVDF binder with a weight ratio of 8:1:1 in NMP. Then the slurry was coated onto the Al foil and dried at 60 °C for 12 h in a vacuum oven. Two pieces of the same electrode (average loading about 0.5 mg cm⁻²) were used as identical working and counter electrodes. 40 μL of electrolyte containing 0.5 M Li₂S₆ and 1 M LiTFSI dissolved in DOL/DME (v/v = 1/1) was added into each coin cell. CV measurements were performed at scan rate of 10 mV s⁻¹ and EIS tests were carried out in the frequency range 100 kHz to 0.01Hz.

Measurement of Nucleation and Dissolution of Li₂S: Nucleation and dissolution of Li₂S were studied in standard 2032 coin cells. Equal amounts of ZnSe/NHC, NHC and Super P composites were dispersed in ethanol and then coated on carbon papers, which worked as the cathode. Li foil was used as the counter electrode. 20 μL of 0.25 M Li₂S₈ with 1.0 M LiTFSI in tetraethylene glycol dimethyl ether solution was used as catholyte, and 20 μL of a 1.0 M LiTFSI solution without Li₂S₈ was used as anolyte. Coin cells were held at 2.06 V to reduce the generation of higher order LiPS than Li₂S₄. After that the cells were potentiostatically discharged at 2.05 V until current decreased to 10⁻⁵ A. The dissolution of Li₂S was tested by assembling fresh coin cells, which were galvanostatically discharged at 0.10 mA until 1.80 V, and subsequently galvanostatically discharged at 0.01 mA to 1.80 V for full transformation of S species into solid Li₂S. Then cells were potentiostatically charged at 2.40 V for the dissolution of Li₂S into soluble LiPS until the charge current was below 10⁻⁵ A.

Details of Theoretical calculations: Density Functional Theory (DFT) calculations were carried out with the projector-augmented wave pseudopotentials (PAW) as implemented in the VASP software. The PBE formula in the GGA was adopted to describe the exchange-correlation. The DFT-D2 correction proposed by Grimme was used to correct the van der Waals interaction between the ZnSe and N-doped Carbon (N-doped C) layers. The k-points grid of 2×2×1, 5×5×1 and 3×3×1 determined by Gamma-centered Monkhorst-Pack method in

the Brillouin zone were employed for monolayer ZnSe, monolayer N-doped C, and mixed heterojunction, respectively.

The plane-wave basis set with a cutoff energy of 500 eV was used. The structural optimization ceased when the force and energy were less than 0.01 eV/Å and 10⁻⁵ eV respectively. Besides, a 35 Å vacuum space in the z-direction was set to avoid the spurious interactions between periodic images. The adsorption energies (E_a) for lithium and LiPS on the ZnSe (002) and ZnSe (111) surface, were defined as:

$$E_{a002} = E_{total} - E_{Li_2S_x} - E_{substrate002}$$

$$E_{a111} = E_{total} - E_{Li_2S_x} - E_{substrate111}$$

where E_{total} stands for the energy of the ZnSe (002) or (111) surface with Li₂S_x, $E_{Li_2S_x}$ is the energy of the Li₂S_x, $E_{substrate}$ is the energy of ZnSe (002) or (111) substrate.

2.4 Results and discussions

A schematic illustration of the process to produce S@ZnSe/NHC is shown in Figure 1a. First, a ZIF-8 precursor powder with polyhedron-shaped particles was synthesized via a modified precipitation method (Supporting Information, Figure S1). In a second step, the obtained precursor was annealed in a Se atmosphere to produce ZnSe/NHC (see experimental section for details). Finally, sulfur was incorporated within ZnSe/NHC by means of a melt-diffusion process. SEM characterization revealed the ZnSe/NHC particles display a polyhedral geometry with empty interiors as observed from some partially broken particles, EDS and TEM characterization (Figure 1b,c, d). We believe the hollow structure to be originated as a consequence of the different diffusion rates of selenium and zinc species through the growing ZnSe/NHC shells. This mechanism of formation of hollow particles is known as the nanoscale Kirkendall effect.^[36,37] EDS and EELS elemental maps showed C, N, Zn and Se to be homogeneously distributed throughout the ZnSe/NHC cages (Figure 1c,e). XRD and HRTEM analyses showed the cubic ZnSe (JCPDS No.37-1463) as the main crystalline phase found within our ZnSe/NHC composites (Figure 1f,g).^[38,39] DFT analysis of the electronic distribution within ZnSe/NHC was analyzed by DFT showed electrons to be transferred from ZnSe to NHC and to accumulate around N atoms (Figure 1h), referring to model of the charge density difference of ZnSe/NHC (Figure S2). This charge redistribution at the interface region might enhance electron mobility in the composite.

XPS survey analysis showed the presence of Zn, Se, C, N and O in the surface of ZnSe/NHC (Figure 2a). The presence of oxygen was attributed to the exposure of the sample to air during handling and transportation. ^[28,40] XPS analysis also showed the material Fermi level to lay within a band of states, consistently with the metallic character of carbon (Figure 2f). The Zn 2p XPS spectrum (Figure 2b) exhibited one doublet at 1044.4 (Zn 2p_{1/2}) and 1021.4 eV (Zn 2p_{3/2}) assigned to Zn²⁺ within a ZnSe chemical environment. ^[38,41] The Se 3d spectrum (Figure 2c) also displayed just one doublet at 54.7 eV (Se 3d_{3/2}) and 53.8 eV (3d_{5/2}) associated to Se²⁻ within ZnSe. ^[42,43] The high-resolution C 1s spectrum (Figure 2d) was fitted using four bands. The main band, at 284.8 eV, was associated to C-C and it was used as reference. The N 1s spectrum (Figure 2e) displayed three bands at 398.2, 399.6 and 400.7 eV, which were associated with pyridinic, pyrrolic and graphitic nitrogen, respectively. ^[44,45] The detection of relatively large amounts of nitrogen confirmed the successful incorporation of nitrogen into the carbon framework. The presence of nitrogen within the carbon material was of interest for the potential of this element to increase the local atomic disorder, producing additional defects in carbon and exposing more active sites. Additionally, N-doping increases the electron concentrations, which could improve the electrical conductivity. ^[46,47]

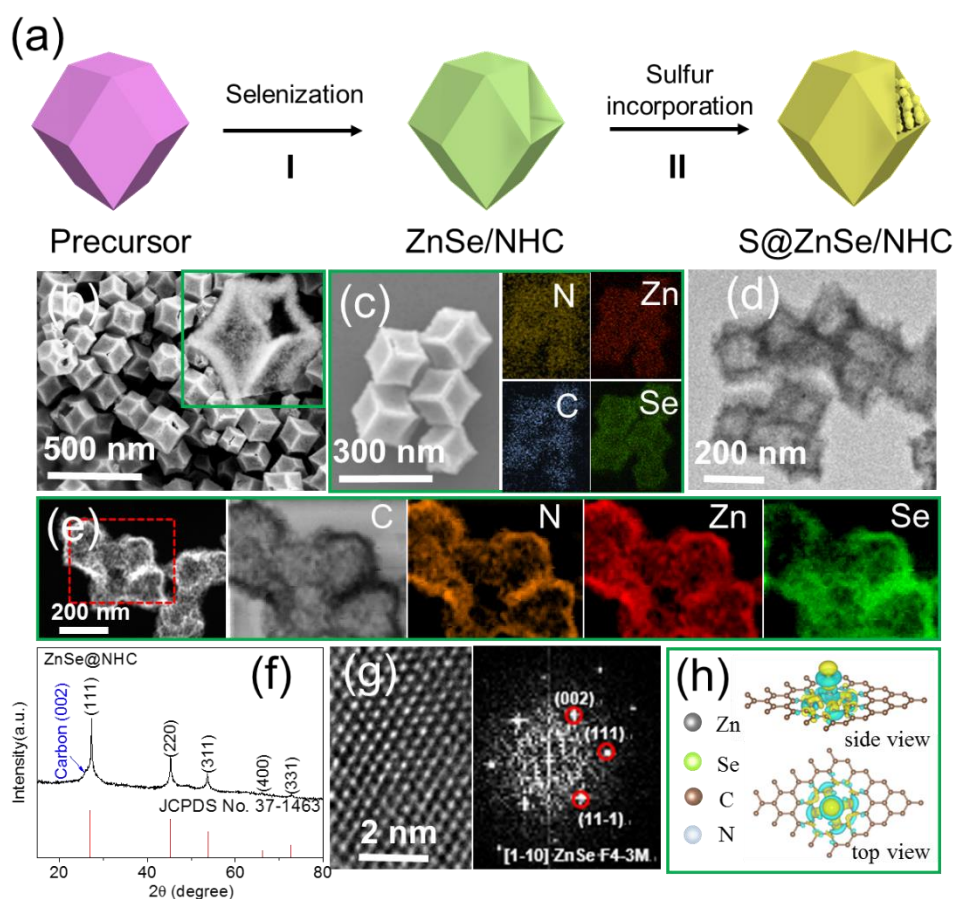


Figure 1. (a) Schematic illustration of the production of S@ZnSe/NHC composites. (b) FESEM image of ZnSe/NHC. Inset shows an enlarged hollow polyhedron. (c) SEM image and corresponding EDX elemental maps of N (yellow), Zn (red), C (blue), and Se (green). (d) TEM image of ZnSe/NHC. (e) STEM micrograph and corresponding EELS chemical composition maps. Individual C K-edge 284 eV (grey), N K-edge 401 eV (blue), Zn $L_{2,3}$ -edge 1020 eV (red), and Se $L_{2,3}$ -edge 1436 eV (green). (f) XRD pattern of ZnSe/NHC, including reference pattern for cubic ZnSe (JCPDS No. 37-1463). (g) HRTEM image of ZnSe/NHC and corresponding FFT spectrum. ZnSe lattice fringe distances were measured to be 0.317 nm, 0.321 nm, and 0.285 nm, at 67.48° and 123.37° which was interpreted as the ZnSe cubic phase visualized along its [1-10] zone axis. (h) Calculated charge density difference of ZnSe/NHC. The yellow and blue regions represent increased and decreased electron density, respectively.

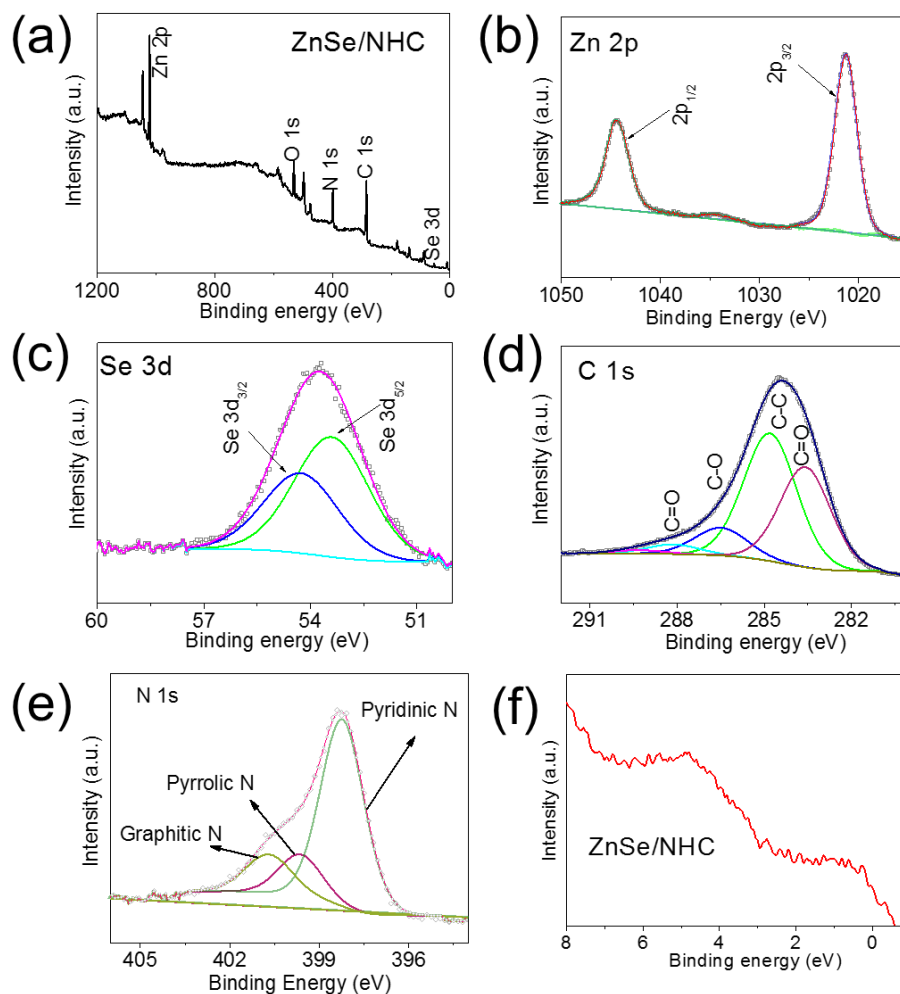


Figure 2. XPS spectra of the ZnSe/NHC composite. (a) Survey XPS spectrum. (b-f) High resolution XPS spectra of the regions: (b) Zn 2p, (c) Se 3d, (d) C 1s and (e) N 1s. (f) Valence band.

S@ZnSe/NHC particles maintained the polyhedral geometry of ZnSe/NHC and ZIF-8 but displayed a partially filled structure (Figure 3a). To further verify the presence of sulfur within the hollow structures, nitrogen adsorption-desorption isotherms of the ZnSe/NHC cages before and after sulfur incorporation were measured (Figure 3b, c). The Brunauer–Emmett–Teller (BET) specific surface area was $275 \text{ m}^2 \text{ g}^{-1}$ for ZnSe/NHC, and decreased to $15.6 \text{ m}^2 \text{ g}^{-1}$ for S@ZnSe/NHC. In parallel, the overall pore volume decreased from 0.29 to $0.05 \text{ cm}^3 \text{ g}^{-1}$, with the sulfur incorporation. These results further suggested the partial filling of the internal cavities of ZnSe/NHC. We believe the partially filled and partially empty voids to be advantageous in terms of buffering the volume change and trap polysulfides during the charge/discharge process. ^[48] Extensive TEM characterization showed the presence of large sulfur aggregates outside the ZnSe/NHC cages (Figure 4a). EELS elemental maps further

demonstrated the homogeneous distribution of sulfur within the cages (Figure 4b). XRD patterns of S@ZnSe/NHC displayed the presence of additional peaks that were indexed as cubic sulfur (Figure 4c). [20] TGA analysis showed a mass decrease of ca. 70% when heating the sample up to 300 °C, which was associated to the evaporation of sulfur and it was consistent with the nominal amount of sulfur introduced within ZnSe/NHC (Figure. 4d).

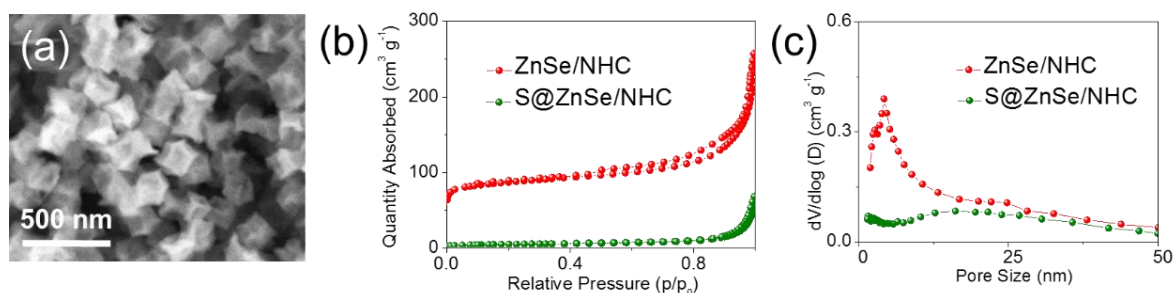


Figure 3. (a) SEM image, (b) N₂ adsorption-desorption isotherms, and (c) Pore size distribution of S@ZnSe/NHC.

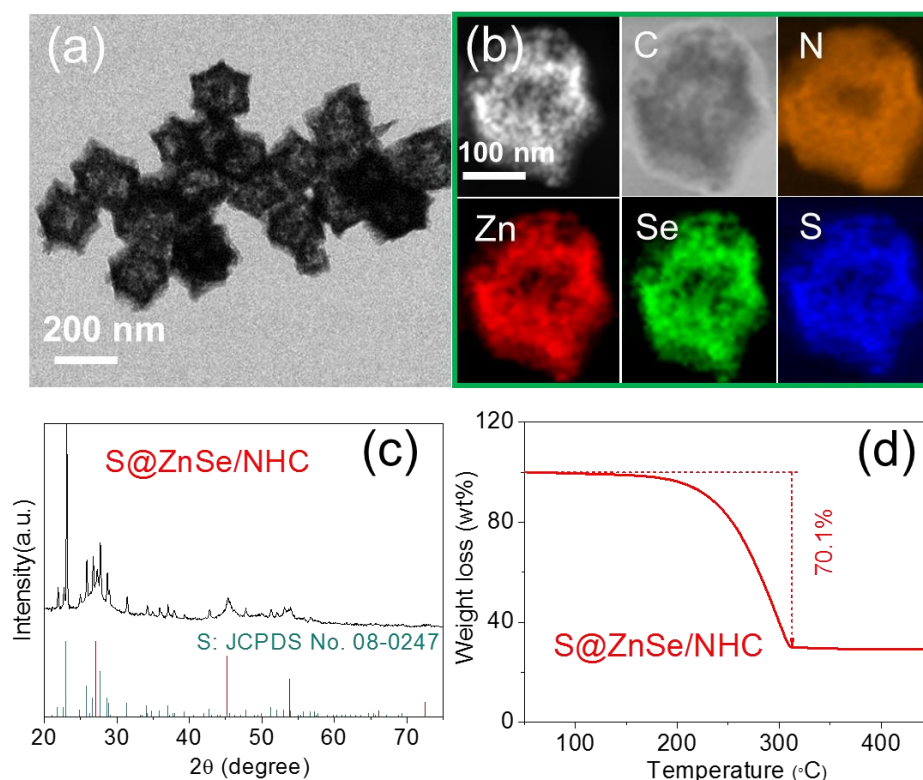


Figure 4. (a) Representative TEM image of a S@ZnSe/NHC composite. (b) STEM micrographs and corresponding EELS chemical composition maps. Individual C K-edge 284 eV (grey), N K-edge 401 eV (orange), Zn L_{2,3}-edge 1020 eV (red), Se L_{2,3}-edge 1436 eV (green), and S L_{2,3}-edge 165 eV (blue). (c) XRD pattern of S@ZnSe/NHC, including reference

patterns for cubic ZnSe (JCPDS No. 37-1463) and cubic sulfur (JCPDS No. 08-0247). (d) TGA curve of S@ZnSe/NHC composite.

The Li_2S_4 adsorption ability of the host material was tested to evaluate its potential to confine LiPS. **Figure 5a** displays optical images of vials that initially contained a 10 mM solution of Li_2S_4 and the same amount of ZnSe/NHC, Super P or NHC. After overnight mixing of the solutions, clear color differences were observed between the different vials. The Li_2S_4 solutions containing ZnSe/NHC and NHC displayed a much paler color than the solution containing Super P. This faded color was associated to a much more effective adsorption of Li_2S_4 on NHC and especially on ZnSe/NHC. UV-vis spectroscopy of the solution supernatants confirmed the notable differences of absorbance in the 400–500 nm region associated to Li_2S_4 ,^[49,50] corroborating the different Li_2S_4 adsorption ability of the various host materials (Figure 5b).

Figure 5c displays the high-resolution N 1s XPS spectrum of ZnSe/NHC before and after the Li_2S_4 adsorption test (ZnSe/NHC- Li_2S_4). A clear shift of the N 1s bands was observed with the Li_2S_4 adsorption. We associate this shift with the binding of Li_2S_4 and N heteroatoms. This binding takes place through a dipole-dipole electrostatic interaction between Li atoms having a Lewis acid character within LiPS and N heteroatoms with extra pair of electrons in carbon materials and a Lewis base character.^[46,51] This Li-N affinity provides NHC with a lithiophilic character that explains the high Li_2S_4 adsorption ability of NHC. Figure 5d displays the high-resolution Zn 2p XPS spectrum of ZnSe/NHC before and after the Li_2S_4 adsorption test. A slight shift of the Zn 2p bands to higher binding energies was also observed after Li_2S_4 adsorption. This shift was consistent with Zn being in a slightly more electronegative chemical environment than within ZnSe, which we associate with a chemical interaction between Zn and sulfur. This Zn-S interaction, which adds up to the N-Li interaction, explains the higher Li_2S_4 adsorption ability of ZnSe/NHC when compared with NHC.

DFT calculations were conducted to understand the chemical anchoring process at the atomic level. The geometries of the adsorption configurations for LiPS at six different lithiation stages on a N-doped C surface are displayed in Figure 6a. The binding energy (E_b) between LiPS species and ZnSe/NHC was calculated to evaluate the LiPS adsorption capability. Figure 6b displays a configuration of a Li_2S_4 molecule immobilized by Li-N bonds on N-doped C surface with a high E_b , -3.03 eV, suggesting a high lithiophilicity of NHC associated to the presence of N. Several adsorption configurations with significantly higher E_b than graphitic carbon demonstrated the affinity of N-doped C toward various LiPS species (Figure 6c).^[52,53]

Several geometrically configurations of LiPS adsorbed at (111) and (002) facets of ZnSe are illustrated in Figure 7a. Figure 7b shows the calculated E_b for Li_2S_4 anchored on ZnSe (111) and (002) surfaces to be -7.08 eV and -7.11 eV, respectively. The E_b of additional LiPS adsorbed on the (111) and (002) surfaces of ZnSe are presented in Figure 7c. These DFT results demonstrated a strong interaction between S within LiPS and Zn within ZnSe, which corroborates the sulfiphilic character of ZnSe within ZnSe/NHC. Overall, both experimental results and DFT calculations proved ZnSe/NHC to have a high affinity toward LiPS, associated to the presence of a multiple sites adsorption effect related to the presence of sulfiphilic sites on ZnSe and of lithiphilic sites on NHC.

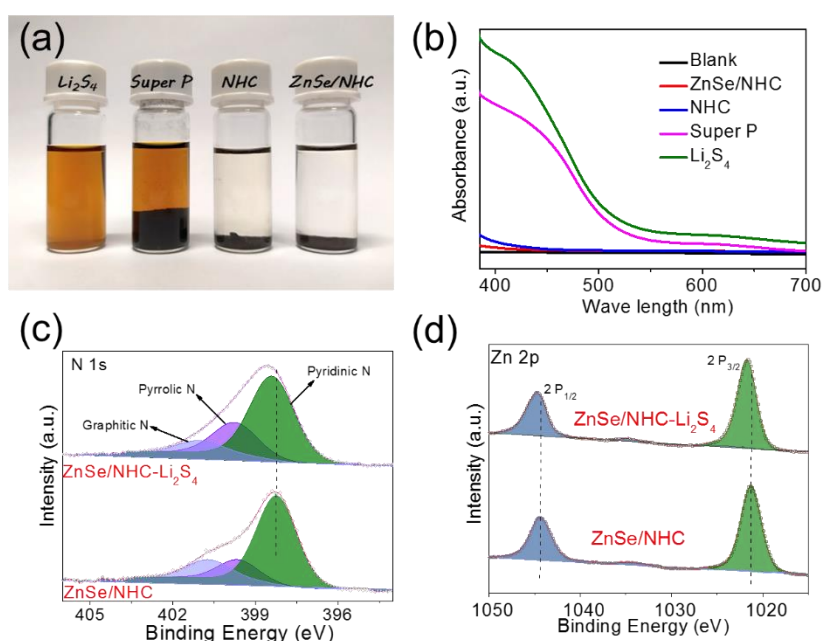


Figure 5. (a) Photograph of Li_2S_4 solutions containing (from left to right and as indicated in the figure): no adsorbent, Super P, NHC and ZnSe/NHC. (b) UV-Vis spectra of the polysulfide solution after overnight mixing with the different adsorbents. A blank spectrum and the spectrum of the Li_2S_4 solution not exposed to any adsorbent are also displayed. (c) N 1s and (d) Zn 2p XPS spectra of ZnSe/NHC before and after adsorption of Li_2S_4 .

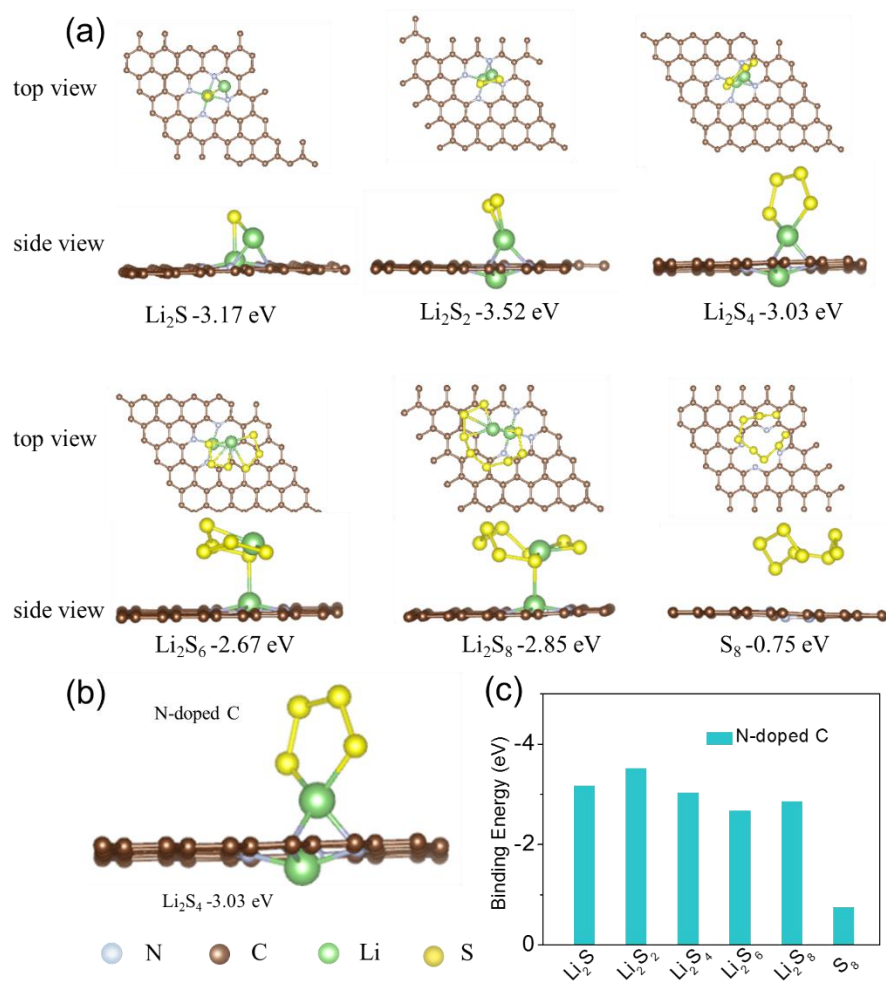


Figure 6. (a) DFT calculation results of optimized geometrical configurations between the surface of N-doped C and LiPS species (Li_2S , Li_2S_2 , Li_2S_4 , Li_2S_6 , Li_2S_8 and S_8). (b) Adsorption configurations for Li_2S_4 on a N-doped C surface. (c) Calculated binding energy between LiPS (Li_2S , Li_2S_2 , Li_2S_4 , Li_2S_6 , Li_2S_8 and S_8) and the N-doped C surface.

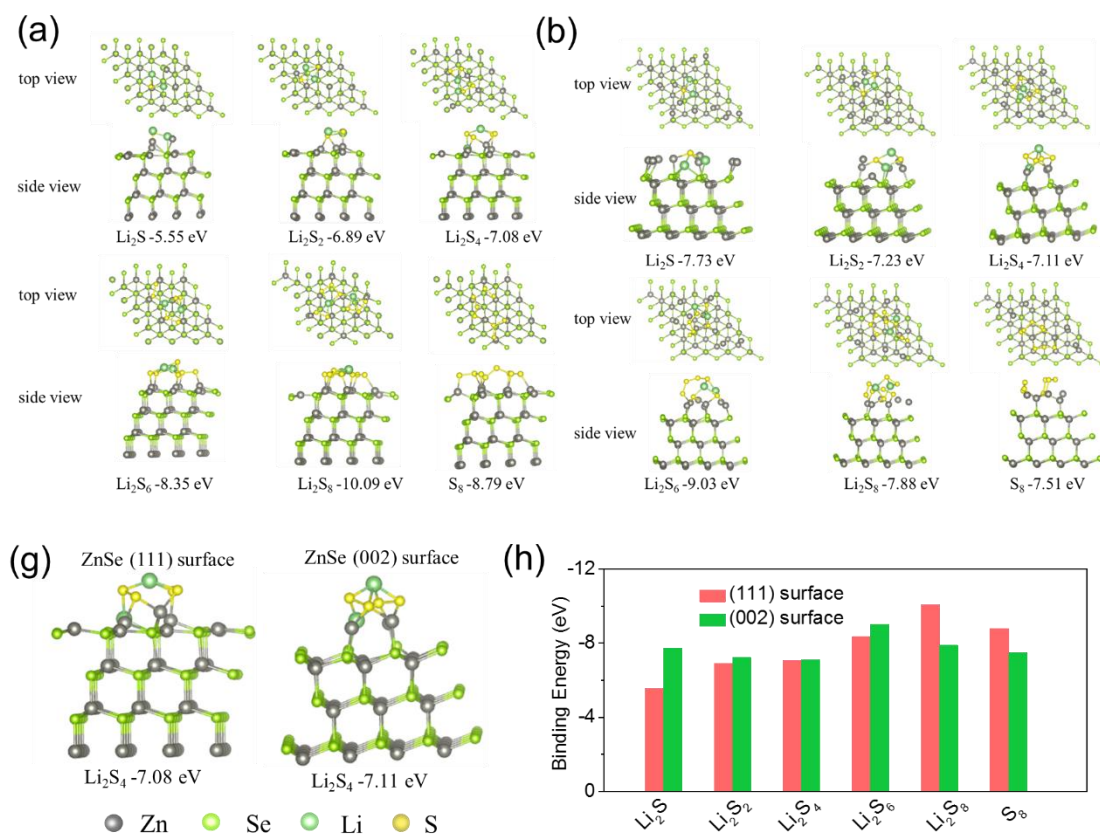


Figure 7. DFT calculation results of optimized geometrical configurations of different surface of ZnSe with LiPS (Li₂S, Li₂S₂, Li₂S₄, Li₂S₆, Li₂S₈ and S₈). (a) (111) surface. (b) (002) surface. (c) Optimized geometrical configurations of ZnSe with Li₂S₄ on both (111) and (002) surfaces. (d) Binding energies for LiPS (Li₂S, Li₂S₂, Li₂S₄, Li₂S₆, Li₂S₈ and S₈) on ZnSe surfaces calculated with DFT.

In order to study the electrocatalytic activity of the materials, CV curves were measured from symmetric cells made using 0.5 mol L⁻¹ Li₂S₆ and 1 mol L⁻¹ LiTFSI dissolved in DOL/DME (v/v = 1/1) as electrolyte and identical ZnSe/NHC (NHC and Super P) electrodes as working and counter electrodes. To be able to eliminate the capacitive contribution, the CV of ZnSe/NHC in a Li₂S₆-free electrolyte was also measured as a reference (Figure 8a). As shown in **Figure 8b**, ZnSe/NHC cells displayed two pairs of reversible redox peaks at a scan rate of 20 mV s⁻¹. During discharge process, the reduction peaks at -0.22 V and -0.62 V were related with the reduction of S to Li₂S₆ and of Li₂S₆ to Li₂S, respectively. In the subsequent charge process, the oxidation peaks at 0.22 and 0.62 V corresponded to the oxidation of Li₂S to Li₂S₆ and of Li₂S₆ to S, respectively. ^[11,26] CV curves of ZnSe/NHC symmetric cells overlapped each other as shown for 10 cycles in Figure 8c, indicating an excellent reversibility. On the other hand, symmetric cells made of NHC and Super P-based electrodes exhibited much lower

current densities and undefined redox peaks, demonstrating the essential role played by ZnSe in the electrochemical process.

Results from EIS analysis of different symmetric cells after CV tests are displayed in Figure 8d. The equivalent circuit shown in the inset was used to fit Nyquist plots. The intersection of the curve with abscissa is assigned to the interphase-contact resistance of the electrolyte and the cells (R_s). The first semicircle in the high frequency is related to the interface between the insulating layer of Li_2S and the electrode (R_{int}). The second semicircle in the middle frequency region is ascribed to the charge transfer resistance (R_{ct}). Finally, the sloping lines in the low frequency region correspond to Warburg impedance (Z_w), which is related to the diffusion of lithium ions into the electrode. [54] According to the fitting results (Figure 8e-g), the R_{int} from the ZnSe/NHC cell (20.15 Ω) was much smaller than the measured from NHC (46.06 Ω) and Super P (66.27 Ω). We associate this smaller R_{int} attributes to the uniform deposition of Li_2S on the surface of the electrodes. And also ZnSe/NHC cells delivered a lower R_{ct} (40.08 Ω) compared to NHC (68.1 Ω) and Super P (82.3 Ω), indicating enhanced charge and ion transfer, possibly due to their high conductivity.

Overall, the analysis of symmetric cells demonstrated that ZnSe/NHC was characterized by significantly enhanced polysulfide redox kinetics enabled by a much faster charge transfer kinetics at the ZnSe/NHC/polysulfide interface. [55-57]

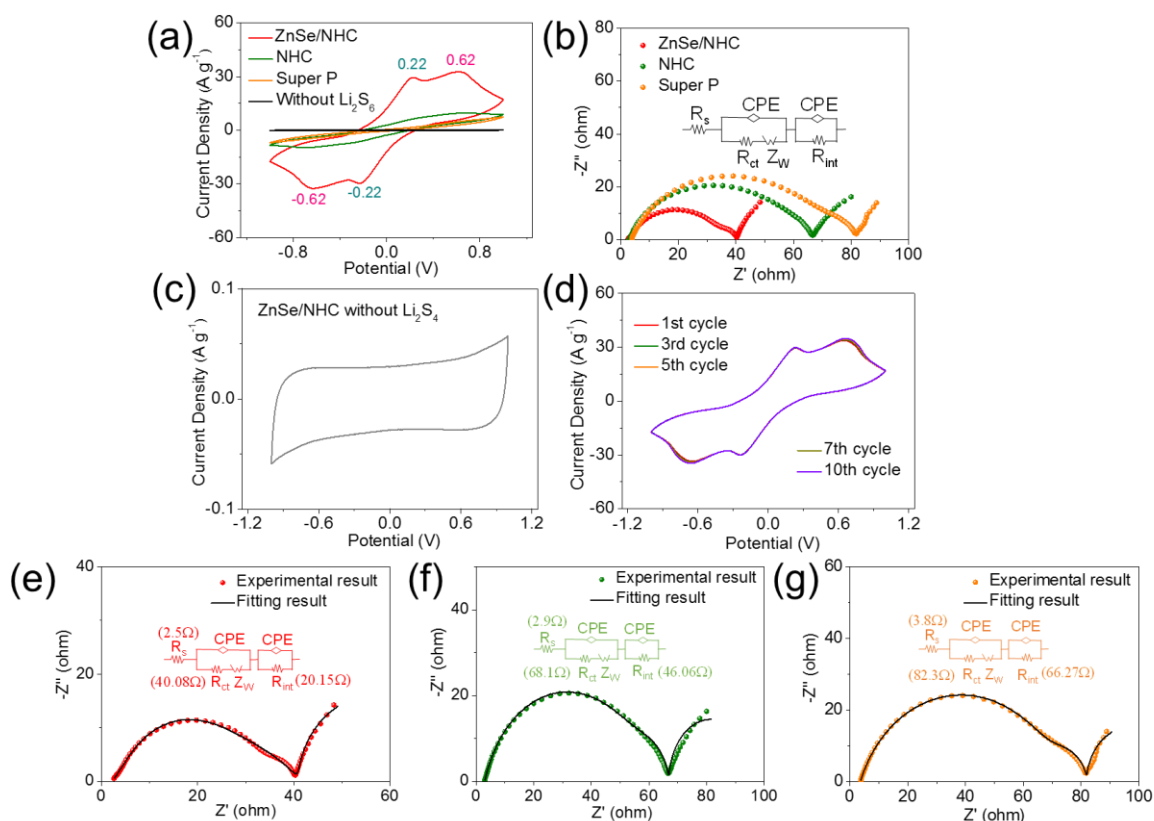


Figure 8. (a) CV curves at a scan rate of 20 mV s^{-1} of symmetrical cells using an electrolyte containing $0.5 \text{ mol L}^{-1} \text{ Li}_2\text{S}_6$. (b) EIS curves of the same cells. Inset shows the fitted equivalent circuit. (c) The CV curve of ZnSe/NHC as electrode measured in symmetric coin cell using an electrolyte without Li_2S_6 . (d) CV curves of symmetric cells of ZnSe/NHC worked as electrodes at a scan rate of 20 mV s^{-1} for the first ten cycles. The Nyquist plots from EIS data and the corresponding fitting curves using the displayed equivalent circuit. (e) ZnSe/NHC. (f) NHC. (g) Super P.

CV curves of Li–S coin cells based on S@ZnSe/NHC, S@NHC and S@Super P cathodes are assembled. CV curves measured from S@ZnSe/NHC cells almost overlapped during the first three cycles, implying a good reversibility of the sulfur redox reactions (Figure 9). S@ZnSe/NHC cathodes showed two representative cathodic peaks and one anodic peak. The two cathodic peaks (peak I and peak II) were associated with the reduction of S_8 molecules to long-chain polysulfides (peak I) and to the further reduction to short-chain sulfides (peak II). The broad anodic peak (Peak III) was ascribed to the multistep oxidation of short-chain sulfides eventually to S_8 (Figure 10a).^[23,55] The S@ZnSe/NHC cathode displayed a more positive potential of the cathodic peaks (peak I at 2.301 and peak II at 2.035 V) and a more negative anodic peak (peak III at 2.355 V) than S@NHC and S@Super P (Figure 10b).

We further determined the onset potential as the potential required to reach a current density of $10 \mu\text{A cm}^{-2}$ beyond the baseline current as conventionally done in electrocatalysis (Figure 10c-f).^[58,59] We observed the cells based on S@ZnSe/NHC cathodes to display higher onset potentials of reduction peaks and lower onset potentials of oxidation peaks than cells based on other materials, which is consistent with the promotion of the polysulfide redox kinetics by the presence of ZnSe/NHC.

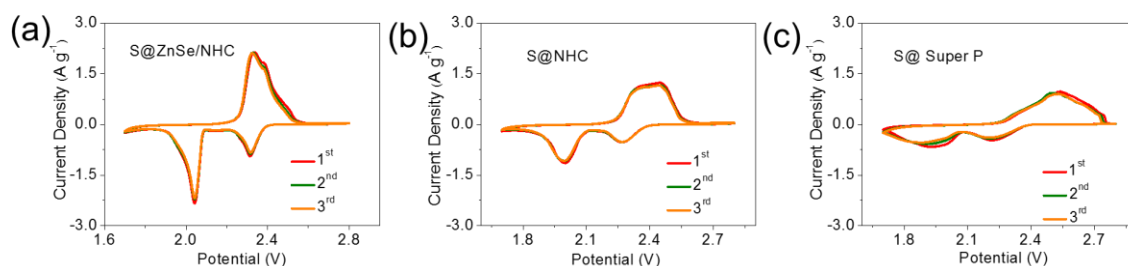


Figure 9. First three cycles of CV curves of (a) S@ZnSe/NHC, (b) S@NHC and (c) S@Super P carried out at a scan rate of 0.1 mV s^{-1} .

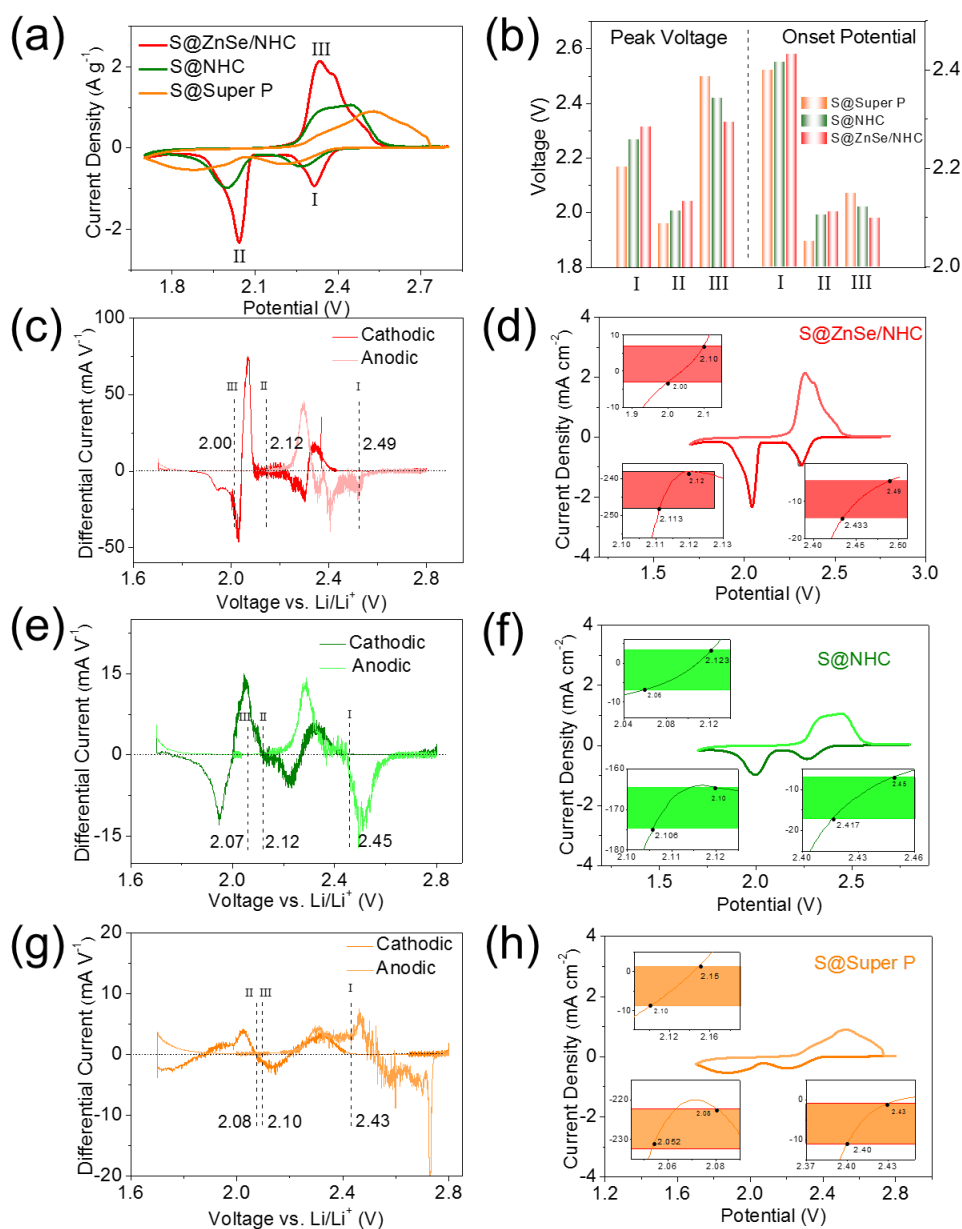


Figure 10. (a) CV curves of different electrodes at a scan rate of 0.1 mV s^{-1} within 1.7-2.8 V versus Li/Li^+ . (b) Values of peak voltages and onset potentials of Li-S cells obtained from the CV curves. Differential CV curves of (c) S@ZnSe/NHC, (e) S@NHC and (g) S@Super P. The base line voltage and current density are defined as the value before the redox peak, where the variation on current density is the smallest, named as $dI/dV=0$. The value of the base line voltages for cathodic peak I, II and anodic peak III were calculated, respectively. CV curves and corresponding onset potentials of redox peak I, II, and III (inset): (d) S@ZnSe/NHC, (f) S@NHC and (h) S@Super P. Following a common definition employed in electrocatalysis, the onset potential is determined when the current density is $10 \mu\text{A cm}^{-2}$ beyond the corresponding baseline current density (more specifically, $10 \mu\text{A cm}^{-2}$ more negative than baseline current

density for cathodic peaks or $10 \mu\text{A cm}^{-2}$ positive than baseline current density for anodic peaks).

CV tests at different scan rates from 0.1 to 0.4 mV s^{-1} were conducted to investigate the electrode reaction kinetics and the lithium ion diffusion properties of S@ZnSe/NHC, S@NHC and S@Super P cathodes. As shown in Figure 11a, with the increase of the scan rates, the peak current density of the S@ZnSe/NHC cathode increased, but its shape was maintained, denoting a good electrochemical stability. Besides, we observed a linear relationship between the cathodic and anodic peak currents and the square root of the scanning rate, as it corresponds to a diffusion-limited process (Figure 11b). From the fitting of this linear dependence, the diffusion constant of the rate limiting species, i.e. D_{Li^+} , was calculated according to the Randles–Sevcik equation: [28,60]

$$I_p = (2.69 * 10^5) n^{1.5} A D_{\text{Li}^+}^{0.5} C_{\text{Li}^+} v^{0.5} \quad \text{Equation 1}$$

Where I_p is the peak current density, n is the number of charge transferred, A is the geometric area of the electrode, C_{Li^+} is the concentration of lithium ions in the cathode, and v is the scan rate. According to the Randles–Sevcik equation, the values of D_{Li^+} calculated for S@ZnSe/NHC at peaks I, II, and III were 3.1×10^{-7} , 4.4×10^{-7} , and $7.2 \times 10^{-7} \text{ cm}^2 \text{ s}^{-1}$, respectively (Figure 11c). Among the three materials tested, S@ZnSe/NHC electrodes exhibited the sharpest slopes, thus the fastest lithium ion diffusion in both reduction and oxidation processes (Figure 12). The enhanced D_{Li^+} may be related to two aspects: i) a higher catalytic activity that lowers the energy barriers for electron transfer; and ii) a strong polysulfide adsorption that reduces the electrolyte viscosity, increasing mobility of electrolyte species and avoiding the deposition of an insulating layer.

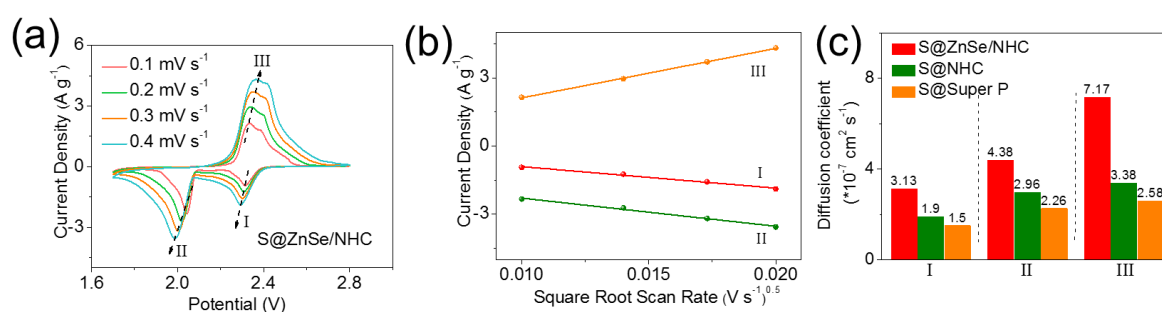


Figure 11. (a) CV curves of a S@ZnSe/NHC cathode at different scan rates. (b) CV redox peak current versus the square root of the scan rate. (c) Li^+ diffusion coefficient calculated from the different CV redox peaks according to the Randles–Sevcik equation. (h) Potentiostatic

discharge profiles with a Li_2S_8 solution at 2.05 V. (i) Potentiostatic charge profile at 2.40 V to evaluate dissolution kinetics of Li_2S .

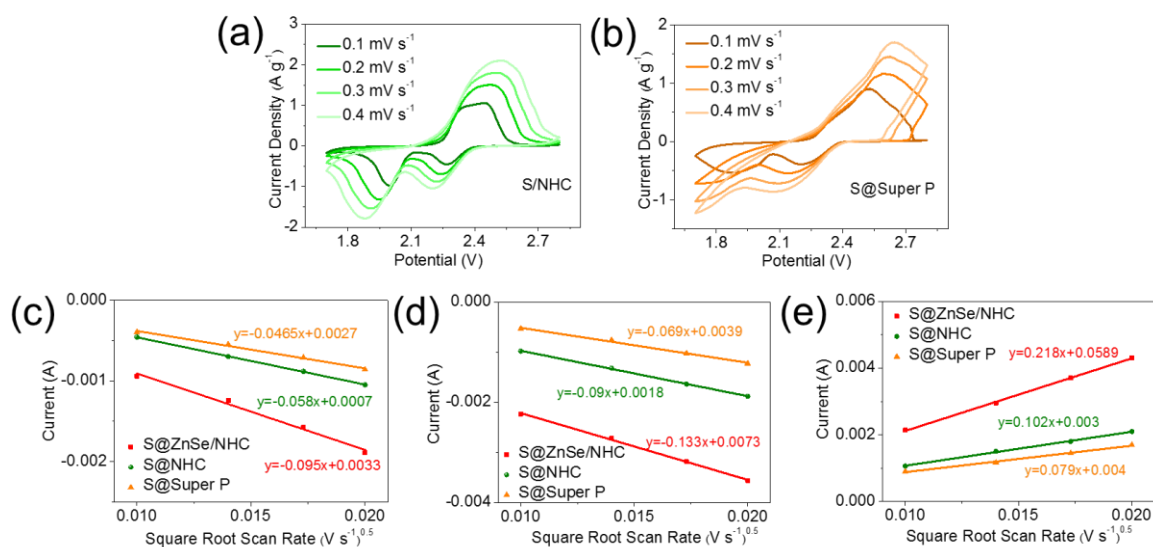


Figure 12. (a) CV curves of S@NHC and (b) S@Super P at different scan rates. (c) Plots of CV peak current for the first cathodic reduction, (d) the second cathodic reduction, (e) anodic oxidation process vs the square root of the scan rates.

To further explore catalytic properties of the cathode materials, the Li_2S nucleation and dissolution was studied through potentiostatic measurements. As observed in Figure 4h, the presence of ZnSe clearly resulted in shorter nucleation and growth times and a higher discharging peak current during the potentiostatic measurement at 2.05 V. Based on the Faraday's law, the capacity of ZnSe/NHC electrodes was calculated at 248.2 mAh g^{-1} , well above that of NHC (168.5 mAh g^{-1}) and Super P electrodes (101.8 mAh g^{-1}). These results suggest that ZnSe significantly improved the kinetics of Li_2S precipitation.^[30] To study the kinetics of the Li_2S dissolution step, the potentiostatic cell charge at 2.40 V was analyzed (Figure 4i). ZnSe/NHC cathodes resulted in significantly higher current densities compared to NHC and Super P, indicating its lower oxidation overpotential for Li_2S dissolution.^[61,62] Furthermore, the capacity of Li_2S dissolution of ZnSe/NHC (505 mAh g^{-1}) was higher than NHC (400 mAh g^{-1}) and Super P (342 mAh g^{-1}).

After 20000 s potentiostatic discharge the coin cells were disassembled to further investigate the ability of ZnSe/NHC in regulating the nucleation of Li_2S . Interestingly, a layer of small Li_2S nanoparticles were uniformly distributed on the surface of ZnSe/NHC (Figure S15a). In contrast, Li_2S nanoparticles aggregated on the surface of Super P, forming a bulky structure (Figure S15b). The differences in the morphology were mainly related to the large density of

lithiophilic and sulfiphilic nucleation sites on the surface of ZnSe/NHC, which captured polysulfides and reduce the energy barrier of Li_2S nucleation. We believe this process significantly limited the shuttle effect.^[30] From the above results, it can be concluded that NHC and ZnSe with lithiophilic and sulfiphilic sites, respectively, are able to capture LiPS efficiently during redox reactions. The presence of ZnSe nanoparticles greatly boosts the reaction kinetics of LiPS.

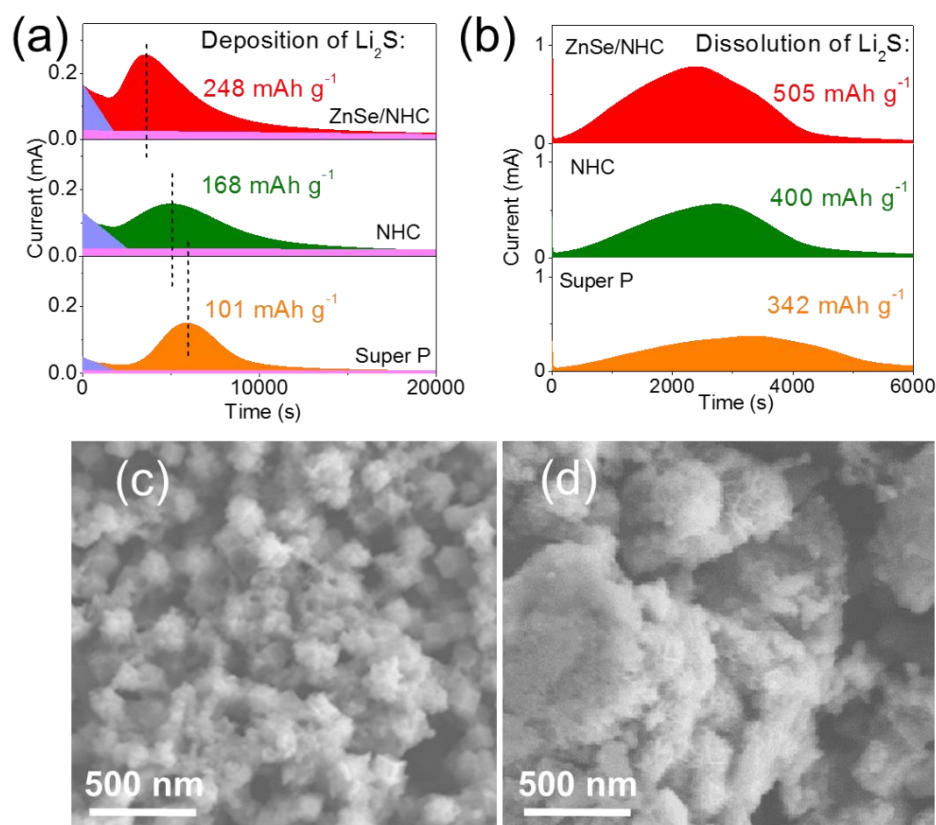


Figure 13. (a) Potentiostatic discharge profiles with a Li_2S_8 solution at 2.05 V. (b) Potentiostatic charge profile at 2.40 V to evaluate dissolution kinetics of Li_2S . SEM images of Li_2S particles on different surfaces. (c) ZnSe/NHC. (d) Super P.

We further verified the boosted redox kinetics of LiPS catalytic conversion by DFT calculations. Figure 14 and 15a show the minimum energy barrier (E_{barrier}) of Li ion diffusion on three facets, suggesting Li ion diffused fastest on the (002) facet of ZnSe than on the other two facets. The schematic diagram of Li ion diffusion on (002) facet is displayed in Figure 15b. Figure 16 exhibit the E_{barrier} of Li ion diffusion for different adsorption sites of the three facets. It was concluded that ZnSe diffuses fastest on the (002) facet, suggesting that the presence of ZnSe accelerates the diffusion of Li ion. Figure 17 shows the initial state, transition state and final state of Li_2S_4 migration on the three facets. The E_{barrier} of Li_2S_4 migration along different

adsorption sites shown in Figure 18. The E_{barrier} for Li_2S_4 migration was calculated to be 0.392, 0.771 and 1.25 eV on (002), (111) and N-doped C surfaces, respectively. These results confirmed that ZnSe facilitated the migration of Li_2S_4 . During the reaction process, LiPS species were anchored through the lithiophilic sites of NHC and sulfiphilic sites of ZnSe. This multiple sites adsorption not only effectively suppressed the shuttle effect, but also accelerated the diffusion of Li^+/LiPS , thereby enhancing the LiPS conversion reaction kinetics (Figure 19).

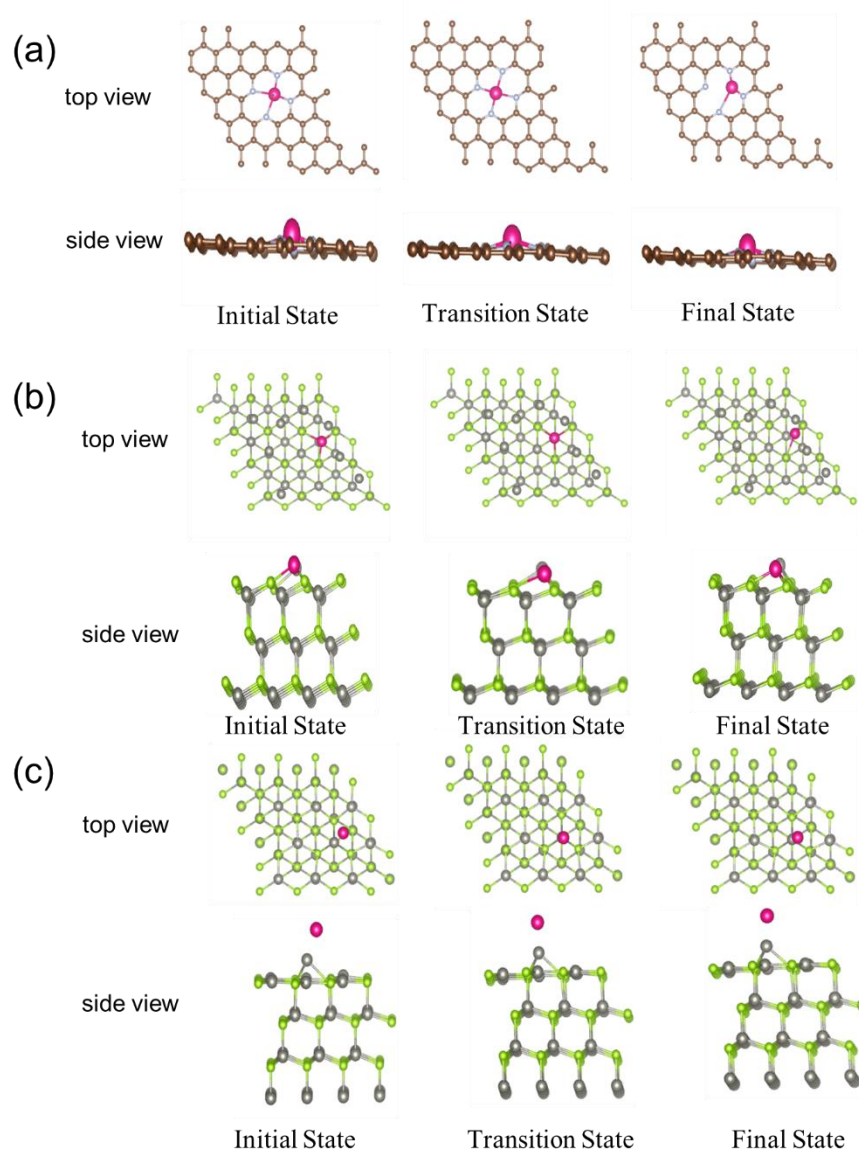


Figure 14. (a) Configurations of the Li ion displacement through the lowest energy path on the surface of N-doped C. Brown, silver and purple balls represent C, N and Li atoms, respectively. The geometrical configurations of Li ion diffusion on (b) (111) and (c) (002) facets of ZnSe. Green, grey and purple balls represent Se, Zn and Li atoms, respectively.

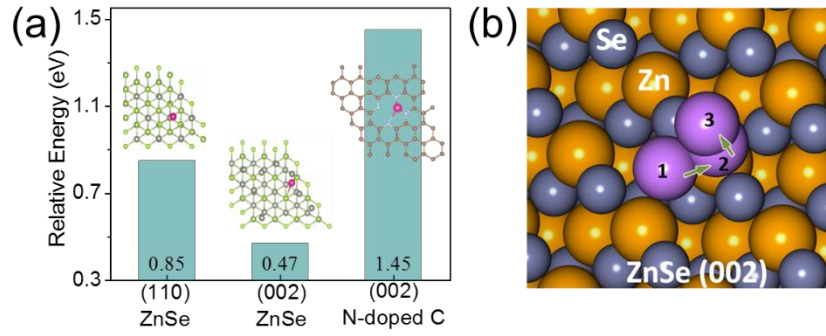


Figure 15. (a) Energy barrier of Li ion diffusion on (111) and (002) facets of ZnSe and (002) facet of N-doped C. (b) Geometrical configurations corresponded to the minimum energy path of Li ion diffusion on (002) facet of ZnSe. 1, 2 and 3 represent initial state, transition state and final state, respectively.

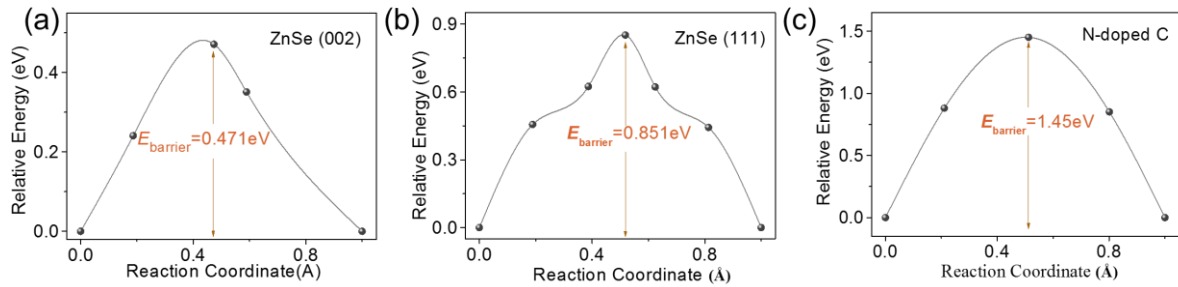


Figure 16. (a) Energy profile for Li ion diffusion on (002) facet at different adsorption sites. E_{barrier} profiles of Li ion diffusion on (b) (111) facet and (c) the surface of N-doped C at different adsorption sites.

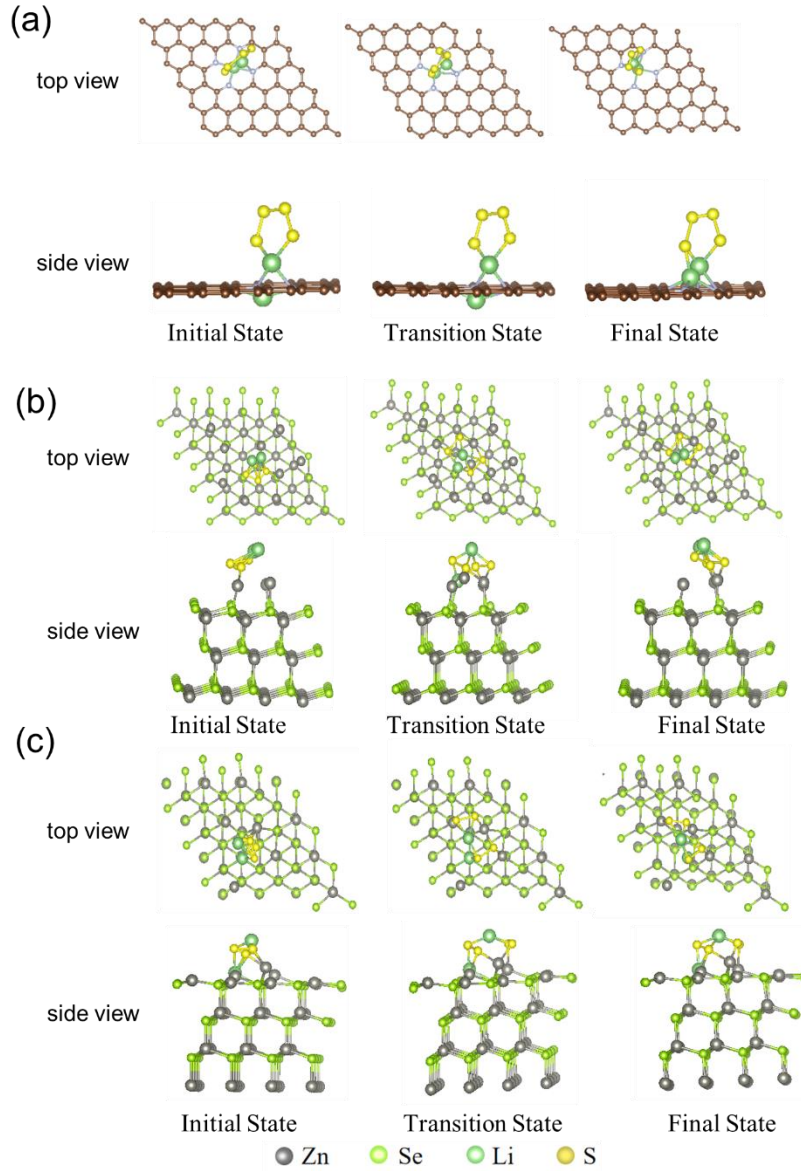


Figure 17. (a) Illustration of Li_2S_4 diffused on the surface of N-doped C. Initial state, transition state and final state of Li_2S_4 diffused on (b) (002) and (c) (111) facets of ZnSe.

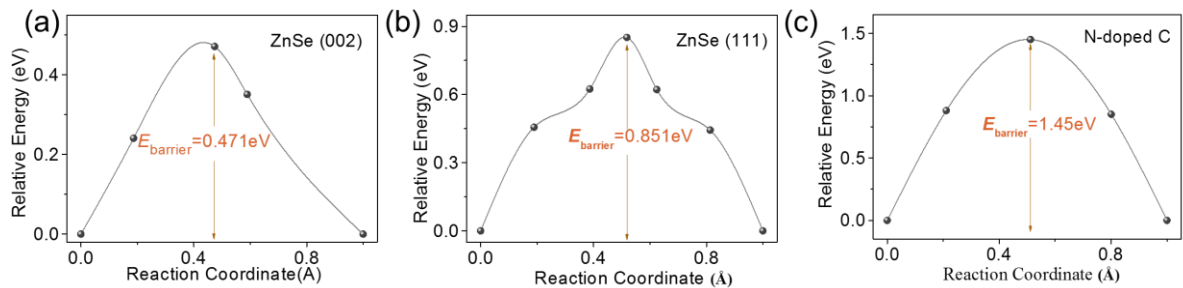


Figure 18. E_{barrier} curves of Li_2S_4 migration on (a) (002), (b) (111) facets of ZnSe and (c) the surface of N-doped C along different adsorption sites.

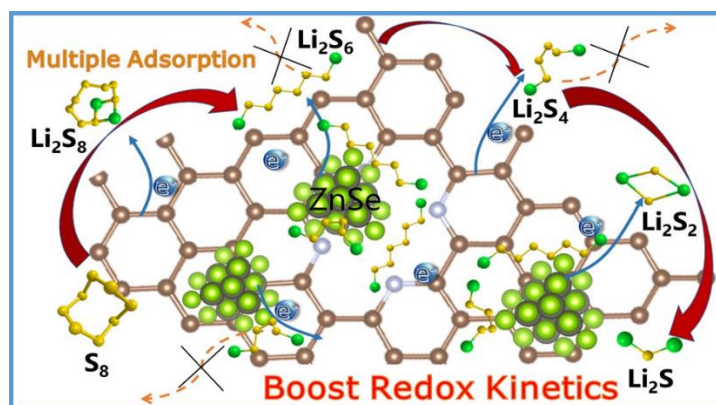


Figure 19. Schematic illustration of the LiPS catalytic conversion on ZnSe during discharge process.

Electrochemical performance was further analyzed through galvanostatic charge–discharge tests. **Figure 20a** shows the charge–discharge curves of S@ZnSe/NHC, S@/NHC and S@Super P at a current density of 0.1 C. Charge–discharge curves displayed two discharge plateaus and one charge plateau. The voltage difference between the oxidation and the second reduction plateaus is the ΔE , referred as ΔE . S@ZnSe/NHC showed lower $\Delta E = 157$ mV than S@NHC ($\Delta E = 190$ mV) and S@Super P electrodes ($\Delta E = 210$ mV) as displayed in Figure 20b. ^[20,51] The first discharge plateau around 2.3 V is related to the reduction of sulfur to soluble LiPS ($S_8 \rightarrow S_6^{2-} \rightarrow S_4^{2-}$). The second discharge plateau, at about 2.1 V, corresponds to the conversion of soluble LiPS to lithium sulfide ($S_4^{2-} \rightarrow Li_2S_2 \rightarrow Li_2S$). ^[22,28] Defining Q1 and Q2 as the capacity of the first and second discharge plateaus, respectively, the ratio Q2/Q1 provides an idea of the material catalytic activity. ^[28] The higher Q2/Q1, the better the catalytic ability, because Q1 measures the amount of soluble polysulfides created and potentially diffusing to the Li metal anode, while Q2 measures how efficiently polysulfides are reduced to Li_2S . ^[63,64] As shown in Figure 20b of the Q2/Q1 ratio for S@ZnSe/NHC was 2.68, well above the values obtained from S@NHC and S@Super P, 2.05 and 1.64, respectively. The high Q2/Q1 ratio further confirmed the superior catalytic activity towards polysulfides redox reaction of ZnSe/NHC. ^[63] The enhanced electrochemical kinetics of S@ZnSe/NHC compared with other electrodes was also in accordance with the lower measured overpotentials for phase conversion between the soluble LiPS and insoluble Li_2S_2/Li_2S during the discharge (Figure 20c) and charge (Figure 20d) processes.

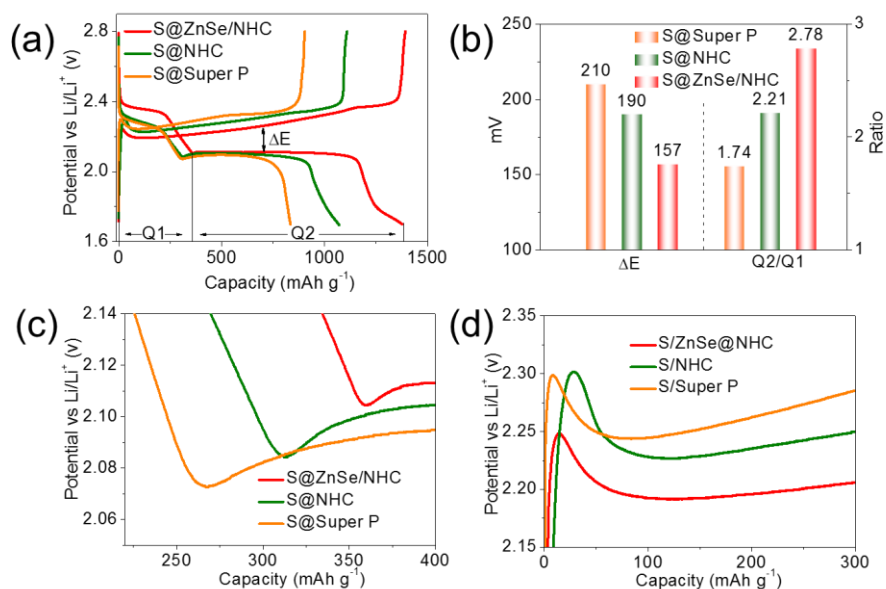


Figure 20. (a) Galvanostatic charge–discharge profiles of different electrodes at a current density of 0.1 C. (b) ΔE and $Q2/Q1$ calculated from the charge–discharge curves. (c) Discharge and (d) charge profiles of S@ZnSe/NHC, S@NHC, and S@Super P electrodes showing the overpotentials for conversion between soluble LiPS and insoluble Li₂S₂/Li₂S.

The galvanostatic charge–discharge voltage profiles of S@ZnSe/NHC at various current densities range from 0.1 to 3 C are presented in Figure 21a, two discharge plateaus and one charge plateau were clearly maintained at the various current rates tested, which is in contrast to results obtained from S@NHC and S@Super P (Figure 21b,c). A high initial specific capacity of 1475 mAh g⁻¹ was delivered by the S@ZnSe/NHC electrode. Additionally, a superior rate performance of this electrode compared was inferred from the average discharge capacities of 1340, 1116, 977, 852, 696 and 542 mAh g⁻¹ at current rates from 0.1 C to 3 C, respectively, which are well above than those obtained from S@NHC and S@Super P (Figure 21d). Even when the current density was returned to 0.2 C, the specific capacity of the S@ZnSe/NHC electrode was recovered to 1068 mAh g⁻¹, suggesting a high stability even after the high rate charge–discharge process.

As shown in Figure 21e, cells based on S@ZnSe/NHC were also characterized by higher energy efficiencies, $E = \int UIdt$, compared to S@Super P. Energy efficiency is a key parameter in energy storage devices, [28] as it determines energy losses during charging/discharging process, especially at high current rates. The significant enhancement in energy efficiency obtained from ZnSe/NHC cells stemmed from the lower ΔE , associated with the exceptional catalytic properties of the cathode material.

The cycling performance of different cathodes was evaluated at a current density of 1 C (Figure 21f). S@ZnSe/NHC electrodes displayed an initial high specific capacity of 858.7 mAh g⁻¹. After 200 cycles, 86.6% of the capacity was still retained, 826.9 mAh g⁻¹. In contrast, the S@NHC cathode presented a discharge capacity of 657.8 mAh g⁻¹ after 200 cycles (76.1% retention), and the S@Super P cathode showed a capacity of only 516.1 mAh g⁻¹ after 200 cycles (67.9% retention). The higher capacity loss in these cathodes was in large part associated to the rapid dissolution of polysulfides into the electrolyte.

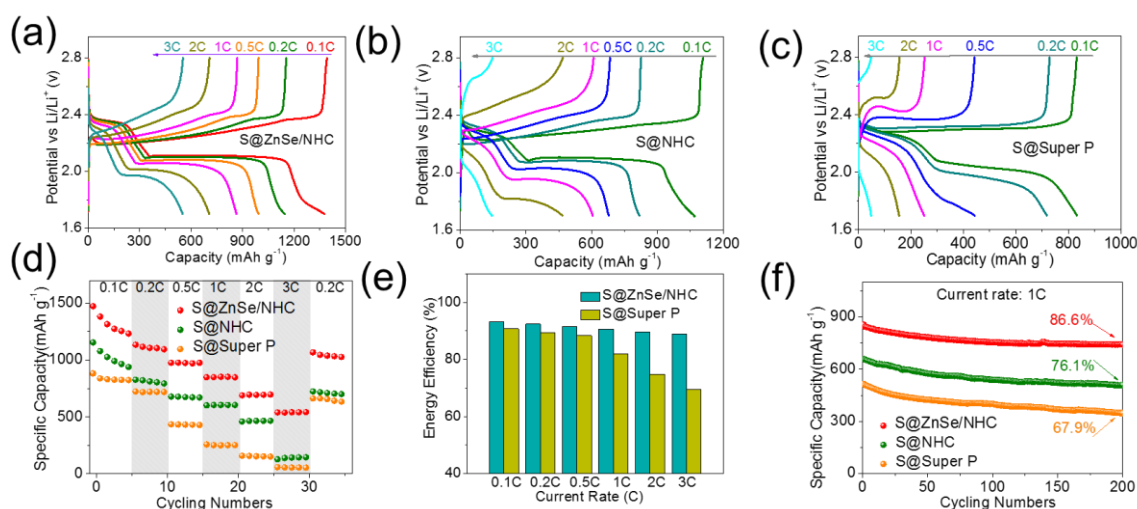


Figure 21. Galvanostatic charge–discharge profiles of (a) S@ZnSe/NHC, (b) S@NHC and (c) S@Super P at different current densities range from 0.1 C to 3 C. (d) Rate capabilities of different electrodes at various current densities. (e) Energy efficiency of S@ZnSe/NHC compared with S@Super P. (f) Cycling life of various cathodes after 200 cycles at 1 C.

The EIS analysis of the S@ZnSe/NHC cathode before the first discharge and after 200 cycles modeled with equivalent circuits was performed. It can be seen clearly from the fresh cells that the first semicircle in the high frequency appears resulted from the deposition of the insulating layer of Li₂S on the electrode surface (R_{int}) after 200 cycles. S@ZnSe/NHC electrodes have a considerably lower R_{int} (8.6 Ω) than S@NHC (35.6 Ω) and S@Super P (68.3 Ω) (Figure 22), may attributing to the introduction of ZnSe that catalyze the conversion reactions of polysulfides, thus suppressing the formation of an insulating layer of solid Li₂S₂/Li₂S on the surface of electrodes. And the second semicircle in the middle frequency region is related to the charge transfer resistance (R_{ct}) and a linear dependence in the low frequency region that reflected the diffusion of lithium ions into the electrode. Compared with S@NHC (50.2 Ω) and S@Super P (98.5 Ω), S@ZnSe/NHC electrodes showed the lowest R_{ct} (28.6 Ω), which means

ZnSe/NHC can facilitate charge transfer, favoring the rapid polysulfide conversion reactions. [29,65]

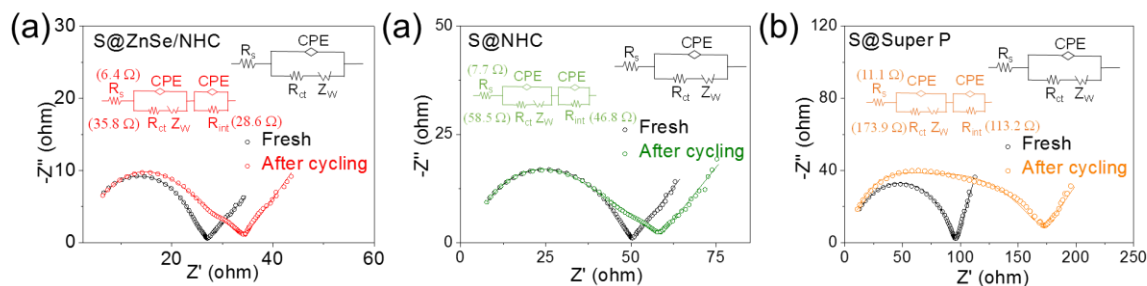


Figure 22. EIS spectrum of (a) S@ZnSe/NHC, (b) S@NHC and (c) S@Super P before and after cycling at 1 C for 200 cycles.

Even at a high current rate of 3 C, S@ZnSe/NHC electrodes displayed stable cycling performance with an average 0.022% capacity decay per cycle after 800 cycles and CEs above 99.5% (Figure 23a). To further demonstrate the potential of S@ZnSe/NHC cathodes for practical applications, a wind car was powered by one S@ZnSe/NHC coin cell, as displayed in Figure 23b.

Coin cells were disassembled after 200 cycles at 1 C. As shown in Figure 23c, after 200 cycles the separator from S@ZnSe/NHC cells exhibited lighter color than that from S@Super P, which indicated that ZnSe/NHC blocked the diffusion of LiPS more effectively. [25] Besides the S@ZnSe/NHC cathode material maintained its original morphology after 200 cycles, demonstrating its excellent structural stability during lithiation/delithiation processes (Figure 23d). In addition, the lithium metal foils from S@ZnSe/NHC showed fewer sulfur signals and less corrosion than those from S@Super P, as displayed by SEM and EDX mapping in Figure 23(e, f). [50]

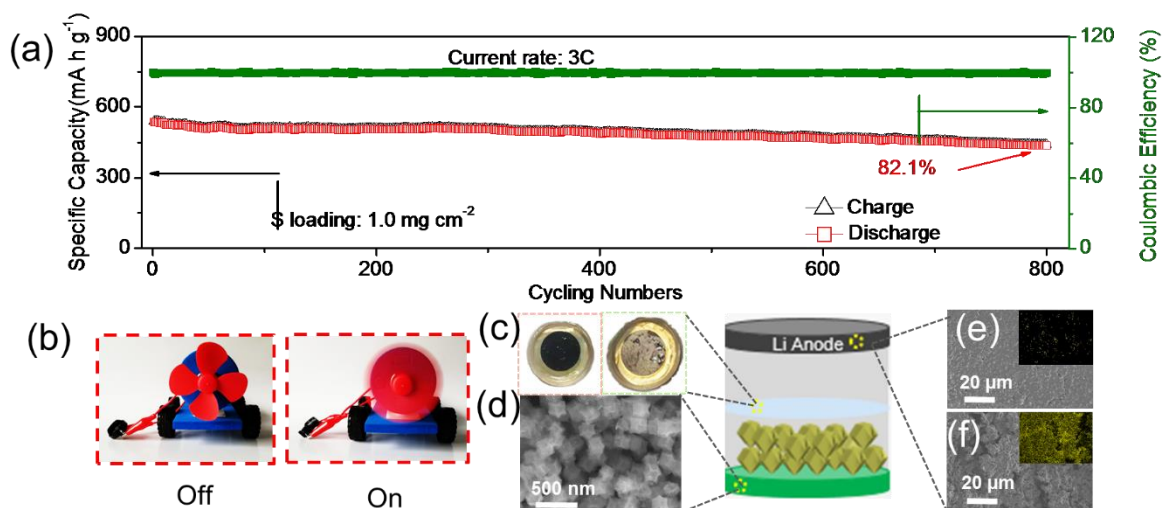


Figure 23. (a) Cycling performances and corresponding CEs of S@ZnSe/NHC cathode at a high current rate of 3 C. (b) Digital photographs of wind car powered by one S@ZnSe/NHC Li–S coin cell. (c) Separators of coin cells with S@ZnSe/NHC as cathode (left) and S@Super P as cathode (right) after cycling at 1 C for 200 cycles. (d) SEM image of S@ZnSe/NHC cathode and (e, f) surface of lithium foil from S@ZnSe/NHC and S@Super P coin cells. Inset images in (e, f) are EDX mapping images showing sulfur signal after cycling.

To meet the demand for high energy density of practical applications, LSBs should contain high sulfur loadings. Therefore, we studied the performance of S@ZnSe/NHC cathodes at a higher sulfur loading of 3.2 mg cm^{-2} . At high S loading, S@ZnSe/NHC cathodes delivered a discharge capacity of $1125.72 \text{ mAh g}^{-1}$ at 0.1 C and 57.7 mAh g^{-1} at 3 C, which corresponded to areal capacities of 3.60 and 1.46 mAh cm^{-2} , respectively (Figure 24a). The excellent rate performances could be attribute to high electrical conductivity and superior catalytic properties of ZnSe/NHC. Long-term cycling tests of S@ZnSe/NHC cathodes with 3.2 mg cm^{-2} of sulfur showed a discharge capacity of 540.5 mAh g^{-1} to be maintained after 600 cycles, with a 0.03% average capacity decay per cycle. Moreover, a high and steady CE above 99.8% was also maintained after long-term cycling, demonstrating an excellent cycling stability (Figure 24c). Compared with other sulfur host materials reported in literatures, the S@ZnSe/NHC cathode showed a high electrochemical performance (Table 1) and lower decay rate per cycle compared with other works even at a high sulfur loading (Figure 24b).^[23,52,58,62,66]

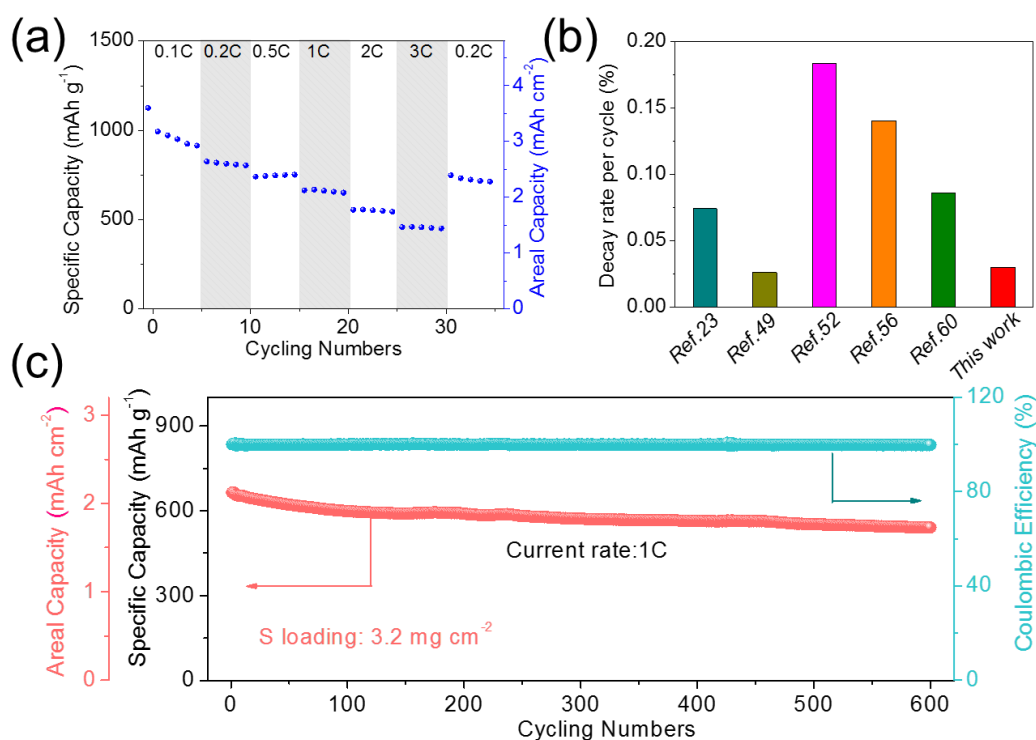


Figure 24. Performance of S@ZnSe/NHC with a high sulfur loading (3.2 mg cm⁻²): (a) Rate performance. (b) Decay rate per cycle compared with reported works. (c) Cycling performance at 1 C.

Table 1 Summary of recent reports on sulfur host cathodes for LSBs compared to ZnSe/NHC.

Host material	Capacity (mAh g ⁻¹) (current rate)	Cycling stability(%) (cycles, current rate)	Decay rate (per cycle, %)	S content (wt%)	Ref
S-3DOMPPy@ZnO	1053.2 (0.1C)	75% (300, 0.1C)	0.081%	60.7%	32
TCS/ZnO	1200 (0.2C)	50.1% (300, 0.2C)	0.16%	72%	67
ZnS/NC	1149 (0.2C)	60.1% (200, 0.2C)	0.19%	69.93%	68
1T-2HMoS ₂ -C	1195 (0.1C)	78.7% (300, 0.5C)	0.07%	79%	69
VTe ₂ @MgO	1160 (0.2C)	69% (500, 2C)	0.062%	60%	70
CoSe ₂ -C	1147.7 (0.1C)	55.2% (700, 2C)	0.064%	70%	56
u-NiCo ₂ Se ₄	1330 (0.1C)	68.6% (2000, 3C)	0.016%	70%	28
Sb ₂ Se ₃ /rGO	1160 (0.2C)	71.5% (500, 1C)	0.057%	70%	29
ZnSe/NHC	1475 (0.1C)	84% (800, 3C)	0.02%	70.1%	Current work

2.4 Conclusions

In summary, we rationally designed new LSBs cathodes based on ZnSe/NHC sulfur hosts with multiple adsorption sites and high catalytic activity. This rational design involves that the hollow geometry not only provide an accommodation for sulfur giving rise to a high stable cyclability, but also integrates LiPS physical separation and promotes and enhances the chemical reaction in this ZnSe/NHC structures that are functionally working like a nanoreactor. ZnSe with sulfiphilic sites and NHC with lithiophilic sites, respectively, were confirmed by experimental results and DFT calculations, showing a strong LiPS adsorbability. At the same time, unlike other compounds, the selenide nanoparticles, ZnSe, facilitate and enhance redox kinetics of LiPS conversion reaction during charge/discharge processes thus improving the sulfur utilization that was revealed by kinetic investigations. These merits contribute to outstanding electrochemical performances of the LSBs with ZnSe/NHC as sulfur hosts. As a

result, S@ZnSe/NHC cathode delivers excellent performances, including a reversible capacity of 540.5 mAh g⁻¹ after 600 cycles at 1 C at a relatively high sulfur loading of 3.2 mg cm⁻². This work not only broadens the application of selenides materials in the field of LSBs, but also designs nanoreactor with multiple adsorption sites serving as sulfur hosts, showing superior electrochemical properties for LSBs.

2.6 References

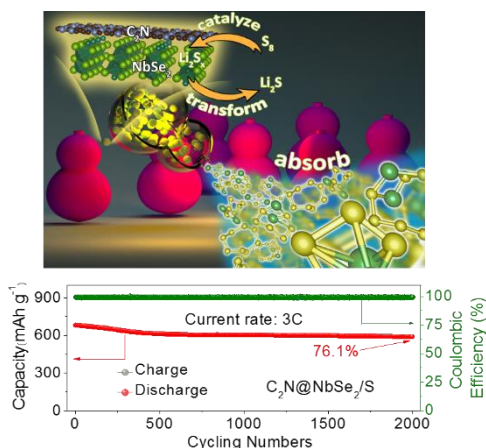
- [1]. A. Manthiram, Y. Fu, S. H. Chung, C. Zu, Y. S. Su, *Chem. Rev.* **2014**, *114*, 11751.
- [2]. H.-J. Peng, J.-Q. Huang, X.-B. Cheng, Q. Zhang, *Adv. Energy Mater.* **2017**, *7*, 1700260.
- [3]. Z. Li, H. B. Wu, X. W. Lou, *Energy Environ. Sci.* **2016**, *9*, 3061.
- [4] H. J. Peng, J. Q. Huang, X. Y. Liu, X. B. Cheng, W. T. Xu, C. Z. Zhao, F. Wei, Q. Zhang, *J. Am. Chem. Soc.* **2017**, *139*, 8458.
- [5] G. M. Zhou, L.-C. Yin, D.-W. Wang, L. Li, S. F. Pei, L. R. Gentle, F. Li, H.-M. Cheng, *ACS Nano* **2013**, *7*, 5367.
- [6] X. Ji, K. T. Lee, L. F. Nazar, *Nat. Mater.* **2009**, *8*, 500.
- [7] C. Ye, L. Zhang, C. X. Guo, D. D. Li, A. Vasileff, H. H. Wang, S.-Z. Qiao, *Adv. Funct. Mater.* **2017**, *27*, 1702524.
- [8] A. Manthiram, S. H. Chung, C. Zu, *Adv. Mater.* **2015**, *27*, 1980.
- [9] J. Schuster, G. He, B. Mandlmeier, T. Yim, K. T. Lee, T. Bein, L. F. Nazar, *Angew. Chem., Int. Ed.* **2012**, *51*, 3591.
- [10] M. Yu, R. Li, M. Wu, G. Shi, *Energy Storage Mater.* **2015**, *1*, 51.
- [11] Z. Du, X. Chen, W. Hu, C. Chuang, S. Xie, A. Hu, W. Yan, X. Kong, X. Wu, H. Ji, L. J. Wan, *J. Am. Chem. Soc.* **2019**, *141*, 3977.
- [12] F. Xu, Z. Tang, S. Huang, L. Chen, Y. Liang, W. Mai, H. Zhong, R. Fu, D. Wu, *Nat. Commun.* **2015**, *6*, 7221.
- [13] Y. Yao, M. Chen, R. Xu, S. Zeng, H. Yang, S. Ye, F. Liu, X. Wu, Y. Yu, *Adv Mater.* **2018**, *30*, e1805234.
- [14] K. Mi, Y. Jiang, J. Feng, Y. Qian, S. Xiong, *Adv. Funct. Mater.* **2016**, *26*, 1571.
- [15] S. Lu, Y. Cheng, X. Wu, J. Liu, *Nano Lett.* **2013**, *13*, 2485.
- [16] L. Xia, S. Wang, G. Liu, L. Ding, D. Li, H. Wang, S. Qiao, *Small* **2016**, *12*, 853.
- [17] H. J. Peng, G. Zhang, X. Chen, Z. W. Zhang, W. T. Xu, J. Q. Huang, Q. Zhang, *Angew. Chem. Int. Ed.* **2016**, *55*, 12990.
- [18] X. Wang, G. Li, J. Li, Y. Zhang, A. Wook, A. Yu, Z. Chen, *Energy Environ. Sci.* **2016**, *9*, 2533.

- [19] Z. Xiao, Z. Yang, L. Wang, H. Nie, M. Zhong, Q. Lai, X. Xu, L. Zhang, S. Huang, *Adv Mater.* **2015**, *27*, 2891.
- [20] L. Kong, B.-Q. Li, H.-J. Peng, R. Zhang, J. Xie, J.-Q. Huang, Q. Zhang, *Adv. Energy Mater.* **2018**, *8*, 1800849.
- [21] C. Dai, L. Hu, M.-Q. Wang, Y. Chen, J. Han, J. Jiang, Y. Zhang, B. Shen, Y. Niu, S.-J. Bao, M. Xu, *Energy Storage Mater.* **2017**, *8*, 202.
- [22] D. R. Deng, F. Xue, Y. J. Jia, J. C. Ye, C. D. Bai, M. S. Zheng, Q. F. Dong, *ACS Nano* **2017**, *11*, 6031.
- [23] T. Chen, L. Ma, B. Cheng, R. Chen, Y. Hu, G. Zhu, Y. Wang, J. Liang, Z. Tie, J. Liu, Z. Jin, *Nano Energy* **2017**, *38*, 239.
- [24] Z. Xiao, Z. Yang, L. Zhang, H. Pan, R. Wang, *ACS Nano* **2017**, *11*, 8488.
- [25] C. Dai, J.-M. Lim, M. Wang, L. Hu, Y. Chen, Z. Chen, H. Chen, S.-J. Bao, B. Shen, Y. Li, G. Henkelman, M. Xu, *Adv. Funct. Mater.* **2018**, *28*, 1704443.
- [26] H. Lin, L. Yang, X. Jiang, G. Li, T. Zhang, Q. Yao, G. W. Zheng, J. Y. Lee, *Energy Environ. Sci* **2017**, *10*, 1476.
- [27] D. Liu, C. Zhang, G. Zhou, W. Lv, G. Ling, L. Zhi, Q. H. Yang, *Adv. Sci.* **2018**, *5*, 1700270.
- [28] C. Zhang, J. J. Biendicho, T. Zhang, R. Du, J. Li, X. Yang, J. Arbiol, Y. Zhou, J. R. Morante, A. Cabot, *Adv. Funct. Mater.* **2019**, *29*, 1903842.
- [29] Y. Tian, G. Li, Y. Zhang, D. Luo, X. Wang, Y. Zhao, H. Liu, P. Ji, X. Du, J. Li, Z. Chen, *Adv. Mater.* **2020**, *32*, e1904876.
- [30] H. Yuan, H.-J. Peng, B.-Q. Li, J. Xie, L. Kong, M. Zhao, X. Chen, J.-Q. Huang, Q. Zhang, *Adv. Energy Mater.* **2019**, *9*, 1802768
- [31] Y. He, L. Wang, C. Dong, C. Li, X. Ding, Y. Qian, L. Xu, *Energy Storage Mater.* **2019**, *23*, 35.
- [32] Y. Zhang, W. Qiu, Y. Zhao, Y. Wang, Z. Bakenov, X. Wang, *Chem. Eng. J* **2019**, *375*, 122055.
- [33] J. Xu, W. Zhang, H. Fan, F. Cheng, D. Su, G. Wang, *Nano Energy* **2018**, *51*, 73-82.
- [34] Y. Boyjoo, H. Shi, E. Olsson, Q. Cai, Z. S. Wu, J. Liu, G. Q. Lu, *Adv. Energy Mater.* **2020**, *10*, 2000651.
- [35] J. Yang, F. Zhang, H. Lu, X. Hong, H. Jiang, Y. Wu, Y. Li, *Angew. Chem. Int. Ed.* **2015**, *54*, 10889.
- [36] A. Cabot, M. Ibáñez, P. Guardia, A. P. Alivisatos, *J. Am. Chem. Soc.* **2009**, *131*, 11326.
- [37] M. Ibáñez, J. Fan, W. Li, D. Cadavid, R. Nafria, A. Carrete, A. Cabot, *Chem. Mater.* **2011**, *23*, 3095.

- [38] S. Lu, T. Zhu, H. Wu, Y. Wang, J. Li, A. Abdelkader, K. Xi, W. Wang, Y. Li, S. Ding, G. Gao, R. V. Kumar, *Nano Energy* **2019**, *59*, 762.
- [39] Q. Peng, Y. Dong, Y. Li, *Angew. Chem. Int. Ed.* **2003**, *42*, 3027.
- [40] C. Dong, L. Guo, Y. He, C. Chen, Y. Qian, Y. Chen, L. Xu, *Energy Storage Mater.* **2018**, *15*, 234.
- [41] D. Su, K. Kretschmer, G. Wang, *Adv. Energy Mater.* **2016**, *6*, 1501785.
- [42] Y. He, M. Luo, C. Dong, X. Ding, C. Yin, A. Nie, Y. Chen, Y. Qian, L. Xu, *J. Mater. Chem. A* **2019**, *7*, 3933.
- [43] M. Wan, R. Zeng, K. Chen, G. Liu, W. Chen, L. Wang, N. Zhang, L. Xue, W. Zhang, Y. Huang, *Energy Storage Mater.* **2018**, *10*, 114.
- [44] C. Dong, J. Liang, Y. He, C. Li, X. Chen, L. Guo, F. Tian, Y. Qian, L. Xu, *ACS Nano* **2018**, *12*, 8277.
- [45] M. Mao, C. Cui, M. Wu, M. Zhang, T. Gao, X. Fan, J. Chen, T. Wang, J. Ma, C. Wang, *Nano Energy* **2018**, *45*, 346.
- [46] Z. R. Ismagilov, A. E. Shalagina, O. Y. Podyacheva, A. V. Ischenko, L. S. Kibis, A. I. Boronin, Y. A. Chesalov, D. I. Kochubey, A. I. Romanenko, O. B. Anikeeva, T. I. Buryakov, E. N. Tkachev, *Carbon* **2009**, *47*, 1922.
- [47] Q. Xia, H. Yang, M. Wang, M. Yang, Q. Guo, L. Wan, H. Xia, Y. Yu, *Adv. Energy Mater.* **2017**, *7*, 1701336.
- [48] Z. Li, J. Zhang, H. B. Wu, X. W. D. Lou, *Adv. Energy Mater.* **2017**, *7*, 1700281.
- [49] J. Song, Z. Yu, M. L. Gordin, D. Wang, *Nano Lett.* **2016**, *16*, 864.
- [50] X. Li, K. Ding, B. Gao, Q. Li, Y. Li, J. Fu, X. Zhang, P. K. Chu, K. Huo, *Nano Energy* **2017**, *40*, 655.
- [51] L. Hu, C. Dai, H. Liu, Y. Li, B. Shen, Y. Chen, S.-J. Bao, M. Xu, *Adv. Energy Mater.* **2018**, *8*, 1800709.
- [52] Y. Qiu, W. Li, W. Zhao, G. Li, Y. Hou, M. Liu, L. Zhou, F. Ye, F. Li, Z. Wei, S. Yang, W. Duan, Y. Ye, Y. Guo, Y. Zhang, *Adv. Mater.* **2014**, *14*, 4281.
- [53] M. Yan, H. Chen, Y. Yu, H. Zhao, C.-F. Li, Z.-Y. Hu, P. Wu, L. Chen, H. Wang, D. Peng, H. Gao, T. Hasan, Y. Li, B.-L. Su, *Adv. Energy Mater.* **2018**, *8*, 1801066.
- [54] J. Li, X. Xu, X. Yu, X. Han, T. Zhang, Y. Zuo, C. Zhang, D. Yang, X. Wang, Z. Luo, J. Arbiol, J. Llorca, J. Liu, A. Cabot, *ACS Appl. Mater. Interfaces* **2020**, *12*, 4414.
- [55] L. Zhang, X. Chen, F. Wan, Z. Niu, Y. Wang, Q. Zhang, J. Chen, *ACS Nano* **2018**, *12*, 9578.
- [56] B. Yuan, D. Hua, X. Gu, Y. Shen, L.-C. Xu, X. Li, B. Zheng, J. Wu, W. Zhang, S. Li, F.

- Huo, *J. Energy. Chem.* **2020**, *48*, 128.
- [57] X. Li, B. Gao, X. Huang, Z. Guo, Q. Li, X. Zhang, P. K. Chu, K. Huo, *ACS Appl. Mater. Interfaces* **2019**, *11*, 2961.
- [58] X. Zhu, W. Zhao, Y. Song, Q. Li, F. Ding, J. Sun, L. Zhang, Z. Liu, *Adv. Energy Mater.* **2018**, *8*, 1800201.
- [59] Z. Yuan, H. J. Peng, T. Z. Hou, J. Q. Huang, C. M. Chen, D. W. Wang, X. B. Cheng, F. Wei, Q. Zhang, *Nano Lett.* **2016**, *16*, 519-27.
- [60] G. Zhou, H. Tian, Y. Jin, X. Tao, B. Liu, R. Zhang, Z. W. Seh, D. Zhuo, Y. Liu, J. Sun, J. Zhao, C. Zu, D. S. Wu, Q. Zhang, Y. Cui, *Proc. Natl. Acad. Sci. USA* **2017**, *114*, 840.
- [61] A. Berger, A. T. S. Freiberg, A. Siebel, R. Thomas, M. U. M. Patel, M. Tromp, H. A. Gasteiger, Y. Gorlin, *J. Electrochem. Soc.* **2018**, *165*, A1288.
- [62] S. Huang, Y. V. Lim, X. Zhang, Y. Wang, Y. Zheng, D. Kong, M. Ding, S. A. Yang, H. Y. Yang, *Nano Energy* **2018**, *51*, 340.
- [63] C.-Y. Fan, Y.-P. Zheng, X.-H. Zhang, Y.-H. Shi, S.-Y. Liu, H.-C. Wang, X.-L. Wu, H.-Z. Sun, J.-P. Zhang, *Adv. Energy Mater.* **2018**, *8*, 1703638.
- [64] D. Su, M. Cortie, H. Fan, G. Wang, *Adv. Mater.* **2017**, *29*, 1700587.
- [65] Z. Guo, H. Nie, Z. Yang, W. Hua, C. Ruan, D. Chan, M. Ge, X. Chen, S. Huang, *Adv. Sci.* **2018**, *5*, 1800026.
- [66] M. Yu, J. Ma, H. Song, A. Wang, F. Tian, Y. Wang, H. Qiu, R. Wang, *Energy Environ. Sci.* **2016**, *9*, 1495.
- [67]. Y R. Yang, H. Du, Z. Lin, L. Yang, H. Zhu, H. Zhang, Z. Tang, X. Gui, *Carbon* **2019**, *141*, 258.
- [68]. W. Li, Z. Gong, X. Yan, D. Wang, J. Liu, X. Guo, Z. Zhang, G. Li, *J. Mater. Chem. A* **2020**, *8*, 433.
- [69]. Y. Zhang, Z. Mu, C. Yang, Z. Xu, S. Zhang, X. Zhang, Y. Li, J. Lai, Z. Sun, Y. Yang, Y. Chao, C. Li, X. Ge, W. Yang, S. Guo, *Adv. Funct. Mater.* **2018**, *28*, 1707578.
- [70]. M. Wang, Y. Song, Z. Sun, Y. Shao, C. Wei, Z. Xia, Z. Tian, Z. Liu, J. Sun, *ACS Nano* **2019**, *13*, 13235.

Chapter 3 NbSe₂ Meets C₂N: A 2D-2D Heterostructure Catalysts as Multifunctional Polysulfide Mediator in Ultra-Long-Life Lithium-Sulfur Batteries



3.1 Abstract

The shuttle effect and sluggish conversion kinetics of LiPS hamper the practical application of LSBs. Toward overcoming these limitations, herein we present an in-situ grown C₂N@NbSe₂ heterostructure with remarkable specific surface area as Li-S catalyst and LiPS absorber. Density functional theory (DFT) calculations and experimental results comprehensively demonstrate that C₂N@NbSe₂ is characterized by a suitable electronic structure and charge rearrangement that strongly accelerates the LiPS electrocatalytic conversion. Besides, heterostructured C₂N@NbSe₂ forms N-Li and Nb-S chemical bonds to trap LiPS species. As a result, LSBs cathodes based on C₂N@NbSe₂/S exhibit a high initial capacity of 1545 mAh g⁻¹ at 0.1 C. Even more exciting, C₂N@NbSe₂/S cathodes are characterized by impressive cycling stability with only 0.012% capacity decay per cycle after 2000 cycles at 3 C. Even at a sulfur loading of 5.6 mg cm⁻², a high areal capacity of 5.65 mAh cm⁻² is delivered. These results demonstrate that C₂N@NbSe₂ heterostructures can act as multifunctional polysulfide mediator to chemically adsorb LiPS, accelerate Li-ion diffusion, chemically catalyze LiPS conversion and lower the energy barrier for Li₂S precipitation/decomposition, realizing the “adsorption-diffusion-conversion” of polysulfides.

3.2 Introduction

LSBs attract enormous interest due to their high theoretical energy density (2600 Wh kg^{-1}) and potential for low cost.^[1-3] However, several challenges remain to be overcome to realize their commercial deployment. First, the electrically insulating character of sulfur and lithium sulfide results in poor charge transport within the cathode, which limits rate capability and sulfur utilization. Besides, intermediate LiPS dissolve into the electrolyte and migrate from the cathode to the anode. This LiPS diffusion, which is known as the shuttle effect, results in irreversible corrosion of the lithium anode and low Coulombic efficiency.^[4,5] Additionally, large volumetric variations of the sulfur cathode ($\approx 80\%$) during charge/discharge processes lead to poor cycling stability.^[6,7]

To suppress the shuttle effect, polar transition metal oxides/sulfides (TMO/TMS) able to strongly bind LiPS and thus effectively confine LiPS to the cathode have been developed.^[8-10] While these materials have allowed achieving notable improvements in cycling stability, TMO/TMS are characterized by moderate electrical conductivities, which can not meet the fast electron transfer required for high charge/discharge rates.^[11,12] Alternatively, TMSe characterized by higher electrical conductivities and similar surface polarity have been engineered as ideal sulfur hosts in LSBs.^[13,14] Among transition metals, owing to their high polysulfide adsorption and catalytic conversion activity, Nb-based materials, like Nb_2O_5 or NbN ,^[15,16] have recently received much interest. Surprisingly, despite its high potential, niobium selenide (NbSe_2), which has raised notable attention in numerous electrocatalytic reactions, has not yet been investigated as a cathode host material in LSBs.

NbSe_2 is characterized by a relatively high density (5.74 g cm^{-3}) and a two-dimensional (2D) structure that makes nanostructured NbSe_2 prone to aggregation limiting its specific surface area (SSA). Besides, it has been recently shown that LiPS species are preferential adsorbed and converted on the edge sites of transition metal dichalcogenides.^[17] However, within the NbSe_2 crystal structure, Nb atoms are sandwiched between two layers of Se atoms, which limits the exposed highly active Nb atoms at the edges.^[18,19] Therefore, NbSe_2 need to be combined with a lightweight support that allows increasing the overall SSA and maximized the NbSe_2 exposed active sites at the edges.

Among the possible supports, while carbon-based materials, such as graphene, and carbon nanotubes, provide the required high SSA, their nonpolar surface weakly interacts with polar LiPS thus not contributing to suppress the shuttle effect.^[13,20] The introduction of nitrogen within the carbon structure can promote interaction with Li atoms within LiPS, as demonstrated

for g-C₃N₄ and N-doped graphene.^[21,22] However, the high band gap of the former (2.6 eV) and the low N concentration of the latter (generally less than 10%) can not meet the requirements of LSBs.

An alternative C-N materials worth to be explored is C₂N, a two dimensional (2D) graphene-like covalent organic framework (COF) in which some of the carbon atoms are replaced with pyrazinic nitrogen atoms and which shows higher SSA, thermal stability, and conductivity than other CN based compounds. C₂N was theoretically anticipated to be characterized by superior catalytic properties as sulfur host in LSBs,^[23] but this prediction is yet to be experimentally proven.

C₂N presents bridging N atoms that have associated a large π electron pool in the structure and generate intrinsic electron density (partially negative),^[23,24] which could act as excellent sites for the nucleation and growth of NbSe₂. Besides, the catalytic activity of catalysts can be significantly augmented by altering their electronic structures through tuning the surface/interface atom environment.^[25,26] Taking into account their band structure, we expect that combining C₂N and NbSe₂ within heterostructures, a charge rearrangement at the heterojunction interface will take place, potentially promoting catalytic activity and suppressing shuttle effect.

In this work, we combine two unexplored materials in the field of LSBs to produce a high-performance catalyst for Li-S reaction. We first detail the synthesis of C₂N@NbSe₂ nanosheets using a two-step process and thoroughly characterize their structural, chemical, and functional properties. Subsequently, the performance of LSBs cathodes based on these nanocomposites is tested. The obtained results are rationalized with the help of density functional theory (DFT) calculations.

3.3 Experimental section

Chemicals: Ethylenediamine (EDA, 99%), hexaketoncyclohexane octahydrate (HACO, 99%), 1,3-dioxolane (DOL, 99.5%), lithium nitrate (LiNO₃, 99.98%), lithium sulfide (Li₂S, 99.9%), poly(vinylidene fluoride) (PVDF, 99%), Super P (99%), chloroanilic acid (CAA, 98%) and 1-octadecene (ODE, 90%) were purchased from Alfa Aesar. Sulfuric acid (95%~98%), N-methyl-2-pyrrolidone (NMP, 99.99%), diethyl ether (99.9%), niobium(V) chloride (NbCl₅, 99%), selenium powder (99%), sublimed sulfur (99.98%) and tetraethylene glycol dimethyl ether (99%) were purchased from Sigma-Aldrich. Oleylamine (OAm, approximate C18 content 80-90%), lithium bis(trifluoromethanesulfonyl) imide (LiTFSI, 99%) was purchased from

Acros Organics and 1,2-dimethoxymethane (DME, 99%) was from Honeywell. All chemicals were used without further purification.

Synthesis of hexaaminobenzene (HAB): CAA was added into a 15 mL glass vial which was placed in a 0 °C ice bath, under vigorous stirring. Next, 5.64 mL EDA and a few drops of concentrated sulfuric acid were added. Then the ice bath was removed and the obtained solution was warmed up to room temperature. Afterward, the solution was transferred to a 15 mL Teflon autoclave, where it was maintained at 80 °C for 12 h to complete the amination reactions. Then the solution was cooled to room temperature and the obtained mixture was vacuum filtrated using a polytetrafluoroethylene (PTFE) membrane (0.47 µm), rinsed with diethyl ether and degassed ethanol three times, and finally dried until further use.

Synthesis of C₂N: An equal molar ratio of HAB and HACO, and degassed NMP were introduced into a three-necked round bottom flask under argon gas placed in an ice bath. Under vigorous stirring, a few drops of concentrated sulfuric acid were added. Then the ice bath was removed and the mixture was warmed up to room temperature. The resultant solution was heated to 175 °C for 12 h. After cooling to room temperature, the mixture was vacuum filtrated, washed with ethanol and water three times and freeze-dried for 24 h. Finally, the obtained black solid was annealed at 450 °C for 3 h under argon gas with a ramp rate of 5 °C/min.

Synthesis of C₂N@NbSe₂ and NbSe₂: 15 mL OAm, 2 mL ODE, and 10 mL of a C₂N ethanol solution (6 mg mL⁻¹) were added in a three-necked flask and heated to 130 °C for about 30 min under Ar atmosphere to remove water, ethanol, and oxygen. Afterward, 1 mmol NbCl₅ and 2 mmol Se powder were added into the solution and the mixture was rapidly heated to 280 °C for 2 h. After cooling, the obtained black product was washed with ethanol and hexane via centrifugation, and then dried in a vacuum oven at 60 °C overnight. As a reference material, NbSe₂ nanosheets were synthesized following the above synthetic protocol but adding no C₂N.

Synthesis of C₂N@NbSe₂/S, NbSe₂/S, and C₂N/S: Host-sulfur composites were obtained through a simple melt diffusion process. In brief, a mixture of the host material (C₂N@NbSe₂, NbSe₂, or C₂N) and sulfur powder with a weight ratio (1:3) was heated at 155 °C for 12 h under Ar atmosphere. The obtained powder was immersed in a 10 mL CS₂ and ethanol solution (1:4, volume ratio) for several times to remove the redundant sulfur not incorporated into the host.

Materials Characterization: Crystal structures were analyzed by X-ray diffraction (XRD) using a Bruker AXS D8 Advance X-ray diffractometer with Cu K radiation ($\lambda = 1.5106 \text{ \AA}$) operating at 40 kV and 40 mA. SEM analysis was performed on a Zeiss Auriga field emission SEM operating at 20 kV. TEM characterization was carried out on a Zeiss Libra 120 operating

at 120 kV. HRTEM, STEM, and EELS composition maps were obtained using a field emission gun FEI Tecnai F20 microscope operated at 200 kV with an embedded Gatan Quantum Spectrometer. XPS measurements were carried out using 150 W and a Phoibos 150 MCD-9 detector. The sulfur content within the sulfur cathode composite was tested by TGA on a PerkinElmer Diamond TG/DTA instrument. UV-vis absorption spectrum were collected on a PerkinElmer LAMBDA 950 UV-vis spectrophotometer. Nitrogen adsorption-desorption isotherms were recorded on a Tristar II 3020 Micromeritics system. Specific surface areas and pore size distributions were determined by Brunauer-Emmett-Teller (BET) and Barrett-Joyner-Halenda (BJH) methods.

Electrochemical Measurements: To prepare working electrodes, active materials ($C_2N@NbSe_2/S$, $NbSe_2/S$ and C_2N/S), PVDF binder, and Super P were mixed with a mass ratio of 8:1:1 in NMP. The prepared homogeneous slurry was coated on an aluminum foil and vacuum dried at 60 °C overnight. The aluminum foil was then punched into 12 mm disks. The sulfur loading for regular electrodes was around 1 mg cm⁻², but higher loadings of 3.0 and 5.6 mg cm⁻² were also prepared. CR2032-type coin cells were assembled in an Ar-filled glove box with Celgard 2400 membranes as separators, and lithium metal as the counter electrode. The electrolyte used consisted of 1.0 M LiTFSI and contained 0.2 M LiNO₃ solution in DOL and DME (v:v=1:1). The electrolyte/sulfur ratio was typically 20 μL mg⁻¹, but decreased to 12 μL mg⁻¹ when using cathodes with higher sulfur loadings. To allow enough time for the electrolyte to penetrate the electrode sufficiently, all coin cells were aged for several hours before testing. Galvanostatic charge/discharge measurements were conducted in a voltage window of 1.7-2.8 V vs. Li⁺/Li using a Neware BTS4008 battery tester. Cyclic voltammetry (CV) curves were obtained at operating potentials of 1.7-2.8 V with a scanning rate range from 0.1 to 0.4 mV s⁻¹. Electrochemical impedance spectroscopy (EIS) analyses were performed in the frequency range of 0.01-10⁵ Hz with an amplitude of 10 mV.

Preparation of Li₂S₄ Solution and Adsorption Test: Li₂S₄ solutions were prepared by dissolving sulfur and Li₂S with a molar ratio of 3:1 in DME/DOL (v:v=1:1) solution under continuous stirring overnight in a glove box. The solution eventually became homogeneous and acquired a dark brown color. To evaluate the polysulfide absorption ability, 20 mg of active materials ($C_2N@NbSe_2$, $NbSe_2$, and C_2N) were added to 3.0 mL 10 mM Li₂S₄ solution. The obtained mixtures were vigorously stirred for 2 h and aged overnight.

Measurement of Nucleation and Dissolution of Li₂S: The nucleation and dissolution of Li₂S were measured to investigate the liquid-solid reaction kinetics. A certain amount of $C_2N@NbSe_2$ (or $NbSe_2$ or C_2N) dissolved in ethanol was coated on carbon papers used as

working electrode. Li foil worked as the counter electrode. A solution containing 20 μL of 0.25 M Li_2S_8 and 1.0 M LiTFSI in tetraethylene glycol dimethyl ether solution was used as catholyte. The anolyte consisted of 20 μL of a 1.0 M LiTFSI solution without Li_2S_8 . During the nucleation test, to reduce the generation of higher-order LiPS than Li_2S_4 , coin cells were initially held at 2.06 V. Subsequently, the cells were held at 2.05 V until the current decreased to 0.01 mA to make Li_2S nucleate and grow. To study the Li_2S dissolution, fresh coin cells were assembled. The cells were firstly discharged at a current of 0.10 mA to 1.80 V, following by galvanostatically discharging at 0.01 mA to 1.80 V to fully transform S to solid Li_2S . After this discharge, the cells were potentiostatically charged at 2.40 V for the dissolution of Li_2S into LiPS species until the charge current was lower than 0.01 mA.

Symmetric Cell Assembly and Measurements: Symmetric coin cells were prepared by assembling two identical electrodes (with an average loading of about 0.5 mg cm^{-2}) as working and counter electrodes with 40 μL of electrolyte (0.5 M Li_2S_6 and 1 M LiTFSI in DOL/DME (v:v=1:1)). Electrodes for symmetrical cells were fabricated using the same process as electrodes for LSBs. CV tests for the symmetrical cells were performed at a scan rate of 2-40 mV s^{-1} in a voltage window between -0.8 and 0.8 V.

Details of Theoretical calculations: All the DFT calculations were performed using the VASP package with VASPKIT code for post-processing the calculated data. GGA with the Perdew-Burke-Ernzerhof functional is employed to treat the exchange-correlation energy. The interaction between core and valence electrons was described by the projected augmented wave (PAW) basis set. A converged cutoff was set to 550 eV. Zero damping DFT-D3 method was used to investigate weak intermolecular interactions. These heterointerfaces were built in a relatively low crystal parameter mismatch level by less than 5.0%. In geometry optimization step, the force convergence standard was set below 0.02 eV/\AA . The density of Monkhorst–Pack k -point mesh (threshold: 0.04) and k -path for band calculation was used according to VASPKIT code's suggestion. A 20 \AA vacuum layer was constructed along the z -axis for each model regardless of periodic layer effect. Contributions of zero-point energies (ZPE), enthalpy and entropy. 1/8 corrected (300 K) S_8 molecular energy and 1/4 bulk Li (4 atoms) crystal energy were used to do the process of energy subtraction of reaction free energy. The calculation details of the Gibbs free energy change (ΔG) were expressed as follows:

$$\Delta G = \Delta E + \Delta E_{\text{ZPE}} + \int C_p dT - T\Delta S$$

where ΔE is the electronic energy difference between the free-standing and the adsorption states of the intermediates; $\int C_p dT$ is the enthalpic temperature correction. In this calculation, temperature for this was set to 300 K. ΔE_{ZPE} and ΔS are the corrections of zero-point energy and variation of entropy, respectively. Frequencies less than 50 cm^{-1} were set to 50 cm^{-1} .

The binding energy of Li-S_x intermediate species was calculated by the following equations:

$$E_{\text{LiS}_x}^{\text{bind}} = E_{\text{slab}} + E_{\text{LiS}_x} - E_{\text{LiS}_x\text{-slab}}$$

where $E_{\text{LiS}_x}^{\text{bind}}$, E_{slab} , E_{LiS_x} and $E_{\text{LiS}_x\text{-slab}}$ are the energies of the binding energy of the Li-S_x species, the DFT energy of the slab, the corrected energy (300 K) of isolated Li-S_x molecules in vacuum, and the total energy after slab absorbing the intermediate Li-S_x species, respectively; x is the amount of S atoms in a Li-S-like molecule. Besides, to get an accurate band gap near Fermi level, all the band structures in this work were calculated in a mix-type basis of screened hybrid *HSE06* functionals.

3.4 Results and discussions

C₂N@NbSe₂ nanoheterostructures were produced by growing NbSe₂ on the surface of preformed C₂N, as schematized in Figure 1. First, C₂N was prepared via a polycondensation reaction and the subsequent annealing of the product (Figure 2).^[27,28] In a second step, C₂N@NbSe₂ heterostructures were produced from the reaction of Nb and Se precursors in the presence of C₂N (see the experimental section for details).

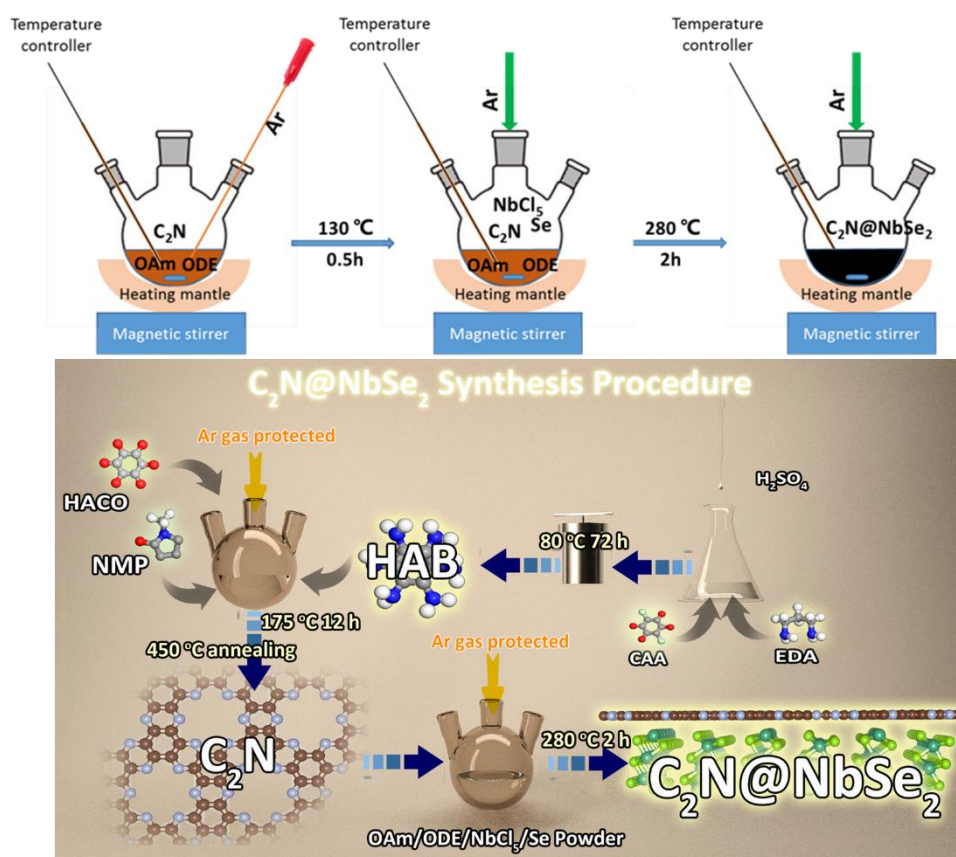


Figure 1. Schematic illustration of the synthetic procedure used to produce $C_2N@NbSe_2$ nanosheets.

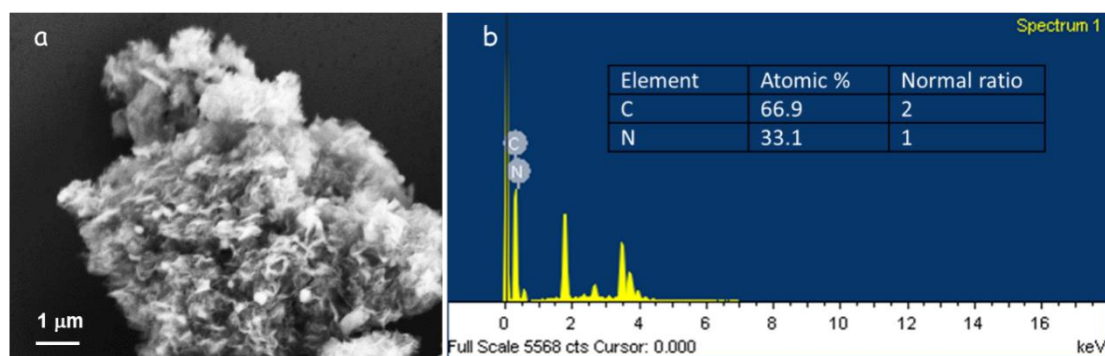


Figure 2. (a) FESEM image and (b) EDS spectrum of C_2N .

Figure 3a,b display the 2D nanosheet geometry of unsupported $NbSe_2$. Figure 3c and 3d show SEM and TEM images of the $C_2N@NbSe_2$ heterostructures, which also display a 2D architecture formed by ultrathin sheets. Nitrogen adsorption-desorption isotherms provided a BET SSA of $389.6 \text{ m}^2 \text{ g}^{-1}$ for $C_2N@NbSe_2$, which is a huge value taking into account the relatively high density of $NbSe_2$, and it is well above the SSA obtained for bare $NbSe_2$ ($152.6 \text{ m}^2 \text{ g}^{-1}$, Figure 4). XRD patterns from $C_2N@NbSe_2$ displayed the characteristic hexagonal $NbSe_2$ diffraction peaks (JCPDS No.18-0921) and a broad band at 26.2° assigned to C_2N

(Figure 5d).^[15,27] Extensive HRTEM analysis displayed the ubiquitous presence of C₂N and NbSe₂ electron diffraction patterns, pointing at a nanometer-scale homogeneous distribution of both structures throughout the whole composite, thus demonstrating the formation of C₂N@NbSe₂ heterostructures (Figure 5a). The lattice fringe spacing of ≈ 0.29 nm, corresponding to the (101) plane of NbSe₂, can be observed in Figure 5b,c. We hypothesize that the 6 N atoms with dangling bond on the hole of C₂N structure preferential adsorb Nb⁵⁺ ions triggering the nucleation and growing of NbSe₂. Additional EELS elemental maps confirmed Nb, Se, N, and C to be homogeneously distributed within the C₂N@NbSe₂ heterostructured nanosheets (Figure 5e). The very small thickness of the sheets and the pieces of evidence showing the presence of both NbSe₂ and C₂N throughout the whole material pointed at a sandwich-like C₂N@NbSe₂ structure with NbSe₂ crystals grown on the surface of C₂N nanosheets. In such a configuration, with highly conductive C₂N in intimate contact with NbSe₂, a simultaneous high electrical conductivity, high surface area and boosted capture and catalytic conversion of LiPS is to be expected.^[29,30]

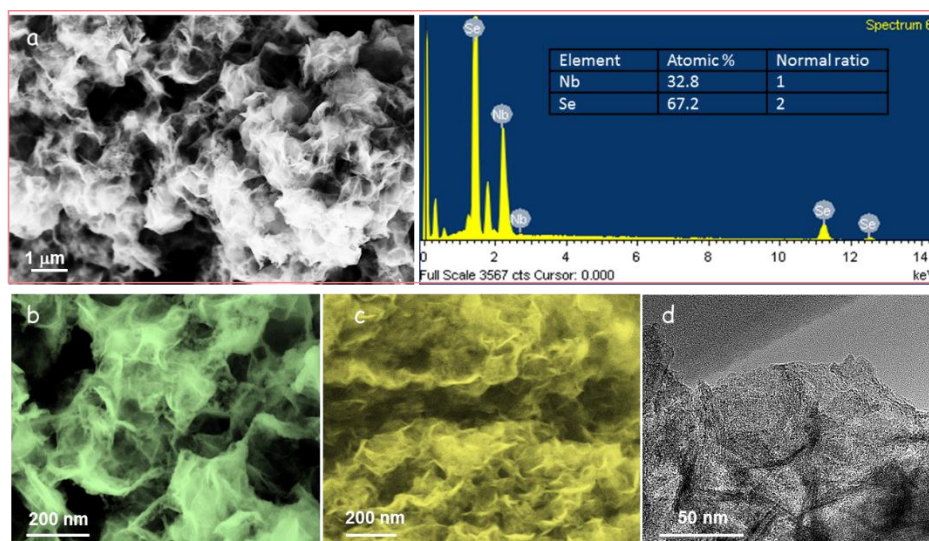


Figure 3. (a) FESEM images and EDS spectrum of NbSe₂ nanosheets. SEM images of (b) NbSe₂ and (c) C₂N@NbSe₂. (d) TEM image of C₂N@NbSe₂.

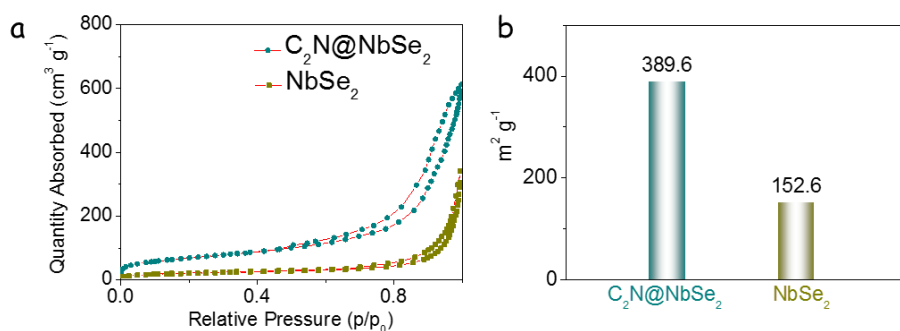


Figure 4. (a) N_2 adsorption-desorption isotherms $NbSe_2$ and $C_2N@NbSe_2$. (B) The corresponding SSA values of $NbSe_2$ and $C_2N@NbSe_2$.

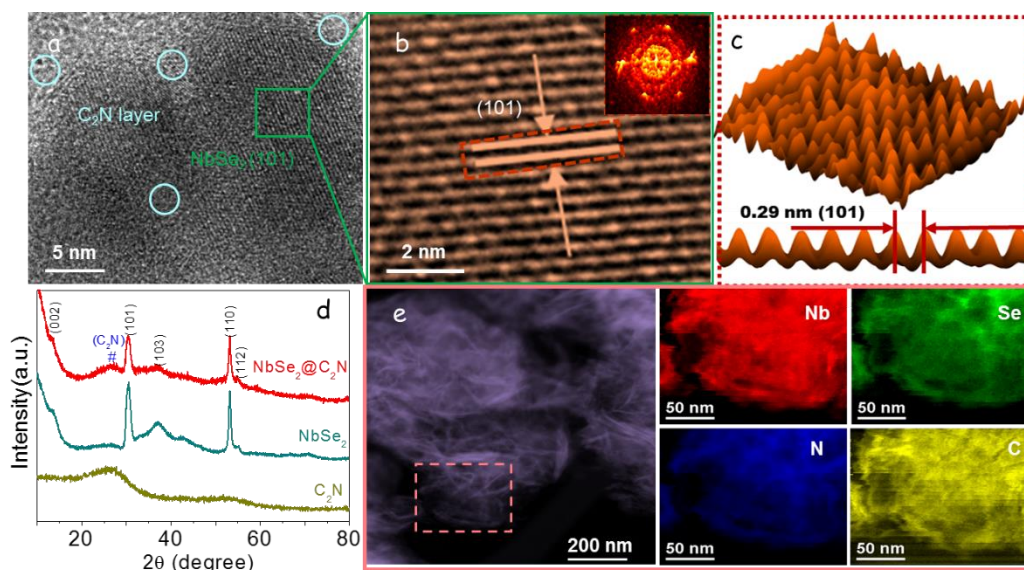


Figure 5. (a) HRTEM image of $C_2N@NbSe_2$ heterostructure. (b,c) FFT spectrum of the enlarged image of the green frame showing lattice fringes at a distance of 0.29 nm, corresponding to the (101) plane of hexagonal $NbSe_2$. (d) XRD patterns of C_2N , $NbSe_2$, and $C_2N@NbSe_2$. (e) EELS chemical composition maps were obtained from the red squared area in the STEM micrograph. Individual Nb M-edge 1020 eV (red), Se L-edge 1436 eV (green), N K-edge 401 eV (blue), and C K-edge 284 eV (yellow).

To further reveal the elemental composition and chemical bonding states of the as-synthesized $C_2N@NbSe_2$, XPS measurements were carried out (Figure 6a). The high-resolution C 1s XPS spectrum (Figure 6b) was fitted using four bands. The main band, at 284.6 eV, was associated with C-C bonds and it was used as a reference. The N 1s XPS spectrum (Figure 6c) displayed two bands at 399.6 and 406.6 eV, which can be assigned to pyrazine-N and oxidized N, respectively.^[31,32] The Nb 3d XPS spectrum (Figure 6d) presented peaks at 203.43 eV ($3d_{5/2}$) and 206.22 eV ($3d_{3/2}$) that were assigned to a Nb^{4+} chemical environment, and peaks at 207.4 ($3d_{5/2}$) and 210.2 eV ($3d_{3/2}$) belonging to Nb^{5+} and associated to the material exposure to air before XPS analysis.^[33] The binding energies of the main component in the Se 3d XPS spectrum, at 53.4 ($3d_{5/2}$) and 54.2 eV ($3d_{3/2}$), are also consistent with Se^{2-} within a MSe environment (Figure 6e).^[33,34] Besides, the bands at 55.3 and 56.2 eV could be assigned to the Se^{4+} species. The valence band XPS spectrum showed the Fermi level to lay within a band of states, thus demonstrating the metallic character of the produced composite (Figure 6f).

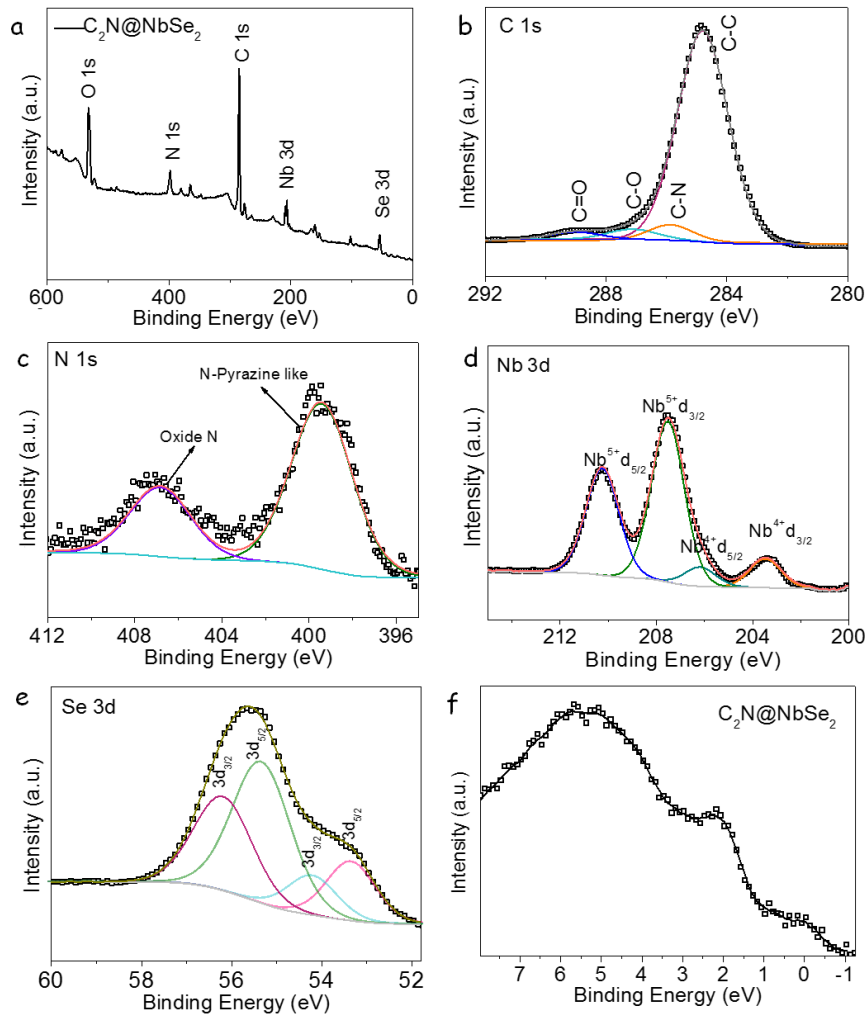


Figure 6. XPS spectra of the $C_2N@NbSe_2$ composite. (a) Survey XPS spectrum. (b-f) High resolution XPS spectra of the regions: (b) C 1s, (c) N 1s, (d) Nb 3d, (e) Se 3d, and (f) Valence band.

DFT calculations were used to determine the $C_2N-NbSe_2$ configuration, its band structure, its charge transfer/redistribution at the atomic scale, and its affinity to polysulfides (Figure 7). $C_2N@NbSe_2$ showed no gap of states at the Fermi level (Figure 7a,b), like $NbSe_2$, which was consistent with its metallic character and XPS data. The electron transfer can be inferred by the work function (WF).^[35,36] The WF of C_2N is around 5.216 eV. The WF of metallic $NbSe_2$ can be estimated at around 4.798 eV (Figure 8). When placed in contact, the difference in Fermi levels drives an injection of electrons from $NbSe_2$ to C_2N , until the WFs of the two materials at the interface are equilibrated. The high-resolution XPS valence band spectrum further confirmed a charge arrangement. An obvious negative shift of the binding energy of pyrazine-N was between the N 1s XPS spectra of C_2N (399.81 eV) and $C_2N@NbSe_2$ (399.60 eV, Figure

7c). This shift was related to the electron gain of C_2N when in contact with $NbSe_2$.^[37] Likewise, the Nb 3d spectrum of $NbSe_2$ displayed a similar shift toward higher binding energies when supported on C_2N , which we believe is associated with the chemical interaction between Nb and the higher electronegativity N atoms, consistent with the charge arrangement at the interface predicted by DFT calculations.^[38,39]

Interestingly, different geometric configurations of $C_2N@NbSe_2$ have associated quite different charge rearrangements (Figure 7e). The charge density differential plot clearly shows that Nb-termination sites could be favored by combining with N of C_2N with an intensive charge transfer. Bader charge analysis allowed calculating the charge redistribution at the Nb-terminated $C_2N/NbSe_2$ interface and quantifying the amount of charge gain/loss of the interfacial atoms (Figure 7f). We calculated that the C_2N layer gains 1.306 electrons from the bottle of $NbSe_2$ unit cell. Taking into account the DFT calculations, the most favorable specific nucleation and growth sites, and the experimental XPS data (Figure 7c,d), it is reasonable to infer that the architecture $C_2N@NbSe_2$ contain a Nb-terminated configuration in contact with the C_2N layer and includes an intense interface charge transfer.

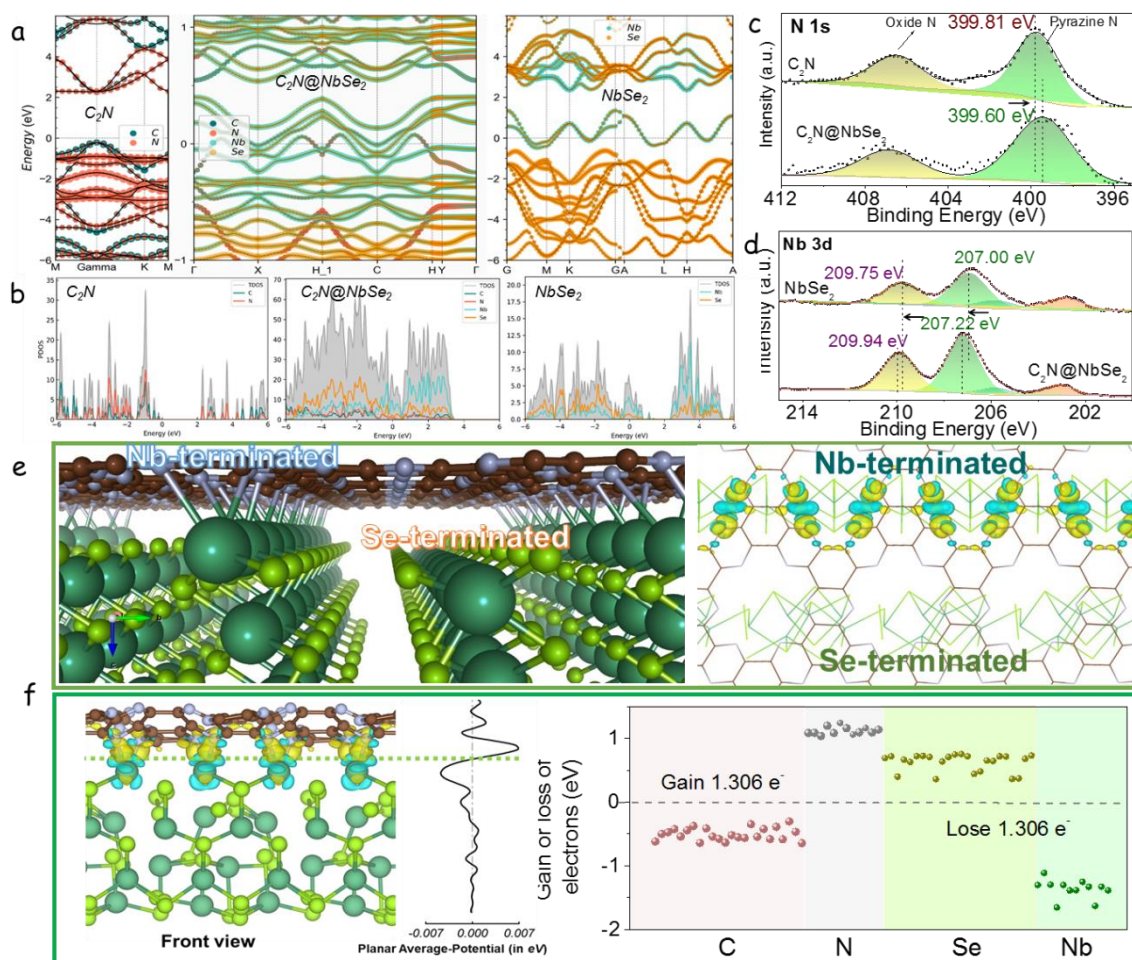


Figure 7. (a,b) HSE06 band structure and density of states of C_2N , $NbSe_2$, and $C_2N@NbSe_2$, respectively. (c) N 1s high-resolution XPS spectra from C_2N and $C_2N@NbSe_2$. (d) Nb 3d high-resolution XPS spectra from $NbSe_2$ and $C_2N@NbSe_2$. (e) The optimized structure of Nb-terminated and Se-terminated $C_2N@NbSe_2$ configurations and charge density difference plot. (f) The charge density difference plot of Nb-terminated $C_2N@NbSe_2$ configuration and gain/loss of electrons of different atoms calculated by Bader charge analysis.

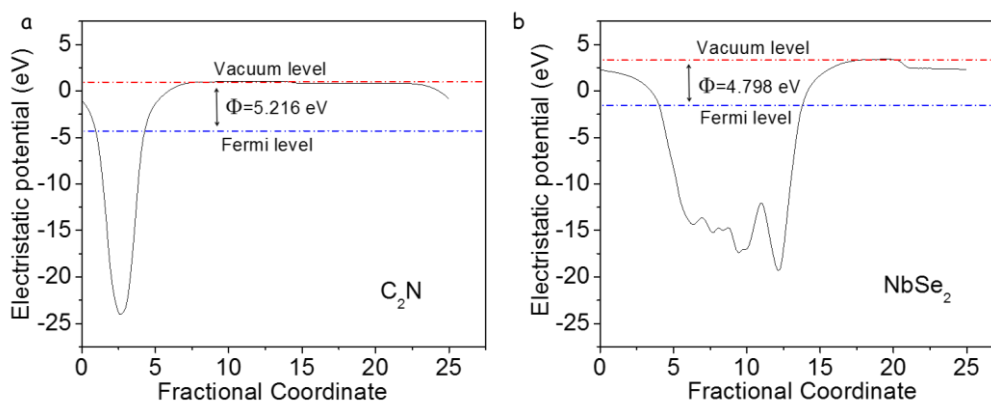


Figure 8. The computed work function of (a) C_2N and (b) $NbSe_2$. The blue and red lines denote the Fermi level and the vacuum energy level, respectively.

Sulfur was introduced within $C_2N@NbSe_2$ via a melt-diffusion process (see the experimental section for details). SEM characterization of the obtained $C_2N@NbSe_2/S$ composites displayed the nanosheet-based structure of the $C_2N@NbSe_2$ to be conserved but to be filled with S (Figure 9a). Independent sulfur agglomerates, outside the $C_2N@NbSe_2$ host, were not observed after processing the material with a CS_2 solution (see details in experimental section). Figure 9b displays the XRD pattern of $C_2N@NbSe_2/S$, showing the presence of the cubic sulfur crystal structure (JCPDS No. 08-0247).^[14,40] STEM and EDX compositional maps further demonstrated the homogeneous loading of sulfur within $C_2N@NbSe_2$ composites (Figure 9d). The amount of sulfur was quantified using TGA at *ca.* 70.3 wt% (Figure 9c). Besides, nitrogen adsorption-desorption isotherms (Figure 10) showed the BET specific surface area of the material to be reduced with the sulfur introduction, from the initial huge value of $389.6 \text{ m}^2 \text{ g}^{-1}$ obtained for $C_2N@NbSe_2$, to $21.58 \text{ m}^2 \text{ g}^{-1}$ for $C_2N@NbSe_2/S$. Simultaneously, the pore volume decreased from 0.29 to $0.05 \text{ cm}^3 \text{ g}^{-1}$ with the loading of sulfur.

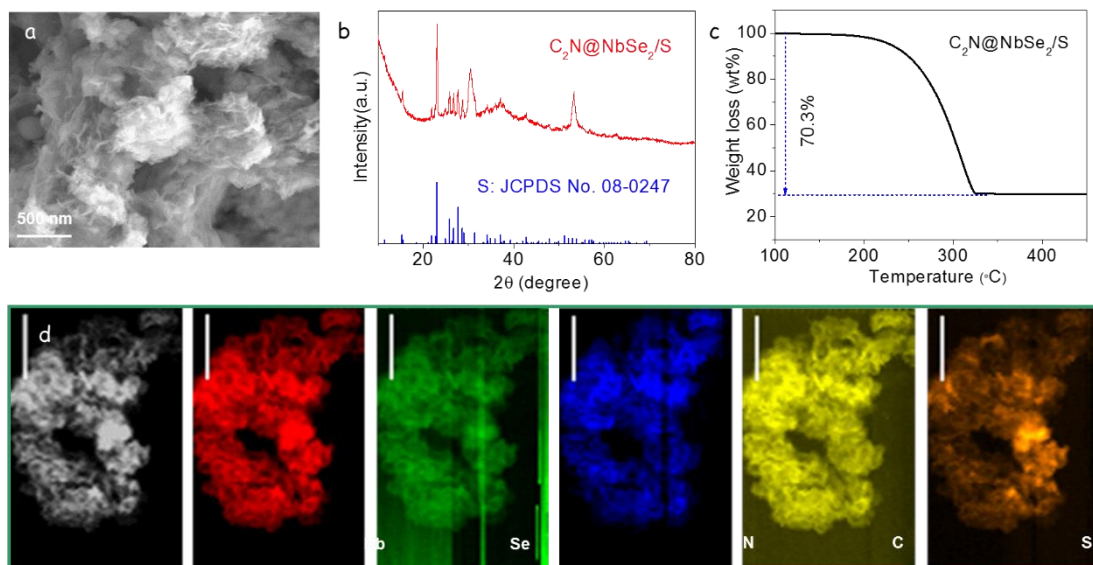


Figure 9. (a) SEM image and (b) XRD pattern of $C_2N@NbSe_2/S$, including reference pattern for cubic sulfur (JCPDS No. 08-0247). (c) TGA curve of $C_2N@NbSe_2/S$ composite measured in N_2 with a weight loss % associated to an initial sulfur loading of 70.3 wt%. (d) EELS chemical composition maps were obtained from the STEM micrograph of a $C_2N@NbSe_2/S$ composite. Individual Nb M-edge 1020 eV (red), Se L-edge 1436 eV (green), S L-edge 165 eV (orange), N K-edge 401eV (blue), and C K-edge 284 eV (yellow). Vertical scale bar = 100 nm.

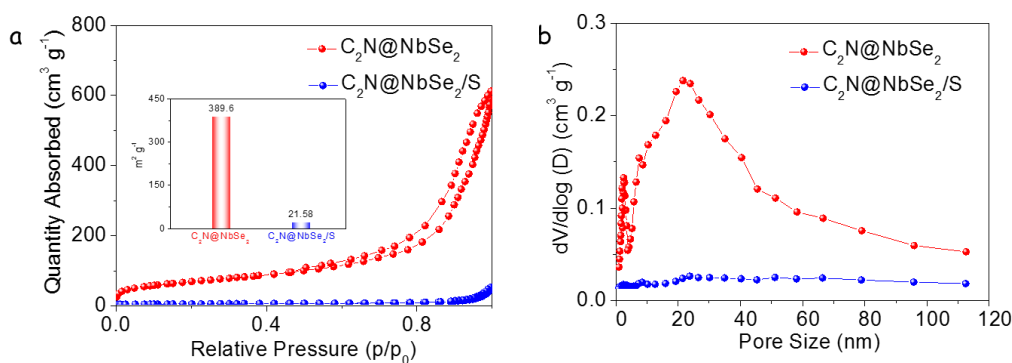


Figure 10. (a) Nitrogen adsorption-desorption isotherms of $C_2N@NbSe_2$ and $C_2N@NbSe_2/S$. Inset shows the SSA values of $C_2N@NbSe_2$ and $C_2N@NbSe_2/S$. (b) Pore size distributions of $C_2N@NbSe_2$, and $C_2N@NbSe_2/S$ composites.

To evaluate the LiPS adsorption potential of $C_2N@NbSe_2$ and the different reference materials (Super P, $NbSe_2$, C_3N_4 , and C_2N), they were immersed in a solution containing Li_2S_4 (Figure 11a). After overnight adsorption, the original orange-brown color of the Li_2S_4 solution containing Super P remained unchanged and the reference solution containing C_3N_4 became just slightly lighter. On the contrary, the color of the Li_2S_4 solutions containing either

$C_2N@NbSe_2$, $NbSe_2$, or C_2N almost fully disappeared pointing at the total Li_2S_4 adsorption on the host materials. This result suggested a strong chemical interaction of Li_2S_4 with $NbSe_2$ and C_2N . Beyond visual inspection, the amount of Li_2S_4 in solution could be followed using UV-vis absorption spectroscopy (Figure 11b).^[41,42] The Li_2S_4 absorption band in the 400–500 nm region was observed to fully disappear from the UV-vis spectrum obtained from the solutions containing C_2N , $NbSe_2$, or $C_2N@NbSe_2$.

XPS analyses were conducted to further evaluate the chemical interactions between $C_2N@NbSe_2$ and Li_2S_4 . Figure 11c exhibits the high-resolution N 1s XPS spectrum of $C_2N@NbSe_2$ before and after the Li_2S_4 adsorption test. After Li_2S_4 adsorption, N 1s bands appeared clearly shifted to higher binding energies with respect to the original N 1s spectrum. This shift is associated with the binding between N heteroatoms in C_2N with Lewis base character and Li atoms in Li_2S_4 having a Lewis acid character.^[40] Figure 11d shows the high-resolution Nb 3d XPS spectrum of $NbSe_2@C_2N$ after and before the Li_2S_4 adsorption test. Compared with the original Nb 3d spectrum, after Li_2S_4 adsorption, Nb 3d bands also shifted to higher binding energies, which we associate with the chemical interaction between Nb and the higher electronegativity S.^[14,43]

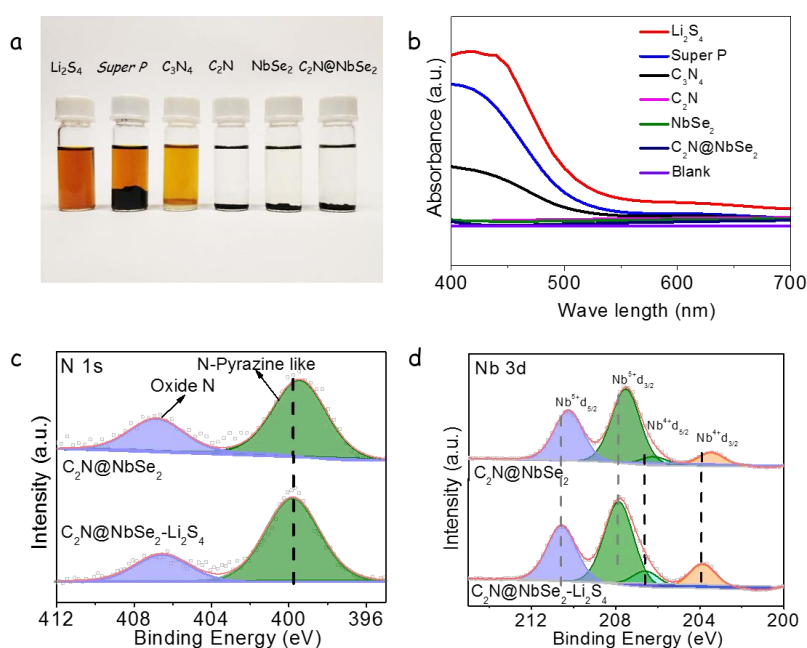


Figure 11. Li_2S_4 adsorption ability. (a) Optical photograph of the flask containing a Li_2S_4 solution and the different adsorbents (as indicated in the image) after 12h adsorption tests. (b) UV-Vis spectrum of the polysulfide solution after exposure to the different adsorbents. (c) N 1s and (d) Nb 3d XPS spectrum of $C_2N@NbSe_2$ before and after adsorption of Li_2S_4 .

DFT calculations were used to evaluate the interaction between LiPS and $C_2N@NbSe_2$. First, we studied the interaction of LiPS with C_2N . The optimized adsorption configuration of six LiPS species at different lithiation stages (Li_2S , Li_2S_2 , Li_2S_4 , Li_2S_6 , Li_2S_8 , and S_8) on the C_2N surface are displayed in Figure 12. Li_2S_4 was immobilized by Li-N bonds on the C_2N surface with a binding energy (E_b) of -2.86 eV, which is much higher (its absolute value) than in previously reported graphene or N-doped carbon (ca.-1 eV), ^[40,44] indicating a stronger chemical affinity of C_2N with LiPS. The calculated E_b for the geometrical configurations of $Li_2S_4-NbSe_2$ on $NbSe_2$ (001) and (101) surfaces were -2.66 eV and -4.67 eV (Figure 13 and Figure 14), respectively, demonstrating a strong LiPS chemisorption through the formation of Nb-S bonds. Interestingly, the (101) plane provide the higher LiPS binding energies, confirming the better adsorption capacity of the edge sites of $NbSe_2$. The stable geometrical configurations of LiPS species adsorbed on the surfaces of $C_2N@NbSe_2$ are illustrated in Figure 15. Considering the complete composite, $C_2N@NbSe_2$, DFT calculations demonstrated even higher binding energies (-6.46 eV) with Li_2S_4 as well as other LiPS species, demonstrating that the $C_2N@NbSe_2$ heterostructure with intense charge transfer and multi-adsorption sites possesses the strongest LiPS chemisorption through the formation of Nb-S and Li-N bonds, which is consistent with results from XPS analysis.

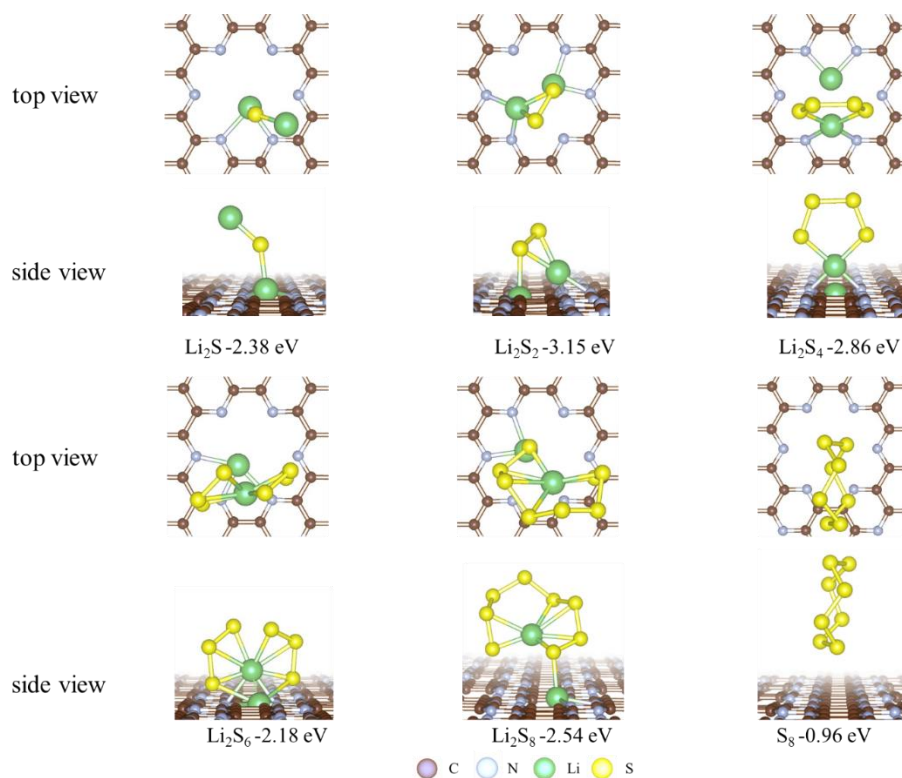


Figure 12. DFT calculation results of optimized geometrical configurations between the

surface of C_2N and LiPS species (Li_2S , Li_2S_2 , Li_2S_4 , Li_2S_6 , Li_2S_8 and S_8).

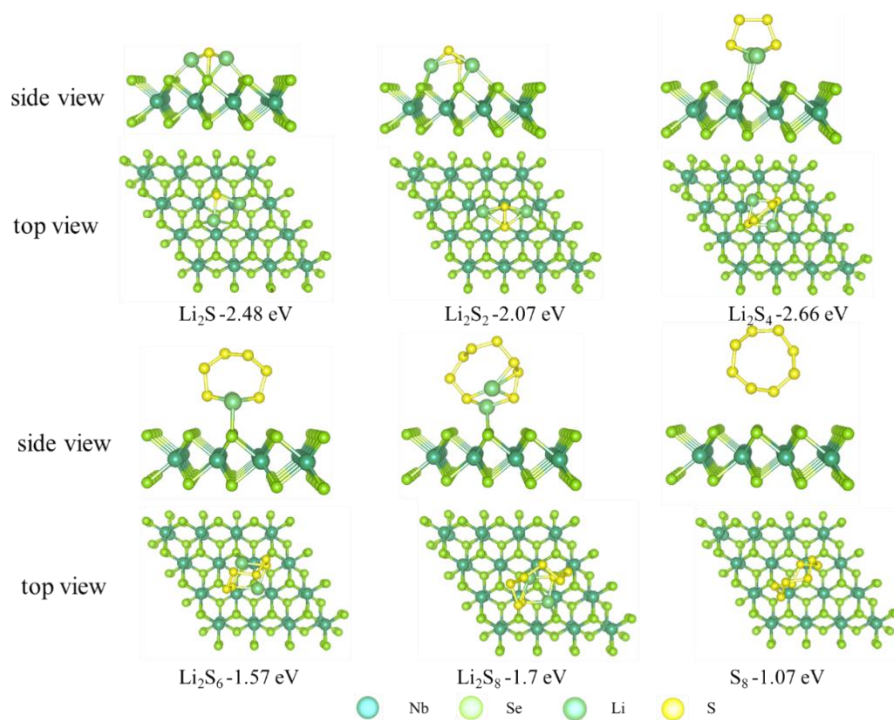


Figure 13. DFT calculation results of optimized geometrical configurations of $NbSe_2$ (001) with LiPS (Li_2S , Li_2S_2 , Li_2S_4 , Li_2S_6 , Li_2S_8 and S_8).

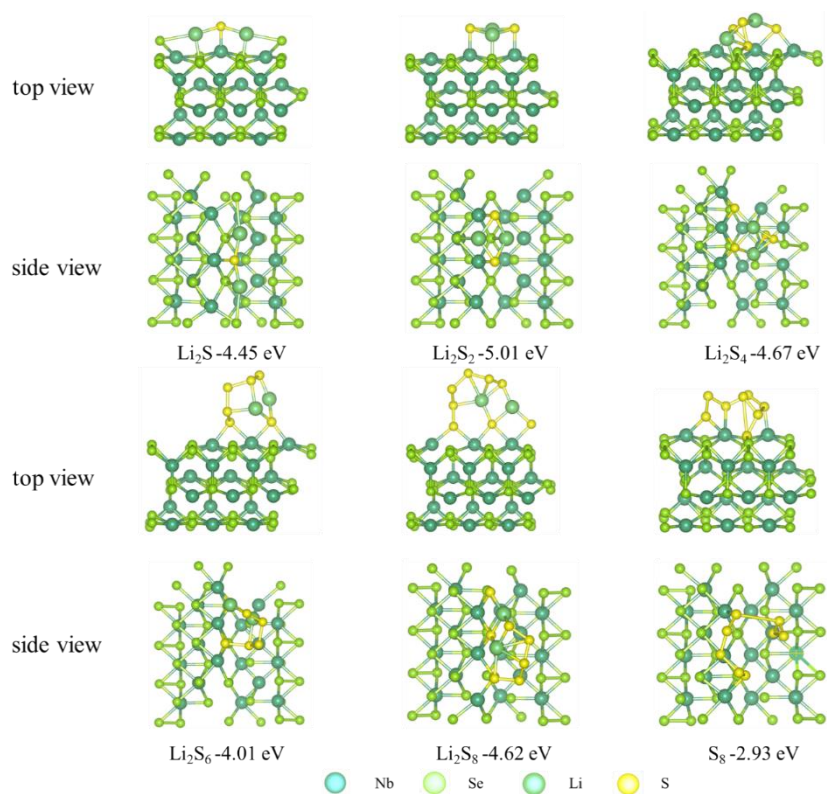


Figure 14. DFT calculation results of optimized geometrical configurations of NbSe₂ (101) with LiPS (Li₂S, Li₂S₂, Li₂S₄, Li₂S₆, Li₂S₈ and S₈).

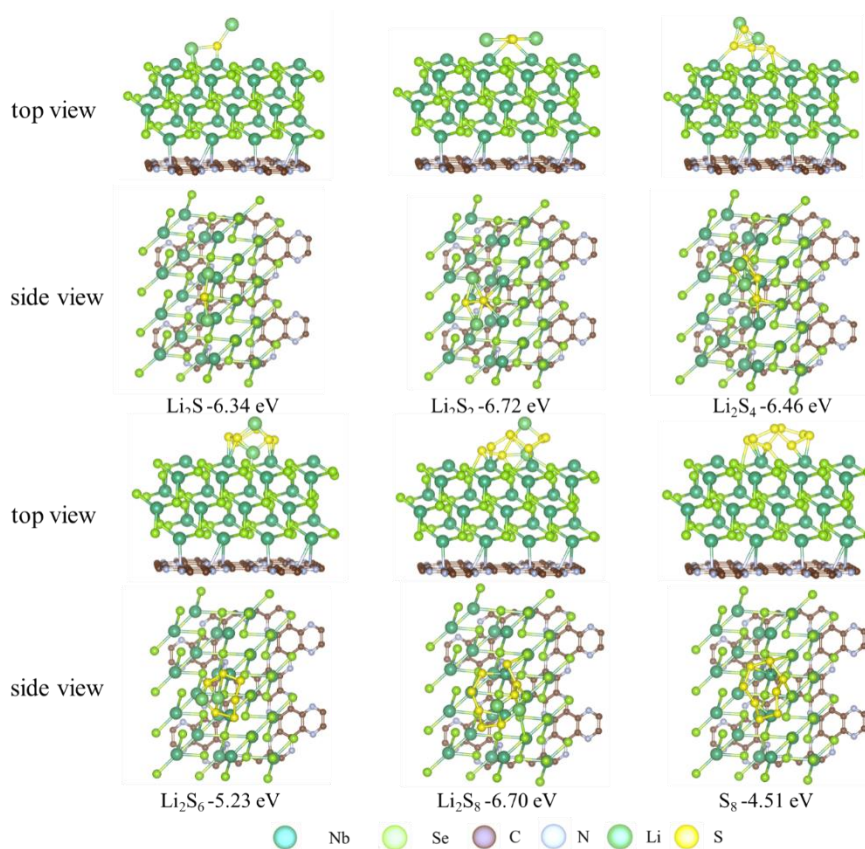
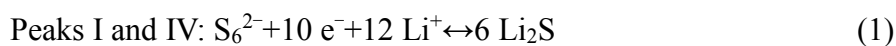


Figure 15. DFT calculation results of optimized geometrical configurations of C₂N@NbSe₂ with LiPS (Li₂S, Li₂S₂, Li₂S₄, Li₂S₆, Li₂S₈ and S₈).

To investigate the electrocatalytic activity of different catalysts toward polysulfide conversion, the first CV on symmetric cells was performed in a voltage window of -0.8 to 0.8 V and with 0.5 mol L⁻¹ Li₂S₆ as electrolyte (Figure 16a). C₂N@NbSe₂ exhibited two reduction peaks at 0.05 and -0.28 V, and two well-defined oxidation peaks at -0.05 and 0.28 V. These peaks are associated with the following forward and reverse chemical reactions:^[14,47]



CV curves of symmetric cells with NbSe₂- and C₂N-based electrodes displayed lower peak current densities compared with C₂N@NbSe₂-based electrodes, pointing at a higher redox activity of the latter. CV curves of C₂N@NbSe₂ electrodes in a Li₂S₆-free electrolyte presented the characteristic rectangular shape of a pure capacitive contribution (Figure 16b). Figure 16c shows 100 consecutive CV cycles of symmetric cells based on C₂N@NbSe₂ demonstrating

good stability. CV profiles of symmetric cells with $C_2N@NbSe_2$ electrodes at different scanning rates showed the redox peaks to be clearly defined and to maintain a small potential gap, further demonstrating a fast polysulfide conversion kinetics and good electrochemical stability (Figure 16d).

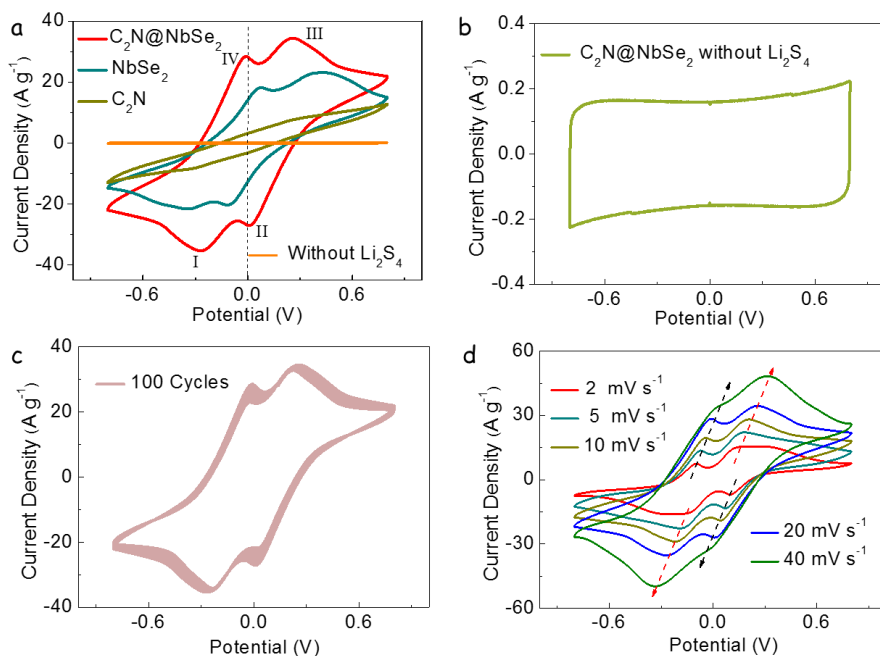


Figure 16. (a) CV curve of $C_2N@NbSe_2$ electrodes in symmetric coin cell using an electrolyte without Li_2S_6 . (b) CV curves of symmetric cells of $C_2N@NbSe_2$ worked as electrodes at a scan rate of 20 mV s^{-1} with 100 cycles. (c). CV curves of symmetric cells of $C_2N@NbSe_2$ at different scan rates.

Results from the electrochemical impedance spectroscopy (EIS) analysis of the different electrodes and the equivalent circuit used to model the symmetric cells are displayed in Figure S15. The intersection of the Nyquist plots with the abscissa is ascribed to the interphase-contact resistance of the electrolyte and the cells (R_s). And the semicircle in the high-frequency region corresponds to the charge transfer resistance (R_{ct}) at the electrode/polysulfide interface.^[15,48] The fitting of the Nyquist plots (Figure 17) showed $C_2N@NbSe_2$ cells to be characterized by significantly lower R_{ct} ($13.5\ \Omega$) than $NbSe_2$ ($38.1\ \Omega$) and C_2N ($76.8\ \Omega$), which demonstrated a significantly faster charge transfer at the $C_2N@NbSe_2$ /polysulfide interface.

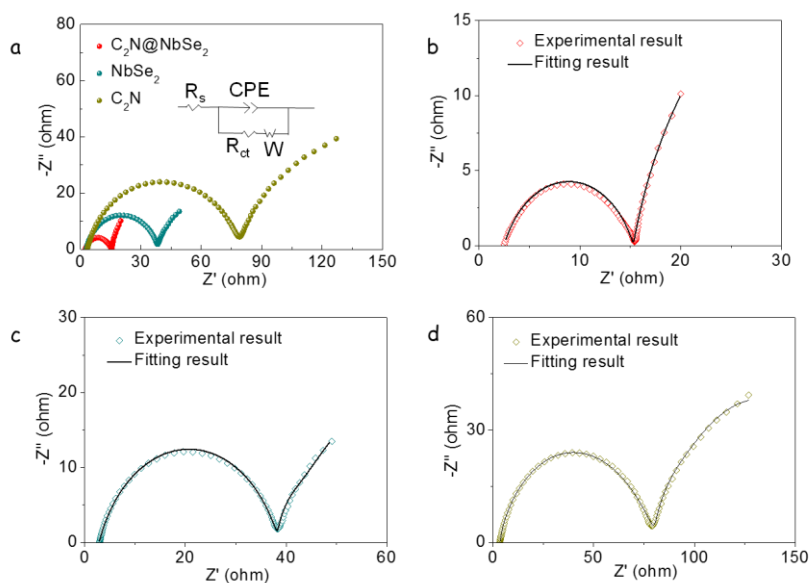


Figure 17. (a) EIS curves of symmetrical cells using an electrolyte containing $0.5 \text{ mol L}^{-1} \text{ Li}_2\text{S}_6$. The corresponding fitting curves: (b) $\text{C}_2\text{N@NbSe}_2$. (c) NbSe_2 . (d) C_2N .

The electrochemical performance of Li–S coin cells based on the cathode materials here developed was subsequently tested. Figure 18a shows the CV profiles of $\text{C}_2\text{N@NbSe}_2/\text{S}$, NbSe_2/S , and $\text{C}_2\text{N}/\text{S}$ cathodes at a scan rate of 0.1 mV s^{-1} . $\text{S}/\text{C}_2\text{N@NbSe}_2$ cathodes displayed two well-defined cathodic peaks associated with the reduction of solid-state sulfur into soluble long-chain LiPS (Li_2S_x , $4 < x < 8$, peak I) and the subsequent conversion to insoluble $\text{Li}_2\text{S}_2/\text{Li}_2\text{S}$ (peak II).⁴¹ The anodic peak (peak III) corresponds to the reverse oxidation conversion from Li_2S to LiPS and ultimately to sulfur.^[49,50] The voltage between the second cathodic and anodic peaks is 0.25 V for cells based on a $\text{C}_2\text{N@NbSe}_2/\text{S}$ cathode, clearly below the 0.30 V and 0.39 V polarizations obtained from NbSe_2/S and $\text{C}_2\text{N}/\text{S}$ cathodes, respectively. $\text{C}_2\text{N@NbSe}_2/\text{S}$ cathodes presented a more positive potential of cathodic peaks (peak I at 2.311 V and peak II at 2.051 V) and a more negative anodic peak (peak III at 2.325 V) than NbSe_2/S and $\text{C}_2\text{N}/\text{S}$ (Figure 18b). To quantify the electrocatalytic activity, the onset potential at a current density of $10 \mu\text{A cm}^{-2}$ beyond the baseline current was determined (Figure 19 and 18b).^[46,51] Cells based on $\text{C}_2\text{N@NbSe}_2/\text{S}$ cathodes showed the highest onset potentials of cathodic peaks and the lowest for the anodic peak which further points out the accelerated redox kinetics obtained through the synergistic combination of these two materials.^[21] Besides, the redox peaks of successive CV curves measured from $\text{C}_2\text{N@NbSe}_2/\text{S}$ cathodes almost overlapped, demonstrating good reversibility of the sulfur redox reactions (Figure 20).

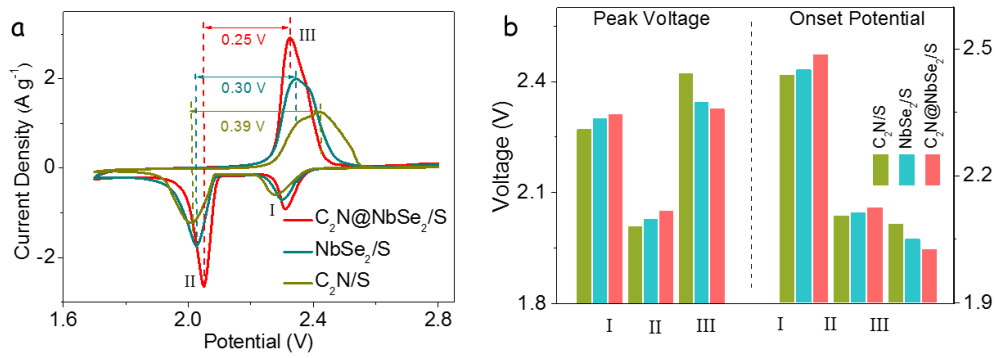


Figure 18. (a) CV profiles of Li-S cells with different electrodes. (b) Corresponding peak voltages and onset potentials of asymmetric Li-S cells.

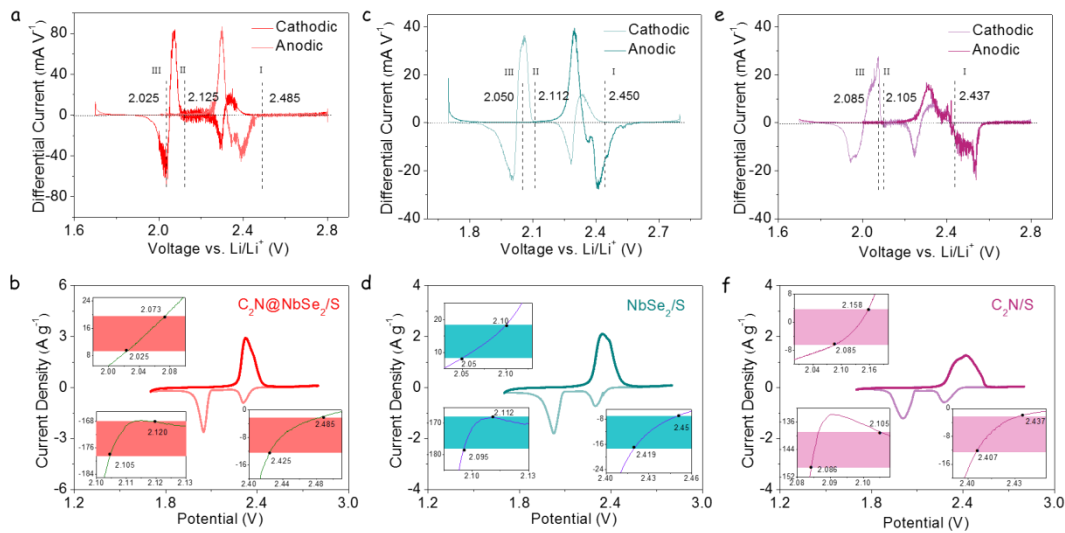


Figure 19. Differential CV curves of (a) $C_2N@NbSe_2/S$, (c) $NbSe_2/S$ and (e) C_2N/S . The base line voltage and current density are defined as the value before the redox peak, where the variation on current density is the smallest, named as $dI/dV=0$. The value of the base line voltages for cathodic peak I, II and anodic peak III were calculated, respectively. CV curves and corresponding onset potentials of redox peak I, II, and III (inset): (b) $C_2N@NbSe_2/S$, (d) $NbSe_2/S$ and (f) C_2N/S . Following a common definition employed in electrocatalysis, the onset potential is determined when the current density is $10 \mu A cm^{-2}$ beyond the corresponding baseline current density (more specifically, $10 \mu A cm^{-2}$ more negative than baseline current density for cathodic peaks or $10 \mu A cm^{-2}$ positive than baseline current density for anodic peaks). As shown in the inset of b, d, and f, the baseline voltages are the same as in a, c, and e while the colored region indicates the gap in current density.

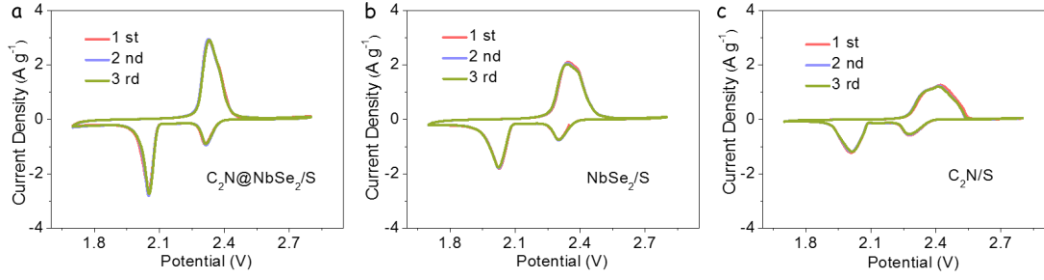


Figure 20. First three cycles of CV curves of (a) $C_2N@NbSe_2/S$, (b) $NbSe_2/S$ and (c) C_2N/S performed at a scan rate of 0.1 mV s^{-1} .

The electrode reaction kinetics and the lithium-ion diffusion properties of $C_2N@NbSe_2/S$, $NbSe_2/S$, and C_2N/S cathodes were evaluated by CV tests at different sweep rates, from 0.1 to 0.4 mV s^{-1} . Figure 21 displays the increase of the peak current density and the shift of the redox peaks when increasing the scan rate. At all scan rates, $C_2N@NbSe_2/S$ -based cells exhibited the highest redox peak current and lower polarization, a consequence of the faster LiPS conversion and lower redox energy barriers. Both cathodic and anodic peak currents showed a linear dependence on the square root of the scanning rate, pointing at a diffusion-limited process. Therefore, the diffusion constant of lithium ions (D_{Li^+}) could be calculated using the classical Randles–Sevcik equation: [52,53]

$$I_p = (2.69 \times 10^5) n^{1.5} A D_{Li^+}^{0.5} C_{Li^+} v^{0.5} \quad (3)$$

where I_p is the peak current density, n is the number of charges transferred, A is the geometric area of the electrode, C_{Li^+} is the concentration of lithium ions in the electrolyte, and v is the scan rate. As shown in Figure 22, for all redox peaks the slopes of I_p vs. $v^{0.5}$ obtained from $C_2N@NbSe_2/S$ cathodes were significantly higher than those obtained for the two reference electrodes, pointing at the fastest lithium-ion diffusion. Based on the Randles–Sevcik equation, $C_2N@NbSe_2/S$ electrodes were characterized by a D_{Li^+} at peaks I, II, and III of 1.06×10^{-7} , 2.24×10^{-7} , and $4.45 \times 10^{-7} \text{ cm}^2 \text{ s}^{-1}$, respectively, well above the values obtained for $NbSe_2/S$ and C_2N/S (Figure 23). We assigned the higher lithium-ion diffusivities measured in $C_2N@NbSe_2/S$ to the improved catalytic activity to accelerate LiPS conversion and to the effective LiPS trapping that blocks the shuttle effect and prevents the deposition of an insulating layer.

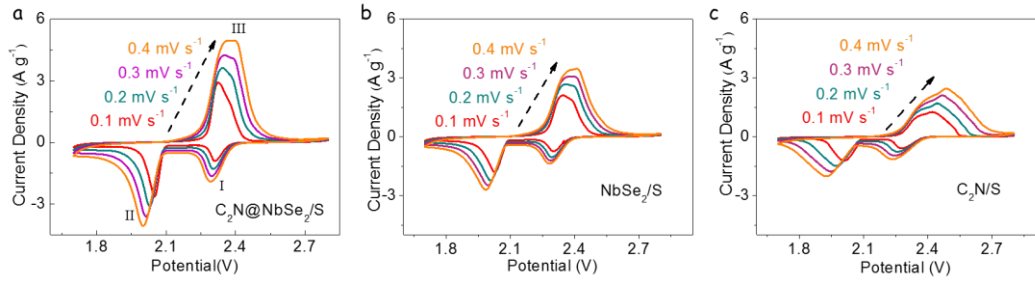


Figure 21. CV curves of (a) $C_2N@NbSe_2/S$, (b) $NbSe_2/S$ and (c) C_2N/S electrodes at various scan rates.

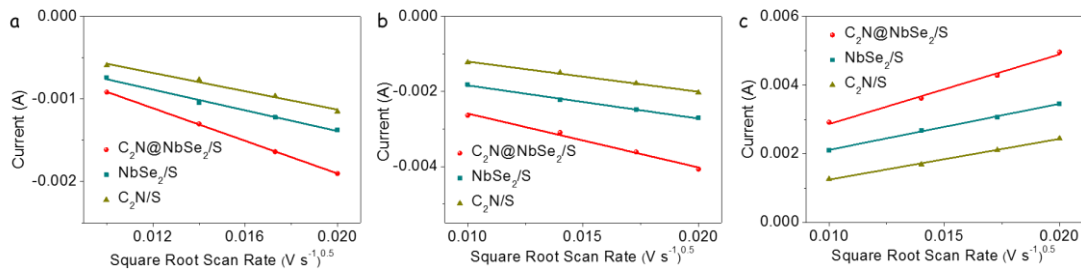


Figure 22. (a) Plots of CV peak current for the first cathodic reduction, (b) the second cathodic reduction, (c) anodic oxidation process vs. the square root of the scan rates.

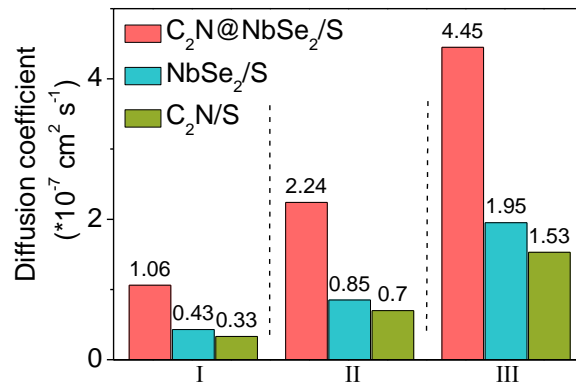


Figure 23. (a) CV curves of S@NHC and (b) S@Super P at different scan rates. (c) Plots of CV peak current for the first cathodic reduction, (d) the second cathodic reduction, (e) anodic oxidation process vs the square root of the scan rates.

Figure 24a compares the charge/discharge profiles of $C_2N@NbSe_2/S$, $NbSe_2/S$, and $S/C_2N/S$ electrodes at a current density of 0.1 C ($1\text{ C} = 1672\text{ mA g}^{-1}$). The voltage gap between the second discharge and the charge plateaus is referred to as the ΔE . $C_2N@NbSe_2/S$ electrodes showed a lower $\Delta E = 140\text{ mV}$ as compared with $NbSe_2/S$ ($\Delta E = 194\text{ mV}$) and C_2N/S electrodes ($\Delta E = 232\text{ mV}$), as a consequence of the superior electrocatalytic activity of $C_2N@NbSe_2$ towards LiPS conversion.^[21,54]

Q1 and Q2 are used to refer to the capacity of the first and second discharge plateaus, respectively. The ratio Q2/Q1 can be used to evaluate the catalytic activity for LiPS conversion reaction: while Q1 is related to the ability to create soluble polysulfides (Li_2S_4), the Q2 stage reveals the amount of polysulfides reduced to Li_2S .^[40,55] Thus, the higher Q2/Q1, the better the catalytic ability. Consistently with the above results, Q2/Q1 values obtained for $\text{C}_2\text{N@NbSe}_2/\text{S}$ electrodes (2.73) were larger than those of NbSe_2/S (2.51) and $\text{C}_2\text{N@NbSe}_2/\text{S}$ (2.30) (Figure 24b).

Looking in more detail at the galvanostatic curves, Figure 24c displays the voltage jump at the initial charging period, which reflects the overpotential required for Li_2S activation.^[45] $\text{C}_2\text{N@NbSe}_2/\text{S}$ electrodes displayed a significantly lower overpotential (25.5 mV) than NbSe_2/S (80.8 mV) and $\text{C}_2\text{N@NbSe}_2/\text{S}$ (95.2 mV) electrodes, verifying the accelerated activation process of Li_2S in the presence of $\text{C}_2\text{N@NbSe}_2$. Complementarily, Figure 24d displays the voltage dip at the beginning of the Li_2S precipitation voltage plateaus in the galvanostatic discharge curves, which is associated with the overpotential for Li_2S nucleation.^[56] Compared with NbSe_2/S (17.5 mV) and $\text{C}_2\text{N}/\text{S}$ (27.1 mV) electrodes, the $\text{C}_2\text{N@NbSe}_2/\text{S}$ electrode demonstrated a much lower overpotential for Li_2S nucleation (10.2 mV), indicating a lower energy barrier.

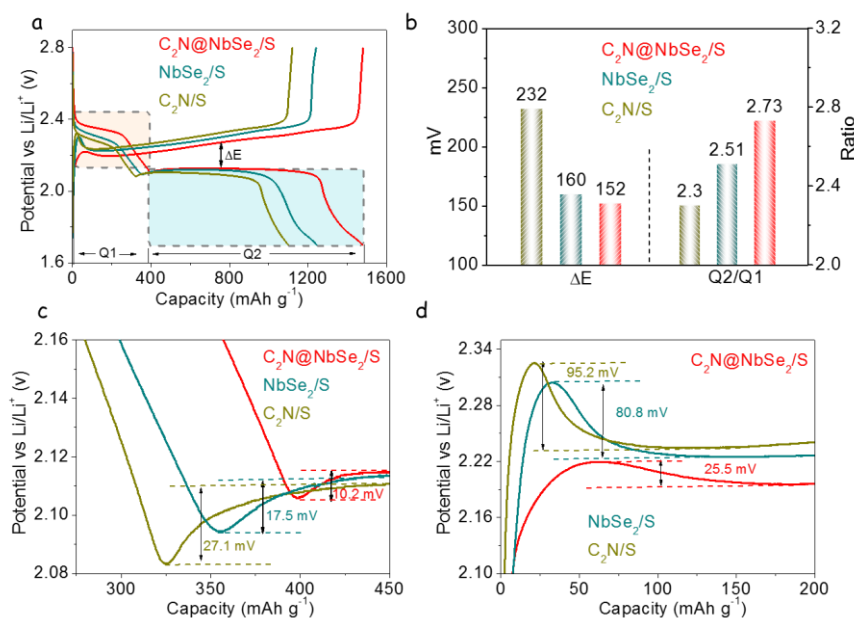


Figure 24. Polysulfide redox activity. (a) Galvanostatic charge–discharge profiles of $\text{C}_2\text{N@NbSe}_2/\text{S}$, NbSe_2/S and $\text{C}_2\text{N}/\text{S}$ electrodes at a current rate of 0.1 C. (b) The value of ΔE and Q2/Q1 obtained from charge–discharge curves of various electrodes. (c) Discharge profiles of $\text{C}_2\text{N@NbSe}_2/\text{S}$, NbSe_2/S , and $\text{C}_2\text{N}/\text{S}$ electrodes showing the overpotentials for conversion

between soluble LiPS and insoluble Li₂S₂/Li₂S. (d) Charge profiles of C₂N@NbSe₂/S, NbSe₂/S, and C₂N/S electrodes showing the overpotentials for conversion between soluble LiPS and insoluble Li₂S₂/Li₂S.

The Li₂S nucleation and dissolution processes were further analyzed to investigate the liquid-solid reaction kinetics (see the experimental section for details). As shown in Figure 25a, NbSe₂@C₂N electrodes exhibited a higher Li₂S precipitation capacity (303.5 mAh g⁻¹) compared with NbSe₂ (238.2 mAh g⁻¹) and C₂N electrodes (115.6 mAh g⁻¹). NbSe₂@C₂N electrodes were also characterized by the shortest Li₂S nucleation and growth times. The constant of Li₂S nucleation and growth can be calculated according to the following equation: [45]

$$Ak^2 = \frac{2}{\pi_m^3} \quad (4)$$

where A is the nucleation rate constant, k is the growth rate, t_m is peak-current-corresponding Li₂S precipitation time. Higher Ak^2 values are associated with faster Li₂S nucleation and growth. As shown in Figure 25b, the Ak^2 of C₂N@NbSe₂ was 3 times and 5.5 times larger than in NbSe₂ and C₂N, respectively. These results suggested that the combination of C₂N and NbSe₂ within C₂N@NbSe₂ heterostructures significantly lower the energy barrier for Li₂S nucleation and accelerates the Li₂S precipitation kinetics. [50,57]

Potentiostatic charge tests were carried out to study the kinetics of the Li₂S dissolution. As displayed in Figure 25c, C₂N@NbSe₂ electrodes delivered higher current densities with a higher capacity of Li₂S dissolution (608 mAh g⁻¹) compared with NbSe₂ (452 mAh g⁻¹) and C₂N electrodes (386 mAh g⁻¹). This result indicates that the heterostructure C₂N@NbSe₂ reduces the oxidation overpotential for Li₂S dissolution. [58] Overall, these results verified the superior electrocatalytic performance of C₂N@NbSe₂ hosts in reducing polarization and promoting redox kinetics of LiPS conversion reaction.

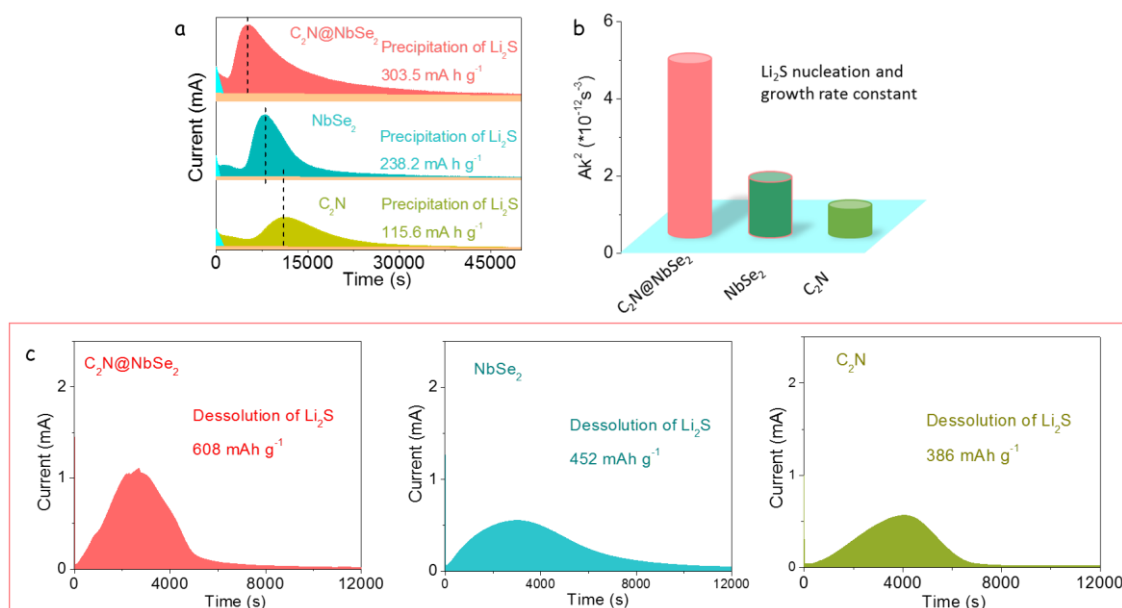


Figure 25. (a) Potentiostatic discharge profile at 2.05 V on different electrodes with Li_2S_8 catholyte for evaluating the nucleation kinetics of Li_2S . (b) Calculated Li_2S nucleation and growth constant. (c) Potentiostatic charge profile at 2.40 V for regulating the dissolution kinetics of Li_2S on $\text{C}_2\text{N}@\text{NbSe}_2$, NbSe_2 , and C_2N .

DFT calculations support a further insight into the electrochemical catalytic effect during the Li-S reaction. Figure 26a exhibits the initial state, transition state, and final state of Li_2S decomposition on different sulfur hosts. The calculated energy barrier for Li_2S decomposition on $\text{C}_2\text{N}@\text{NbSe}_2$, NbSe_2 , and C_2N surface was 0.56 eV, 0.88 eV, and 1.25 eV, respectively. These results demonstrate that the heterostructured $\text{C}_2\text{N}@\text{NbSe}_2$ can greatly reduce the Li_2S decomposition energy barrier and enhance the redox reversibility between Li_2S and LiPS.

To further verify the catalytic activity of catalysts on the LiPS conversion, the Gibbs free energy changes during the S reduction on $\text{C}_2\text{N}@\text{NbSe}_2$, NbSe_2 , and C_2N were calculated (Figure 26b). The overall reaction based on the reversible formation of Li_2S from S_8 and Li was considered. During the discharge process, the first step involves the double reduction of S_8 with two Li^+ to form Li_2S_8 , and then Li_2S_8 undergoes further reduction, forming three intermediate LiPS, such as Li_2S_6 , Li_2S_4 , Li_2S_2 and producing Li_2S as the final product. The largest increase of Gibbs free energy was obtained for the conversion from Li_2S_2 to Li_2S species, suggesting this step as the rate-limiting for the total discharge process.^[59,60] $\text{C}_2\text{N}@\text{NbSe}_2$ exhibited the lowest Gibbs free energy changes (0.66 eV), when compared with NbSe_2 (0.83 eV) and C_2N (0.95 eV), which suggested that the reduction of S is more thermodynamically favorable on $\text{C}_2\text{N}@\text{NbSe}_2$ than on NbSe_2 and C_2N . The lowest Gibbs free energy change in the reduction of Li_2S_2 demonstrated

$C_2N@NbSe_2$ to be an excellent catalyst to promote the LiPS conversion kinetics and accelerate the Li_2S formation, consistent with experimental data obtained from discharge curves and the Li_2S nucleation test.

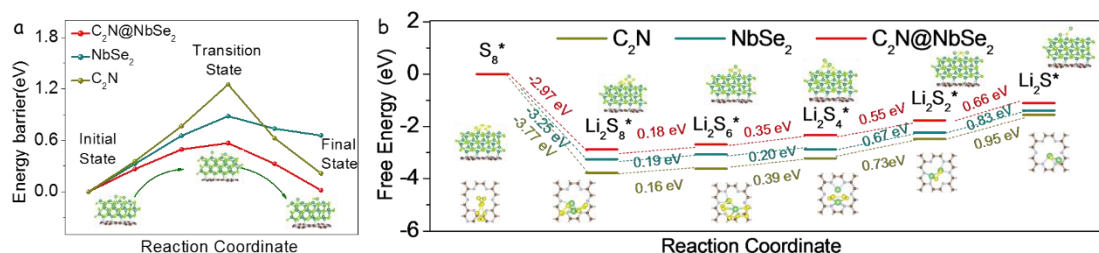


Figure 26. (a) Energy barrier profiles of Li_2S cluster decomposition on C_2N , $NbSe_2$, and $C_2N@NbSe_2$ along with different reaction coordinates. The initial, transition, and final structures are also displayed. The green, yellow, brown, silver, light green, and blue balls represent Li, S, C, N, Se and Nb atoms, respectively. (b) Gibbs free energy profiles of LiPS species on $C_2N@NbSe_2$, $NbSe_2$, and C_2N , showing a lowest reaction free energy from Li_2S_2 to Li_2S on $C_2N@NbSe_2$ than that on $NbSe_2$ and C_2N .

Figure 27a and Figure 28 show the galvanostatic charge/discharge profiles of $C_2N@NbSe_2/S$, $NbSe_2/S$ and C_2N/S at various current densities, from 0.1 to 5 C. Galvanostatic profiles displayed two discharge plateaus and one charge plateau, consistently with CV results and the multistep sulfur reaction mechanism. The higher discharge plateau at around 2.3 V is associated with the conversion of sulfur to long-chain LiPS (Li_2S_x , $4 \leq x \leq 8$). The lower discharge plateau at about 2.1 V ascribes to the reduction of LiPS to insoluble products (Li_2S_2/Li_2S).^[50,55]

Figure 27b compares the rate performances of the different cells. Among the tested cathodes, $C_2N@NbSe_2/S$ -based cells exhibited the highest rate capability with average discharge capacities of 1432, 1198, 1060, 955, 830, 746, and 683 mAh g^{-1} at current rates from 0.1 C to 5 C, respectively. Even after switching the current density back to 0.2 C, the recovered specific capacity of $C_2N@NbSe_2/S$ electrodes reached a similar value of 1068 mAh g^{-1} , indicating remarkable electrochemical reversibility.

Energy efficiency was calculated according to:^[14]

$$E = \int UI dt \quad (5)$$

As shown in Figure 27c, $C_2N@NbSe_2/S$ delivered a higher energy efficiency compared to $NbSe_2/S$ and C_2N/S electrodes, especially at high current densities. For instance, $C_2N@NbSe_2/S$ -based cells displayed an energy efficiency of 87.8% at 5 C, higher than $NbSe_2/S$ (83.5%) and C_2N/S (76.8%) cells. The significant enhancement in energy efficiency is associated with the lower ΔE and better catalytic properties of $C_2N@NbSe_2$.

Galvanostatic cycling performances of cells with different cathodes are presented in Figure 27d. $C_2N@NbSe_2/S$ cells were characterized by a remarkable initial capacity of 905 mAh g^{-1} , and maintained a capacity of 752.1 mAh g^{-1} after 500 cycles at 1 C, which corresponds to a capacity retention of 83.1%. On the other hand, after 500 cycles $NbSe_2/S$ and C_2N/S electrodes displayed discharge capacities of 657.8 mAh g^{-1} and 516.1 mAh g^{-1} , with a capacity retention of 75.8 % and 85.7%, respectively.

Results of the EIS analysis of $C_2N@NbSe_2/S$, $NbSe_2/S$, and C_2N/S cathodes after 500 cycles at 1 C are displayed in Figure 27e. The semicircle in the high-frequency region is ascribed to the deposition of the insulating discharge products of Li_2S on the electrode surface (R_d), and the second semicircle in the middle frequency region corresponds to the charge transfer resistance (R_{ct}).^[40] The $C_2N@NbSe_2/S$ electrode showed a considerably lower R_d and R_{ct} compared with $NbSe_2/S$ and C_2N/S electrodes, which is consistent with the accelerated polysulfide conversion reaction offered by the combination of the two materials, as well as by the facilitated charge transfer kinetics during lithiation/delithiation reaction.

Besides, cells were disassembled to evaluate the morphology of the cathodes after cycling. As displayed in Figure 27f, the $C_2N@NbSe_2/S$ cathode material maintained its original morphology after 50 cycles, demonstrating its excellent structural stability during lithiation/delithiation processes.

An ultra-long cycling test was conducted for the $C_2N@NbSe_2/S$ -based cathode at a higher current density of 3 C (Figure 27g). $C_2N@NbSe_2/S$ -based cells delivered stable cycling life with only 0.012% capacity decay per cycle after 2000 cycles. The coulombic efficiencies of $C_2N@NbSe_2/S$ stabilized at around 99.8%, demonstrating outstanding cycling stability. Notice, that after the initial 500 cycles, a capacity loss of just 3.3 % was measured during the subsequent 1500 cycles.

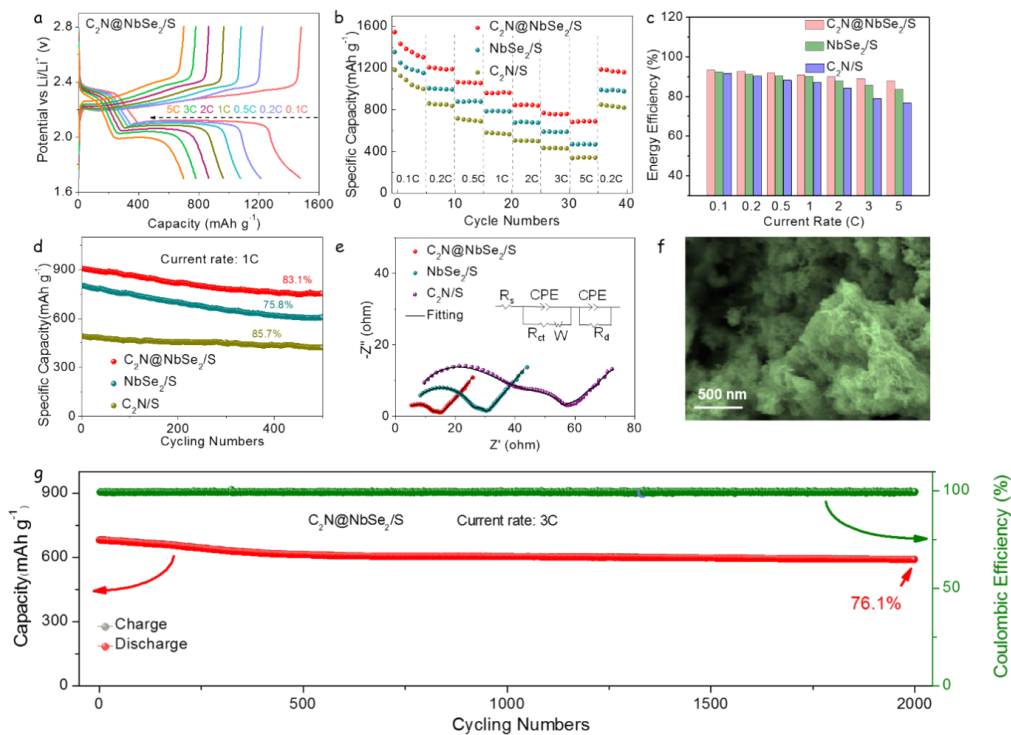


Figure 27. Electrochemical performance of lithium-sulfur coin cells. (a) Galvanostatic charge/discharge profiles of a $C_2N@NbSe_2/S$ electrode at various rates, from 0.1 C to 5 C (1 C = 1672 mA g⁻¹). (b) Rate capability of $C_2N@NbSe_2/S$, $NbSe_2/S$, and C_2N/S electrodes at various C rates, from 0.1 C to 5 C. (c) The energy efficiencies of three different electrodes at different current densities. (d) Cycling performances of different electrodes over 500 cycles at 1 C. (e) Nyquist plot of EIS data of $C_2N@NbSe_2/S$, $NbSe_2/S$, and C_2N/S cathodes after cycling. (f) SEM image of $C_2N@NbSe_2/S$ electrode after cycling at 1 C. (g) Ultra-long cycling test of the $C_2N@NbSe_2/S$ electrode at 3 C over 2000 cycles.

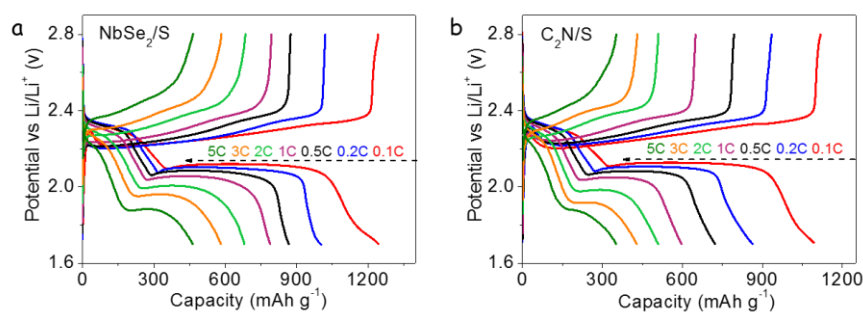


Figure 28. Galvanostatic charge–discharge profiles of (a) $NbSe_2/S$ and (b) C_2N/S at different current densities range from 0.1 C to 5 C.

To meet the high energy density requirement for LSB commercialization, the electrochemical performances of cells based on cathodes containing higher sulfur loadings were investigated. $C_2N@NbSe_2/S$ cathodes with sulfur loadings of 3.0 and 5.6 $mg\ cm^{-2}$ still displayed one charge and two discharge plateaus, with a low polarization between charge and discharge processes (Figure 29a). Galvanostatic charge/discharge curves at different current rates were also measured for $C_2N@NbSe_2/S$ cathodes containing 3.0 $mg\ cm^{-2}$ (Figure 29b,c) and 5.6 $mg\ cm^{-2}$ of sulfur (Figure 29d). $C_2N@NbSe_2/S$ cathodes delivered average areal capacities of 3.53 and 5.63 $mAh\ cm^{-2}$ under sulfur loadings of 3.0 and 5.6 $mg\ cm^{-2}$, respectively. These values are in the range of the areal capacities industrially required for LIB ($\sim 4\ mAh\ cm^{-2}$). Even at a current rate of 0.5 C, $C_2N@NbSe_2/S$ cathodes still showed a high areal capacity of 4.01 $mAh\ cm^{-2}$ when loaded with 5.6 $mg\ cm^{-2}$ of sulfur. These results demonstrate the high potential $C_2N@NbSe_2/S$ cathodes to realize low ΔE s and fast sulfur reaction kinetics even under high loading configurations. Notably, at high sulfur loadings, $C_2N@NbSe_2/S$ -based cells maintained well the voltage profile during the first 50 cycles, with just a small potential hysteresis, indicating a minor LiPS shuttling and stable sulfur electrochemistry (Figure 30a). Figure 30b presents the cycling performances of $C_2N@NbSe_2/S$ cathodes with various sulfur loading at a current of 0.2 C. The initial areal capacities were 2.84 and 4.56 $mAh\ cm^{-2}$ at sulfur loadings of 3.0 and 5.6 $mg\ cm^{-2}$, respectively. After 80 cycles, high areal capacities around 2.6 and 3.7 $mAh\ cm^{-2}$ were still maintained with a sulfur loading of 3.0 and 5.6 $mg\ cm^{-2}$, respectively. Figure 30d and Table 1 displays a comparison of several parameters of state-of-the-art Nb-based and carbon-based materials as cathode hosts for LSBs. Notice that the $C_2N@NbSe_2$ host presented here is characterized by the highest capacities and stabilities. Finally, to illustrate the promising practical application of LSBs based on $C_2N@NbSe_2/S$ cathodes, Figure 30c shows how two $C_2N@NbSe_2/S$ -based coin cells in series were used to light up a “2021”-shaped LED panel containing 60 LEDs. All these results indicate that $C_2N@NbSe_2/S$ electrodes can definitively help LSBs to reach practical applications.

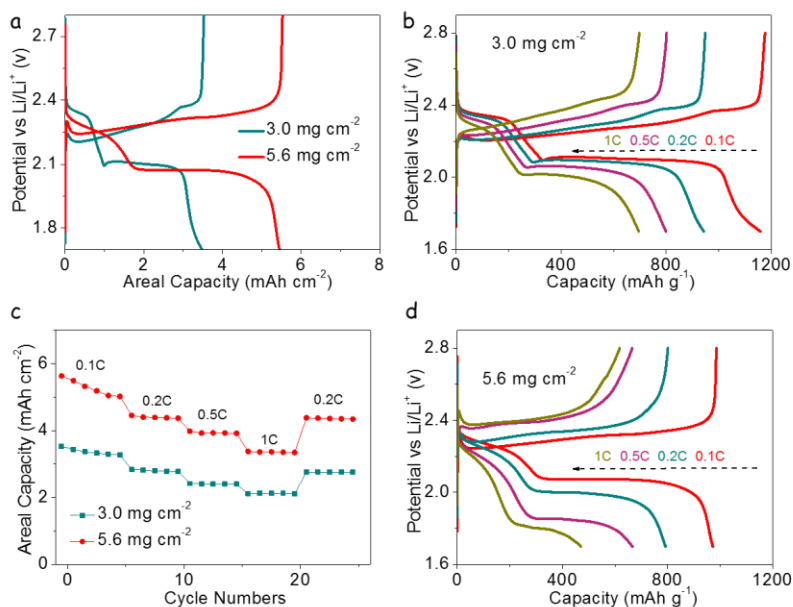


Figure 29. (a) Charge/discharge profiles at 0.1 C of $C_2N@NbSe_2/S$ cathodes with sulfur loadings of 3.0 and 5.6 mg cm^{-2} . (b) Charge/discharge profiles of $C_2N@NbSe_2/S$ cathodes at different current densities, from 0.1 C to 1 C. (c) Rate capabilities with different sulfur loadings at various current densities as indicated in the graph. (d) Galvanostatic charge/discharge profiles of $C_2N@NbSe_2/S$ at various current rates with a high sulfur loading of 5.6 mg cm^{-2} .

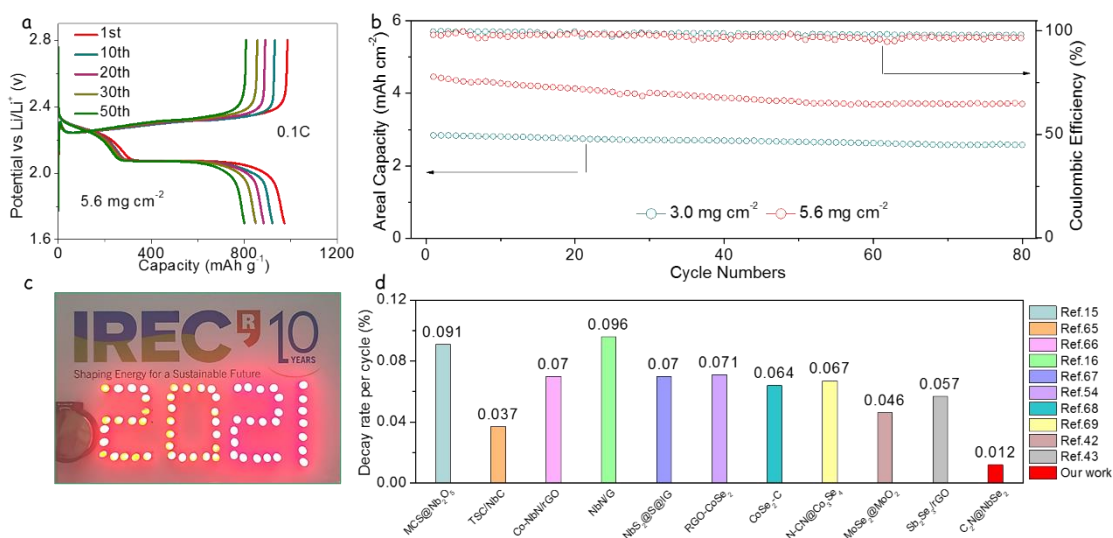


Figure 30. (a) Galvanostatic charge/discharge profiles at 0.1 C with a sulfur loading of 5.6 mg cm^{-2} . (b) Cycling performances at 0.2 C of $C_2N@NbSe_2/S$ cathodes with different sulfur loadings. (c) Optical photograph of a “2021” shape composed of 60 LED lamps (2.2-3.0 V) being charged by two Li-S cells based on $C_2N@NbSe_2/S$ electrodes. (d) Decay rate per cycle compared with other reported works.

Table 1 Summary of recent reports on sulfur host cathodes for LSBs compared to C₂N@NbSe₂.

Host material	Capacity (mAh g ⁻¹) (current rate)	(cycles, current rate)	Decay rate (per cycle, %)	Ref
MCS@Nb ₂ O ₅	1358 (0.2C)	(500, 2C)	0.091%	15
TSC/NbC	1283 (0.1C)	(500, 0.1C)	0.037%	61
Co-NbN/rGO	1360 (0.1C)	(800, 1C)	0.07%	62
NbN/G	1394 (0.1C)	(300, 1C)	0.096%	16
NbS ₂ @S@IG	1190 (0.2C)	(350, 0.5C)	0.07%	63
RGO-CoSe ₂	1045 (0.2C)	(400, 1C)	0.071%	52
CoSe ₂ -C	1147.7 (0.1C)	(700, 2C)	0.064%	64
N-CN@Co ₃ Se ₄	1437 (0.1C)	(800, 0.2C)	0.067%	65
MoSe ₂ @MoO ₂	1205 (0.1C)	(500, 0.5C)	0.046%	42
Sb ₂ Se ₃ /rGO	1160 (0.2C)	(500, 1C)	0.057%	43
C₂N@NbSe₂	1545 (0.1C)	(2000, 3C)	0.012%	This work

3.5 Conclusions

In summary, we rationally designed and engineered a new and high-performance LSB cathode based on an in-situ grown C₂N@NbSe₂ heterostructured catalyst. We used a facile and effective two-step strategy to produce the composites with a nanosheet geometry that provided outstanding specific surface areas up to 389.6 m² g⁻¹. The unique architecture of the C₂N@NbSe₂ nanosheets delivered a conductive framework for electron/ion transfer and a cushion to mitigate the effect of the volume variation of the sulfur cathode during cycling. DFT calculations and experimental results comprehensively demonstrated that C₂N@NbSe₂ was characterized by a suitable electronic structure and charge rearrangement, that not only accelerated the LiPS conversion and lowered the energy barrier for Li₂S precipitation/decomposition, but also strongly promoted LiPS adsorption through Li-N and Nb-S bonds. Consistent with these excellent qualities, C₂N@NbSe₂/S cathodes delivered exceptional long-term cycling stability with a very low capacity decay of 0.012% per cycle over 2000 cycles at 3 C, with only a total of 3.3% capacity loss in the last 1500 cycles, and exceptional rate performance of 683 mAh g⁻¹ at 5 C. Moreover, C₂N@NbSe₂/S cathodes

delivered a high areal capacity of 5.65 mAh cm⁻² at a sulfur loading of 5.6 mg cm⁻². This work not only emphasizes the potential capabilities of TMSe and particularly the so far unexplored NbSe₂, but also proposes heterostructured architectures as highly effective catalyst for the Li-S reaction.

3.6 References

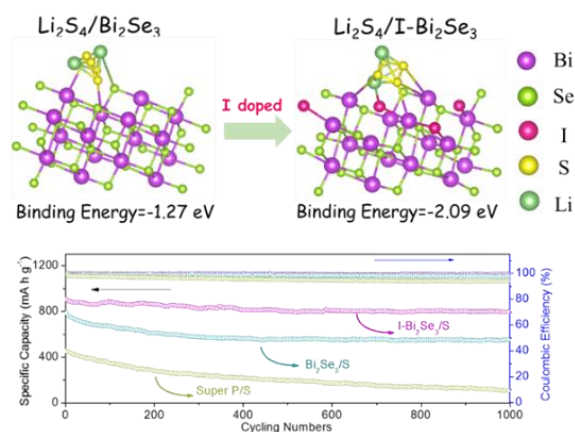
- [1] S. Chu, Y. Cui, N. Liu, *Nat. Mater.* **2016**, *16*, 16-22.
- [2] G. Zhou, D.-W. Wang, F. Li, P.-X. Hou, L. Yin, C. Liu, G. Q. Lu, I. R. Gentle, H.-M. Cheng, *Energy Environ. Sci.* **2012**, *5*, 8901.
- [3] S.-L. Chou, S.-X. Dou, *Adv. Mater.* **2017**, *29*, 1705871.
- [4] Z. W. Seh, Y. Sun, Q. Zhang, Y. Cui, *Chem. Soc. Rev.* **2016**, *45*, 5605-5634.
- [5] A. Manthiram, Y. Fu, S. H. Chung, C. Zu, Y. S. Su, *Chem. Rev.* **2014**, *114*, 11751-11787.
- [6] Z. Li, H. B. Wu, X. W. Lou, *Energy Environ. Sci.* **2016**, *9*, 3061-3070.
- [7] J. He, L. Luo, Y. Chen, A. Manthiram, *Adv. Mater.* **2017**, *29*, 1702707.
- [8] Z. Li, J. Zhang, B. Guan, D. Wang, L. M. Liu, X. W. Lou, *Nat. Commun.* **2016**, *7*, 13065.
- [9] L. Hu, C. Dai, H. Liu, Y. Li, B. Shen, Y. Chen, S.-J. Bao, M. Xu, *Adv. Energy Mater.* **2018**, *8*, 1800709.
- [10] T. Lei, W. Chen, J. Huang, C. Yan, H. Sun, C. Wang, W. Zhang, Y. Li, J. Xiong, *Adv. Energy Mater.* **2017**, *7*, 1601843.
- [11] Q. Pang, D. Kundu, L. F. Nazar, *Mater. Horiz.* **2016**, *3*, 130-136.
- [12] C. Ye, Y. Jiao, H. Jin, A. Slattery, K. Davey, H. Wang, S.-Z. Qiao, *Angew. Chem., Int. Ed.* **2018**, *57*, 16703-16707.
- [13] W. Tian, B. Xi, Z. Feng, H. Li, J. Feng, S. Xiong, *Adv. Energy Mater.* **2019**, *9*, 1901896.
- [14] Zhang, J. J. Biendicho, T. Zhang, R. Du, J. Li, X. Yang, J. Arbiol, Y. Zhou, J. R. Morante, A. Cabot, *Adv. Funct. Mater.* **2019**, *29*, 1903842.
- [15] Y. Tao, Y. Wei, Y. Liu, J. Wang, W. Qiao, L. Ling, D. Long, *Energy Environ. Sci.*, **2016**, *9*, 3230-3239.
- [16] H. Shi, Z. Sun, W. Lv, S. Xiao, H. Yang, Y. Shi, K. Chen, S. Wang, B. Zhang, Q.-H. Yang, F. Li, *J. Energy Chem.*, **2020**, *45*, 135-141.
- [17] G. Babu, N. Masurkar, H. A. Salem, L. M. Reddy Arava, *J. Am. Chem. Soc.* **2017**, *139*, 171-178.
- [18] X. Xi, S. Huang, H. Berger, L. Forró, J. Shan, K. F. Mak, *Phys. Rev. Lett.* **2016**, *117*, 106801.

- [19] X. Xi, Z. Wang, W. Zhao, J. Park, K. T. Law, H. Berger, L. Forró, J. Shan, K. F. Mak, *Nature Phys.* **2016**, *12*, 139–143.
- [20] X.-B. Cheng, J.-Q. Huang, Q. Zhang, H.-J. Peng, M.-Q. Zhao, F. Wei, *Nano Energy* **2014**, *4*, 65-72.
- [21] L. Zhang, D. Liu, Z. Muhammad, F. Wan, W. Xie, Y. Wang, L. Song, Z. Niu, J. Chen, *Adv. Mater.* **2019**, *31*, e1903955.
- [22] Q. Pang, L. F. Nazar, *ACS nano* **2016**, *10*, 4111–4118.
- [23] J. Wu, L.-W. Wang, *J. Mater. Chem. A* **2018**, *6*, 2984-2994.
- [24] Y. Zheng, H. Li, H. Yuan, H. Fan, W. Li, J. Zhang, *Appl. Surf. Sci.* **2018**, *434*, 596-603.
- [25] Y. Wang, R. Zhang, J. Chen, H. Wu, S. Lu, K. Wang, H. Li, C. J. Harris, K. Xi, R. V. Kumar, S. Ding, *Adv. Energy Mater.* **2019**, *9*, 1900953.
- [26] X. Du, J. Huang, J. Zhang, Y. Yan, C. Wu, Y. Hu, C. Yan, T. Lei, W. Chen, C. Fan, J. Xiong, *Angew. Chem. Int. Ed.* **2019**, *58*, 4484.
- [27] S. S. Shinde, C. H. Lee, J.-Y. Jung, N. K. Wagh, S.-H. Kim, D.-H. Kim, C. Lin, S. U. Lee, J.-H. Lee, *Energy Environ. Sci.* **2019**, *12*, 727-738.
- [28] J. Mahmood, F. Li, S.-M. Jung, M. S. Okyay, I. Ahmad, S.-J. Kim, N. Park, H. Y. Jeong, J.-B. Baek, *Nat. Nanotechnol.* **2017**, *12*, 441-446.
- [29] H. Li, S. Ma, H. Cai, H. Zhou, Z. Huang, Z. Hou, J. Wu, W. Yang, H. Yi, C. Fu, Y. Kuang, *Energy Storage Mater.* **2019**, *18*, 338-348.
- [30] R. Li, H. Peng, Q. Wu, X. Zhou, J. He, H. Shen, M. Yang, C. Li, *Angew. Chem. Int. Ed.* **2020**, *59*, 12129–12138.
- [31] F. Xiao, G.-L. Xu, C.-J. Sun, M. Xu, W. Wen, Q. Wang, M. Gu, S. Zhu, Y. Li, Z. Wei, X. Pan, J. Wang, K. Amine, M. Shao, *Nano Energy* **2019**, *61*, 60-68.
- [32] J. Mahmood, E. K. Lee, M. Jung, D. Shin, I. Y. Jeon, S. M. Jung, H. J. Choi, J. M. Seo, S. Y. Bae, S. D. Sohn, N. Park, J. H. Oh, H. J. Shin, J. B. Baek, *Nat. Commun.* **2015**, *6*, 6486.
- [33] J. Zhang, C. Du, J. Zhao, H. Ren, Q. Liang, Y. Zheng, S. Madhavi, X. Wang, J. Zhu, Q. Yan, *ACS Appl. Mater. Interfaces* **2018**, *10*, 37773-37778.
- [34] Y. Wang, A. Chen, S. Lai, X. Peng, S. Zhao, G. Hu, Y. Qiu, J. Ren, X. Liu, J. Luo, *J. Catal.* **2020**, *381*, 78-83.
- [35] Y.-L. Wang, Y. Tian, Z.-L. Lang, W. Guan, L.-K. Yan, *J. Mater. Chem. A* **2018**, *6*, 21056.
- [36] Z. Zhuang, Y. Li, Z. Li, F. Lv, Z. Lang, K. Zhao, L. Zhou, L. Moskaleva, S. Guo, L. Mai, *Angew. Chem.* **2018**, *130*, 505.
- [37] Q. Zhu, B. Qiu, H. Duan, Y. Gong, Z. Qin, B. Shen, M. Xing, J. Zhang, *Appl. Catal. B Environ.* **2019**, *259*, 118078.

- [38] X. Wang, X. Tian, Y. Sun, J. Zhu, F. Li, H. Mu, J. Zhao, *Nanoscale* **2018**, *10*, 12315. [39] J.-X. Feng, S.-Y. Tong, Y.-X. Tong, G.-R. Li, *J. Am. Chem. Soc.* **2018**, *140*, 5118.
- [40] D. Yang, C. Zhang, J. J. Biendicho, X. Han, Z. Liang, R. Du, M. Li, J. Li, J. Arbiol, J. Llorca, Y. Zhou, J. R. Morante, A. Cabot, *ACS nano* **2020**, *14*, 15492–15504.
- [41] J. Song, Z. Yu, M. L. Gordin, D. Wang, *Nano Lett.* **2016**, *16*, 864-870.
- [42] Q. Hao, G. Cui, Y. Zhang, J. Li, Z. Zhang, *Chem. Eng. J.*, **2020**, *381*, 122672.
- [43] Y. Tian, G. Li, Y. Zhang, D. Luo, X. Wang, Y. Zhao, H. Liu, P. Ji, X. Du, J. Li, Z. Chen, *Adv. Mater.* **2020**, *32*, e1904876.
- [44] T.-Z. Hou, W.-T. Xu, X. Chen, H.-J. Peng, J.-Q. Huang, Q. Zhang, *Angew. Chem. Int. Ed.* **2017**, *129*, 8290–8294.
- [45] M. Wang, L. Fan, X. Sun, B. Guan, B. Jiang, X. Wu, D. Tian, K. Sun, Y. Qiu, X. Yin, Y. Zhang, N. Zhang, *ACS Energy Letter* **2020**, *5*, 3041-3050.
- [46] X. Liu, Q. He, H. Yuan, C. Yan, Y. Zhao, X. Xu, J.-Q. Huang, Y.-L. Chueh, Q. Zhang, L. Mai, *J. Energy Chem.* **2020**, *48*, 109-115.
- [47] H. Lin, L. Yang, X. Jiang, G. Li, T. Zhang, Q. Yao, G. W. Zheng, J. Y. Lee, *Energy Environ. Sci.* **2017**, *10*, 1476-1486.
- [48] J. Zhou, X. Liu, L. Zhu, J. Zhou, Y. Guan, L. Chen, S. Niu, J. Cai, D. Sun, Y. Zhu, J. Du, G. Wang, Y. Qian, *Joule* **2018**, *2*, 2681-2693.
- [49] L. Zhang, X. Chen, F. Wan, Z. Niu, Y. Wang, Q. Zhang, J. Chen, *ACS nano* **2018**, *12*, 9578-9586.
- [50] S. Huang, Y. V. Lim, X. Zhang, Y. Wang, Y. Zheng, D. Kong, M. Ding, S. A. Yang, H. Y. Yang, *Nano Energy* **2018**, *51*, 340-348.
- [51] Z. Yuan, H. J. Peng, T. Z. Hou, J. Q. Huang, C. M. Chen, D. W. Wang, X. B. Cheng, F. Wei, Q. Zhang, *Nano Lett.* **2016**, *16*, 519-527.
- [52] L. Chen, W. Yang, J. Liu, Y. Zhou, *Nano Res.*, **2019**, *12*, 2743–2748.
- [53] G. Zhou, H. Tian, Y. Jin, X. Tao, B. Liu, R. Zhang, Z. W. Seh, D. Zhuo, Y. Liu, J. Sun, J. Zhao, C. Zu, D. S. Wu, Q. Zhang, Y. Cui, *Proc. Natl. Acad. Sci. USA* **2017**, *114*, 840.
- [54] H. Zhang, D. Tian, Z. Zhao, X. Liu, Y.-N. Hou, Y. Tang, J. Liang, Z. Zhang, X. Wang, J. Qiu, *Energy Storage Mater.* **2019**, *21*, 210-218.
- [55] D. Su, M. Cortie, H. Fan, G. Wang, *Adv. Mater.* **2017**, *29*, 1700587.
- [56] Z. Du, X. Chen, W. Hu, C. Chuang, S. Xie, A. Hu, W. Yan, X. Kong, X. Wu, H. Ji, L. J. Wan, *J. Am. Chem. Soc.* **2019**, *141*, 3977-3985.
- [57] Y. Wang, R. Zhang, Y.-c. Pang, X. Chen, J. Lang, J. Xu, C. Xiao, H. Li, K. Xi, S. Ding, *Energy Storage Mater.* **2019**, *16*, 228-235.

- [58] H. Yuan, H.-J. Peng, B.-Q. Li, J. Xie, L. Kong, M. Zhao, X. Chen, J.-Q. Huang, Q. Zhang, *Adv. Energy Mater.* **2019**, *9*, 1802768.
- [59] Y. Pan, X. Cheng, M. Gao, Y. Fu, J. Feng, H. Ahmed, L. Gong, H. Zhang, V. S. Battaglia, *ACS Appl. Mater. Interfaces* **2020**, *12*, 32726.
- [60] R. Wang, C. Luo, T. Wang, G. Zhou, Y. Deng, Y. He, Q. Zhang, F. Kang, W. Lv, Q. Yang, *Adv. Mater.* **2020**, *32*, 2000315.
- [61] S. Shen, X. Xia, Y. Zhong, S. Deng, D. Xie, B. Liu, Y. Zhang, G. Pan, X. Wang, J. Tu, *Adv. Mater.*, **2019**, *31*, 1900009.
- [62] W. Ge, L. Wang, C. Li, C. Wang, D. Wang, Y. Qian, L. Xu, *J. Mater. Chem. A*, **2020**, *8*, 6276-6282.
- [63] Z. Xiao, Z. Yang, L. Zhang, H. Pan, R. Wang, *ACS nano*, **2017**, *11*, 8488–8498.
- [64] B. Yuan, D. Hua, X. Gu, Y. Shen, L.-C. Xu, X. Li, B. Zheng, J. Wu, W. Zhang, S. Li, F. Huo, *J. Energy Chem.*, **2020**, *48*, 128-135.
- [65] D. Cai, B. Liu, D. Zhu, D. Chen, M. Lu, J. Cao, Y. Wang, W. Huang, Y. Shao, H. Tu, W. Han, *Adv. Energy Mater.*, **2020**, *10*, 1904273.

Chapter 4 Enhanced Polysulfide Conversion with Highly Conductive and Electrocatalytic Iodine-Doped Bismuth Selenide Nanosheets in Lithium-Sulfur Batteries



4.1 Abstract

The shuttling behavior and sluggish conversion kinetics of the intermediate LiPS represent the main obstructions to the practical application of LSBs. Herein, we propose an innovative sulfur host, based on an iodine-doped bismuth selenide (I-Bi₂Se₃), able to solve these limitations by immobilizing the LiPS and catalytically activating the redox conversion at the cathode. We detail here the synthesis of I-Bi₂Se₃ nanosheets and thoroughly characterize their morphology, crystal structure and composition. We use density-functional theory and experimental tools to demonstrate that I-Bi₂Se₃ nanosheets are characterized by a proper composition and micro- and nano-structure to facilitate Li⁺ diffusion and fast electron transportation, and to provide numerous surface sites with strong LiPS adsorbability and extraordinary catalytic activity. Overall, I-Bi₂Se₃/S electrodes exhibit outstanding initial capacities up to 1500 mAh g⁻¹ at 0.1 C and cycling stability over 1000 cycles, with an average capacity decay rate of only 0.012% per cycle at 1 C. Besides, at a sulfur loading of 5.2 mg cm⁻², a high areal capacity of 5.70 mAh cm⁻² at 0.1 C is obtained with an electrolyte/sulfur ratio of 12 μL mg⁻¹. This work demonstrated the doping is an effective way to optimize the MSe catalysts in LSBs.

4.2 Introduction

There is an urgent need for a new generation of rechargeable energy storage devices that offer a step higher capacity and durability, well beyond the limitations of current LIBs. Among the

possible candidates, LSBs attract significant attention due to their very high theoretical specific energy, 2600 Wh Kg⁻¹, their potential for low cost associated with the abundance of sulfur, and their lack of toxicity.^[1-5] However, their practical use is still hindered by the electrically insulating nature of sulfur and its discharge products (Li₂S/Li₂S₂),^[6-8] a low utilization of the active material, and a moderate cycling stability associated with the large volume expansion of the cathode upon lithiation^[9-12] and the shuttle of the soluble intermediate LiPS.^[13-15] These drawbacks call for an improved design and engineering of the sulfur cathode.^[16-20]

Conductive porous carbons have been widely used to improve the electrical conductivity of the cathode, encapsulate sulfur and restrain the dissolution and diffusion of LiPS.^[21,22] However, the encapsulation of sulfur within porous carbon can be detrimental to the cathode redox reaction kinetics by reducing sulfur reactivity and slowing the desolvation process.^[23,24] To overcome current cathode limitations, metal-based compounds and metal-organic frameworks have been added to strengthen the chemical interaction with LiPS and reduce the shuttle effect.^[25-29] Among the tested metal compounds, sulfides such as MoS₂, VS₂, CoS₂, Ni₃S₂, and Sb₂S₃, have demonstrated particularly strong sulfiphilic ability toward LiPS trapping and low lithiation voltages.^[30-35] However, cathodes based on metal sulfides are generally characterized by moderate electrical conductivities, limited sulfur utilization, insufficient cycling stability and low rate capabilities.^[36-40]

Recently, we and others have demonstrated MSe, such as ZnSe, NbSe₂ and NiCo₂Se₄, as promising sulfur hosts in LSB cathodes, owing to their notable polarity, excellent catalytic activity, and high electrical conductivity.^[3,5,33,41] However, among the extended family of possible chalcogenides, a particularly interesting candidate has been so far overlooked. Bismuth selenide (Bi₂Se₃) is generally an n-type degenerated semiconductor, with a low bandgap of 0.3 eV, that is widely used in the field of thermoelectricity due to its high electrical conductivity.^[41, 42] Its n-type electronic behavior is related to the presence of Se vacancies that act as electron donors. Bi₂Se₃ has a layered crystal structure consisting of stacks of covalently bonded quintuple atomic layers, Se-Bi-Se-Bi-Se, that are held together by weak van der Waals interactions. Such high electrical conductivity and layered structure is highly suitable for its use as sulfur hosts in LSB cathodes. Besides, the variable chemical valences of Bi and Se anticipates a high potential catalytic activity.

In this work, we evaluate the potential of iodine-doped Bi₂Se₃ nanosheets as sulfur host in LSBs. We first detail the synthesis of Bi₂Se₃ nanosheets using a high yield and scalable solution-based method. These Bi₂Se₃ nanosheets are doped with iodine to further improve their adsorption and catalytic activity. The obtained material is used as sulfur host in LSB cathodes

and its performance is experimentally analyzed and computationally rationalized. Results demonstrate the I-Bi₂Se₃ nanosheets to provide high electrical conductivity, enhanced confinement of LiPS, the mitigation of the sulfur volume expansion effects, and an excellent electrocatalytic activity towards the redox reaction of sulfur and lithium sulfide.

4.3 Experimental section

Chemicals: Bismuth(III) nitrate pentahydrate (Bi(NO₃)₃ · 5H₂O, ≥ 99.99%), sodium selenite (Na₂SeO₃, ≥ 98%), ethylene glycol (EG, HOCH₂CH₂OH, 99%), and potassium hydroxide (KOH, ≥ 98%) were acquired from Fisher. Polyvinylpyrrolidone (PVP, (C₆H₉NO)_n, AMW ~55,000), were purchased from Sigma Aldrich. Ethanol and acetone were obtained from various sources at analytical grade.

Synthesis of Bi₂Se₃: Bi(NO₃)₃ · 5H₂O (2 mmol), Na₂SeO₃ (3 mmol), KOH (10 mmol), and PVP (0.1 g) were dissolved in a three-neck flask containing EG (50 ml) under Ar atmosphere at ambient temperature for 0.5 h. The solution was then heated to 180 °C and kept at this temperature for 3 hours. Immediately after the reaction was completed, the solution was allowed to cool naturally to room temperature by removing the heating mantle. The solution was divided into several centrifuge tubes and acetone was added to collect the solid product by centrifugation. In the next step, ethanol was introduced to re-disperse the particles and acetone to precipitate them again. This step was repeated twice. After that, purified Bi₂Se₃ particles were dried under vacuum overnight at room temperature.

Synthesis of I-Bi₂Se₃: 2.5 mg KI were dissolved in 5 ml deionized water. Then, 0.2 g dried Bi₂Se₃ nanosheets were added to the solution, kept in N₂-filled vials and vigorously stirred at room temperature for 48 h. After that, ethanol was added to the mixture to precipitate the nanosheets by centrifugation. Subsequently, the nanosheets were washed one more time with ethanol, centrifuged and dried under vacuum.

Synthesis of I-Bi₂Se₃/S, Bi₂Se₃/S and Super P/S: Sulfur was added through a simple melting diffusion process. I-Bi₂Se₃/S was obtained by mixing I-Bi₂Se₃ nanosheets and sublimed sulfur in a weight ratio of 1:3 and heated at 155 °C for 12 h in a glass bottle under an Ar atmosphere. After that, the powder was immersed in a 10 mL CS₂ and ethanol solution (1:4 volume ratio) for 10 min twice. For comparison, Bi₂Se₃/S and Super P/S were obtained by the same process.

Materials Characterization: An Auriga Zeiss field emission scanning electron microscope (SEM) was used to determine the nanoparticle morphology. An Oxford energy dispersive X-ray spectrometer (EDX) was used to measure the material composition at 20.0 kV. XRD was performed on a Bruker AXS D8 Advance diffractometer. XPS was performed on a Specs

system with the material inside the chamber at a pressure below 10^{-7} Pa. Data processing was carried out using the CasaXPS program. Crystallographic structure and chemical composition were analyzed by HRTEM and EELS, respectively, using a Tecnai F20 field-emission gun microscope at 200 kV with an embedded Gatan Quantum image filter. TGA was performed to record the ratio of S within prepared composites (PerkinElmer Diamond TG/DTA instrument). A Perkin Elmer Lambda 950 UV-vis spectrophotometer was used to measure UV-vis absorption spectra. Nitrogen adsorption-desorption isotherms were measured on a Tristar II 3020 Micromeritics system to evaluate the specific surface area and the pore size distribution using a Brunauer-Emmett-Teller method.

Electrochemical Measurements: Cathodes were prepared by mixing the active materials (I-Bi₂Se₃/S, Bi₂Se₃/S and Super P/S), Super P and PVDF binders in a weight ratio of 8:1:1 in N-methyl-2-pyrrolidone. The slurry was applied on aluminum foil and dries under vacuum at 60 °C overnight. Subsequently, the coated aluminum foil was punched into small disks (12.0 mm) with a sulfur content of about 1 mg cm⁻², and assembled into a coin unit in a glove box filled with Ar. Li foil was used as the counter electrode and Celgard 2400 membranes as separators. The electrolyte was prepared by dissolving 1.0 M lithium bis(trifluoromethanesulfonyl)imide and 0.2 M LiNO₃ in a mixture of DOL and DME with a volume ratio of 1:1. The amount of electrolyte was about 20 μL for each coin cell. For the higher sulfur loading electrodes, 3.2 mg cm⁻², 50 μL of electrolyte was added to the coin cell. Before cycling, all coin cells undergo ageing for several hours to ensure that the electrolyte fully penetrates the electrodes. Galvanostatic charge/discharge (GCD) measurements were performed with a voltage window of 1.7-2.8 V vs Li⁺/Li at different current densities using a Neware BTS4008 battery cycler. Cyclic voltammetry (CV) tests were performed on a BCS-810 battery tester from BioLogic at different scan rates in the range of 0.1-0.5 mV s⁻¹. Sinusoidal voltage with an amplitude of 10 mV in the frequency range 100 kHz to 0.01 Hz was used to measure electrochemical impedance spectroscopy (EIS).

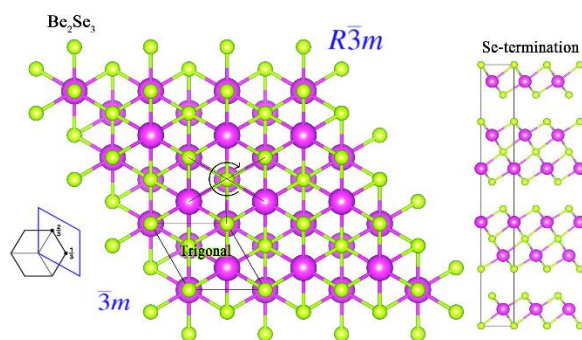
Synthesis of Li₂S₄ Solution and Adsorption Test: Sulfur and Li₂S with a molar ratio of 3:1 were dissolved in the DME and DOL solution (volume ratio of 1:1), then vigorous magnetic stirring overnight and turned to a dark brown solution. For the polysulfide absorption ability test, 20 mg of I-Bi₂Se₃, Bi₂Se₃ and Super P was immersed into a 3.0 mL mixture solution above, respectively, shaken and aged overnight.

Symmetric Cell Assembly and Measurements: Electrodes (I-Bi₂Se₃, Bi₂Se₃ and Super P) for symmetric cells were fabricated in the same way as electrodes for LSBs. Two pieces of the same electrode (average loading about 0.5 mg cm⁻²) were used as identical working and counter

electrodes. A 40 μL amount of electrolyte containing 0.5 M Li_2S_6 and 1 M LiTFSI dissolved in DOL/DME (v/v = 1:1) was added into each coin cell. CV measurements were performed at scan rate of 10 mV s^{-1} , and EIS tests were carried out in the frequency range 100 kHz to 0.01 Hz.

Measurement of Nucleation of Li_2S : Nucleation of Li_2S were studied in standard 2032 coin cells. Dispersing the same amount of I- Bi_2Se_3 , Bi_2Se_3 and Super P composites in ethanol, and then coat them in carbon paper as the cathode. Li foil was used as the counter electrode. A 20 μL amount of 0.25 M Li_2S_8 with 1.0 M LiTFSI in tetraethylene glycol dimethyl ether solution was used as catholyte, and 20 μL of a 1.0 M LiTFSI solution without Li_2S_8 was used as anolyte. Coin cells were held at 2.06 V to reduce the generation of higher order LiPS than Li_2S_4 . Then the cells were potentiostatically discharged at 2.05 V until the current decreased to 10^{-5} A.

Details of Theoretical calculations: The most important properties for Li-S batteries is the LiPS-electrode binding energy as well as the conversion free energy for LiPS on the specific surface. To explain the outstanding performance of our I-doped Be_2Se_3 material used for Li-S electrode, theoretical calculation was employed to offer an electronic-level insight of LiPS's behavior in the working state. $R\bar{3}m$ Space group XRD simulation patterns of Be_2Se_3 (mp-541837) matches the powder XRD patterns well, which was used for further theoretical calculation.



Metal exposed facet can be the most possible active facet, while non-metal element termination always offers a weaker electronic manipulation for the LiPS conversion in most cases. So according to the XRD and pre-test of DFT Bader calculation, it was confirmed that Be_2Se_3 (110) plane may be possible the active plane so that it was selected to make a further investigation. Experimental lattice parameters typically not be the minimum, in other words, the most stable state, thus the optimization for atom coordinates and cell was firstly implemented and reached less than 0.05 eV/A stress. Then a Be_2Se_3 (110) slab with 2 nm vacuum layer and I-doped slab were built and optimized with the bottom 2 layers fixed to obtain a more realistic surface

electronic structure, for the following LiPS binding energy and conversion free energy. SCAN functional with rVV10 long-distance correction was adopted in the whole energy-involved calculation because SCAN+rVV10 was determined the best combination for describing crystal parameter which in the closet agreement with experimental observation as well as accurate energy presentation exceed that PBE functional family. The other computation details are the same as our previous work.¹ 1 x 2 x 1 Monkhorst k-mesh was sampled for each slab model.

4.4 Results and discussions

Bi_2Se_3 nanosheets, assembled into flower-like structures (Figure 1a), were produced at 180 °C from a basic solution containing bismuth nitrate, sodium selenite and polyvinylpyrrolidone (see details in the experimental section in the supporting information). XRD analysis showed the nanosheets to have high crystallinity and their crystal structure to match the rhombohedral Bi_2Se_3 phase (JCPDS No. 00-033-0214, Figure 1b). HRTEM characterization confirmed the Bi_2Se_3 rhombohedral phase (space group =Pbnm) with $a=11.6230 \text{ \AA}$, $b=11.8310 \text{ \AA}$ and $c=4.0900 \text{ \AA}$ (Figure 1c). Besides, EELS chemical composition maps demonstrated a uniform distribution of both elements, Bi and Se, through the nanosheet (Figure 1d).

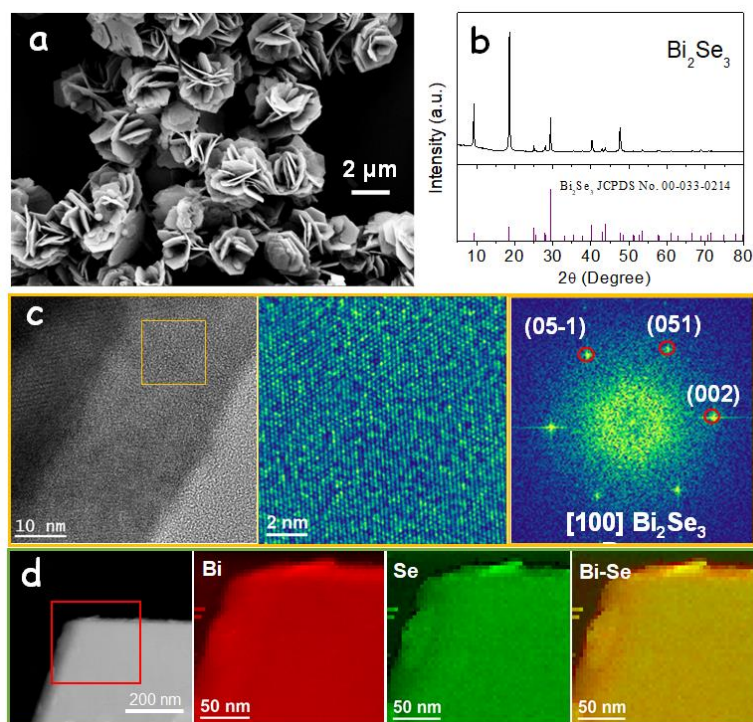


Figure 1. (a) SEM images of the Bi_2Se_3 nanosheets. (b) XRD patterns of Bi_2Se_3 nanosheets. (c) HRTEM images of the Bi_2Se_3 nanosheets and its corresponding power spectrum. (d) EELS chemical composition maps obtained from the red squared area of the STEM micrograph.

Individual Bi $N_{2,3}$ -edges at 679 eV (red), Se $L_{2,3}$ -edges at 162 eV (green) and composites of Bi-Se.

Iodine ions were incorporated to pre-synthesized Bi_2Se_3 by dispersing the Bi_2Se_3 nanosheets in an aqueous solution of potassium iodide under vigorous stirring at room temperature for 48 h. Iodine-doped Bi_2Se_3 (I- Bi_2Se_3) nanosheets preserved the flower-like morphology and the rhombohedral crystal structure of undoped Bi_2Se_3 (Figure 2a,b,d). EDX analysis quantified the iodine concentration at a 5 at%. Besides, EELS chemical composition maps displayed a homogeneous distribution of Bi, Se and I within the I- Bi_2Se_3 nanosheets (Figure 2c).

XPS was used to determine the surface composition of I- Bi_2Se_3 and the chemical environment of its elements (Figure 2e). The high-resolution Bi 4f XPS spectrum was fitted with two doublets. The lowest energy doublet was associated with Bi^{3+} within a Bi_2Se_3 chemical environment (Bi 4f_{7/2} binding energy at 157.5 eV). The highest energy doublet was associated with Bi^{3+} within a more electronegative environment, as it could be Bi_2O_3 , $\text{Bi}_2(\text{SeO}_3)_3$, Bi_2SeO_2 or another oxidized form of Bi_2Se_3 (Bi 4f_{7/2} binding energy at 158.5 eV).^[44, 45] The presence of an oxide component was related to the transportation and handling of the particles in the air. The high-resolution Se 3d XPS spectrum was also fitted with two doublets, which were associated with Se^{2-} within Bi_2Se_3 (Se 3d_{5/2} at 52.8 eV) and SeO_2 , $\text{Bi}_2(\text{SeO}_3)_3$, Bi_2SeO_2 or another form of Se within a more electronegative environment (Se 3d_{5/2} at 53.7 eV), related to the partial oxidation of the material surface.^[42,44] The high resolution I 3d XPS spectrum was fitted with two peaks, at 618.5 eV (I 3d_{5/2}) and 630 eV (3d_{3/2}), which were associated with an I^{-1} chemical state.^[46]

The electrical conductivity of both Bi_2Se_3 and I- Bi_2Se_3 samples decreased with temperature, implying a degenerated semiconductor behavior (Figure 2f). Besides, the Seebeck coefficient of both samples was negative in the whole temperature range, implying an n-type conductivity. With the introduction of iodine, a twofold increase of the Bi_2Se_3 electrical conductivity was measured. The rise of the electrical conductivity was correlated with a decrease of the absolute value of the Seebeck coefficient, which is consistent with an increase of the charge carrier concentration with the iodine doping.

Sulfur was introduced via a melt-diffusion process (see details in the experimental section).^[5,33] The morphology of the I- Bi_2Se_3 /S composite resembled that of the original I- Bi_2Se_3 nanosheets assembled into flowers (Figure 2g). EDX elemental maps displayed a homogeneous distribution of the four elements, I, Bi, Se and S, within the composite (Figure 2g), with no independent sulfur particle. Upon sulfur incorporation, the nitrogen adsorption-desorption

isotherms showed the Brunauer–Emmett–Teller (BET) specific surface area to be reduced from $128.6 \text{ m}^2 \text{ g}^{-1}$ for I-Bi₂Se₃ to $13.2 \text{ m}^2 \text{ g}^{-1}$ for I-Bi₂Se₃/S (Figure 3a). Besides, the pore volume of I-Bi₂Se₃, decreased from $0.5 \text{ cm}^3 \text{ g}^{-1}$, to $0.026 \text{ cm}^3 \text{ g}^{-1}$ with the incorporation of sulfur, which further demonstrated the successful loading of sulfur within the pore structure of the assembled I-Bi₂Se₃ nanosheets. The loaded mass of sulfur was quantified at *ca.* 70.2 wt% using thermogravimetry analysis (TGA, Figure 3b).

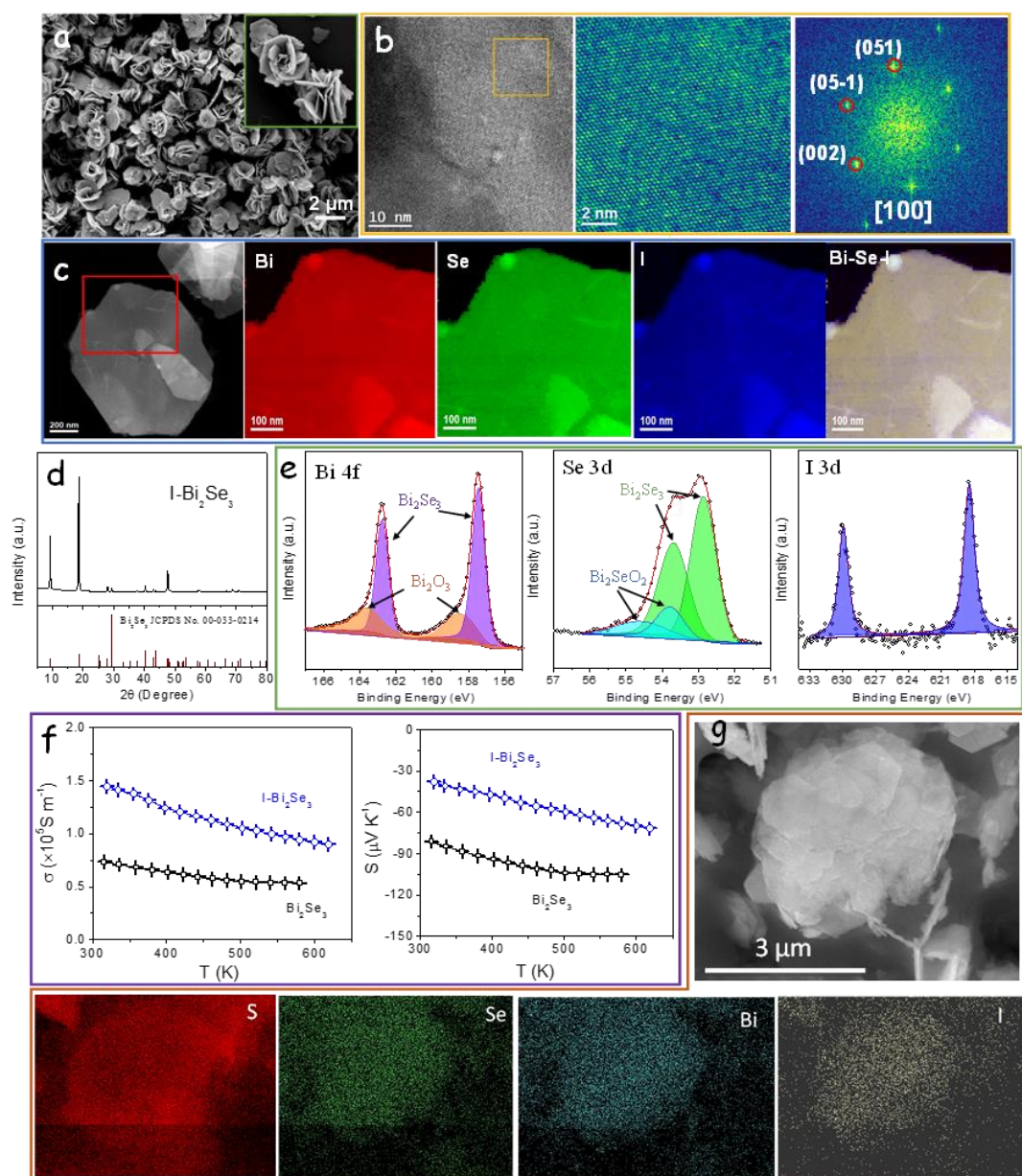


Figure 2. Characterization of I-Bi₂Se₃ nanosheets: (a) SEM image. (b) HRTEM image and its corresponding power spectrum. (c) EELS chemical composition maps obtained from the red squared area of the STEM micrograph. Individual Bi N_{6,7}-edges at 157 eV (red), Se M₁-edge at 232 eV (green), I M_{4,5}-edge 619 eV (blue) and composite of Bi-Se-I. (d) XRD pattern. (e) Bi 4f, Se 3d and I 3d high-resolution XPS spectra. (f) Temperature dependence of the electrical

conductivity (σ) and Seebeck coefficient (S) of Bi_2Se_3 and $\text{I-Bi}_2\text{Se}_3$. (g) SEM image EDX elemental maps of $\text{I-Bi}_2\text{Se}_3/\text{S}$ composite.

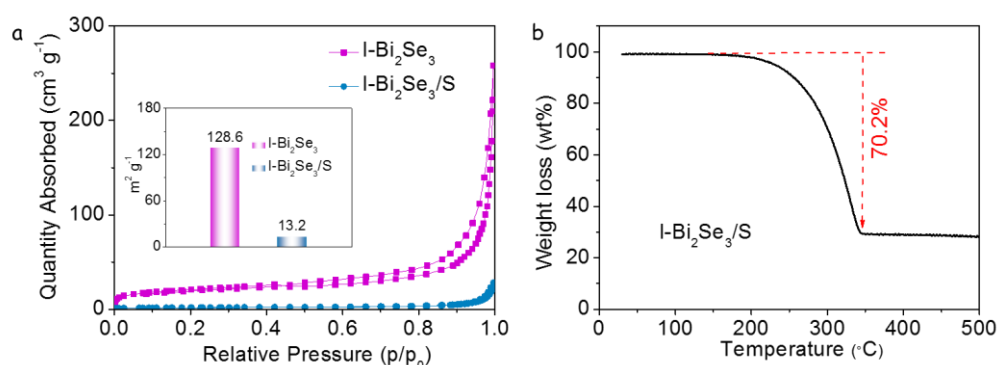


Figure 3. (a) Nitrogen adsorption-desorption isotherms of as synthesized $\text{I-Bi}_2\text{Se}_3$ and $\text{I-Bi}_2\text{Se}_3/\text{S}$ composites. (b) TGA curve of $\text{I-Bi}_2\text{Se}_3/\text{S}$ composite measured in N_2 with a sulfur loading ratio of 70.2 wt%.

The interaction between $\text{I-Bi}_2\text{Se}_3$ and LiPS was analyzed using Li_2S_4 adsorption tests (see details in experimental section). Figure 4a,b displays an optical image and the UV-vis spectra of several flasks that contain 3 mL of a 0.01 M Li_2S_4 solution and the exact same amount (20 mg) of each of the tested adsorbers, Super P, Bi_2Se_3 or $\text{I-Bi}_2\text{Se}_3$, after overnight ageing. We observe that the color of the Li_2S_4 solution, and the absorbance intensity in the 400–500 nm region associated with Li_2S_4 , was almost unchanged in the presence of Super P. On the contrary, the color of the Li_2S_4 solutions and the visible absorbance became much lighter in the presence of Bi_2Se_3 and especially $\text{I-Bi}_2\text{Se}_3$, suggesting a strong chemical interaction of LiPS with Bi_2Se_3 and particularly with $\text{I-Bi}_2\text{Se}_3$. $\text{I-Bi}_2\text{Se}_3$ exhibited the clearest solution and the lowest visible absorption, indicating the presence of the lowest amount of Li_2S_4 in the solution and thus the greatest LiPS adsorbability.

Figure 4c displays the high-resolution Bi 4f XPS spectra of $\text{I-Bi}_2\text{Se}_3$ before and after the Li_2S_4 adsorption test. Compared with the original spectra of $\text{I-Bi}_2\text{Se}_3$, the Bi 4f binding energies in $\text{I-Bi}_2\text{Se}_3\text{-Li}_2\text{S}_4$ shifted to lower values, revealing the interaction of S with surface Bi.^[5]

Density functional theory (DFT) calculations were carried out to further evaluate the interaction between LiPS and $\text{I-Bi}_2\text{Se}_3$. The optimized LiPS adsorption configuration at six different lithiation stages (Li_2S , Li_2S_2 , Li_2S_4 , Li_2S_6 , Li_2S_8 and S_8) on the Bi_2Se_3 and $\text{I-Bi}_2\text{Se}_3$ surfaces are displayed in Figures 5 and 6. DFT calculations showed the binding energies (E_b) of LiPS species at the six tested lithiation stages to be higher on $\text{I-Bi}_2\text{Se}_3$ than on Bi_2Se_3 (Figure 4e). Figure 4d displays the relaxed adsorption structure of Li_2S_4 on the (110) surface of Bi_2Se_3

and I-Bi₂Se₃, respectively. The calculated E_b for the relaxed configuration of Li₂S₄ adsorbed on Bi₂Se₃ (110) and I-Bi₂Se₃ (110) surfaces are -1.27 eV and -2.09 eV, respectively. These DFT results demonstrate a strong interaction between S within LiPS and Bi within Bi₂Se₃, which corroborates the sulfiphilic character of Bi₂Se₃. These results also demonstrate that the presence of I on the Bi₂Se₃ surface further increases the absolute value of the binding energy, thus favoring LiPS adsorption and hence potentially reducing the shuttle effect.

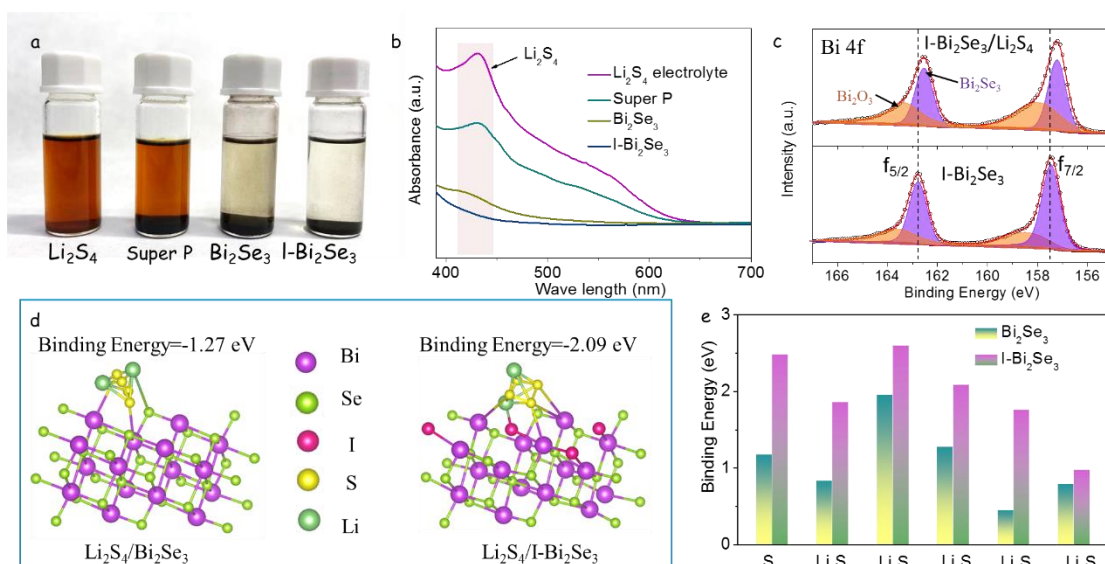


Figure 4. (a) Optical photograph of flasks containing 3 mL of a 0.01 M Li₂S₄ solution and 20 mg of Super P, Bi₂Se₃ or I-Bi₂Se₃ after overnight ageing. (b) UV-vis spectra of the supernatants. (c) Bi 4f XPS spectra of I-Bi₂Se₃ before and after Li₂S₄ adsorption. (d) Optimized geometrical configurations of Li₂S₄ on Bi₂Se₃ and I-Bi₂Se₃ surfaces. (e) Calculated binding energies of LiPS (Li₂S, Li₂S₂, Li₂S₄, Li₂S₆, Li₂S₈ and S₈) on Bi₂Se₃ and I-Bi₂Se₃ surfaces.

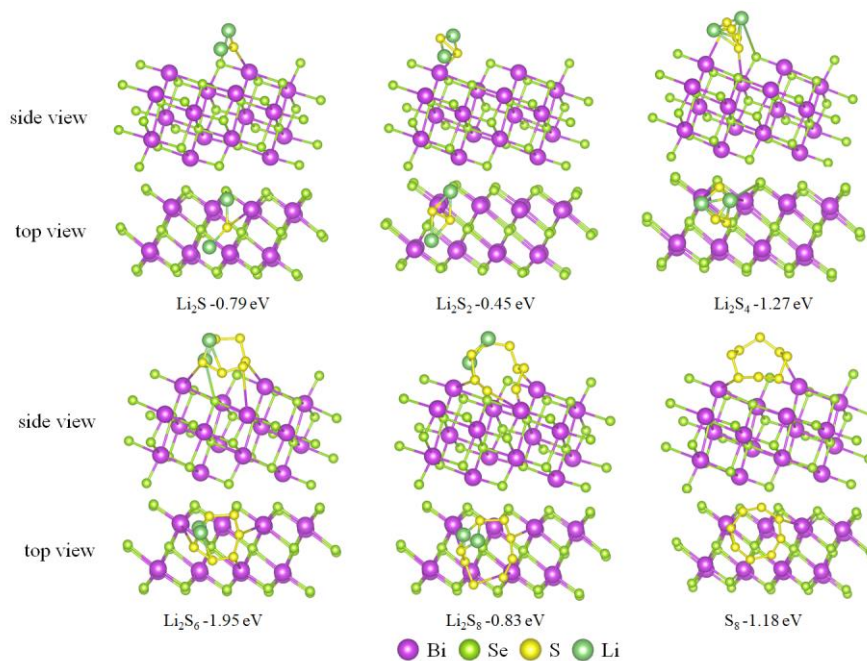


Figure 5. DFT calculation results of optimized geometrical configurations of the surface (110) of Bi_2Se_3 with LiPS (Li_2S , Li_2S_2 , Li_2S_4 , Li_2S_6 , Li_2S_8 and S_8).

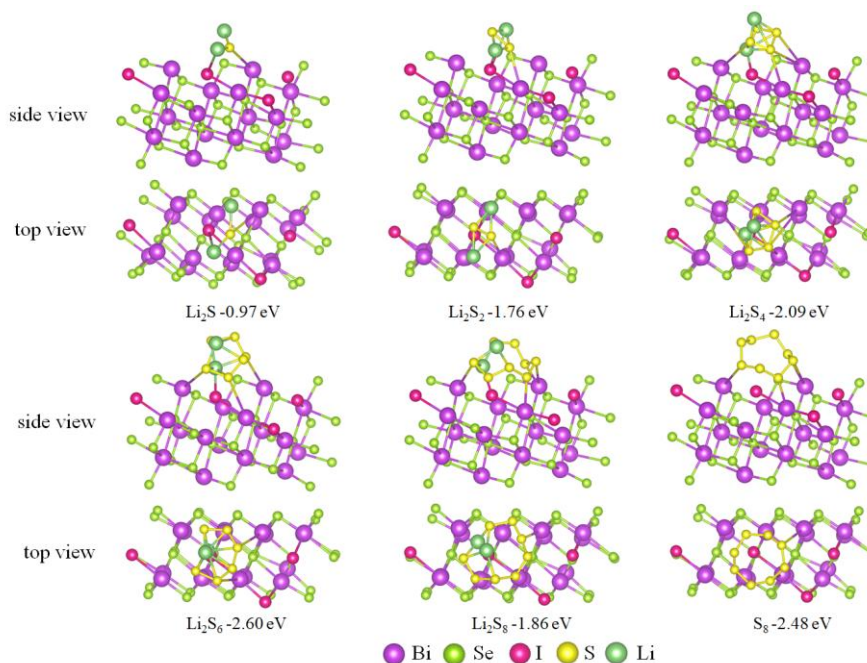


Figure 6. DFT calculation results of optimized geometrical configurations of the surface (110) of $\text{I-Bi}_2\text{Se}_3$ with LiPS (Li_2S , Li_2S_2 , Li_2S_4 , Li_2S_6 , Li_2S_8 and S_8).

Figure 7a displays the band structure and DOS of Bi_2Se_3 and $\text{I-Bi}_2\text{Se}_3$. Calculations show $\text{I-Bi}_2\text{Se}_3$ to be characterized by a significantly smaller bandgap than Bi_2Se_3 . Besides, consistently with results from electrical transport measurements, DFT calculations show the presence of

iodine to upward shift the Fermi level, which appears lying within the I-Bi₂Se₃ conduction band thus promoting the intrinsic conductivity and degenerated/metallic character of I-Bi₂Se₃.^[47]

Figure 7b and Figure 8 exhibit the initial state, transition state and final state of Li₂S decomposition on Bi₂Se₃ and I-Bi₂Se₃. The calculated energy barrier for Li₂S decomposition on Bi₂Se₃ and I-Bi₂Se₃ surfaces was 0.56 and 0.98 eV, respectively (Figure 2g). These results demonstrate that I-Bi₂Se₃ can greatly reduce the Li₂S decomposition energy barrier and enhance the redox reversibility between Li₂S and LiPS.

The S reduction pathways on both Bi₂Se₃/S and I-Bi₂Se₃/S cathodes were calculated considering the overall reversible reaction between Li₂S and S₈ + Li. The first step of the discharge process involves the reduction of S₈ with two Li⁺ to form Li₂S₈. Subsequently, Li₂S₈ undergoes further reduction to three intermediate LiPS, Li₂S₆, Li₂S₄, Li₂S₂ and finally Li₂S as the end product. Figure 7c displays the optimized configuration of the intermediates and their Gibbs free energy profiles. For both materials, Bi₂Se₃/S and I-Bi₂Se₃/S, the largest increase of Gibbs free energy was obtained for the conversion from Li₂S₂ to Li₂S, suggesting this step as the rate-limiting for the discharge process.^[48] The free energy increase of this step was lower for I-Bi₂Se₃ (0.71 eV) than for Bi₂Se₃ (0.89 eV), suggesting that the reduction of S was more thermodynamically favorable on I-Bi₂Se₃ than on Bi₂Se₃.

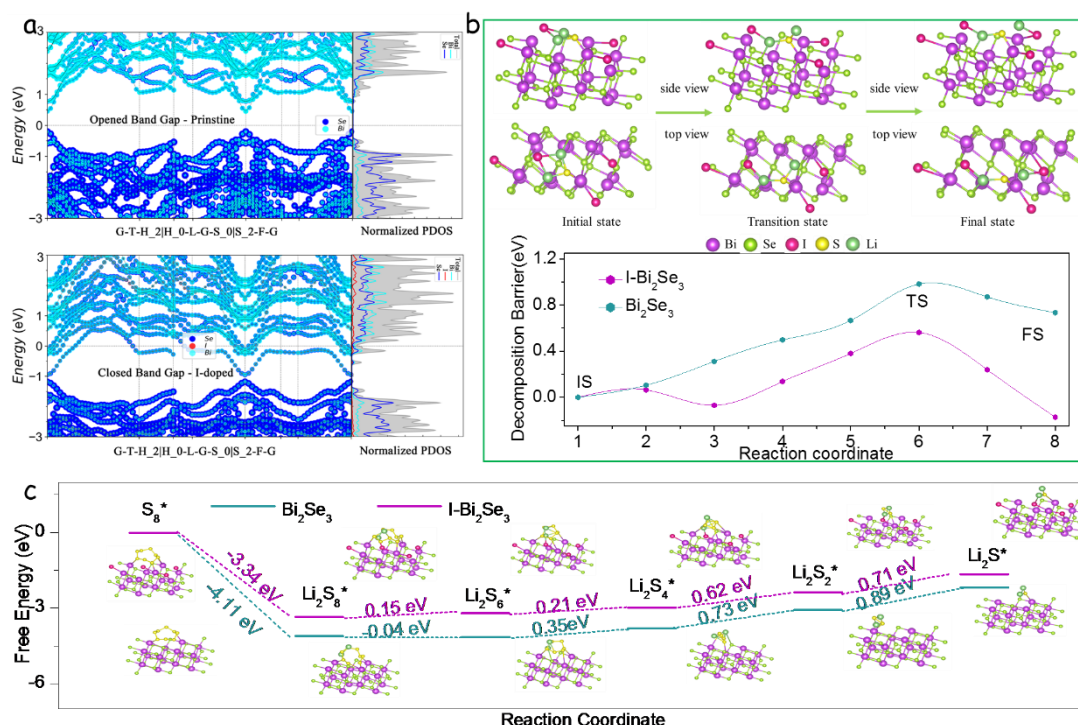


Figure 7. (a) HSE06 band structure and density of states of Bi₂Se₃ and I-Bi₂Se₃. (b) Optimized adsorption configuration for the Li₂S decomposition on I-Bi₂Se₃ and energy barrier profiles of Li₂S cluster decomposition on Bi₂Se₃ and I-Bi₂Se₃ along with different reaction coordinates.

(c) Gibbs free energy profiles and optimized adsorption conformation of LiPS species on Bi_2Se_3 and $\text{I-Bi}_2\text{Se}_3$, showing a much lower reaction free energy from Li_2S_2 to Li_2S on $\text{I-Bi}_2\text{Se}_3$ than on Bi_2Se_3 .

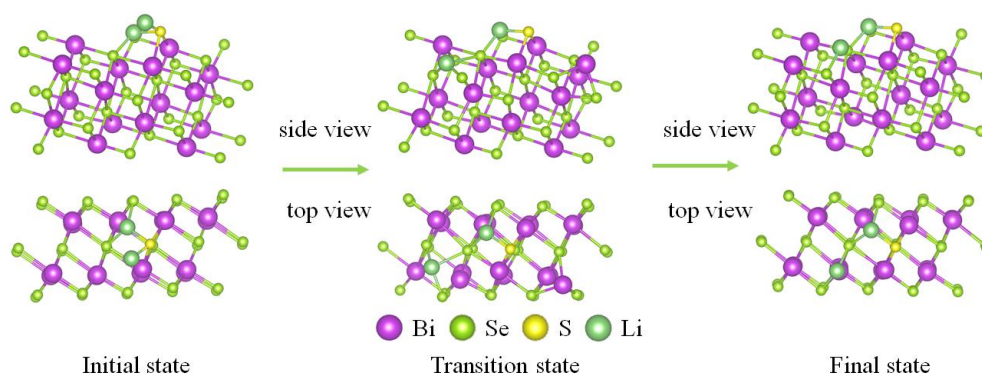


Figure 8. The optimized adsorption configuration of Li_2S decomposition on Bi_2Se_3 .

The electrochemical performance of Li-S coin cells containing an $\text{I-Bi}_2\text{Se}_3/\text{S}$ cathode was evaluated and compared with that of cells based on $\text{Bi}_2\text{Se}_3/\text{S}$ and Super P/S cathodes. Figure 9a displays the CV curves obtained at 0.1 mV s^{-1} . All cathodes displayed two well-defined cathodic peaks associated with the reduction of solid-state S into soluble long-chain LiPS (Li_2S_x , $4 < x < 8$, peak C1) and the subsequent conversion of these LiPS to insoluble $\text{Li}_2\text{S}_2/\text{Li}_2\text{S}$ (peak C2).^[3] Besides, an anodic peak is observed (peak A), corresponding to the reverse oxidation conversion from Li_2S to LiPS and ultimately to S.^[33] The peak current density of the reduction and oxidation peaks of $\text{I-Bi}_2\text{Se}_3/\text{S}$ was clearly higher than that of the two reference cathodes, all containing the same amount of sulfur, thus suggesting a higher sulfur utilization in the $\text{I-Bi}_2\text{Se}_3/\text{S}$ cathode. The C2 peak of the $\text{I-Bi}_2\text{Se}_3/\text{S}$ cathode at about 2.042 V shows a much larger current density and is slightly shifted to a higher potential compared with the other cathodes, suggesting a promoted conversion of LiPS to insoluble $\text{Li}_2\text{S}_2/\text{Li}_2\text{S}$ within the $\text{I-Bi}_2\text{Se}_3/\text{S}$ cathode. Besides, the A oxidation peak of $\text{I-Bi}_2\text{Se}_3/\text{S}$ is shifted to a lower potential, 2.33 V, and displays a larger current density, indicating an enhanced Li_2S decomposition (Figure 9a,b).

The onset potentials at a current density of $10 \mu\text{A cm}^{-2}$ beyond the baseline current were used to quantitatively estimate the electrocatalytic activity (Figure 9b and Figure 10).^[23] Cells based on $\text{I-Bi}_2\text{Se}_3/\text{S}$ cathodes showed the highest onset potentials of cathodic peaks and the lowest onset potentials for the anodic peak, which further demonstrates the accelerated redox kinetics obtained with the I-doped Bi_2Se_3 nanosheets. Figure 11 displays the first five CV cycles measured from $\text{I-Bi}_2\text{Se}_3/\text{S}$ cells. All CV curves almost overlapped, which suggests excellent reversibility of the sulfur redox reactions.

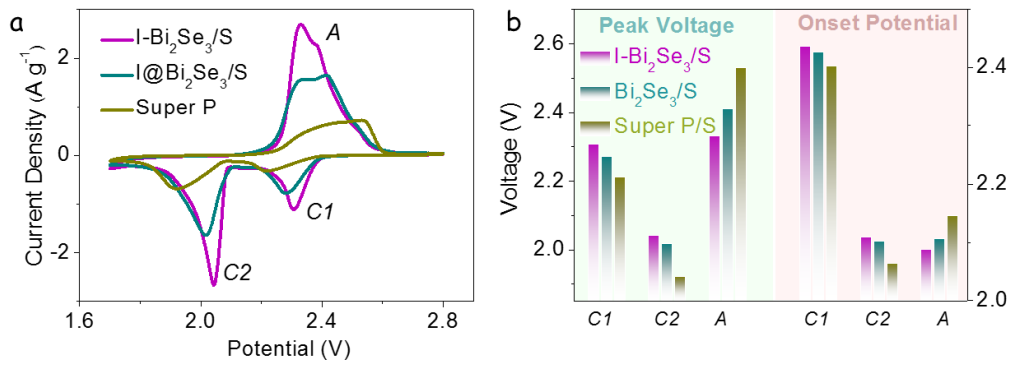


Figure 9. (a) CV profiles of Li-S cells with I-Bi₂Se₃/S, Bi₂Se₃/S and Super/S cathodes at a 0.1 mV s⁻¹ scan rate. (b) Peak potential and onset potential of asymmetrical Li-S cells obtained from CV curves.

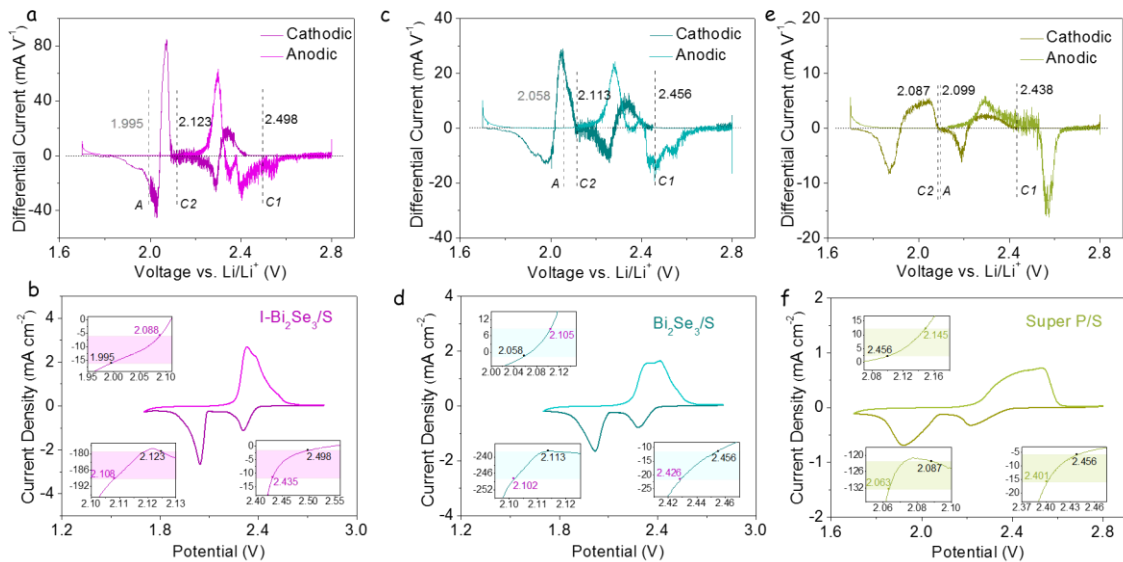


Figure 10. Differential CV curves of (a) I-Bi₂Se₃/S, (c) Bi₂Se₃/S and (e) Super P/S. The baseline voltage and current density are defined as the value before the redox peak, where the variation on current density is the smallest, named as $dI/dV=0$. The value of the baseline voltages for cathodic peak C1, C2 and anodic peak A were calculated, respectively. CV curves and corresponding onset potentials of redox peak C1, C2, and A (inset): (b) I-Bi₂Se₃/S, (d) Bi₂Se₃/S and (f) Super P/S. Following a common definition employed in electrocatalysis, the onset potential is determined when the current density is 10 $\mu\text{A cm}^{-2}$ beyond the corresponding baseline current density (more specifically, 10 $\mu\text{A cm}^{-2}$ more negative than baseline current density for cathodic peaks or 10 $\mu\text{A cm}^{-2}$ positive than baseline current density for anodic peaks). As shown in the inset of b, d, and f, the baseline voltages are the same as in a, c, and e while the colored region indicates the gap in current density.

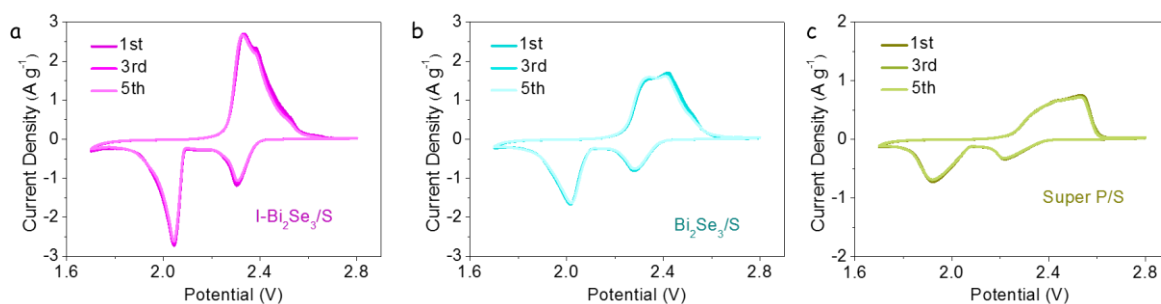


Figure 11. First five cycles of CV curves of (a) I-Bi₂Se₃/S, (b) Bi₂Se₃/S and (c) Super P/S performed at a scan rate of 0.1 mV s⁻¹.

CV tests at different scan rates in the range 0.1-0.5 mV s⁻¹ were conducted to investigate the reaction kinetics and the lithium-ion diffusion properties of I-Bi₂Se₃/S (Figure 12a). The peak current density of the I-Bi₂Se₃/S cathode increases with the scan rate, and its shape is maintained, which denotes good electrochemical stability. In contrast, Bi₂Se₃/S and especially Super P/S cathodes display more remarkable changes in the CV curve when increasing the scan rate, denoting limited reaction kinetics (Figure 12b,c).

I-Bi₂Se₃/S cathodes exhibited a linear relationship between the cathodic and anodic peak currents and the square root of the scanning rate, as it corresponds to a diffusion-limited process (Figure 13a-c). From the fitting of this linear dependence, the diffusion constant of the rate-limiting species, *i.e.* D_{Li^+} , was calculated according to the Randles-Sevcik equation:^[5]

$$I_p = (2.69 * 10^5)n^{1.5}AD_{Li^+}^{0.5}C_{Li^+}v^{0.5} \quad (1)$$

where I_p is the peak current density, n is the number of charges transferred, A is the geometric area of the electrode, C_{Li^+} is the concentration of lithium ions in the cathode, and v is the scan rate. I-Bi₂Se₃/S electrodes displayed the sharpest I_p vs $v^{0.5}$ slopes, indicating the fastest lithium-ion diffusion in both the reduction and oxidation processes. According to the Randles-Sevcik equation, the values of D_{Li^+} calculated for I-Bi₂Se₃/S at peaks C1, C2 and A were 2.3×10^{-7} , 3.7×10^{-7} , and 5.9×10^{-7} cm² s⁻¹, respectively. All these values were well above those obtained for Bi₂Se₃/S and Super P/S electrodes (Figure 13d). Taking into account the similar morphology of I-Bi₂Se₃ and Bi₂Se₃, the enhanced lithium-ion diffusivities must be related to the improved catalytic activity of the former, which accelerates the LiPS conversion, and to the stronger LiPS adsorption that suppresses the shuttle effect and prevents the deposition of an insulating layer at the anode side.^[49]

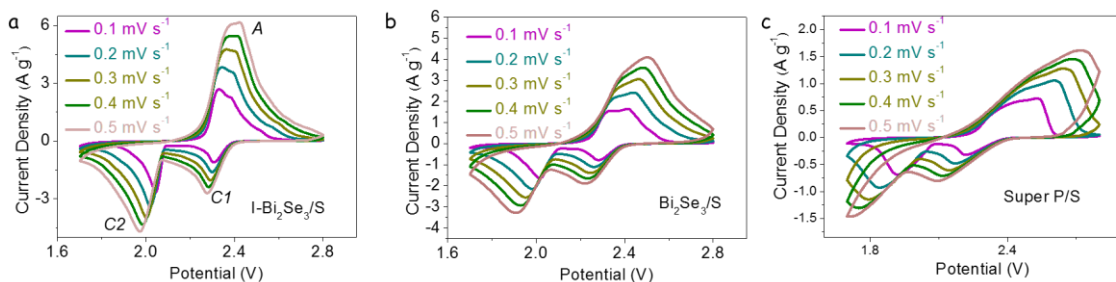


Figure 12. LiPS adsorption ability. (a) Optical photograph of the flask containing a Li_2S_4 solution and the different adsorbents (as indicated in the image) after 12h adsorption tests. (b) UV-Vis spectrum of the polysulfide solution after exposure to the different adsorbents. (c) N 1s and (d) Nb 3d XPS spectrum of $\text{C}_2\text{N}@\text{NbSe}_2$ before and after adsorption of Li_2S_4 .

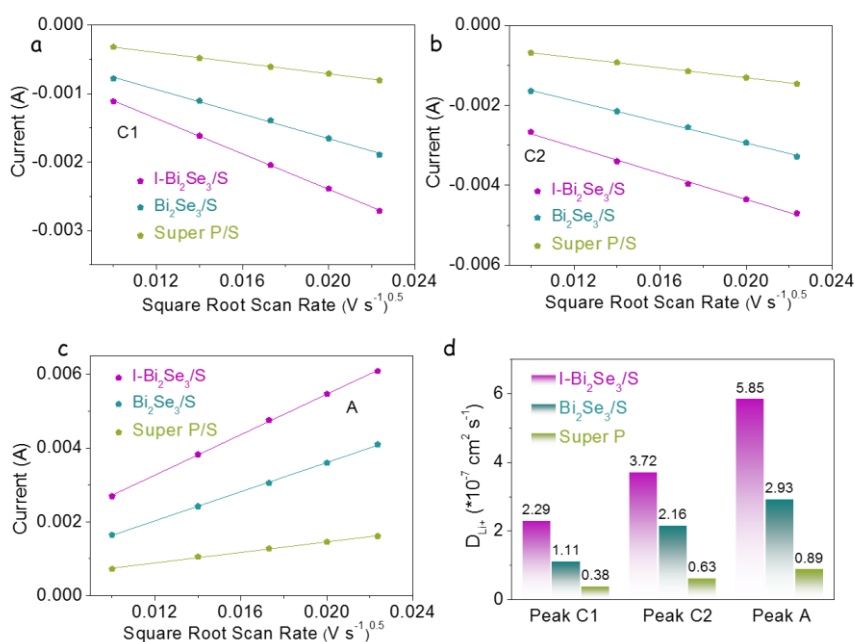


Figure 13. (a-c) Peak current vs the square root of the scan rate (v) for the cathodic reduction processes (C1, C2) and anodic oxidation process (A) in Li-S cells with different electrodes. (d) Li^+ diffusion coefficient calculated from the CV redox peaks according to the Randles-Sevcik equation.

To further analyse the electrocatalytic activity of the different materials toward the polysulfide conversion, CV profiles were measured on symmetric cells within the voltage window -1.0 to 1.0 V and using a 0.5 M Li_2S_6 electrolyte (Figure 14a).^[5,33] To eliminate the capacitive contribution, the CV curve of I- Bi_2Se_3 in a Li_2S_6 -free electrolyte was also measured as a reference (Figure 14b). The CV curve of the symmetric cells with a Li_2S_6 -free electrolyte delivered a low current, well below that of CV curves of all symmetric cells having Li_2S_6 in

their electrolyte, which indicates that the lithiation/delithiation reactions dominate the current response.^[50] Besides, the I-Bi₂Se₃ symmetric cells including Li₂S₆ additive exhibited a much higher current density than those of Bi₂Se₃ and Super P cells, which we associate with an enhanced polysulfide absorption and a higher catalytic activity.

The Li₂S nucleation and dissolution processes were analysed to investigate the liquid-solid reaction kinetics. Compared with the Bi₂Se₃ cathode, the I-Bi₂Se₃ cathode exhibited significantly shorter nucleation and growth times and a higher discharging peak current during the potentiostatic measurement at 2.05 V (Figure 14c). Based on Faraday's law, the capacity of the I-Bi₂Se₃ electrode was calculated at 287.5 mAh g⁻¹, well above that of the Bi₂Se₃ electrode, 206.8 mAh g⁻¹.^[51] Taking into account the similar morphology and crystal structure of the two materials, the significant differences obtained must be ascribed to the effect of iodine doping, which significantly improves the Li₂S precipitation kinetics.

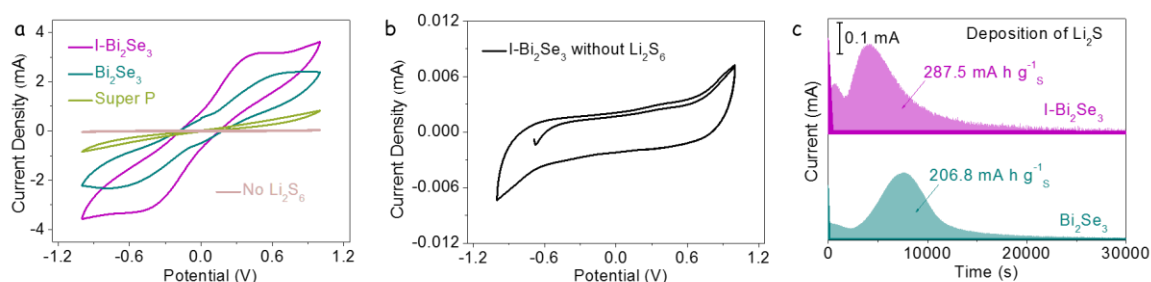


Figure 14. (a) CV curves of symmetric cells at a scan rate of 20 mV s⁻¹. (b) The CV curve of I-Bi₂Se₃ as electrode measured in symmetric coin cell using an electrolyte without Li₂S₆. (c) Potentiostatic discharge profile at 2.05 V on different electrodes with Li₂S₈ catholyte for evaluating the nucleation kinetics of Li₂S.

The galvanostatic charge/discharge curves of I-Bi₂Se₃/S, Bi₂Se₃/S and Super P/S electrodes at a current density of 0.1 C (1672 mA g⁻¹) are shown in Figure 15a. Charge/discharge curves display two discharge plateaus and one charge plateau, consistently with CV curves. The first discharge plateau at around 2.3 V is related to the reduction of sulfur to soluble LiPS (S₈ → S₆²⁻ → S₄²⁻).^[52] The second discharge plateau corresponds to the conversion of soluble LiPS to lithium sulfide (S₄ → Li₂S₂ → Li₂S) at about 2.1 V.^[53] The voltage difference between the oxidation and the second reduction plateaus is considered as the, ΔE .^[54] Among the tested materials, I-Bi₂Se₃/S showed the lowest ΔE , at 131 mV, well below that of Bi₂Se₃/S, 162 mV, and Super P/S, 205 mV (Figure 15b).

Q1 and Q2 are defined as the capacity of the first and the second discharge plateaus, respectively. Q1 measures the amount of soluble polysulfides created and potentially diffusing to the Li metal anode. Q2 measures how efficiently the created polysulfides are reduced to Li_2S . Thus the ratio $Q2/Q1$ can be used as a measure of the catalytic activity for LiPS conversion reaction.^[55] The $Q2/Q1$ ratio for I- $\text{Bi}_2\text{Se}_3/\text{S}$ was 2.71, close to the theoretical limit of 3, and well above the values obtained from $\text{Bi}_2\text{Se}_3/\text{S}$ and Super P/S, 2.23 and 1.85, respectively (Figure 15b). The high $Q2/Q1$ ratio of I- $\text{Bi}_2\text{Se}_3/\text{S}$ implies a high catalytic activity toward polysulfide's redox reaction.

The charge and discharge profiles of the different electrodes displayed in Figure 15c,d show the I- $\text{Bi}_2\text{Se}_3/\text{S}$ electrode to be characterized by significantly lower overpotentials for phase conversion between soluble LiPS and insoluble $\text{Li}_2\text{S}_2/\text{Li}_2\text{S}$, which further demonstrates the enhanced electrochemical kinetics of I- $\text{Bi}_2\text{Se}_3/\text{S}$.^[56]

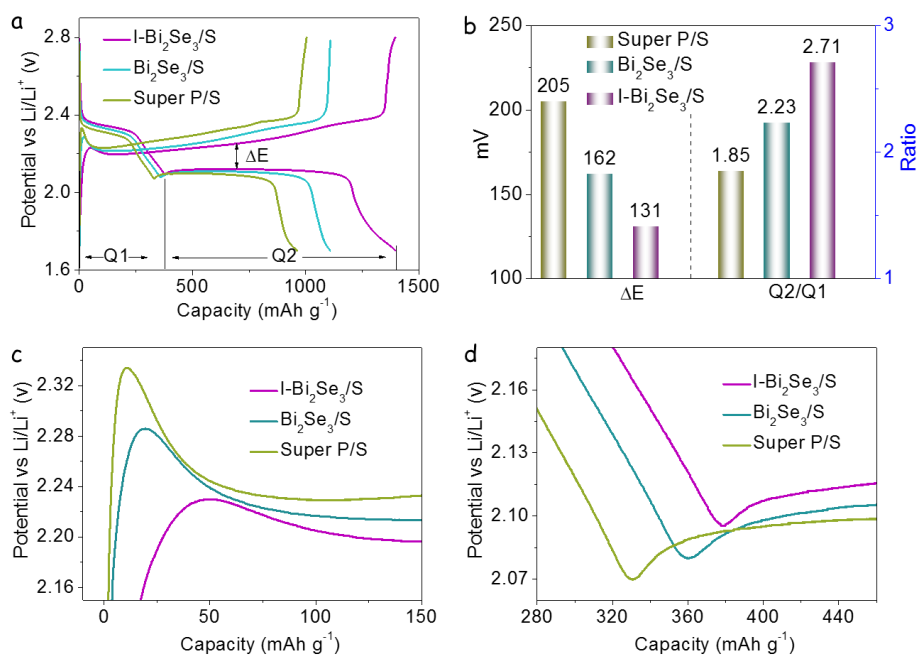


Figure 15. (a) Galvanostatic charge/discharge profiles of I- $\text{Bi}_2\text{Se}_3/\text{S}$, $\text{Bi}_2\text{Se}_3/\text{S}$ and Super/S electrodes at a 0.1 C current rate. (b) ΔE and $Q2/Q1$ obtained from the charge/discharge curves. (c) Charge, and (d) discharge profiles of I- $\text{Bi}_2\text{Se}_3/\text{S}$, $\text{Bi}_2\text{Se}_3/\text{S}$, and Super P/S electrodes showing the overpotentials for conversion between soluble LiPS and insoluble $\text{Li}_2\text{S}_2/\text{Li}_2\text{S}$.

The galvanostatic charge/discharge voltage profiles of I- $\text{Bi}_2\text{Se}_3/\text{S}$ electrodes at various current densities, from 1.0 C to 4 C, are shown in Figure 16a. Two discharge plateaus and one charge plateau were maintained even at the highest current rates tested, which is in contrast with the results obtained from Super P/S electrodes (Figure 16b,c). An outstanding initial specific capacity of 1496 mAh g^{-1} was measured from the I- $\text{Bi}_2\text{Se}_3/\text{S}$ electrode. Additionally, this

electrode demonstrated a superior rate performance, with average discharge capacities of 1361, 1168, 1002, 897, 795 and 651 mAh g⁻¹ at current rates from 0.1 C to 4 C, respectively (Figure 16d). Even when the current density was returned to 0.2 C, the specific capacity of the I-Bi₂Se₃/S electrode was recovered to 1138 mAh g⁻¹, suggesting high stability even after the high rate charge/discharge process. All these values were clearly above those obtained from Bi₂Se₃/S and Super P/S electrodes.

Among the tested materials, the cells based on I-Bi₂Se₃/S were also characterized by the highest energy efficiencies (Figure 16e), as calculated from $E = \int UIdt$.^[57] I-Bi₂Se₃/S based cells displayed an energy efficiency of 89.7% at 4 C, higher than Bi₂Se₃/S (85.7%) and Super P/S (66.1%) cells. The high energy efficiency measured for I-Bi₂Se₃/S was consistent with the lower ΔE and higher catalytic properties of I-Bi₂Se₃.

Figure 16f shows the cycling performance of the different cathodes. In this test, the first three cycles were measured at a current density of 0.1C, and then 100 cycles were tested at a current density of 0.2C. The three electrodes showed a notably stable cycling performance during 100 cycles, with a coulombic efficiency (CE) above 99%. At 0.2C, I-Bi₂Se₃/S electrodes displayed a high initial specific capacity (1274 mAh g⁻¹), well above that of Bi₂Se₃/S (1045 mAh g⁻¹), and Super P/S (727 mAh g⁻¹). After 100 cycles, 97.7% of the initial capacity was still retained for the I-Bi₂Se₃/S electrodes (1245 mAh g⁻¹). In contrast, the Bi₂Se₃/S cathode maintained just an 84.4% (882 mAh g⁻¹) of the initial discharge capacity, and the Super P/S cathode preserved just a 69.6% (506 mAh g⁻¹) of the initial capacity. The capacity loss in these cathodes was mainly associated with the dissolution of polysulfides into the electrolyte. Thus the high cycling stability of I-Bi₂Se₃/S was related to the effective inhibition of this dissolution.

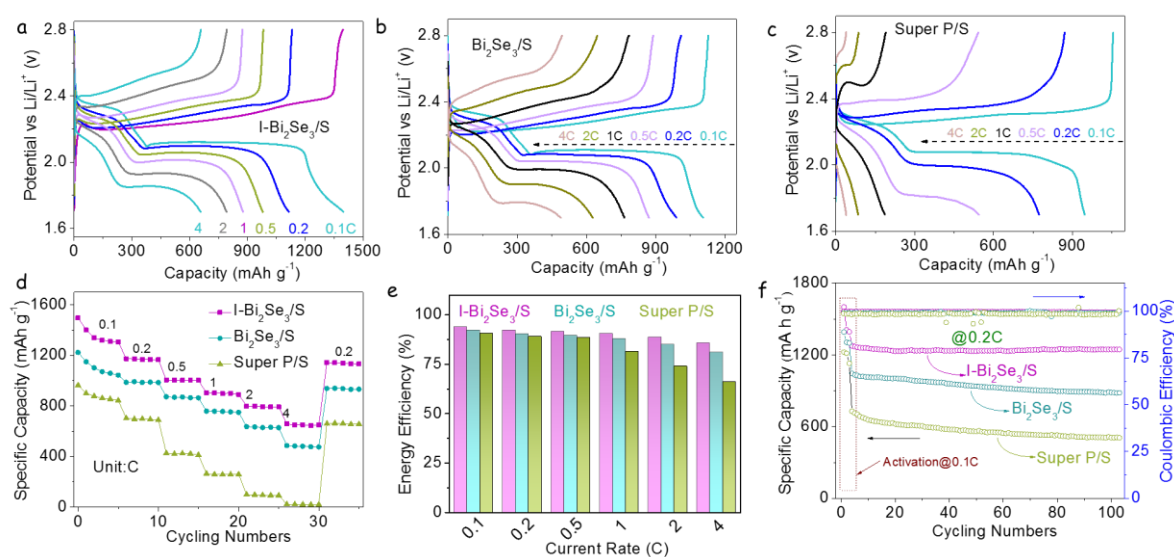


Figure 16. Galvanostatic charge–discharge profiles of (a) I-Bi₂Se₃/S, (b) Bi₂Se₃/S and (c) Super P/S electrodes at different current densities range from 0.1C to 4C. (d) Rate capability of different electrodes at various C rates, from 0.1 C to 4 C. (e) Energy efficiency of different cathodes at different current rates. (f) Cycling performances of I-Bi₂Se₃/S, Bi₂Se₃/S, and Super/S electrodes at 0.2 C.

Electrochemical impedance spectroscopy (EIS) was used to gain understanding of the parameters behind the enhanced redox kinetics of I-Bi₂Se₃/S electrodes. Figure 17 displays the Nyquist plots of the EIS data obtained from I-Bi₂Se₃/S, Bi₂Se₃/S and Super P/S coin cells before and after cycling. The fresh electrodes displayed a semicircle in the high-frequency region associated with the charge-transfer resistance (R_{ct}), followed by a linear dependence in the low-frequency region that is related to the diffusion of lithium ions.^[58] After charge/discharge loops, an additional semicircle appeared in the high-frequency range, which is associated with the deposition of the insulating discharge products of Li₂S on the electrode surface (R_{in}) during cycling. Based on the equivalent circuit displayed in Figure 17,^[59] the I-Bi₂Se₃/S electrode has a considerably lower R_{in} and R_{ct} compared with Bi₂Se₃/S and Super P/S electrodes. These lower resistances indicate that the I-Bi₂Se₃/S electrode is characterized by a faster polysulfide conversion reaction, as well as a faster charge transfer kinetics during lithiation/delithiation reaction.

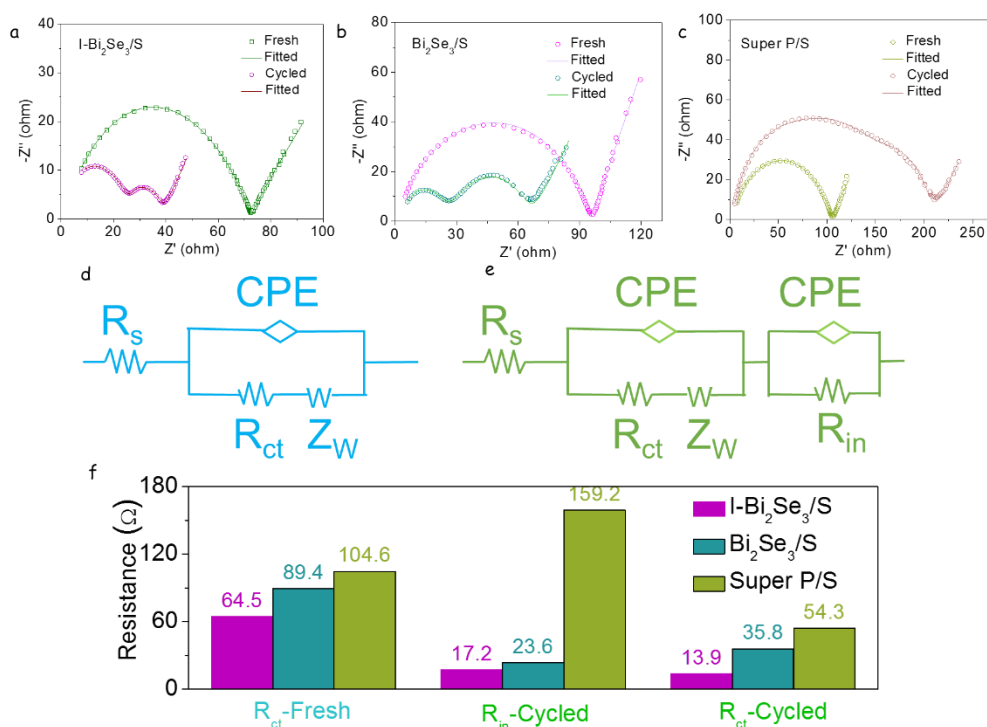


Figure 17. (a) EIS spectrum of the I-Bi₂Se₃/S electrode after and before cycling. (b,c) EIS spectra of (b) Bi₂Se₃/S and (c) Super P/S coin cells before and after cycling. The solid line corresponding to the fitting result from the equivalent circuit (d) and (e), and the R_s, R_{in}, R_{ct}, and Z_w stand for the resistance of the electrolyte, insoluble Li₂S₂/Li₂S layer, interfacial charge-transportation, and semi-infinite Warburg diffusion, respectively; and CPE stands for the corresponding capacitance. (f) Different resistances of three coin cells were obtained from the equivalent circuit.

Even at a high current rate of 1C, I-Bi₂Se₃/S electrodes displayed a high specific capacity and stable cycling performance, with an average 0.012% capacity decay per cycle after 1000 cycles and CEs above 99.6%. The performance of I-Bi₂Se₃/S electrodes in this direction was also clearly above that of Bi₂Se₃/S and Super P/S (Figure 18).

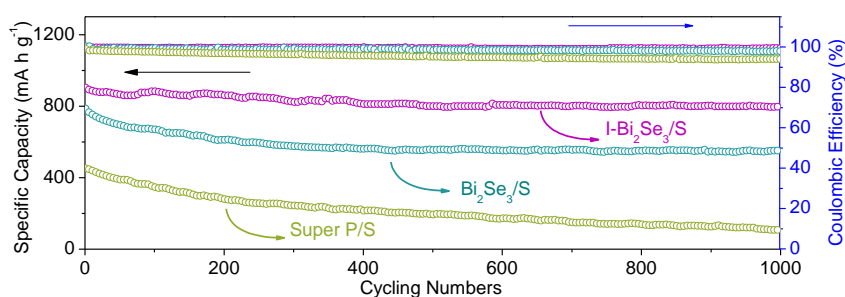


Figure 18. Cycling performance and coulombic efficiency of the three cathodes at a current rate of 1 C.

I-Bi₂Se₃ electrodes were further tested with a high sulfur loading (5.2 mg cm⁻²) and a lean electrolyte (8 μL mg⁻¹) to demonstrate their potential application in practical LSBs. As shown in Figure 19a, high sulfur loading cells exhibited an excellent rate performance, with areal capacities of 5.70 mAh cm⁻² at 0.1C, and 4.12 mAh cm⁻² at 0.5C, *i.e.* exceeding the industrially requested areal capacity of LIBs (~4 mAh cm⁻²).^[60] The corresponding charge/discharge profiles at different current rates are shown in Figure 19b. With the current rate increasing to 0.5C, the discharge profile still presented the intact second plateau, demonstrating excellent electrochemical kinetics within the cell. The performance of the cell under lean electrolyte conditions, with an electrolyte/sulfur ratio of 8 μL mg⁻¹, is displayed in Figure 19c. At a current rate of 0.5C, the initial discharge capacity was 527 mAh g⁻¹ and it rapidly increased to 686 mAh g⁻¹ after 15 cycles. After 300 cycles, a capacity of 576 mAh g⁻¹ was still measured, which corresponds to an ultralow capacity decay of 0.053% per cycle with respect to the maximum achieved capacity. Besides, I-Bi₂Se₃-based cells maintained the voltage profile during the 300

cycles, with just a small potential hysteresis, indicating a minor LiPS shuttling and stable sulfur electrochemistry (Figure 20).

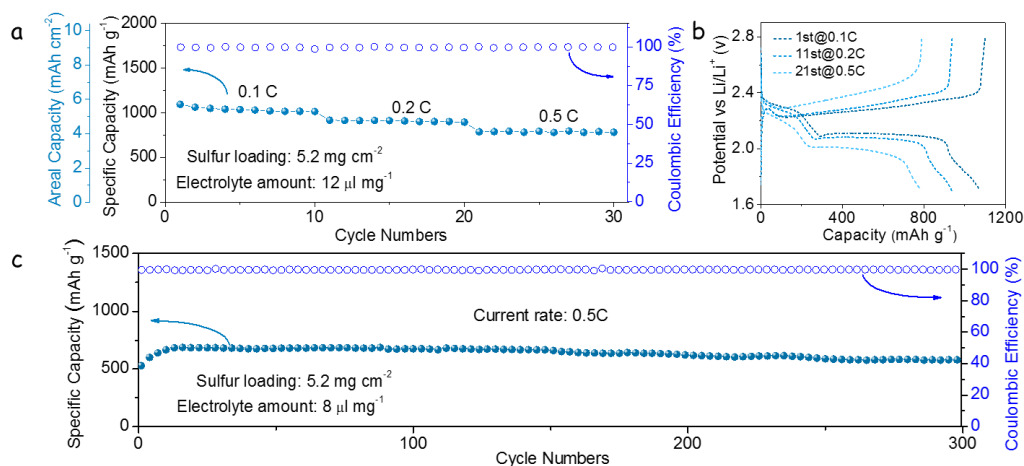


Figure 19. (a) Rate performance of the Li–S coin cells at different current rates with a sulfur loading of 5.2 mg cm⁻². (b) Initial charge/discharge profiles at the various current rates. (c) Cycling performances of I-Bi₂Se₃/S cathodes at a current rate of 0.5C under lean electrolyte conditions.

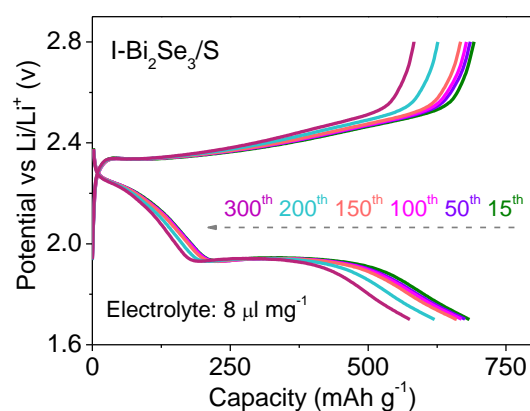


Figure 20. Galvanostatic charge/discharge profiles of I-Bi₂Se₃/S at 0.5C under a lean electrolyte condition with a high sulfur loading of 5.2 mg cm⁻².

Figure 5d and Table S1 display a comparison of several parameters of state-of-the-art Bi-based and Se-based materials as cathode hosts for LSBs. Notice that the I-Bi₂Se₃ host presented here is characterized by the highest capacities and stabilities. This strategy offers a new route to design multifunctional sulfur immobilizer with highly adoptive and catalytic capabilities for

rapid LiPS adsorption-conversion process, holding a great promise in promoting the practical application of LSBs.

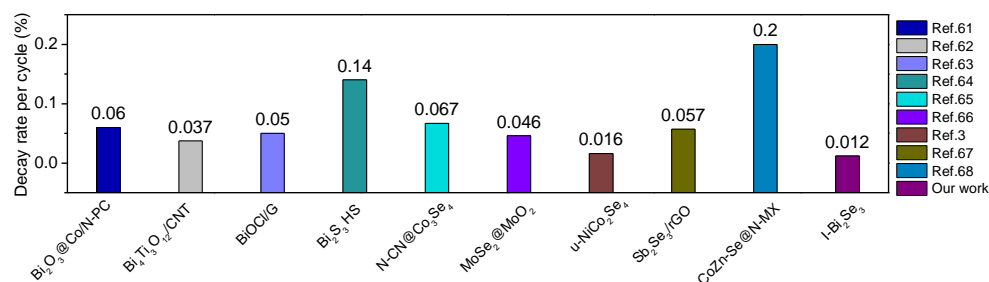


Figure 21. Decay rate per cycle compared with other reported works.

Table 1 Summary of the comparison of I-Bi₂Se₃ electrochemical performance as host cathode for LSBs with state-of-the-art Bi-based or Se-based materials.

Host material	Capacity (mAh g ⁻¹) (current rate)	Cycling stability(%) (cycles, current rate)	Decay rate (per cycle, %)	S content (wt%)	Ref
Bi ₂ O ₃ @Co/N-PC	1086 (0.25C)	70% (500, 1.5C)	0.06%	62.7%	[2]
Bi ₄ Ti ₃ O ₁₂ /CNT	1256 (0.1C)	63% (1000, 1C)	0.037%	72.5%	[3]
BiOCl/G	1414 (0.1C)	85% (200, 0.2C)	0.05%	69%	[4]
Bi ₂ S ₃ HS	1051 (0.1C)	30% (500, 1C)	0.14%	64%	[5]
N-CN@Co ₃ Se ₄	1437 (0.1C)	46% (800, 0.2C)	0.067%	61.5%	[6]
MoSe ₂ @MoO ₂	1205 (0.1C)	77% (500, 0.5C)	0.046%	66%	[7]
u-NiCo ₂ Se ₄	1330 (0.1C)	68.6% (2000, 3C)	0.016%	70%	[8]
Sb ₂ Se ₃ /rGO	1160 (0.2C)	71.5% (500, 1C)	0.057%	70%	[9]
CoZn-Se@N-MX	1270 (0.2C)	80% (100, 0.2C)	0.2%	70%	[10]
I-Bi₂Se₃	1496 (0.1C)	88% (1000, 1C)	0.012%	70.2%	Our work

4.5 Conclusions

In summary, we rationally designed and engineered new LSBs cathodes based on I-Bi₂Se₃ sulfur hosts through a facile and efficient strategy. This unique architecture not only establishes a conductive framework for electron/ion transfer and buffers the volume variation of the sulfur cathode during cycling, but also constructs a multifunctional LiPS barrier that effectively suppresses polysulfide shuttling. I-Bi₂Se₃ was characterized by a high electrical conductivity due to the doping of iodine and significantly enhanced the redox kinetics of sulfur species, especially for the conversion between soluble LiPS species and Li₂S₂/Li₂S during charge/discharge processes. As a result of these excellent qualities, I-Bi₂Se₃/S cathodes deliver excellent long-term cycling stability with a capacity decay of 0.012% per cycle over 1000 cycles at 1C. Moreover, at a sulfur loading of 5.2 mg cm⁻², I-Bi₂Se₃/S cathodes delivered a high areal capacity of 5.70 mAh cm⁻². Overall, this work shows an effective way to enhance the performance of LSB cathodes by the heteroatom doping of a MSe catalyst.

4.6 References

- [1] J. Zheng, J. Tian, D. Wu, M. Gu, W. Xu, C. Wang, F. Gao, M. H. Engelhard, J. G. Zhang, J. Liu, J. Xiao, *Nano Lett.* **2014**, *14*, 2345–2352.
- [2] Z. Wang, B. Wang, Y. Yang, Y. Cui, Z. Wang, B. Chen, G. Qian, *ACS Appl. Mater. Interfaces* **2015**, *7*, 20999–21004.
- [3] C. Zhang, J. J. Biendicho, T. Zhang, R. Du, J. Li, X. Yang, J. Arbiol, Y. Zhou, J. R. Morante, A. Cabot, *Adv. Funct. Mater.* **2019**, *29*, 1903842.
- [4] Y. Song, Y. Peng, M. Zhao, Y. Lu, J. Liu, B. Li, Q. Zhang, *Small Sci.* **2021**, *1*, 2100042.
- [5] D. Yang, Z. Liang, C. Zhang, J. J. Biendicho, M. Botifoll, M. C. Spadaro, Q. Chen, M. Li, A. Ramon, A. O. Moghaddam, J. Llorca, J. Wang, J. R. Morante, J. Arbiol, S. L. Chou, A. Cabot, *Adv. Energy Mater.* **2021**, *11*, 2101250.
- [6] S. Bai, X. Liu, K. Zhu, S. Wu, H. Zhou, *Nat. Energy* **2016**, *1*, 16049.
- [7] C. Zhao, X. Dai, T. Yao, W. Chen, X. Wang, J. Wang, J. Yang, S. Wei, Y. Wu, Y. Li, *J. Am. Chem. Soc.* **2017**, *139*, 8078–8081.
- [8] C. Zheng, S. Niu, W. Lv, G. Zhou, J. Li, S. Fan, Y. Deng, Z. Pan, B. Li, F. Kang, Q. H. Yang, *Nano Energy* **2017**, *33*, 306–312.

- [9] S. Tu, X. Chen, X. Zhao, M. Cheng, P. Xiong, Y. He, Q. Zhang, Y. Xu, *Adv. Mater.* **2018**, *30*, 1804581.
- [10] H. Jiang, X.-C. Liu, Y. Wu, Y. Shu, X. Gong, F.-S. Ke, H. Deng, *Angew. Chemie* **2018**, *130*, 3980–3985.
- [11] M. Tian, F. Pei, M. Yao, Z. Fu, L. Lin, G. Wu, G. Xu, H. Kitagawa, X. Fang, *Energy Storage Mater.* **2019**, *21*, 14–21.
- [12] X. J. Hong, C. L. Song, Y. Yang, H. C. Tan, G. H. Li, Y. P. Cai, H. Wang, *ACS Nano* **2019**, *13*, 1923–1931.
- [13] Y. Chen, W. Zhang, D. Zhou, H. Tian, D. Su, C. Wang, D. Stockdale, F. Kang, B. Li, G. Wang, *ACS Nano* **2019**, *13*, 4731–4741.
- [14] J. Shen, X. Xu, J. Liu, Z. Liu, F. Li, R. Hu, J. Liu, X. Hou, Y. Feng, Y. Yu, M. Zhu, *ACS Nano* **2019**, *13*, 8986–8996.
- [15] B. Jin, L. Yang, J. Zhang, Y. Cai, J. Zhu, J. Lu, Y. Hou, Q. He, H. Xing, X. Zhan, F. Chen, Q. Zhang, *Adv. Energy Mater.* **2019**, *9*, 1902938.
- [16] Z. Li, Z. Xiao, S. Wang, Z. Cheng, P. Li, R. Wang, *Adv. Funct. Mater.* **2019**, *29*, 1902322.
- [17] J. Xie, B. Q. Li, H. J. Peng, Y. W. Song, M. Zhao, X. Chen, Q. Zhang, J. Q. Huang, *Adv. Mater.* **2019**, *31*, 1903813.
- [18] L. Zhang, D. Liu, Z. Muhammad, F. Wan, W. Xie, Y. Wang, L. Song, Z. Niu, J. Chen, *Adv. Mater.* **2019**, *31*, 1903955.
- [19] H. Chen, Y. Xiao, C. Chen, J. Yang, C. Gao, Y. Chen, J. Wu, Y. Shen, W. Zhang, S. Li, F. Huo, B. Zheng, *ACS Appl. Mater. Interfaces* **2019**, *11*, 11459–11465.
- [20] Y. He, Y. Qiao, Z. Chang, X. Cao, M. Jia, P. He, H. Zhou, *Angew. Chemie* **2019**, *131*, 11900–11904.
- [21] B. Li, L. Kong, C. Zhao, Q. Jin, X. Chen, H. Peng, J. Qin, J. Chen, H. Yuan, Q. Zhang, J. Huang, *InfoMat* **2019**, *1*, 533–541.
- [22] Y. Zheng, S. Zheng, H. Xue, H. Pang, *J. Mater. Chem. A* **2019**, *7*, 3469–3491.
- [23] H. Chu, H. Noh, Y. J. Kim, S. Yuk, J. H. Lee, J. Lee, H. Kwack, Y. K. Kim, D. K. Yang, H. T. Kim, *Nat. Commun.* **2019**, *10*, 188.

- [24] S. Zhou, S. Yang, S. Yang, X. Ding, Y. Lai, H. Nie, Y. Zhang, D. Chan, H. Duan, S. Huang, Z. Yang, *ACS Nano* **2020**, *14*, 7538–7551.
- [25] L. Luo, J. Li, H. Yaghoobnejad Asl, A. Manthiram, *ACS Energy Lett.* **2020**, *5*, 1177–1185.
- [26] Z. Sun, S. Vijay, H. H. Heenen, A. Y. S. Eng, W. Tu, Y. Zhao, S. W. Koh, P. Gao, Z. W. Seh, K. Chan, H. Li, *Adv. Energy Mater.* **2020**, *10*, 201904010.
- [27] Z. Cheng, Y. Wang, W. Zhang, M. Xu, *ACS Appl. Energy Mater.* **2020**, *3*, 4523–4530.
- [28] G. Li, F. Lu, X. Dou, X. Wang, D. Luo, H. Sun, A. Yu, Z. Chen, *J. Am. Chem. Soc.* **2020**, *142*, 3583–3592.
- [29] W. Liu, C. Luo, S. Zhang, B. Zhang, J. Ma, X. Wang, W. Liu, Z. Li, Q. H. Yang, W. Lv, *ACS Nano* **2021**, *15*, 7491–7499.
- [30] T. Feng, T. Zhao, S. Zhu, N. Zhang, Z. Wei, K. Wang, L. Li, F. Wu, R. Chen, *Small Methods* **2021**, *5*, 1–10.
- [31] Z. Ma, Y. Liu, J. Gautam, W. Liu, A. N. Chishti, J. Gu, G. Yang, Z. Wu, J. Xie, M. Chen, L. Ni, G. Diao, *Small* **2021**, *17*, 2102710.
- [32] X. Zhou, R. Meng, N. Zhong, S. Yin, G. Ma, X. Liang, *Small Methods* **2021**, *5*, 2100571.
- [33] D. Yang, C. Zhang, J. J. Biendicho, X. Han, Z. Liang, R. Du, M. Li, J. Li, J. Arbiol, J. Llorca, Y. Zhou, J. R. Morante, A. Cabot, *ACS Nano* **2020**, *14*, 15492–15504.
- [34] Y. Zhang, S. Yang, S. Zhou, L. Zhang, B. Gu, Y. Dong, S. Kong, D. Cai, G. Fang, H. Nie, Z. Yang, *Chem. Commun.* **2021**, *57*, 3255–3258.
- [35] Y. Zhang, J. Liu, J. Wang, Y. Zhao, D. Luo, A. Yu, X. Wang, Z. Chen, *Angew. Chemie* **2021**, 202108882.
- [36] Y. Li, S. Lin, D. Wang, T. Gao, J. Song, P. Zhou, Z. Xu, Z. Yang, N. Xiao, S. Guo, *Adv. Mater.* **2020**, *32*, 1906722.
- [37] S. Li, J. Lin, Y. Ding, P. Xu, X. Guo, W. Xiong, D.-Y. Wu, Q. Dong, J. Chen, L. Zhang, *ACS Nano* **2021**, *15*, 13803–13813.
- [38] T. Zhang, F. Hu, W. Shao, S. Liu, H. Peng, Z. Song, C. Song, N. Li, X. Jian, *ACS Nano* **2021**, *15*, 15027–15038.

- [39] H. Lin, H. Shi, Z. Wang, Y. Mu, S. Li, J. Zhao, J. Guo, B. Yang, Z. Wu, F. Liu, *ACS Nano* **2021**, DOI 10.1021/acsnano.1c04961.
- [40] T. Yang, J. Xia, Z. Piao, L. Yang, S. Zhang, Y. Xing, G. Zhou, *ACS Nano* **2021**, *15*, 13901–13923.
- [41] C. Zhang, R. Du, J. J. Biendicho, M. Yi, K. Xiao, D. Yang, T. Zhang, X. Wang, J. Arbiol, J. Llorca, Y. Zhou, J. R. Morante, A. Cabot, *Adv. Energy Mater.* **2021**, *11*, 1–14.
- [42] M. Li, Y. Zhang, T. Zhang, Y. Zuo, K. Xiao, J. Arbiol, J. Llorca, Y. Liu, A. Cabot, *Nanomaterials* **2021**, *11*, 1827.
- [43] M. Hong, Z. G. Chen, L. Yang, G. Han, J. Zou, *Adv. Electron. Mater.* **2015**, *1*, 1–9.
- [44] P. H. Le, K. H. Wu, C. W. Luo, J. Leu, *Thin Solid Films* **2013**, *534*, 659–665.
- [45] A. J. Green, S. Dey, Y. Q. An, B. O’Brien, S. O’Mullane, B. Thiel, A. C. Diebold, *J. Vac. Sci. Technol. A Vacuum, Surfaces, Film.* **2016**, *34*, 061403.
- [46] T. Li, Y. Hu, C. A. Morrison, W. Wu, H. Han, N. Robertson, *Sustain. Energy Fuels* **2017**, *1*, 308–316.
- [47] J. Betancourt, S. Li, X. Dang, J. D. Burton, E. Y. Tsybal, J. P. Velev, *J. Phys. Condens. Matter* **2016**, *28*, 395501.
- [48] Z. Li, P. Li, X. Meng, Z. Lin, R. Wang, *Adv. Mater.* **2021**, *33*, 2102338.
- [49] S. Kim, W.-G. Lim, H. Im, M. Ban, J. W. Han, J. Lee, J. Hwang, J. Lee, *J. Am. Chem. Soc.* **2021**, *143*, 15644–15652.
- [50] H. Zhang, L. K. Ono, G. Tong, Y. Liu, Y. Qi, *Nat. Commun.* **2021**, *12*, 4738.
- [51] W. Xiao, W. Weng, J. Xiao, Y. Shen, X. Liang, T. Lv, *Angew. Chemie* **2021**, *60*, 202111707.
- [52] J. Kim, H. Shin, D. J. Yoo, S. Kang, S. Y. Chung, K. Char, J. W. Choi, *Adv. Funct. Mater.* **2021**, 2106679.
- [53] J. Liu, H. Li, J. Wang, Y. Zhang, D. Luo, Y. Zhao, Y. Li, A. Yu, X. Wang, Z. Chen, *Adv. Energy Mater.* **2021**, *11*, 2101926.
- [54] Y. Ji, K. Yang, M. Liu, S. Chen, X. Liu, B. Yang, Z. Wang, W. Huang, Z. Song, S. Xue, Y. Fu, L. Yang, T. S. Miller, F. Pan, *Adv. Funct. Mater.* **2021**, *31*, 2104830.
- [55] D. Cai, J. Yang, T. Liu, S. Zhao, G. Cao, *Nano Energy* **2021**, *89*, 106452.

- [56] Y. Huang, M. Shaibani, T. D. Gamot, M. Wang, P. Jovanović, M. C. Dilusha Cooray, M. S. Mirshekarloo, R. J. Mulder, N. V. Medhekar, M. R. Hill, M. Majumder, *Nat. Commun.* **2021**, *12*, 5375.
- [57] S. Chen, Z. Song, Y. Ji, K. Yang, J. Fang, L. Wang, Z. Wang, Y. Zhao, Y. Zhao, L. Yang, F. Pan, *Small Methods* **2021**, *5*, 2100839.
- [58] H. Kang, M. J. Park, *Nano Energy* **2021**, *89*, 106459.
- [59] D. Wang, K. Ma, J. Hao, W. Zhang, C. Wang, C. Xu, H. Shi, Z. Ji, X. Yan, Y. Gu, *Nano Energy* **2021**, *89*, 106426.
- [60] C. Shang, G. Li, B. Wei, J. Wang, R. Gao, Y. Tian, Q. Chen, Y. Zhang, L. Shui, G. Zhou, Y. Hu, Z. Chen, X. Wang, *Adv. Energy Mater.* **2021**, *11*, 2003020.
- [61] H. Liu, Z. Chen, L. Zhou, X. Li, K. Pei, J. Zhang, Y. Song, F. Fang, R. Che, D. Sun, *J. Mater. Chem. A* **2019**, *7*, 7074–7081.
- [62] Y. Zhou, H. Shu, Y. Zhou, T. Sun, M. Han, Y. Chen, M. Chen, Z. Chen, X. Yang, X. Wang, *J. Power Sources* **2020**, *453*, 227896.
- [63] X. Wu, N. Liu, M. Wang, Y. Qiu, B. Guan, D. Tian, Z. Guo, L. Fan, N. Zhang, *ACS Nano* **2019**, *13*, 13109–13115.
- [64] B. Long, Z. Qiao, J. Zhang, S. Zhang, M. S. Balogun, J. Lu, S. Song, Y. Tong, *J. Mater. Chem. A* **2019**, *7*, 11370–11378.
- [65] D. Cai, B. Liu, D. Zhu, D. Chen, M. Lu, J. Cao, Y. Wang, W. Huang, Y. Shao, H. Tu, W. Han, *Adv. Energy Mater.* **2020**, *10*, 1904273.
- [66] Q. Hao, G. Cui, Y. Zhang, J. Li, Z. Zhang, *Chem. Eng. J.* **2020**, *381*, 122672.
- [67] Y. Tian, G. Li, Y. Zhang, D. Luo, X. Wang, Y. Zhao, H. Liu, P. Ji, X. Du, J. Li, Z. Chen, *Adv. Mater.* **2020**, *32*, 1904876.
- [68] Z. Ye, Y. Jiang, L. Li, F. Wu, R. Chen, *Adv. Mater.* **2021**, *33*, 2101204.

Result and Discussions

LSBs attract extensive interest due to their high theoretical energy density (2600 Wh kg^{-1}) and low cost. However, several challenges remain to be overcome to realize their commercial deployment. First, the electrically insulating character of sulfur and lithium sulfide results in poor charge transport within the cathode, which limits rate capability and sulfur utilization. Besides, intermediate LiPS dissolve into the electrolyte and migrate from the cathode to the anode. This LiPS diffusion, which is known as the shuttle effect, results in the irreversible corrosion of the lithium anode and low Coulombic efficiency. Additionally, large volumetric variations of the sulfur cathode ($\approx 80\%$) during charge/discharge processes lead to poor cycling stability. Therefore, it is highly desired to develop a sulfur host that provides high electrical conductivity, effectively adsorbs LiPS and rapidly catalyze their redox conversion to solid $\text{Li}_2\text{S}_2/\text{Li}_2\text{S}$, blocking their dissolution, and which is able to accommodate large volume changes without disintegrating.

Firstly, I synthesized ZnSe nanoparticles decorating N-doped hollow polyhedrons (ZnSe/NHC) as a nanoreactor for stable LSBs. In terms of geometry, hollow structures and particularly hollow cages are a particularly interesting form of carbon. Hollow carbon materials can physically confine the polysulfides, preventing the shuttle effect and promoting their conversion reaction. In terms of composition, the use of N-doped carbon can not only improve electrical conductivity, but also promote LiPS adsorption through Li-N chemical binding. On the other hand, Zn compounds and particularly ZnO and ZnS have recently gained high interest as cathode material in LSBs owing to their good adsorption capability, notable catalytic activity toward polysulfide conversion and low cost. Thus we consider the still unexplored selenide, ZnSe, an excellent candidate to be combined with hollow N-doped hollow carbon as sulfur host in LSBs. Density functional theory calculations and experimental results clearly demonstrate the lithiophilic sites of NHC and sulfiphilic sites of ZnSe, realizing dual effect adsorption to effectively trap polysulfide. The hollow nanoreactor design not only promote redox reaction kinetics with the present of ZnSe, but also accommodates volumetric expansion and relieve the electrodes destroy.

Afterwards, I presented an in-situ grown $\text{C}_2\text{N}@\text{NbSe}_2$ heterostructure with remarkable specific surface area as Li-S catalyst and LiPS absorber. NbSe_2 is characterized by a relatively high density (5.74 g cm^{-3}) and a two-dimensional (2D) structure that makes nanostructured NbSe_2 prone to aggregation limiting its specific surface area (SSA). However, within the NbSe_2

crystal structure, Nb atoms are sandwiched between two layers of Se atoms, which limits the exposed highly active Nb atoms at the edges. Therefore, NbSe₂ need to be combined with a lightweight support that allows increasing the overall SSA and maximized the NbSe₂ exposed active sites at the edges. C₂N presents bridging N atoms that have associated a large π electron pool in the structure and generate intrinsic electron density (partially negative), which could act as excellent sites for the nucleation and growth of NbSe₂. Besides, the catalytic activity of catalysts can be significantly augmented by altering their electronic structures through tuning the surface/interface atom environment. Taking into account their band structure, we expect that combining C₂N and NbSe₂ within heterostructures, a charge rearrangement at the heterojunction interface will take place, potentially promoting catalytic activity and suppressing shuttle effect. Density functional theory (DFT) calculations and experimental results comprehensively demonstrate that C₂N@NbSe₂ is characterized by a suitable electronic structure and charge rearrangement that strongly accelerates the LiPS electrocatalytic conversion. Besides, heterostructured C₂N@NbSe₂ forms N-Li and Nb-S chemical bonds to trap LiPS species.

In addition, I used a low temperature and high yield, solution-based strategy to prepare Bi₂Se₃ nanosheets (NSs) doped with iodine elements. The layered structure of bismuth selenide and its good conductivity are very suitable for use as the promising sulfur hosts at LSBs cathodes. The variable valence characteristic of a Bi cation can provide the possibility for a high catalytic effect. Moreover, engineering non-metallic atomic defects into nanomaterials has been reported as an effective way to regulate its electronic structure, relieve polarization and increase the active sites to LiPS, which in turn improves the device performance. Thus we studied the performance of LSBs based on Bi₂Se₃ and I@Bi₂Se₃ NSs both experimentally and through theoretical calculations. The results show the I@Bi₂Se₃ NSs have high conductivity for rapid electron transfer, enhanced confinement of LiPS, mitigation of volume expansion effects, and a catalytic enhancement of the electrochemical reaction kinetics.

Conclusions

In this thesis, I detailed the production and characterization of sulfur hosts of LSBs by two main solution-processed strategies, with remarkably improved LSBs performance by means of controllable nanoengineering. The characterization of nanomaterials has been investigated in detail in each chapter, including: NC phase, morphology, optical property, surface chemistry, etc. Two main optimization methodologies to achieve higher LSBs performance were specifically explored in this thesis: atomic doping and heterostructure formation. The related mechanism to improved LSBs performance was further analysed to explain how to achieve the desired LSBs properties.

In the first part, I demonstrated a rational design and engineering of LSBs cathodes based on ZnSe/NHC sulfur hosts with multiple adsorption sites and high catalytic activity can improve LSB performance. I demonstrated that the hollow geometry not only provides an accommodation for sulfur giving rise to a high stable cyclability, but also integrates LiPS physical separation and promotes and enhances the chemical reaction in this ZnSe/NHC structures that are functionally working like a nanoreactor. ZnSe with sulfiphilic sites and NHC with lithiophilic sites, respectively, were confirmed by experimental results and DFT calculations, showing a strong LiPS adsorbability. At the same time, unlike other compounds, the selenide nanoparticles, ZnSe, facilitated and enhance redox kinetics of LiPS conversion reaction during charge/discharge processes thus improving the sulfur utilization that was revealed by kinetic investigations. These merits contribute to outstanding electrochemical performances of the LSBs with ZnSe/NHC as sulfur hosts. As a result, S@ZnSe/NHC cathode delivered excellent performances, including a reversible capacity of 540.5 mAh g⁻¹ after 600 cycles at 1 C at a relatively high sulfur loading of 3.2 mg cm⁻². This work not only broadened the application of selenides materials in the field of LSBs, but also proved the designed nanoreactors with multiple adsorption sites serving as sulfur hosts, showing superior electrochemical properties for LSBs.

In the second part, I rationally designed and engineered a new and high-performance LSB cathode based on an in-situ grown C₂N@NbSe₂ heterostructured catalyst. I used a facile and effective two-step strategy to produce the composites with a nanosheet geometry that provided outstanding specific surface areas up to 389.6 m² g⁻¹. I demonstrated that the unique architecture of the C₂N@NbSe₂ nanosheets delivered a conductive framework for electron/ion transfer and a cushion to mitigate the effect of the volume variation of the sulfur cathode during

cycling. DFT calculations and experimental results comprehensively demonstrated that $C_2N@NbSe_2$ was characterized by a suitable electronic structure and charge rearrangement, that not only accelerated the LiPS conversion and lowered the energy barrier for Li_2S precipitation/decomposition, but also strongly promoted LiPS adsorption through Li-N and Nb-S bonds. Consistent with these excellent qualities, $C_2N@NbSe_2/S$ cathodes delivered exceptional long-term cycling stability with a very low capacity decay of 0.012% per cycle over 2000 cycles at 3 C, with only a total of 3.3% capacity loss in the last 1500 cycles, and exceptional rate performance of 683 mAh g^{-1} at 5 C. Moreover, $C_2N@NbSe_2/S$ cathodes delivered a high areal capacity of 5.65 mAh cm^{-2} at a sulfur loading of 5.6 mg cm^{-2} . This work not only emphasized the potential capabilities of TMs and particularly the so far unexplored $NbSe_2$, but also proposed heterostructured architectures as highly effective catalyst for the Li-S reaction.

In the third part, I rationally designed and engineered new LSBs cathodes based on I- Bi_2Se_3 sulfur hosts through a facile and efficient strategy. I demonstrated that this unique architecture not only establishes a conductive framework for electron/ion transfer and buffers the volume variation of the sulfur cathode during cycling, but also constructs a multifunctional LiPS barrier that effectively suppresses polysulfide shuttling. I- Bi_2Se_3 was characterized by a high electrical conductivity due to the doping of iodine and significantly enhanced the redox kinetics of sulfur species, especially for the conversion between soluble LiPS species and Li_2S_2/Li_2S during charge/discharge processes. As a result of these excellent qualities, I- Bi_2Se_3/S cathodes delivered excellent long-term cycling stability with a capacity decay of 0.012% per cycle over 1000 cycles at 1C. Moreover, at a sulfur loading of 5.2 mg cm^{-2} , I- Bi_2Se_3/S cathodes delivered a high areal capacity of 5.70 mAh cm^{-2} . Overall, this work showed an effective way to enhance the performance of LSBs cathodes by the heteroatom doping of a MSe catalyst.

In summary, this thesis has detailed different strategies to improve LSB performance by optimizing cathode host nanomaterials produced from solution processed methods. In addition, it demonstrated that solution processed synthesis appears to be a high-throughput, high yield, low cost, feasible at ambient pressure and low temperature chemical routes, which allows production of LSBs materials with composition, size, shape and phases control to optimize their LSBs properties.

Future work

Increasing the speed of transformations between the captured LiPS and the insoluble $\text{Li}_2\text{S}_2/\text{Li}_2\text{S}$ is key to suppressing the shuttle effect, and combining the “positive” catalytic effects with the “passive” approaches of physical and chemical confinement shows a much more promising way to solve the shuttling of LiPS, which is expected as a final solution to the development of high performance and practical LSBs. I will continue my research in the future in the following areas:

- i) Development of novel sulfur host materials based on low-cost metal selenides.
- ii) Designing sulfur hosts based on defect engineering that can tailor the electronic structures of these polar inorganics toward enhanced conductive features as well as interactive affinity. It will offer a promising approach to concurrently realize strong sulfur confinement and expedite the LiPS conversion in Li–S systems
- iii) To further improve the property of Bi_2Se_3 -based cathodes, the doping with alkaline metal will allow additional tuning of the DOS and bandgap, which should be a promising strategy to further enhance their activity for LiPS conversion.
- iv) Designing an out/in-plane heterostructure, which is built with interfaced highly adsorptive component and catalytic component, will be also an effective way to realize a smooth trapping–diffusion–conversion of LiPS and finally obtain an ultra-long life LSBs.
- v) To develop new sulfur host materials based on scalable solution synthesis method, with high LSBs performance, further fabrication of devices, and proving the LSB cost-effectiveness at the device level
- vi) To optimize the polysulfides adsorption-catalysis process in LSBs, an integrated catalyst comprising isolated metal atoms can improve the reversible conversion of intercepted polysulfides and inhibits the shuttle effect during charge/discharge process. These outcomes will open a new avenue for practically feasible, high-efficiency, and long-lasting LSBs.

CURRICULUM VITAE

Personal Information

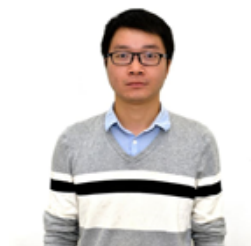
Name: Dawei Yang

Address: Jardins de les Dones de Negre, 1, Barcelona

Tel: +86 18351232461

Email: daweiirec@163.com

Date of Birth: July 20, 1992



Education

- 2018.10-present: PhD, Nanoscience, Catalonia Institute for Energy Research-IREC, University of Barcelona, Spain
Thesis: Metal selenide-based cathodes for high-performance lithium-sulfur batteries
Supervisor: Prof. Andreu Cabot
- 2015.9-2018.7: Master, Chemical Engineering, Southeast University, China
- 2011.9-2015.7: Bachelor, Applied Chemistry, Anhui Jianzhu University, China

Research Experience

My PhD research is focused on optimizing lithium-sulfur batteries performance based on metal selenide cathodes (ZnSe, NbSe₂, Bi₂Se₃, Cu_{2-x}Se). My research experience mainly covers:

- ✧ Solution synthesis of nanocrystals
- ✧ Bottom-up processed lithium-sulfur batteries nanomaterials
- ✧ Designing a sulfur host with heterostructure to realize a smooth trapping-diffusion-conversion of LiPS
- ✧ To further enhance the catalytic activity for LiPS conversion, the doping/defect was introduced within the sulfur host

Research Projects

1. **National natural science foundation project of China (2018-2021)**, “*The surface of the metal oxide oxygen vacancy on the effect of electron transport in the photoelectric conversion device*”, (61774033), participant , ¥640000.

2. **Jiangsu province science and technology department (2017-2020)**, “MoS₂ controllable

preparation of core-shell nano array structure and photoelectric catalysis performance”, participant , ¥200000.

Awards

- Nov. 2015 First-class scholarship Southeast University
- Nov. 2016 First-class scholarship Southeast University
- 2016-2017 Merit graduate student Southeast University
- 2017-2018 Outstanding graduate student Southeast University
- May. 2018 Chinese Scholarship Council

Conferences

Energy Chemistry Frontiers Question Symposium (Poster) 2016.12 Nanjing

- ◆ Theme: Supercapacitors, Lithium ion batteries, Sodium ion batteries, Fuel cell and etc.

The 2nd Inorganic Chemistry Frontiers International Symposium (Poster)

- ◆ Theme: Inorganic materials, Coordination chemistry and etc.

2017.03 Nanjing university

The 3rd International Symposium on Energy Conversion and Storage

- ◆ Lithium Ion Battery, Electrocatalysis and etc.

2017.06 Nanjing university

Nanjing Forum 2017

- ◆ Theme: Focus on frontier science, look forward cutting-edge technology for the future

2017.10 Nanjing university

The Heraeus "Exciting nanostructures" Conference in Bad Honnef (July 2019)

- ◆ Theme: Materials Synthesis, Morphology and etc. Technische Universität München

Publications

1. **Dawei Yang**, Zhifu Liang, Pengyi Tang, Chaoqi Zhang, Mingxue Tang, Qizhen Li, Jordi Jacas Biendicho, Junshan Li, Marc Heggen, Rafal E. Dunin-Borkowski, Ming Xu*, Jordi Llorca, Jordi Arbiol*, Joan Ramon Morante, Shu-Lei Chou*, Andreu Cabot,* *A High Conductivity 1D π -d Conjugated Metal–Organic Framework with Efficient Polysulfide Trapping-Diffusion-Catalysis in Lithium–Sulfur Batteries.* **Adv. Mater.** DOI: 10.1002/adma.202108835 (IF: 30.849).
2. **Dawei Yang**, Zhifu Liang, Chaoqi Zhang*, Jordi Jacas Biendicho, Marc Botifoll, Maria Chiara Spadaro, Qiulin Chen, Mengyao Li, Alberto Ramon, Ahmad Ostovari Moghaddam, Jordi Llorca, Jiaao Wang*, Joan Ramon Morante, Jordi Arbiol, Shu-Lei Chou*, Andreu

- Cabot,* *NbSe₂ Meets C₂N: A 2D-2D Heterostructure Catalysts as Multifunctional Polysulfide Mediator in Ultra-Long-Life Lithium–Sulfur Batteries. **Adv. Energy Mater.** 2021, 11, 2101250. (IF: 29.368).*
3. **Dawei Yang**, Chaoqi Zhang*, Jordi Jacas Biendicho, Xu Han, Zhifu Liang, Ruifeng Du, Mengyao Li, Junshan Li, Jordi Arbiol, Jordi Llorca, Yingtang Zhou*, Joan Ramon Morante, and Andreu Cabot,* *ZnSe/N-Doped Carbon Nanoreactor with Multiple Adsorption Sites for Stable Lithium–Sulfur Batteries. **ACS Nano** 2020, 14, 11, 15492–15504. (IF: 15.881).*
 4. Zhifu Liang#, **Dawei Yang**#, (Co-first author) Pengyi Tang#, Chaoqi Zhang, Jordi Jacas Biendicho, Yi Zhang, Jordi Llorca, Xiang Wang, Junshan Li, Marc Heggen, Jeremy David, Rafal E. Dunin-Borkowski, Yingtang Zhou*, Joan Ramon Morante, Andreu Cabot*, Jordi Arbiol,* *Atomically dispersed Fe in a C₂N Based Catalyst as a Sulfur Host for Efficient Lithium–Sulfur Batteries. **Adv. Energy Mater.** 2021, 11, 2003507. (IF: 29.368).*
 5. Mengyao Li#, **Dawei Yang**#,* (Co-first author and Corresponding Author) Jordi Jacas Biendicho, Xu Han, Chaoqi Zhang, Kun Liu, Jiefeng Diao, Junshan Li, Marc Heggen, Rafal E. Dunin-Borkowski, Jiaao Wang*, Graeme Henkelman, Joan Ramon Morante, Jordi Arbiol, Shu-Lei Chou*, Andreu Cabot,* *Enhanced Polysulfide Conversion with Highly Conductive and Electrocatalytic Iodine-Doped Bismuth Selenide Nanosheets in Lithium-Sulfur Batteries. **Adv. Funct. Mater.** DOI: 10.1002/adfm.202200529 (IF: 18.808).*
 6. **Dawei Yang**, Yuqiao Wang*, Qiuyu Wang, Wen Wang, Tao Wei*, Yueming Sun, *Preparation and supercapacitive properties of hierarchical ZnCo₂O₄@Ni₃S₂ core/shell nanowire arrays on Ni foam. **Mater. Lett.** 2018, 213, 222-226. (IF: 3.423).*
 7. Yuqiao Wang*, **Dawei Yang**, (Tutor is the first author) Jianing Lian, Jie Pan, Tao Wei*, Yueming Sun, *Cedar leaf-like CuCo₂O₄ directly grow on nickel foam by a hydrothermal/annealing process as an electrode for a high-performance symmetric supercapacitor. **J. Alloys Compd.** 2018, 735, 2046-2052. (IF: 5.316).*
 8. Yuqiao Wang*, **Dawei Yang**, (Tutor is the first author) Jianing Lian, Tao Wei*, Yueming Sun, *Ordered corn-like CuCo₂O₄ nanoforests covering Ni foam for a high-performance all-solid-state supercapacitor. **J. Alloys Compd.** 2018, 741, 527-531. (IF: 5.316).*
 9. Yuqiao Wang*, **Dawei Yang**, (Tutor is the first author) Tianyue Zhou, Jie Pan, Tao Wei*, Yueming Sun, *Oriented CuCo₂S₄ nanograss arrays/Ni foam as an electrode for a high-*

- performance all-solid-state supercapacitor. Nanotechnology* 2017, 28, 465402. (IF: 3.874).
10. **Dawei Yang**, Mengyao Li*, Xuejiao Zheng, Xu Han, Chaoqi Zhang, Jordi Jacas Biendicho, Jordi Llorca, Jiaao Wang, Hongchang Hao, Junshan Li, Graeme Henkelman, Jordi Arbiol, Joan Ramon Morante, David Mitlin, Shu-Lei Chou*, Andreu Cabot,* *Synergistically Induce Enhanced Electrochemical Kinetics by Phase Engineering of Defective Copper Selenide toward Robust Lithium-Sulfur Batteries. Energy Environ. Sci. (Under Review).*
 11. Chaoqi Zhang, Ban Fei, **Dawei Yang**, Hongbing Zhan, Jiaao Wang, Jiefeng Diao, Junshan Li, Graeme Henkelman, Daoping Cai, Jordi Jacas Biendicho, Joan Ramon Morante, Andreu Cabot,* *Robust Lithium-Sulfur Batteries Enabled by Highly Conductive WSe₂-based Superlattices with Tunable Interlayer Space. Adv. Funct. Mater. DOI: 10.1002/adfm.202201322 (IF: 18.808).*
 12. Chaoqi Zhang, Ruifeng Du, Jordi Jacas Biendicho, Mingjie Yi, Ke Xiao, **Dawei Yang**, Ting Zhang, Xiang Wang, Jordi Arbiol, Jordi Llorca, Yingtang Zhou*, Joan Ramon Morante, Andreu Cabot,* *Tubular CoFeP@CN as a Mott–Schottky Catalyst with Multiple Adsorption Sites for Robust Lithium–Sulfur Batteries. Adv. Energy Mater.* 2021, 11, 2100432. (IF: 29.368).
 13. Mengyao Li, Yu Liu*, Yu Zhang, Cheng Chang, Ting Zhang, **Dawei Yang**, Ke Xiao, Jordi Arbiol, Maria Ibáñez, Andreu Cabot,* *Room temperature aqueous-based synthesis of copper-doped lead sulfide nanoparticles for thermoelectric application. Chem. Eng. J.* <https://doi.org/10.1016/j.cej.2021.133837>. (IF: 13.273).
 14. Junshan Li, Xijun Xu, Xiaoting Yu, Xu Han, Ting Zhang, Yong Zuo, Chaoqi Zhang, **Dawei Yang**, Xiang Wang, Zhishan Luo, Jordi Arbiol, Jordi Llorca, Jun Liu*, and Andreu Cabot,* *Monodisperse CoSn and NiSn Nanoparticles Supported on Commercial Carbon as Anode for Lithium- and Potassium-Ion Batteries. ACS Appl. Mater. Interfaces* 2020, 12, 4, 4414–4422. (IF: 9.229).

Annex